

**Simulation of chiral ordering process  
in the adsorption of chiral organic molecules on metal surfaces  
by Monte Carlo methods**

by

Serge Olivier Ayissi

M.S. (Ecole Nationale Supérieure de Chimie (Clermont-ferrand, FRANCE)) 2003

A dissertation submitted in partial satisfaction  
of the requirements for the degree of

Doctor in Philosophy

in

Computational Physics/Chemistry

in the

CHEMISTRY DEPARTMENT

of the

UNIVERSITY OF LIVERPOOL, UNITED KINGDOM

Committee in charge:

Professor Axel Groß, External  
Doctor George Darling, Internal

January 2008

The dissertation of Serge Olivier Ayissi is approved:

---

Chair

Date

---

Date

---

Date

---

Date

University of Liverpool, United Kingdom

January 2008

**Simulation of chiral ordering process  
in the adsorption of chiral organic molecules on metal surfaces  
by Monte Carlo methods**

**Copyright 2008**

**by**

**Serge Olivier Ayissi**

## ABSTRACT

Simulation of chiral ordering process  
in the adsorption of chiral organic molecules on metal surfaces  
by Monte Carlo methods

by

Serge Olivier Ayissi

Doctor in Philosophy in Computational Physics/Chemistry

University of Liverpool, United Kingdom

Professor Werner Hofer

Experimental observations have shown that haloalkane molecules, e.g. 1-chlorododecane, physisorbed on Si(111)-(7 × 7) self-assemble to form dimers stable to 100° C which corral silicon adatoms. The corral size is governed by the haloalkane chain-length. Spectroscopic and theoretical evidence shows that the haloalkane dimer induces electron transfer to the corralled adatom. The enclosed silicon adatom, within a bistable dimeric corral of self-assembled chlorododecane molecules, switches its energy levels permanently (Type-II corrals) or discontinuously (Type-I corrals). Both types of corral, switching and stable, can be seen to alter the local surface charge distribution. Density Functional Theory and electron transport (STM) simulations of the switch and the stable molecular configurations can help the theoretical understanding of both phenomena in order to characterize the exact molecular conformations that produce field effects to the corralled silicon adatom and local surface charge distribution.

Chiral heterogeneous catalysts are mostly fabricated from chiral molecules on a metal support. They play a crucial role in intermediate reactions in the fabrication of pharmaceuticals, itself and important part of today's health economy. However, the key parameters in the fabrication of these catalysts, a requirements for their rational design, are still poorly

understood despite years of experimental research. In essence, such an understanding can only come from high-level simulations.

Here, we present the first predictions about the structure of such a catalyst, tartaric acid on a copper support, over the whole phase space of temperature and coverage. Interestingly, we find that molecular vibrations play a key role in the ensuing ordered structures, and that tuning the fabrication temperature should allow for a wide range of molecular separations, which can be targeted at specific molecules and reactions in chiral heterogeneous catalysis.

## DEDICATION

To my parents  
for letting me pursue my dream  
for so long  
and learning to be patient

&

To my brothers and sisters  
for giving me  
strength and good advices

## ACKNOWLEDGMENTS

I would like to thank my supervisor, Werner Hofer, for supporting me over the years, and for giving me so much freedom to explore and discover new areas of science especially theoretical physics and chemistry. His excellent communication skills added to a good sense of improvisation and a higher ambition helped the projects to be built around strong collaboration contacts and to be finished in a reasonable amount of time. Werner brought the science research to a higher level where good scientific skills are not enough to be successful! The scientist, today, has to be able to sell his results and to present them as clearly as possible for anyone to be able to understand.

I also thank him for giving me the opportunity to work with John Polanyi and his team. I did my work in such a way that they could understand our field of research and trust the accuracy of our calculation and simulation results. The collaboration with Karsten Reuter at the Fritz-Haber institut was a chance to step into the dynamic simulations and be able to develop a complicated Monte carlo program on our own. The difficulty of studying chiral behavior by these methods can still be overcome in a reasonable amount of time. The idea of trying to implement new parameters like the OH-bond vibration, as Werner told me so, turned out to be quite a good move forward! Werner's leadership and independence helped a group like ours to be competitive against bigger institutions and to be proud of our work. His lectures and weekly meetings have also proved to be very good learning experiences at the University of Liverpool.

I would also like to thank Karsten Reuter for welcoming me into his group in the Fritz-Haber institut in Berlin, and for teaching me Monte Carlo methods and statistical mechanics for almost a year. My special thanks go to Yongsheng Zhang, for the help he provided me on Monte Carlo and for his friendship.

I would like to thank my many friends and colleagues in the theory group with whom I have had the pleasure of working over the years. These include Mario Gattobigio, Krisztian Palotas, Gilberto Teobaldi, Haiping Lin, Linda Zotti, Helen Williams, Bozydar Wrona and

all the members of the postgraduate and postdoctoral office of the surface science research centre.

I would like to give special thanks to Edwin Kellenbach (Organon, Akzo Nobel) and Andre De Roy (Universite Blaise Pascal) for giving me the opportunity to work on their project of collaboration in 2002. This short period of time has been the most impressive scientific experience, for me being a student, between two powerful scientists that really showed me what competency and passion together were. I did the best I could to provide them a good work even if I missed some experience at that time, but then I learned so much. I still remember freshly the relevant advices Mr Kellenbach gave me regarding science, the scientists, and life in general.

I would also like to give special thanks to the Sol-Gel laboratory of the "Commissariat a l'Energie Atomique" (CEA) in Tours, France. First, working within this group was an excellent experience. I also more specifically thank Philippe Belleville, Philippe Prene for giving me the opportunity to express my talents and use my skills without barriers. The freedom they gave me to try everything I had in mind and to build serious collaborations by myself helped this project to succeed in 6 months only! The work I've done for the sol-gel laboratory is the best production I've done in science, even if the outcome had to stay confidential. Now I realize that this was a privilege, and this atmosphere is something I really miss. A special thank to Karine Valle for her friendship, and to the rest of the sol-gel team.



# Contents

<b>1</b>	<b>Introduction</b>	<b>1</b>
1.1	Motivation . . . . .	1
1.2	Objectives . . . . .	2
1.3	Outline . . . . .	3
1.3.1	Static Simulations . . . . .	3
1.3.2	Dynamic Simulations . . . . .	4
1.4	Organization of the Research . . . . .	4
1.4.1	Chlorododecane/Si(111) systems: Chapter 3 and 4 . . . . .	4
1.4.2	Monte Carlo on Bitartrate/Cu(110) system: Chapter 5 and 6 . . . . .	4
<b>2</b>	<b>Theoretical approach</b>	<b>5</b>
2.1	Adsorption of atoms and molecules . . . . .	6
2.2	The electronic regime . . . . .	10
2.2.1	Density functional theory . . . . .	11
2.2.2	Models to describe metallic surfaces . . . . .	14
2.2.3	Plane-wave basis sets . . . . .	14
2.2.4	Pseudopotentials . . . . .	15
2.2.5	Approximating the exchange-correlation functional . . . . .	18
2.3	The Vienna Ab initio Simulation Package . . . . .	21
2.4	The mesoscopic regime . . . . .	22
2.4.1	Thermodynamics . . . . .	23
2.4.2	Statistical mechanics . . . . .	23

2.4.3	The Ising and Ising-like models . . . . .	29
2.4.4	Monte Carlo Methods . . . . .	30
2.5	Multiscale modelling: bridging the regimes . . . . .	38
2.5.1	The lattice-gas model . . . . .	39
2.5.2	The cluster expansion method . . . . .	40
2.6	Summary . . . . .	46
<b>3</b>	<b>Self-assembled corrals on Si (111)-(7 × 7)</b>	<b>48</b>
3.1	Experimental methods and research . . . . .	48
3.1.1	STM imaging . . . . .	49
3.1.2	Halododecane molecules . . . . .	49
3.1.3	Halododecanes on Silicon(111)-(7 × 7) . . . . .	49
3.1.4	Type-II configuration of Chlorododecane . . . . .	53
3.1.5	Experimental results on TypeII-Chlorododecane . . . . .	53
3.2	TypeII-Chlorododecane adsorption energies and geometries . . . . .	57
3.2.1	Computational details . . . . .	57
3.2.2	Chlorododecane molecules in Vacuum . . . . .	57
3.2.3	Chlorododecane on Si(111)-(7 × 7) . . . . .	59
3.3	STM Simulations of Chlorododecane/Si111 systems . . . . .	60
3.3.1	STM simulations using bSKAN . . . . .	60
3.3.2	Dipole moments . . . . .	61
3.3.3	Summary . . . . .	62
<b>4</b>	<b>Electronic Switching of Single Silicon Atoms by Molecular Fields Effects</b>	<b>63</b>
4.1	Experiments . . . . .	63
4.1.1	Experimental methods and results . . . . .	63
4.1.2	Type-I corral formation mechanism . . . . .	64
4.1.3	Type-I configuration of Chlorododecane . . . . .	66
4.1.4	TypeI-Chlorododecane corral study . . . . .	66

4.2	Type-I Chlorododecane adsorption energies and geometries . . . . .	72
4.2.1	Computational details . . . . .	72
4.2.2	Cholododecane molecules in vacuum . . . . .	72
4.2.3	Type-I Chlorododecane/Si111 systems calculated by DFT . . . . .	73
4.3	STM Simulations on the TypeI-Chlorododecane/Si111 system . . . . .	74
<b>5</b>	<b>Monte Carlo and statistical mechanics for a simple model</b>	<b>78</b>
5.1	Order parameter . . . . .	79
5.1.1	Discrete Fourier transform . . . . .	79
5.1.2	The (2 × 2) ordering . . . . .	80
5.2	Thermodynamic approach . . . . .	82
5.2.1	Thermodynamics . . . . .	82
5.3	Statistical mechanics approach . . . . .	85
5.4	Theory of phase transitions . . . . .	88
5.4.1	Two-Dimensional phase transition . . . . .	89
5.5	Metropolis/Monte Carlo approach . . . . .	91
5.5.1	Limitations . . . . .	94
5.6	Wang-Landau/Monte Carlo approach . . . . .	95
5.7	Monte Carlo simulations on a simple model . . . . .	97
5.7.1	Order parameter . . . . .	97
5.7.2	Heat capacity . . . . .	98
5.8	Summary . . . . .	99
<b>6</b>	<b>Chiral Ordering Process in the Adsorption of Tartaric Acid Molecules on Cu(110)100</b>	
6.1	Experimental research . . . . .	101
6.1.1	STM imaging conditions . . . . .	101
6.1.2	Adsorption of Tartaric acid on Copper(110) . . . . .	101
6.2	Theoretical Research . . . . .	106
6.2.1	Phase transitions in two dimensions . . . . .	106

6.2.2	Molecular theory of 2D phase transitions . . . . .	109
6.2.3	Molecular vibrations . . . . .	111
6.3	Application to the Bi-tartrate/Cu(110) system . . . . .	115
6.3.1	Periodic Boundary conditions and limits of the system . . . . .	115
6.3.2	Lattice Gas Hamiltonian (LGH) . . . . .	115
6.3.3	LGH and Chirality for the R,R-Bitartrate/Cu110 system . . . . .	117
6.3.4	Lateral interactions . . . . .	117
6.4	Metropolis/Monte Carlo Simulations (First part) . . . . .	120
6.4.1	Simulations with complete Lattice Gas hamiltonian . . . . .	121
6.5	Metropolis/Monte Carlo Simulations (Second Part) . . . . .	124
6.5.1	Order parameter . . . . .	124
6.5.2	Vibration of the OH bonds of the R,R-bitartrate . . . . .	128
6.5.3	Implementing the OH bond vibration in the LGH . . . . .	130
6.5.4	Bitartrate/Cu(110) thermodynamic properties . . . . .	131
6.5.5	Diagrams of phase and ordering limits . . . . .	133
6.5.6	Summary . . . . .	135
<b>7</b>	<b>Conclusion</b> . . . . .	<b>137</b>
7.1	The Chlorododecane/Si(111) systems . . . . .	137
7.1.1	Stable corral . . . . .	137
7.1.2	Switching corral . . . . .	137
7.2	The Bitartrate/Cu(110) system . . . . .	138
7.2.1	First-principles calculations and ground state line . . . . .	138
7.2.2	Macroscopic study . . . . .	138
7.3	Final words . . . . .	139
<b>A</b>	<b>Metropolis/Monte carlo program on a simple model in Fortran 90</b> . . . . .	<b>140</b>
A.1	Diagram of Metropolis/Monte carlo step by step (canonical ensemble) . . . . .	140
A.2	Diagram of Metropolis/ Monte carlo in the canonical ensemble . . . . .	141

A.3	Main features of Metropolis/Monte carlo program . . . . .	142
A.4	Parameters of the simulations . . . . .	143
A.5	Initial configurations . . . . .	144
A.6	Metropolis probabilities to accept or reject a move . . . . .	145
A.7	Subroutine for the nearest neighbors detection . . . . .	146
A.8	Subroutine for the total energy of the system . . . . .	147
A.9	Subroutine for random selection of a particle . . . . .	148
A.10	Subroutines of the heat capacity $C_V$ and the order parameter $\Psi$ . . . . .	149
<b>B</b>	<b>Tartaric acid on Copper(110) / Lattice Gas Hamiltonian</b>	<b>150</b>
B.1	Clean surface . . . . .	150
B.2	Bitartrate ion . . . . .	150
B.3	Positions on Copper surfaces . . . . .	151
B.4	Adsorption energy of one molecule at the R position . . . . .	151
B.5	Adsorption energy of two molecules at R and A . . . . .	152
B.6	Adsorption energy of two molecules at R and E . . . . .	152
B.7	Adsorption energy of two molecules at R and B . . . . .	153
B.8	Adsorption energy of two molecules at R and D . . . . .	153
B.9	Adsorption energy of two molecules at R and C . . . . .	154
B.10	Adsorption energy of two molecules at T and Q . . . . .	154
B.11	Adsorption energy of two molecules at R and F . . . . .	155
B.12	Adsorption energy of two molecules at R and J . . . . .	155
B.13	Adsorption energy of two molecules at R and G . . . . .	156
B.14	Adsorption energy of two molecules at R and I . . . . .	156
B.15	Adsorption energy of two molecules at R and H . . . . .	157
B.16	Adsorption energy of two molecules at R and T . . . . .	157
B.17	Adsorption energy of two molecules at R and K . . . . .	158
B.18	Adsorption energy of two molecules at R and O . . . . .	158
B.19	Adsorption energy of two molecules at T and L . . . . .	159

B.20 Adsorption energy of two molecules at T and G . . . . .	159
B.21 Adsorption energy of three molecules at T, R and P . . . . .	160
B.22 Adsorption energy of three molecules at W, M and C . . . . .	160
B.23 Adsorption energy of three molecules at I, S and L . . . . .	161
B.24 Adsorption energy of three molecules at H, S and Q . . . . .	161
B.25 Adsorption energy of three molecules at E, M and U . . . . .	162
B.26 Adsorption energy of three molecules at A, M and Y . . . . .	162
B.27 Adsorption energy of three molecules at E, G and N . . . . .	163
B.28 Adsorption energy of three molecules at A, I and L . . . . .	163
B.29 Adsorption energy of three molecules at J, C and S . . . . .	164
B.30 Adsorption energy of three molecules at C, F and Q . . . . .	164

**Bibliography**

**165**

# Chapter 1

## Introduction

### 1.1 Motivation

The theoretical foundations of our microscopic understanding of matter and energy were laid down one century ago, when quantum mechanics and statistical mechanics were developed. Now those laws are known and accepted. In the 21st century, one of the main endeavors in science is to understand, predict, and to engineer the consequences of these laws found one hundred years ago. The advent of powerful computer systems in the past few years has allowed first-principles theories (based on the electronic structure of matter) to be developed and applied to materials of technological interest. Thus, computer simulations are gradually becoming another tool beside experiments for studying and engineering materials.

In a computer simulation (or computer experiment) a model is provided by theory, and the calculations are carried out in a machine by following a "recipe" (the algorithm, implemented in a suitable programming language). In this way, complexity can be introduced and more realistic systems can be investigated, opening a road towards a better understanding of nature.

On one hand, simulations can be considered as theory, since they deal with models and not with reality. On the other hand, the procedure of running calculations and analyzing the results closely resembles an experiment. There is no sharp distinction between the theoretical or experimental nature of computer simulation, it is therefore best viewed as a branch on its own.

The optimum approach to modern scientific research often requires the interplay between theory, experiment, and simulation as shown schematically in Fig. (1.1). Both, simulations and experiments are related to theory. An understanding of the theoretical principles behind the natural phenomena being studied is thus an indispensable requisite for the experiments and simulations.

To become a useful tool in studying nature and technological processes, simulations have to have predictive power. This means, the results of the simulations should be based, as much as possible, only on the basic laws of nature, and not on experimentally determined model parameters. This requirement poses a big burden to computer simulations, because as the systems studied come closer to systems of technological interest, the theoretical

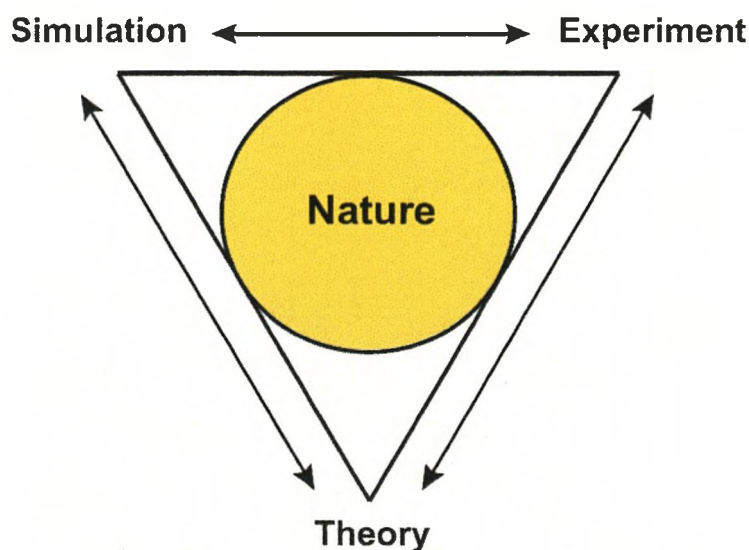


Figure 1.1: Schematic representation of the modern approach to scientific research in science (adapted from Ref [1])

description becomes very complex.

Thus, the application of simulations to "real world" problems requires the development of transformations and coarse graining algorithms to suitably and systematically simplify the enormous complexity of macroscopic systems in terms of microscopic processes.

The theoretical link from microscopic processes to macroscopic phenomena is provided by statistical mechanics (SM), and models trying to capture how macroscopic phenomena are related to microscopic phenomena and microscopic processes are necessarily based on SM. When the parameters of the SM model are derived from first-principles calculations, we are talking about first-principles statistical mechanics. Such an approach allows for the model to be based completely on the electronic structure of the system. As a result, such model has predictive power.

## 1.2 Objectives

In this thesis, we pursue the study of first-principles statistical mechanics applied to the calculation of adsorbate macroscopic ordering and phase transitions. The study of these phenomena is a central topic in modern surface science and enters directly into the discussion of many important processes at surfaces such as heterogeneous catalysis. For this purpose, we applied the methodology to the Bitartrate/Cu(110) system. This system has a variety of technological applications in finechemicals and pharmaceuticals. We shall also explore the ability of surfaces to recognise chirality in the critical step from the molecular gas phase to the adsorption on chiral centres at extended surfaces.

The methodology has already been applied to the calculation of the phase diagram of adsorbates on metal surfaces. However, at present there is not a standard and general procedure in order to systematically obtain phase diagrams from first-principles statistical mechanics



calculations.

In this work, these questions are therefore studied thoroughly with the aim of gaining insight into first-principles statistical mechanics in the context of molecular ordering and phase transitions. We discuss and assess many of the approaches which have been proposed in the literature in order to address these problems.

Concerning the object of study, i.e. the Bitartrate/Cu(110) system, we show how the microscopic and macroscopic approaches complement each other in order to obtain a complete picture of the system. Special emphasis is put on showing how the observed behavior of the system at the macroscopic level is nothing but the result of interactions operating at the microscopic level. Thus, we pursue a multiscale modelling approach.

Since our methodology is based on the electronic structure of matter, all of our results are based only on theory. That is, experimental results (from the literature and from the different collaborations) are used exclusively for comparison and no fitting to the experiments is carried out. Applications include: TPD spectra[6], island nucleation and growth[7] and the study of reactions on metal surfaces[8].

## 1.3 Outline

The theory behind the first-principles statistical mechanics approach used in this thesis is discussed in Chapter 2. In particular, emphasis is put on the microscopic and macroscopic description and the bridge between both of them. This approach in surface science is partially known as the ab-initio lattice gas Hamiltonian method and in alloy theory more commonly known as the cluster expansion method.

### 1.3.1 Static Simulations

In Chapter 3, a review of the experiments concerning the different Halododecane/Si(111) systems is presented. A general mechanism leading to the formation of the type-I and type-II chlorododecane adsorbates studied in the Chapter 3 and 4 respectively is demonstrated. Chapter 3 studies the darkened silicon adatom phenomenon surrounded by two chlorododecane molecules forming the Type-II adsorbate once physisorbed at Si(111). The first-principles calculations are performed within the DFT-GGA approximation and the PW91 method as implemented in the computing code VASP[101,102]. The STM simulations are performed with bSKAN36 using a Tungsten tip.

The chapter 4 is a review of the experiments concerning Type-I Chlorododecane physisorbed at Si(111). This chapter studies the switching states of the free silicon adatom around the corner hole of the silicon surface, where the 5 remaining adatoms are supporting the two chlorododecane molecules forming the Type-I adsorbate. The first-principles DFT calculations and the STM simulations are performed under the same conditions as the work done in chapter 3.

## 1.3.2 Dynamic Simulations

Chapter 5 reviews the parameters used in a Metropolis Monte Carlo simulations:  $\Psi$ , the order parameter and  $C_V$ , the heat capacity, by performing simulations using a simple adsorbate/substrate. This simple model helps to understand the interpretation of an order-disorder transition and to predict the general behavior of a more complicated system such as bitartrate/Cu(110) described in the following Chapter.

In Chapter 6, a review of the literature concerning the Bitartrate/Cu(110) system is presented. Also, a first principles study, with the aim of identifying the most important microscopic factors governing the cooperative behavior of Tartaric Acid molecules on the Cu(110) surface, is carried out. The first principles calculations are performed within the DFT-GGA approximation, using a supercell geometry and the PW91 method as implemented in the computing code VASP[101,102]. The general statistical mechanics model is described in Chapter 5, together with the simplifications in the model based on first-principles study, leading to a Lattice-gas model. The set of first-principles calculations needed in order to parameterize the lattice gas Hamiltonian is presented. The parameters of the Hamiltonian are derived in a simple way by considering only short-range interactions. Metropolis Monte Carlo simulations are carried out based on this Hamiltonian in order to identify and characterize order-disorder phase transitions in the Bitartrate/Cu(110) system.

The conclusions related to the first-principles statistical mechanics methodology employed in this thesis and the Bitartrate/Cu(110) system are discussed in Chapter 7. Finally Appendix A shows, in Fortran 90, the skeleton of the Monte Carlo program. This simple program is written in the canonical ensemble for a simple cubic system, its subroutines are also described, which are useful to determine the order parameter  $\Psi$ , and the heat capacity  $C_V$ . Appendix B explains in detail the Lattice gas Hamiltonian parameters. They are determined taking in account the limits of the system added to the periodic boundary conditions.

## 1.4 Organization of the Research

### 1.4.1 Chlorododecane/Si(111) systems: Chapter 3 and 4

- Collaboration with: John Polanyi / University of Toronto (Toronto, Canada)
- Experiments: Polanyi Group / University of Toronto (Toronto, Canada)
- Supervision: Werner Hofer

### 1.4.2 Monte Carlo on Bitartrate/Cu(110) system: Chapter 5 and 6

- Collaboration with: Karsten Reuter / Fritz-Haber Institut (Berlin, Germany)
- Experiments: Rasmita Raval Group / Surface Science R.C. (Liverpool, UK)
- Supervision: Werner Hofer and Karsten Reuter

## Chapter 2

# Theoretical approach

Microscopic insight into the nature of macroscopic behavior is only possible by adopting a multiscale approach. Such an approach models macroscopic phenomena based on microscopic models, the energetics of which are determined by the use of quantum mechanics. Multiscale modelling of materials aims to develop improved descriptions of material behavior through the incorporation of information about material structures and processes from various length- and time-scales.

Fig. 2.1 highlights the elements of a multiscale methodological approach. At the electronic regime, methods based on quantum mechanics, especially density functional theory (DFT), link to e.g. atomic/molecular dynamics, lattice gas models and Monte carlo simulations in the mesoscopic regime. For each length and time scale regime alone, a number of methodologies are well established. It is however, the appropriate linking of the methodologies that is only now evolving. Conceptually quite challenging in this hierarchy of scales are the transitions from the electronic to the mesoscopic, and from the mesoscopic to the macroscopic regime. The former transition is dominated by the importance of statistics due to the large number of particles and possible processes involved; while in the latter, the discrete nature of matter is neglected and treated as a continuum.

The theoretical framework of this thesis deals with the transition from the electronic to the mesoscopic regime. A number of methodologies (for a review [11,12]) have been developed to extract quantities in the electronic regime, which can be used to define parameters of the model operating in the mesoscopic regime. These methods are mostly based on matching or combining DFT data with concepts from statistical mechanics or thermodynamics in order to reach a proper description of the statistical interplay of the large number of processes taking place in the electronic regime. The thermodynamic matching is more appropriate if we are only interested in the macroscopic properties of matter. It is possible to match thermodynamics with DFT and obtain a first-principles description with the so-called "ab-initio atomistic thermodynamics" approach [13-16]. The approach is limited to equilibrium structures and its predictive power extends only to the structures which are directly considered.

The statistical mechanics (SM) matching [11,17,18] is more general and more applicable, but usually more involved and difficult. SM are the bridge linking thermodynamics with mechanics (especially quantum mechanics) it tries to interpret and predict the macroscopic properties of matter in term of its microscopic constituents [19]. Due to its microscopic na-

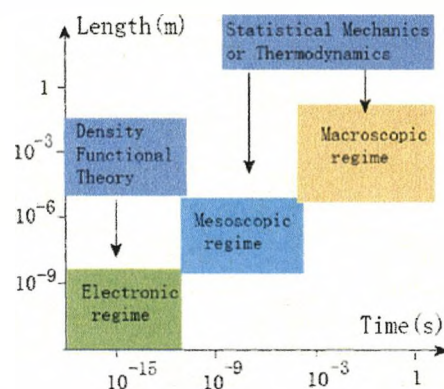


Figure 2.1: Schematic representation of the time and length scales relevant for most material science applications. The elementary molecular, which rule the behavior of a system, take place in the electronic regime. However, the observable effects only develop over meso and macroscopic lengths and times [11]

ture, SM provides insight into the microscopic structure of matter. SM allows for studying atoms and molecules. By directly considering the interactions among atoms and molecules, SM is able to predict the behavior of macroscopic systems based on the postulated microscopic interaction model.

In the following, we describe a generic system, and the concepts necessary to study its behavior. Next, the theory behind every regime in the multi-scale modelling approach of a system is described. In particular, the electronic regime was treated with the help of DFT, simulations in the mesoscopic regime were carried out using Monte Carlo methods. The electronic and mesoscopic regimes were linked using tools from statistical mechanics. For the purposes of this study, only equilibrium states are included, kinetic processes remain unconsidered.

## 2.1 Adsorption of atoms and molecules

The general system, which the theoretical discussion in this chapter refers to, consists of adsorbate species (i.e. atoms or molecules) on a close packed single-crystal metal surface (Fig. 2.2). We are interested in the collective behavior of the adsorbed species. The behavior is characterized by the phase diagram of the species adsorbed on the surface, i.e. the arrangement as a function of the gas phase conditions (e.g. temperature  $T$  and pressure  $p$  of the gas phase, or temperature  $T$  and coverage  $\Theta$  on the surface). The study of adsorbate phase diagrams is a central topic in modern surface science and enters directly into the discussion of many important processes at surfaces such as heterogeneous catalysis. One can address the question of what happens when atoms or molecules become attached to a surface, i.e. adsorbed, at three levels; specifically one can aim to identify:

- the adsorption mechanisms, i.e. the kinetics of adsorption.
- the nature of the adsorbed species and its local adsorption geometry, i.e. its chemical

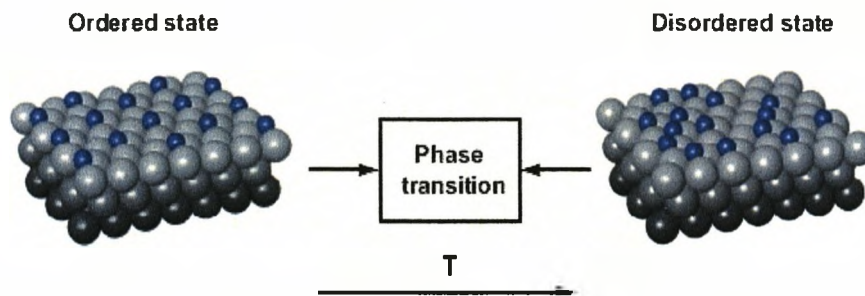


Figure 2.2: Section of a close packed metal with adsorbed atoms on its surface occupying ordered adsorption sites at low  $T$  (left) and random adsorption sites at high  $T$  (right). At intermediate temperature there is an order-disorder phase transition.

structure and co-ordination to adjacent substrate atoms.

- the overall structure of the extended adsorbate/substrate interface, i.e. the long range ordering at the surface.

All of these levels are intimately related; together they describe the adsorption of atoms and molecules on metal surfaces. Comprehensively, any of these levels constitutes today an active field of research, mainly because of the ultimate microscopic nature of the processes and phenomena being studied. The emphasis in this thesis is on the last item, i.e. the collective behavior of adsorbates on surfaces. To this aim, we leave aside the question of the adsorption mechanism and concentrate on the nature of the adsorbed species and the overall structure of the extended adsorbate/substrate interface.

Molecules and atoms can attach to surfaces in two ways:

- physisorption: The only bonding is polarization (i.e. Van der Waals) forces. There is no significant redistribution of electron density in either the molecule or at the substrate surface.
- chemisorption: A chemical bond, involving substantial rearrangement of electron density, is formed between the adsorbate and substrate. The nature of this bond lies anywhere between the extremes of virtually complete ionic or complete covalent character.

The problem of distinguishing between chemisorption and physisorption is basically the same as that of distinguishing between chemical and physical interaction in general. No sharp distinction can be made and intermediate cases exist (e.g. adsorption involving strong hydrogen bonds or weak charge transfer). Typical binding energies are 1-10 eV for chemisorption and 10-110 meV for physisorption [25].

It has been experimentally determined that adsorbed species often occupy a series of distinct sites on a solid surface, i.e. minima in the potential energy surface of the substrate-adsorbate system. The extent of surface coverage is then expressed as a fractional coverage  $\Theta$  in terms of the adsorption sites

$$\Theta = \frac{\text{number of adsorption sites occupied}}{\text{number of adsorption sites available}} \quad (2.1)$$

The symmetry of overlayers of adsorbates may be related to the symmetry of the underlying surface. One can distinguish three regimes [22]:

- Random adsorption corresponds to the lack of two-dimensional order in the overlayer even though the adsorbates may occupy (one or more) well-defined adsorption sites (fig. 2.2).
- Commensurate structures are formed when the overlayer structure corresponds to the structure of the substrate in some rational fraction, i.e. the overlayer exhibits two dimensional order (fig. 2.2).
- Incommensurate structures are formed when the overlayer exhibits two dimensional order; however, the periodicity of the overlayer is not related in a simple manner to the periodicity of the substrate.

Adsorbed species on single-crystal surfaces frequently reveal long-range commensurate structures; that is to say that the adsorbed species form a well-defined overlayer structure. Each particular structure may only exist in a limited region as the surface coverage is gradually increased. This phenomenon is caused by interactions between the adsorbed particles, which may have different origins and be repulsive as well as attractive. These give rise to a wealth of two-dimensional phases and phase transformations[25].

If the interactions are strongly attractive, the adsorbate molecules will have a tendency to cluster together in small patches, called islands. If the adsorbate is mobile, additional adsorbate molecules will be drawn into small patches so that the rest of the surface will be cleared of adsorbate. The result is a situation where small patches of the surface are covered by adsorbate but the rest of the surface is almost adsorbate free.

The periodic potential "seen" by a single adsorbed particle due to the periodicity of the substrate lattice and the interaction potential between particles determines, whether a second particle will still prefer a site defined by the substrate geometry (leading to so-called lattice-gas structures) or if its location is governed by the mutual interaction (causing the formation of incommensurate structures with the underlying lattice). Frequently, a compromise between both situations is reached in that the lattice of an incommensurate structure (lattice constant  $b$ ) matches with the substrate lattice (lattice constant  $a$ ) after a certain number of lattice constants (e.g.  $4b = 5a$ , "coincidence lattice"), leading again to a commensurate structure [26].

The ordering behavior of adsorbates on surfaces depends amongst other things on the temperature  $T$  of the system. Generally, random site filling occurs when the interactions between adsorbate molecules at adjacent sites is small with respect to  $k_B T$ , where  $k_B$  is the Boltzmann constant; In this case there is no preference for one site over another. Ordered adsorption occurs when the *adsorbate/adsorbate* interactions are larger than  $k_B T$ . In such cases the sites in close proximity to the ones already are occupied filled with enhanced or reduced probability depending on whether the *adsorbate/adsorbate* interaction is attractive or repulsive.

Each ordered surface has a limited temperature range of stability. At the boundaries of this range, phase transitions occur. These transitions may be reversible or irreversible. In a case of a reversible transition, the low temperature phase changes upon heating to a high-temperature phase, but is reordered upon cooling. In case of an irreversible transition, the

high-temperature phase, once being formed, remains stable also upon cooling[25].

Another subdivision of transitions includes order-order transitions and order-disorder transitions. An order-order transition means a transition between two ordered surface phases with different structures. The loss of ordering is described by order-disorder transitions; this process is known as symmetry-breaking (Fig. 2.2).

Transitions are also subdivided into first order (discontinuous) transitions and second order (continuous) transitions. In first order transitions, the system changes abruptly from one distinct surface phase to a second distinct surface phase. Phase coexistence, nucleation, and growth of the domains of a new phase are the features of first-order transitions. By contrast, in second-order transitions, one phase transfers continuously to a second phase and the competing phases are indistinguishable at the transition temperature [25].

Earlier efforts to microscopically understand the adsorption of atoms and molecules on surfaces began with the seminal work of Langmuir[27]. Based on rather indirect evidence obtained from measurements of the equilibrium gas uptake of metal surfaces at very low pressures, Langmuir was able to draw a remarkably accurate picture of adsorbate/surface interactions. His ideas are still alive and accessible to direct experimental investigation by using well-defined single crystal surfaces and the arsenal of modern surface physics [26].

A Product of those early investigations is the Langmuir isotherm which was developed to describe the dependence of the surface coverage of an adsorbed gas on the pressure of the gas above the surface at fixed temperatures. However, the simple Langmuir model is limited by the fact that it neglects the forces between adjacent adsorbed particles (a problem which Langmuir himself recognized [27]). Such forces are responsible for the wealth of two-dimensional phases and phase transformations which have been firmly established experimentally [26].

Modern systematic studies of phases and phase transformations (i.e. two-dimensional phase diagrams) of adsorbates on surfaces have been carried out by means of experiments [26]. The magnitude of the lateral interactions between adjacent particles has been usually derived by fitting two-dimensional Ising-like models to the experimental data. It is only the recent development in computing power and numerical algorithms which has opened the possibility of studying adsorbate/surface systems from first-principles.

The accurate theoretical description of substrate-adsorbate binding is very demanding, especially when the substrate is a transition metal. The reason is that in a metal most of the bonding occurs via the conduction band (i.e. the electrons that can move more or less freely through the metal and hence carry electricity). Long-range electrostatic attractions between the cores (atomic nuclei) in the metal play a minor role. Thus, the chemical binding is a product of electronic interactions (electronic regime) and their quantitative description demands a quantum mechanical approach.

The theoretical study of a system consisting of a collection of adsorbate species on a surface can, in principle, be studied by methods based on the positional space of the adsorbates such as molecular dynamics. Due to the quantum mechanical nature of the adsorbate chemical binding, the potential energy needed for a molecular dynamics simulation of adsorbates on surfaces should be obtained from first-principles calculations. This is today the approach of choice to study the adsorption of single molecules[23,24]; it is unpractical/unfeasible for the study of a collection of adsorbates, due to the enormous computational requirements which such an approach would require.

Instead of searching the positional space, it is more efficient to search the configurational space of the system in order to study the phase behavior of the adsorbed layer (mesoscopic regime). Thus statistical methods are best suited to tackle the theoretical description of the mesoscopic behavior of adsorbate species on surfaces [22].

In the following sketch, the theory behind the electronic and mesoscopic regimes on the basis of first principles simulations of adsorbed overlayers is outlined.

## 2.2 The electronic regime

In general, the physics in the electronic regime is determined by the laws of quantum mechanics. The energies are computed by solving the Schrödinger equation, which for stationary electron reads

$$H\Psi(\mathbf{r}_1\sigma_1, \dots, \mathbf{r}_N\sigma_N) = E\Psi(\mathbf{r}_1\sigma_1, \dots, \mathbf{r}_N\sigma_N), \quad (2.2)$$

where  $\mathbf{r}_i$  are the spatial and  $\sigma_i$  are the spin coordinates of the  $N$  electrons, and

$$\begin{aligned} \widehat{H} &= \widehat{T}_e + \widehat{V}_{ee} + \widehat{V}_{en} \\ &= \frac{1}{2} \sum_{i=1}^N \nabla_i^2 + \sum_{i=1}^N \sum_{j>1}^N \frac{1}{|\mathbf{r}_i - \mathbf{r}_j|} - \sum_{i=1}^N \sum_{\alpha=1}^{N_\alpha} \frac{Z_\alpha}{|\mathbf{r}_i - \mathbf{R}_\alpha|}, \end{aligned} \quad (2.3)$$

is the Hamiltonian (in atomic units) of the electronic system in the Born-Oppenheimer [28] approximation, where the "slow" nuclei coordinates  $\mathbf{R}_\alpha$  are treated as fixed parameters. The Hamiltonian operator  $\widehat{H}$  consist of a sum of three terms:

- the kinetic energy  $\widehat{T}_e$
- the electron-electron coulomb interaction  $\widehat{V}_{ee}$
- the interaction of the electrons with the external potential  $\widehat{V}_{en}$ , i.e. the Coulomb interaction with  $N_\alpha$  nuclei of charges  $Z_\alpha$  and coordinates  $\mathbf{R}_\alpha$ .

It is thus understood that the electronic wave function  $\Psi$  depends parametrically on the specific positions of the nuclei used in the electron-nucleus interaction, and that the total energy of the system is  $E + V_{nn}$ , where  $V_{nn}$  is the total repulsive energy among the nuclei. Since the wave function describes a system of fermions, it should satisfy the anti-symmetry requirement

$$\Psi(\dots r_i\sigma_i \dots r_j\sigma_j \dots) = -\Psi(\dots r_j\sigma_j \dots r_i\sigma_i \dots). \quad (2.4)$$

In most circumstances, we are content with finding only the lowest energy eigenvalue (i.e. the ground state energy)  $E_0$  of the electronic problem, and Eqs. (2.2-2.4) embody then all the information that is needed in order to obtain this quantity.

The calculation of the many-body wave function  $\Psi(r_i\sigma_i)$  of a system of interacting electrons is a formidable task which can only be carried out in a meaningful way for systems with a few tens of electrons [29]. If observables for larger systems are to be determined, the calculations of the many body wave function has to be avoided. One possibility is to write the desired quantities as functionals of the electronic density  $\rho$ , a scalar function of only three variables  $r_x, r_y, r_z$ . A modern and rigorous approach to do this is density functional theory (DFT).



### 2.2.1 Density functional theory

The development of density functional theory dates back to 1964 by Hohenberg and Kohn[31], a compact review of the formalism has been done by Jones and Gunnarsson[181]. Its goal is to replace the many-particle wavefunction by the electron density  $n$  which is defined as

$$n(\mathbf{r}) = N \int d\mathbf{r}_2 \cdots \int \psi^*(\mathbf{r}, \mathbf{r}_2, \cdots, \mathbf{r}_N) \psi(\mathbf{r}, \mathbf{r}_2, \cdots, \mathbf{r}_N) d\mathbf{r}_N, \quad (2.5)$$

The energy of an electronic system can thus be written as a functional of the density,

$$E[n] = \min_{\psi|n} \langle \psi | \widehat{H} | \psi \rangle, \quad (2.6)$$

where  $\widehat{H}$  is the Hamiltonian of a many-electron system in an external potential  $V_{ext}$ ,

$$\widehat{H} = \sum_i \left( -\frac{1}{2} \nabla_i^2 + V_{ext}(\mathbf{r}_i) \right) + \frac{1}{2} \sum_{i \neq j} \frac{1}{|\mathbf{r}_i - \mathbf{r}_j|}, \quad (2.7)$$

$\min_{\psi|n}$  denotes a minimization with respect to the wavefunctions  $\psi$  which are consistent with the density  $n(\mathbf{r})$ .

The groundstate of the many-electron Hamiltonian can be found by minimizing the functional  $E[n]$  with respect to the density which is subject to the constraint

$$\int n(\mathbf{r}) d\mathbf{r} = N, \quad (2.8)$$

where  $N$  is the total number of electrons.

Hohenberg and Kohn proved that (a) for every ground-state density a unique external potential  $V_{ext}$  exists and (b) indeed  $\min_n E[n] = E_0$ ,  $E_0$  being the ground-state energy, relative to all density functions  $n'(\mathbf{r})$  fulfilling (2.8) that are associated with some other external potential  $V'_{ext}$ . There is a slight flaw in their argument, however, since by the possible existence of other densities not realisable with an external potential but satisfying (2.8) one may exceed the range of definition when applying the variational principle to minimize  $E[n]$ . This problem has been solved by Levy[182], who has extended the argument to  $N$ -representable density-functions, which can be obtained from some antisymmetric wavefunctions. Soon thereafter it was shown by Harriman[183] that indeed every nonnegative, normalized density can be constructed from such wavefunctions.

Investigating the energy functional (2.6) further, it can easily be seen that the contribution including the external potential  $V_{ext}$  does not depend explicitly on the wavefunction, but only on the density  $n(\mathbf{r})$ . It can therefore be extracted from the minimization. We thus arrive at the equation:

$$E[n] = \min_{\psi|n} [\langle \psi | H_0 | \psi \rangle] + \int V_{ext}(\mathbf{r}) n(\mathbf{r}) d\mathbf{r}, \quad (2.9)$$

with

$$H = H_0 + V_{ext}(\mathbf{r}). \quad (2.10)$$

The part to be minimized in (2.9) can be written as a new functional of the density,

$$F[n] = \min_{\psi|n} \langle \psi | H_0 | \psi \rangle. \quad (2.11)$$

The functional  $F[n]$  is universal and holds for every external potential. Instead of finding the multi-particle wavefunction for a given Hamiltonian one has now "only" to deal with the problem of determining the universal functional  $F[n]$  for an electron number  $N$ .

What follows is a crucial step for the success of density functional theory, which was first suggested by Kohn and Sham[32]. Two additional terms are extracted from the functional  $F[n]$ . The first one is the classical Coulomb energy, whose separation is already suggested by Hohenberg and Kohn[31] because of its long range. The second is kinetic energy of a system of noninteracting electrons with density  $n(\mathbf{r})$ ,  $T[n]$ . Eq. (2.9) becomes now

$$E[n] = T[n] + \int V_{ext}(\mathbf{r})n(\mathbf{r})d\mathbf{r} + \frac{1}{2} \int d\mathbf{r} \int \frac{n(\mathbf{r})n(\mathbf{r}')}{|\mathbf{r} - \mathbf{r}'|} d\mathbf{r}' + E_{xc}[n]. \quad (2.12)$$

The minimum requirement for  $E[n]$  under the constraint (2.8) leads to

$$\frac{\partial T[n]}{\partial n(\mathbf{r})} + V_{ext}(\mathbf{r}) + \int n(\mathbf{r}') \frac{1}{|\mathbf{r} - \mathbf{r}'|} d\mathbf{r}' + \frac{\partial E_{xc}[n]}{\partial n(\mathbf{r})} = \lambda n(\mathbf{r}), \quad (2.13)$$

with the Lagrange parameter  $\lambda$ . The form of equation (2.13) is identical to that of an Euler-Lagrange equation following from the Hohenberg-Kohn variational principle for a system of non-interacting electrons in an external effective potential. In this non-interacting case the ground-state energy and density can be obtained by calculating the eigenfunctions and eigenvalues of a single-particle Schrödinger equation. Defining the exchange-correlation potential  $V_{xc}[n]$  as

$$V_{xc}[n(\mathbf{r})] = \frac{\partial E_{xc}[n]}{\partial n(\mathbf{r})}, \quad (2.14)$$

and treating all but the first terms in (2.13) as an "effective potential"  $V_{eff}(\mathbf{r})$ ,

$$V_{eff}(\mathbf{r}) = V_{ext}(\mathbf{r}) + V_{xc}(\mathbf{r}) + \int n(\mathbf{r}') \frac{1}{|\mathbf{r} - \mathbf{r}'|} d\mathbf{r}', \quad (2.15)$$

the solutions satisfy the so-called Kohn-Sham equations which are equations of the form of single-particle Schrödinger equations:

$$\left( -\frac{1}{2}\nabla^2 + V_{eff}(\mathbf{r}) \right) \psi_k(\mathbf{r}) = \epsilon_k \psi_k(\mathbf{r}). \quad (2.16)$$

The groundstate density is then given by

$$n(\mathbf{r}) = \sum_{k=1}^N |\psi_k(\mathbf{r})|^2. \quad (2.17)$$

Note that neither the eigenfunctions  $\psi_k$  nor the eigenvalues  $\epsilon_k$  have any directly observable meaning except for the influence on the density  $n(\mathbf{r})$ , Eq. (2.17). The highest occupied energy value  $\epsilon_k$  relative to the vacuum being the ionisation energy.

The Hamiltonian in (2.16) depends on the density, therefore we have to solve an implicit

equation of  $n(\mathbf{r})$  which is done selfconsistently. Comparing (2.16) and (2.12) one can determine the ground state energy to be

$$E = \sum_{k=1}^N \epsilon_k - \frac{1}{2} \int d\mathbf{r} \int \frac{n(\mathbf{r})n(\mathbf{r}')}{|\mathbf{r} - \mathbf{r}'|} d\mathbf{r}' + E_{xc}[n] - \int V_{xc}[n(\mathbf{r})]n(\mathbf{r})d\mathbf{r}, \quad (2.18)$$

where the sum goes over all occupied states. (The  $\epsilon_k$  are generally named Kohn-Sham eigenvalues.)

The only unknown in the whole formalism is now the exchange-correlation functional  $E_{xc}[n]$  and its functional derivative, the exchange-correlation potential  $V_{xc}[n]$ . They can both be approximated as local functionals of the electron-density  $n(\mathbf{r})$ . In principle, the expression for the groundstate energy (Eq. 2.18) is exact and contains no approximations, as long as the exchange-correlation functional can be derived exactly.  $E_{xc}$  contains the electron exchange energy, which is treated exactly in the Hartree-Fock approximation. However, this neglects the whole correlation part of  $E_{xc}$ , which consists of the difference between the kinetic energy of noninteracting and an interacting electron system (remember that  $T[n]$  is only the kinetic energy functional of a noninteracting electron gas), i.e. the dynamic correlation effects due to Coulomb interaction between the electrons. The only result that shall be mentioned at this point is that in case of a slowly varying electron densities  $n(\mathbf{r})$  the local exchange-correlation energy can be approximated by one of a uniform electron gas. A more detailed discussion of the approximation to  $E_{xc}$  will follow in Section 2.2.5.

## 2.2.2 Models to describe metallic surfaces

The calculations cannot describe all atoms in a solid surface, and a strategy must be chosen to limit the number of atoms treated explicitly. Two basic types of methods exist, today:

- *Cluster methods*, which describe only a limited cluster of surface atoms in the hope that the surface atoms farther away from the adsorbates of interest are not important.
- *Slab methods*, whereby the surface is described as a slab with a periodic structure along the surface. The size of the surface unit cell determines the computational effort.

The cluster method is a local approach which focuses on the interaction of the adsorbed molecules only with the nearest atoms on a surface and it corresponds to a truncated model of the environment. The slab method is a localized approach which is based on the band theory of the electronic structure of solids. For metals, the slab method is generally found to describe the surface properties better than the cluster approach [37].

A simple, but effective geometric surface model is the repeated slab geometry, i.e. the supercell method (Fig. 2.3). Through an infinite array of slabs, the surface is cast into a three dimensional periodicity, which e.g. allows one to exploit 3D periodicity and make efficient use of plane waves and fast fourier transforms in the solutions of the DFT equations.

In order to give a reliable description of surfaces, firstly the vacuum layer between the slabs, and secondly the slabs themselves have to be thick enough to be a reasonable model for the surface of a semi-infinite substrate. Both these properties can be checked by convergence tests of any calculated property with respect to the width of the vacuum layer and the thickness of the slab.

## 2.2.3 Plane-wave basis sets

To solve the Kohn-Sham equations (2.16) numerically, the one-particle wave-functions  $\psi_i(\mathbf{r})$  need to be approximated. In the modelling of macroscopic systems periodic boundary conditions are an obvious choice. In this context a plane-wave basis set is convenient, since any periodic function can be expressed as a sum of plane waves. The (discretised) single-particle wave-functions are written as

$$\psi_i(\Gamma_{\mathbf{k}}) = \sum_{\mathbf{n}} c_{\mathbf{n},i} e^{2\pi i \frac{\mathbf{n}\mathbf{k}}{N}}, \quad (2.19)$$

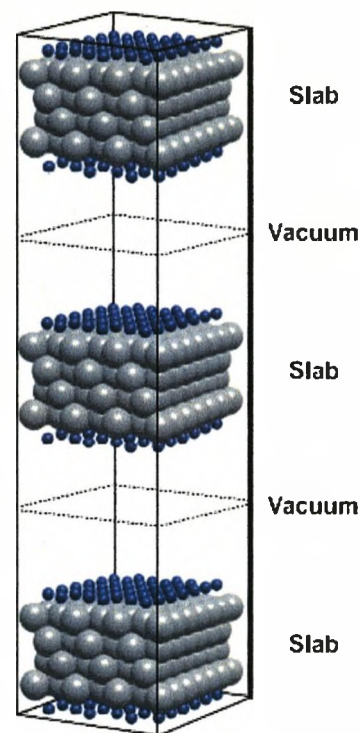


Figure 2.3: Illustration of the supercell approach, in which surfaces are represented through an infinite array of slabs

and the sum is truncated at some finite value  $N$ . Now only the plane wave coefficients  $c_{n,i}$  need to be stored. The use of plane waves brings about several advantages:

- The electronic structure of many solids conforms relatively well with a nearly-free electron picture. The wave-functions of free electrons are plane waves.
- Basis set convergence is easily checked by increasing the highest kinetic energy of the plane waves contained in the basis set.
- Passing from real to reciprocal space requires a Fourier transformation which can by the use of fast-Fourier transformations (FFT) be implemented very efficiently in computer codes. Using the wave-function alternately in real and reciprocal space allows very efficient evaluations of operations like  $H\psi$ . Plane-wave basis functions are independent of the locations of the atoms. Hence, in the calculations of the forces acting on the ions, no corrections for the spatial variation of the basis set have to be taken into account.

In practice it turns out that the plane-wave method is entirely inapplicable to real atomic potentials. The reason for this failure lies in the atomic potential becoming very large inside the core. This results in the need for a prohibitively large number of plane waves to reach reasonable results. However, the core electrons do not participate in the inter-atomic interactions, the tractability of the problem can be reestablished by the use of pseudopotentials.

## 2.2.4 Pseudopotentials

The concept of pseudopotentials goes back to the 1930s when Fermi and Hellman independently suggested dealing with the Schrödinger equation for the valence electrons only in a subspace of Hilbert-space orthogonal to the core states. This idea was continuously advanced ever since, leading to the rise of norm-conserving pseudopotentials in the early 80s, ultrasoft pseudopotentials in 1990, and PAW potentials that already go beyond pseudopotentials in 1994.

### General ideas

A comprehensive review of the development of pseudopotential methods with many references (though in German) can be found in Kresse[101]. Here the most important steps can be briefly sketched.

As mentioned above, in most materials the core electrons do not contribute to the bonding. Only their absolute energy is affected by the average electrostatic potential in the vicinity of the core (core level shift). A fundamental idea therefore is the "frozen-core approximation". The core electrons are calculated for a (in general spherical) reference configuration and are kept fixed thereafter. The wave-functions for the valence electrons are "pseudised" to give the same energy levels as the all-electron wave-functions. The pseudo wave-functions differ from all-electron wave-function only inside a region around the nucleus and are constructed to be nodeless. If the pseudo wave-functions still contained nodes they would not

describe the lowest valence-states. It can be shown that the removal of nodes from the all-electron wave-functions has no effect on the scattering properties of the atom for valence electrons, since the number of nodes of the valence wave-functions in the core region only add multiples of  $\pi$  to the phase shift  $\delta$ . The nodes in the valence wave-functions are necessary to make valence states orthogonal to the core states. Node-less pseudo-wavefunctions reduces the number of required plane waves considerably.

The procedure is therefore as follows:

- Solve the spherical radial Schrodinger equation for an atomic or ionic reference configuration

$$-\frac{1}{r} \frac{d^2}{dr^2} (r\psi_{nl}(r)) + \frac{l(l+1)}{r^2} \psi_{nl}(r) + V_{sc} \psi_{nl}(r) = \epsilon_{nl} \psi_{nl}(r), \quad (2.20)$$

within the framework of density functional theory. This yields the self-consistent potential  $V_{sc}$  as well as the all-electron energy eigenvalues and wave-functions.

- Inside some core radius  $R_c$  the valence wavefunctions  $\psi_{nl}$  are replaced by nodeless pseudo wavefunctions  $\tilde{\psi}_{nl}$ . Outside the radius  $R_c$  the all electron and the pseudo-wavefunction are identical.
- The corresponding pseudopotential is found by the "inversion" of the spherical Schrodinger equation for the pseudo-wavefunctions.

Obviously one gets different pseudopotentials for each spherical quantum number  $l$ . To combine them to a single potential, projection operators are used that subsequently also enter the energy functional (2.12).

The pseudo-wavefunction inside the core region is chosen to reproduce the scattering properties of the all-electron wavefunction in an energy window around the atomic reference energy. A central role in this context is played by the logarithmic derivative  $x_{l\epsilon}$  of the wave-function and its energy dependence,

$$x_{l\epsilon}(r) = \frac{d}{dr} \ln(\psi_{l\epsilon}(r)) = \frac{1}{\psi_{l\epsilon}(r)} \frac{d}{dr} \psi_{l\epsilon}(r), \quad (2.21)$$

since it essentially describes the scattering properties.

Topp and Hopefield have found that the requirement of an identical energy derivative of  $x_{l\epsilon}$  for all-electron and pseudo wavefunction at  $R_c$  is equivalent to the two wavefunctions having the same norm inside the core. This idea was extended to the general concept of norm-conserving pseudopotentials by Hamann[184].

The norm-conserving pseudopotentials work well for all elements except for the first period and the 3d transition metals. In those elements the requirement of norm-conservation prohibits the use of large cutoff radii and soft pseudopotentials, therefore the energy cutoff for the plane waves still lies at 30-70 Rydberg. The reason for this is that for those elements the all-electron valence wavefunctions are already nodeless, consequently the construction of the pseudopotential only shifts the maximum of the valence wave-function and does not improve it considerably. To solve these problems Vanderbilt[42] developed a new concept for so called "ultra-soft" pseudopotentials, improving previous pseudopotentials in several

ways. The two most important improvements are the removal of the constraint of norm conservation to optimize smoothness, and the matching of the logarithmic derivatives at several energies to improve transferability. The drawbacks are twofold: On one hand, the hermiticity of the nonlocal pseudopotential operator can only be preserved by the introduction of an overlap operator in the Hamiltonian. On the other hand, the non-conservation of the charge density leads to the need for augmentation charge density operators for the valence wavefunctions. However the reduction of the number of plane-waves by a factor of 3-4 largely outweighs the small computational overhead.

### PAW method

In the previously described pseudopotential methods a potential and its corresponding pseudo-wavefunctions are constructed to reproduce the atomic scattering properties in an energy window around the atomic eigenvalues. They are then used as input parameters to the many-particle density functional calculation. The projector augmented-wave (PAW) method is in principle a frozen-core all electron method that aims to make the advantages and accuracy of all-electron methods available to the formally more simple (and computationally less demanding) pseudopotential approach. It was established by Blochl[43]. Its close connection to ultrasoft pseudopotentials was derived by Kresse and Joubert[185].

The PAW method starts from a simple linear transformation that connects the exact valence wavefunction  $|\psi\rangle$  to a pseudo (PS) wave function  $|\tilde{\psi}\rangle$  which is the one expanded into plane waves,

$$|\psi\rangle = |\tilde{\psi}\rangle - \sum_{N,i} |\tilde{\phi}_{N,i}\rangle \langle \tilde{p}_{N,i} | \tilde{\psi}\rangle + \sum_{N,i} |\phi_{N,i}\rangle \langle \tilde{p}_{N,i} | \tilde{\psi}\rangle. \quad (2.22)$$

All quantities related to the (PS) representation of the wave function are indicated by a tilde. The  $\phi$  are local wavefunctions, the index  $N$  goes over all sites,  $i$  over the quantum numbers  $n, l, m$ . The  $\tilde{p}_i$  are localized projector functions that have to fulfill the condition

$$\sum_i |\tilde{\phi}\rangle \langle \tilde{p}_i | = 1. \quad (2.23)$$

Defining  $c_{N,i}$  of an arbitrary wave function  $\tilde{\psi}$  at the atomic site  $N$  as

$$c_{N,i} = \langle \tilde{p}_{N,i} | \tilde{\psi}\rangle, \quad (2.24)$$

the pseudo-electron and all-electron wavefunctions at an atomic site  $N$  can be easily reconstructed from the plane-wave expanded pseudo wave function as

$$|\tilde{\psi}_N\rangle = |\tilde{\phi}_{N,i}\rangle c_{N,i}, \quad (2.25)$$

$$|\psi_N\rangle = \sum_i |\phi_{N,i}\rangle c_{N,i}. \quad (2.26)$$

The variational quantities that need to be determined during the ground state calculation are the PS wavefunctions  $\tilde{\psi}$ . However, contrary to the "simple" pseudopotential methods

the operators  $A$  representing physical quantities need to be consistently extended to their all-electrons forms,

$$\tilde{A} = A + \sum_{N,i,j} |\tilde{p}_{N,i}\rangle \left( \langle \phi_{N,i} | A | \phi_{N,j} \rangle - \langle \tilde{\phi}_{N,i} | A | \tilde{\phi}_{N,j} \rangle \right) \langle \tilde{p}_{N,j} |. \quad (2.27)$$

This equation is valid for local and quasilocal operators such as the kinetic energy. Truly nonlocal operators need a special treatment but are also tractable.

The valence-only PAW method is implemented in the program package VASP. Its results are almost identical to the most accurate density functional calculation presently available, which are based on the full-potential linearized augmented plane-wave method (FLAPW) [185]. This scheme describes all electrons essentially exact (with a much higher computational effort), even in the most difficult cases such as strong magnetic moments or large electronegativity differences[185].

## 2.2.5 Approximating the exchange-correlation functional

From its definition it is clear that the exchange-correlation functional can be written as

$$E_{xc}[n] = T[n] - T_0[n] + U_{xc}[n], \quad (2.28)$$

where the first two terms describe the difference in the kinetic energy of an interacting and the non-interacting electronic system and  $U_{xc}$  is the Coulomb interaction of the electrons with their exchange-correlation hole (the classical Coulomb energy is treated separately, cf. Eq. (2.12)). The exchange-correlation hole  $n_{xc}$  around an electron at the position  $\mathbf{r}$  and with spin  $\sigma$  is defined from the two-electron density matrix  $\rho_2$  as

$$\rho_2(\mathbf{r}\sigma, \mathbf{r}'\sigma') \equiv n_\sigma(\mathbf{r})(n_{\sigma'}(\mathbf{r}) + n_{xc}(\mathbf{r}\sigma, \mathbf{r}'\sigma')), \quad (2.29)$$

which can be further decomposed into exchange and correlation contributions,

$$n_{xc}(\mathbf{r}\sigma, \mathbf{r}'\sigma') = n_x(\mathbf{r}\sigma, \mathbf{r}'\sigma') + n_c(\mathbf{r}\sigma, \mathbf{r}'\sigma'). \quad (2.30)$$

The exchange correlation hole is local,

$$\lim_{|\mathbf{r}-\mathbf{r}'| \rightarrow \infty} n_{xc}(\mathbf{r}\sigma, \mathbf{r}'\sigma') = 0, \quad (2.31)$$

since there is no interaction over infinite distances, at this limit the two-electron density matrix can consequently be written as the product of two single-particle density matrices (Eq. 2.29). Furthermore, the Pauli exclusion principle for electrons with parallel spin is satisfied,

$$n_{xc}(\mathbf{r}\sigma, \mathbf{r}\sigma) = -n_\sigma(\mathbf{r}). \quad (2.32)$$

The exchange hole is negative semi-infinite and obeys the integral condition

$$\int n_x(\mathbf{r}\sigma, \mathbf{r}'\sigma') d\mathbf{r} = -\delta_{\sigma,\sigma'}, \quad (2.33)$$



which may be deduced from the fact that the non-interacting wave-function is antisymmetric. The integral condition for the correlation hole comes from the normalization of the two-electron density matrix,

$$\int n_c(\mathbf{r}\sigma, \mathbf{r}'\sigma') d\mathbf{r} = 0. \quad (2.34)$$

The expression for  $E_{xc}$  can be rewritten by introducing a coupling parameter  $\lambda$  that describes the strength of the electron-electron interaction. The non interacting system corresponds to  $\lambda = 0$  while  $\lambda = 1$  describes electrons interacting by the full Coulomb interaction. The exchange-correlation energy of the interacting system can then be expressed exactly in terms of the interaction of the density and the exchange-correlation hole averaged over the coupling constant [186,187],

$$E_{xc}[n] = \frac{1}{2} \int n(\mathbf{r}) d\mathbf{r} \int d\mathbf{r}' \int_0^1 \frac{n_{xc,\lambda}(\mathbf{r}, \mathbf{r}')}{|\mathbf{r} - \mathbf{r}'|} d\lambda, \quad (2.35)$$

where we have summed over the spin variables  $\sigma$  and  $\sigma'$ . The above result is also known as adiabatic connection formula. By a simple variable substitution  $\mathbf{R} \equiv \mathbf{r} - \mathbf{r}'$  one can see that the exchange-correlation energy depends only on the spherical average of the exchange-correlation hole.

### Local density approximation (LDA)

The simplest approximation to the exchange-correlation energy is to replace it in every point  $r$  in space by the exchange-correlation energy  $\epsilon_{xc}$  of a uniform electron gas with the constant densities  $n_\uparrow$  and  $n_\downarrow$ ,

$$E_{xc} = \int n(\mathbf{r}) \epsilon_{xc}(n(\mathbf{r})) d\mathbf{r}. \quad (2.36)$$

Using the spin-decomposed electron density the approximation is called local spin-density approximation (LSDA). The exchange acts only between electrons having the same spin while the correlation describes interactions between all electrons. The exchange energy in the LSDA is exactly known, it is given as

$$E_x = \sum_\sigma -\frac{3}{2} \left( \frac{3}{4\pi} \right)^{\frac{1}{3}} \int n_\sigma^{\frac{4}{3}}(\mathbf{r}) d\mathbf{r}. \quad (2.37)$$

The correlation part can be obtained from the quantum Monte carlo simulations and then be parameterized. VASP uses a parametrization by Perdew and Zunger[188] based on calculations by Ceperly and Alder[34].

Although this approximation leads to a qualitatively wrong picture for the exchange-correlation hole (it is symmetric and centered at the electron, whereas the exact hole is highly asymmetric and centered around the nucleus), the LSDA yields surprisingly good results for the exchange-correlation energy. The spherical averages of LSDA and the exact hole are remarkably similar, and only these averages enter into the exchange-correlation energy (see above). One reason for its success is that the LSDA describes the exchange-correlation effects of a physical system (the uniform electron gas) and therefore obeys all of the exact universal relations except the non-uniform scaling relations.

### Gradient expansion approximation (GEA)

The first possible improvement to the purely local LSDA, the gradient expansion approximation, was already proposed by Kohn and Sham[32]. It considers the LSDA as the first term in a Taylor expansion for  $E_{xc}[n_{\uparrow}, n_{\downarrow}]$  around the uniform density. The exchange-correlation energy then becomes

$$E_{xc}^{GEA}[n_{\uparrow}, n_{\downarrow}] = \int n(\mathbf{r}) \epsilon_{xc}(n_{\uparrow}(\mathbf{r}), n_{\downarrow}(\mathbf{r})) d\mathbf{r} \quad (2.38)$$

$$+ \sum_{\sigma, \sigma'} C_{\sigma, \sigma'}(n_{\uparrow}(r), n_{\downarrow}(r)) \frac{\nabla n_{\sigma}}{n_{\sigma}^{2/3}} \frac{\nabla n_{\sigma'}}{n_{\sigma'}^{2/3}}.$$

While the GEA is an improvement over the LSDA for slowly-varying systems, it typically worsens results on real electronic systems. The exchange-correlation hole is not the hole of any physical system, which is probably one reason for its failure.

### Generalized gradient approximation (GGA)

One way to rectify the failure of the GEA is to include the (spin) density gradient in a more general way and allow all powers of  $\nabla n_{\sigma}$  to occur in the exchange-correlation energy. Such approximations are called generalized gradient approximations (GGA). Eq. 2.38 takes the form:

$$E_{xc}^{GGA}[n_{\uparrow}, n_{\downarrow}] = \int f(n_{\uparrow}(\mathbf{r}), n_{\downarrow}(\mathbf{r}), \nabla n_{\uparrow}(\mathbf{r}), \nabla n_{\downarrow}(\mathbf{r})) d\mathbf{r}, \quad (2.39)$$

with the function  $f$  being chosen by some set of criteria. Exchange-correlation approximations of the form of (Eq. 2.39) are semilocal, in the sense that the energy density at  $r$  depends on the electron density at an infinitesimal neighborhood of  $r$ . In the following a few GGA functionals are presented in their chronological order.

- **Langreth-Mehl approximation (LM)**

One of the earlier popular works going beyond the GEA was the approximation by Langreth and Mehl[189]. The small k-vector contributions are eliminated by replacing the correlation term for small gradients by zero. The corrections to the GEA are in the right direction, however the LM functional still shows some major shortcomings, e.g. the uniform gas limit is not correct.

- **Perdew-Wang 86 (PW86)**

Perdew and Wang [191] introduced a real space cut-off on the exchange part of the GEA to restore the negative semi-definiteness as well as the integral condition of the exchange hole. The correlation contribution is approximated similar to the LM procedure. The resulting functional obeys some of the exact conditions better than the LM approximation.

- **Becke-Perdew (BP)**

Becke[190] constructed an improved exchange functional by restoring the correct asymptotic behaviour of the energy as  $r \rightarrow \infty$  in finite systems. It is only semi-empirical since it contains a single adjustable parameter that was fitted to achieve minimum error for a large number of atoms. This exchange functional was combined with Perdew's correlation term[191] to form the BP functional.

- **Lee-Yang-Parr (LYP)**

The Lee-Yang-Parr correlation functional[192] starts from the Colle-Salvetti formula which is derived from a number of theoretical approximations and fitted to the correlation energy of the helium atom. The non-interacting kinetic energy density in the Colle-Salvetti formula is replaced by its second-order density-gradient expansion. The LYP correlation is often combined with Becke exchange, together named BLYP. The resulting exchange-correlation functional violates many of the universal relations but does scale correctly for uniform high densities, a quality that even the otherwise superior PW91 functional does not have.

- **Perdew-Wang 91 (PW91)**

The second exchange-correlation functional by Perdew and Wang discussed here (PW91)[193] is like LSDA and GEA and unlike other GGAs discussed here purely ab-initio. It is constructed using only uniform electron gas data and exact conditions. PW91 includes a real space cutoff also for the correlation functional and takes the Becke exchange with only small refinements. It fulfills almost all of the scaling relations known, including such that were only found after the functional's formulation.

- **Perdew-Burke-Ernzerhof (PBE)**

Perdew, Burke, and Ernzerhof[194] simplified the cumbersome derivation of PW91 and corrected some of its minor flaws such as the spurious wiggles in the exchange-correlation potential for small and large (dimensionless) density gradients. The resulting energies change only marginally.

- **Revised Perdew-Burke-Ernzerhof (RPBE)**

Zhang and Yang[195] proposed a small modification of the local exchange enhancement factor in the PBE functional, introducing the revPBE functional, which improves atomization energies of atoms and molecules on transition metal surfaces. However, revPBE violates the Lieb-Oxford criterion[196]. Subsequently, Hammer, Hansen, and Norskov[197] devised the RPBE functional which gives the same improvements of the chemisorption energies but at the same time fulfills the Lieb-Oxford criterion locally.

## 2.3 The Vienna Ab initio Simulation Package

The previous sections gave a brief overview of density functional theory with special consideration of exchange-correlation functionals and their different degrees of sophistication and accuracy. There was also a description of the advantages of plane-wave basis sets and the concepts of pseudopotentials, as an indispensable ingredient for efficient plane-wave based calculations.

The following paragraph outlines the key features of the Vienna Ab-initio Simulation package (VASP), a plane-wave based density functional code developed by Georg Kresse and Jurgen Furthmuller[101,102], maintained and extended under the direction of Georg Kresse by many people from the Computational Materials Science group at Institut für Materialphysik of the University of Vienna. VASP includes an optimised set of ultrasoft pseudopo-

tentials and PAW potentials for all elements of the periodic system. The first parts of the code were written in the early 90's of the last century, currently it consists of more than 80000 lines written in Fortran90.

VASP solves the Kohn-Sham equations of local density or spin-density functional theory iteratively within a plane-wave basis set. The electronic ground state is determined either by a conjugate gradient algorithm as optimised by Teter[198], by a blocked Davidson scheme as first proposed by Davidson[199]), or via an unconstrained band-by-band matrix-diagonalisation scheme based on a residual minimization method (RMM)[102,200]. A comprehensive review of iterative minimisation techniques have been written by Kresse and Furthmuller[102]. After each iteration the charge density has to be recalculated. To guarantee numerical stability the new density is mixed with the input charge density of the previous cycle by use of an improved Pulay mixing[201].

Besides the pure local density approximation (LDA) for exchange-correlation functional the following gradient corrected functionals as presented in Section (2.2.5) are implemented in VASP to account for the nonlocality in exchange and correlation:

- LM
- BP
- PW91
- PBE
- RPBE

The PKZB metaGGA functional is included in a non-selfconsistent way based on orbitals obtained by selfconsistent PBE calculation. Implementation of hybrid functionals is in its initial stages.

Another important issue is the energy band dispersion in the Brillouin-zone. Sampling in the reciprocal space is done on points of Monkhorst-Pack special grids[45]. For the integration over the Brillouin zone the tetrahedron method with Blochl corrections[43] and a generalized Gaussian smearing[202] are available among other less involved methods. Further informations about VASP can be found at <http://cms.mpi.univie.ac.at/vasp/>.

## 2.4 The mesoscopic regime

The mesoscopic regime deals with entities composed by a large number of particles (i.e. atoms and molecules); yet, the discrete nature of matter is still explicitly taken into account. Characteristic length scales range from fractions to hundreds of microns. Such scales are presently intractable by direct implementation of computational quantum mechanics; yet, in a multiscale modelling approach we need to have atomic resolution even in this regime. The way to deal with such a large number of degrees of freedom is to adopt a coarse grained approach and match or combine data from first-principles calculations with concepts from thermodynamics or statistical mechanics (fig. 2.1).

## 2.4.1 Thermodynamics

Thermodynamics can only formulate relationships among macroscopic properties derived from the laws of thermodynamics [19]. The formulations of these laws are derived from, and are precise representations of, the essential features of the observed behavior of matter at the macroscopic level. Since these laws are statements of observation at the macroscopic level, they are independent of any assumption about the microscopic structure of matter, which could be either atomic or continuous as far as the principles of thermodynamics are concerned. As such, thermodynamics alone does not give insight into the microscopic structure of matter.

The laws of thermodynamics must be postulated. They cannot be proven in any way and have been developed through the observation of a large number of systems.

- *Zeroth* law: if systems A and B are in thermodynamic equilibrium, and systems B and C are in thermodynamic equilibrium, then systems A and C are also in thermodynamic equilibrium.
- *First* law: Energy can be changed from one form to another, but it cannot be created or destroyed. The total amount of energy and matter in the Universe remains constant, merely changing from one form to another.
- *Second* law: The second law can be stated either in its classical form or its statistical form.
  - Heat can only flow from a higher temperature to a lower temperature.
  - The entropy of a closed system (i.e. a system of particles which does not exchange heat, work or particles with its surroundings) tends to remain constant or increases monotonically over time.
- *Third* law: The entropy of a system approaches a constant as the temperature approaches zero Kelvin.

A thermodynamic description of a system containing many molecules is characterized by the use of a small number of macroscopic variables, whereas a complete microscopic mechanical description needs a vast number of variables. It is very clear, from the nature of the different analysis, that, if a thermodynamic description of a system is to be consistent with a microscopic description, some grouping together, or averaging, or systematic ignoring of microscopic variables must be an inherent part of the connection between the two theories. The thermodynamic description of a system is inevitably coarser than the microscopic description.

## 2.4.2 Statistical mechanics

Statistical mechanics (SM) provides the link between the microscopic properties of matter and its bulk properties, i.e. the link between the microscopic mechanical and thermodynamic descriptions. Instead of looking for exact solutions to the microscopic mechanical equations of motion, SM deals with the probabilities of the system being in one state or

another. Hence the name statistical mechanics[19].

The objects whose properties are calculated by statistical mechanics are known as systems. SM deals with the states of the system. To specify a state, one specifies values for every variable of the complete microscopic description. Specifying values for all of the microscopic variables is sufficient to fully specify the state of the system.

Statistical mechanics can deal with classical or quantum systems. Even though the microscopic description of the adsorbate/substrate system studied in this thesis requires a quantum mechanical treatment; its mesoscopic description can be satisfactorily carried out within classical statistical mechanics (this point will be extensively discussed in Chapter 5). As a result, we are concerned here with the statistical mechanics description of ensembles of classical systems.

The state space of a given system  $S$  consists of all possible configurations  $i$ , i.e. microstates. The system evolves in time occupying different configurations, which gives a probability distribution over configuration space. For each point  $C$  in configuration space, the probability  $P(i, t)$  of finding the system in configuration  $i$  at time  $t$  satisfies the master equation

$$\frac{\partial P(i, t)}{\partial t} = - \sum_j W(i \rightarrow j)P(i, t) + \sum_j W(j \rightarrow i)P(j, t), \quad (2.40)$$

where  $j$  is any point in configuration space, and  $W(i \rightarrow j)$  and  $W(j \rightarrow i)$  are the probabilities of making a transition from configuration  $i$  to  $j$  and vice versa [19]. In fact, there is an equation like Eq. (2.40) for each point in configuration space, and the set of all such equations constitute the master equation. The probabilities  $P(i, t)$  must also obey the sum rule

$$\sum_i P(i, t) = 1, \quad (2.41)$$

for all  $t$ , since the system must always be in some state.

In general, a master equation (also known as the Chapman-Kolmogorov equation in probability [19]) is a phenomenological first order differential equation describing the time-evolution of the probability of a system to occupy each one of a discrete set of states. The master equation and its sum rule, Eqs. (2.40) and (2.41), can be considered as a "continuity equation" expressing the fact that the total probability is conserved. Probability of a state  $i$  that is "lost" by transitions to state  $j$ , is gained in the probability of state  $i$ , and vice versa. Eq. (2.40) just describes the balance of gain and loss processes.

An observable macroscopic property  $Q$  of the system at time  $t$  is related to the configurations  $C$  by the expectation value of  $Q$

$$\langle Q(t) \rangle = \sum_i Q_i P(i, t), \quad (2.42)$$

where  $Q_i$  is the value of the system observable  $Q$  in configuration  $C$ .

Since the master equation Eq. (2.40) is first order with real parameters, and since the variables  $P(i, t)$  are constrained to lie between zero and one (which effectively prohibits exponentially growing solutions to the equations), all systems governed by these equations must come to equilibrium at the end. Thus, at equilibrium, there exists a unique distribution  $P_i$  which satisfies the following stationary condition:  $\partial P(i, t)/\partial t = 0$ , i.e.

$$\sum_j W(i \rightarrow j)P_i = \sum_j W(j \rightarrow i)P_j, \quad (2.43)$$

which expresses the condition of global equilibrium. A numerical method based on Markov processes (e.g. Metropolis Monte Carlo method) using transitions given by this condition does not guarantee that the transition probabilities lead to an equilibrium distribution irrespective of the initial state. Indeed, the system can satisfy Eq. (2.40) and actually be rotating in a so-called limit cycle (dynamic equilibrium), where the probability distribution is not invariant after one transition, but only after  $n$  transitions [48]. In practice, this problem can be avoided by imposing a stronger condition called detailed balance:

$$W(i \rightarrow j)P_i = W(j \rightarrow i)P_j, \quad (2.44)$$

which is essentially assuming local equilibrium for every allowed transition in order to force global equilibrium.

The condition of detailed balance given by Eq. (2.44) implies that, at equilibrium, the average number of moves  $i \rightarrow j$  is the same as the average number of inverse moves  $j \rightarrow i$ . This is also known as the principle of microscopic reversibility; i.e. every microscopic process in the system is exactly balanced by its inverse process so that there is no net effect on the system. As this is true for any two arbitrary conformations it follows that if the system in equilibrium is submitted to moves that obey the detailed balance condition there will be no change in the probability of any conformation and the system will remain in equilibrium.

The fundamental postulate of equilibrium statistical mechanics can be stated as follows:

- All possible quantum states (microstates) of an isolated system consistent with a given set of macroscopic parameters of constraints are to be considered as equally probable.

This postulate of equal a priori probabilities is also known as the ergodic hypothesis and cannot be obtained from more fundamental arguments. Although eminently reasonable, and consistent with the laws of mechanics, the postulate stated must be recognized as a fundamental assumption in the development of the statistical theory. Such an assumption can only be indirectly verified a posteriori by the success of theoretical calculations in interpreting and reproducing the results of observation.

The ergodic hypothesis can be equivalently formulated by saying that time average and average over statistical ensembles are the same [50]. This formulation allows for the development of ensemble theory in statistical mechanics (Fig. 2.4).

In practice, during the time of measurement on a single system, the system undergoes a large number of changes from one microstate to another. The observed macroscopic properties of the system are time averages of the properties of the instantaneous microstates, i.e. of the mechanical properties. Simulating the evolution of the system in time would in principle require one to follow the trajectory of every particle in the system. It is not feasible to solve the equations of motion for such a system because there are simply too many equations. An alternative to time averaging is provided by the concept of an ensemble average.

An ensemble (Fig. 2.4) is a very large set of similar systems, i.e. replicas of the system, considered all at once. The systems in the ensemble could interact with each other and with a system called reservoir (or heat bath). Thus, instead of looking at one system over a period of time, one looks at a collection of a large number of systems (all of which are replicas of the system under consideration) at a given instance of time. The nature of the boundaries between the systems determines the type of ensemble:

- If the boundaries are impermeable, each system is completely isolated, and there are no interactions among the systems, the ensemble is called micro-canonical. The systems are constrained to a fixed number of particles  $N$ , fixed volume  $V$ , and fixed energy  $E$ .
- If the walls are permeable to energy but not to anything else, and only energy can be transferred among systems, the ensemble is called canonical. The systems are constrained to fixed number of particles  $N$ , fixed volume  $V$ , and fixed temperature  $T$ .
- If both energy and matter can be exchanged among systems, but the walls are impermeable to all other influences, the ensemble is called grand canonical. The systems are constrained to fixed  $V$ , fixed chemical potential  $\mu$  and fixed temperature  $T$ .

These are the "standard" ensembles; however, it is possible to define ensembles with different types of constraints [19].

Every ensemble has a characteristic partition function. The partition function is the sum over all available microstates of the system. It encodes the statistical properties of a system in thermodynamic equilibrium, i.e. all thermodynamic properties can be derived from it. The partition function in statistical mechanics is the equivalent of the Schrödinger equation in quantum mechanics. Table 2.1 shows the partitions function and the constraints for each ensemble. The microcanonical partition function is denoted by  $\Omega$ . The Dirac delta function  $\delta$  ensure that there is a contribution only from those states with an energy equal to  $E$ .  $\Omega$  is

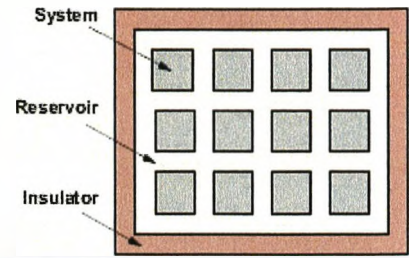


Figure 2.4: An ensemble, or collection, of macroscopic systems in equilibrium with a reservoir. The whole ensemble is isolated from the universe.



	Microcanonical	Canonical	Grand canonical
Constraints	$(N, V, E)$	$(N, V, T)$	$(\mu, V, T)$
Partition function	$\Omega = \sum_i \delta(E_i - E)$	$Z = \sum_i e^{-E_i/k_B T}$	$\Xi = \sum_i e^{-(E_i + \mu_i N_i)/k_B T}$

Table 2.1: Ensembles in statistical mechanics

equal to the degeneracy of the system, i.e. the number of microstates with the energy  $E$ . The canonical partition function is denoted by  $Z$ . Roughly,  $Z$  is a measure of how many different energy states of the system are appreciably populated when the system is in thermal equilibrium at temperature  $T$ , i.e. it indicates how the energy is partitioned among the different states. The energy of the microstates  $E_i$  is weighted by the factor  $(k_B T)^{(-1)}$  where  $k_B$  is the Boltzmann constant. The grand canonical partition function is denoted by  $\Xi$ . It is analogous to  $Z$  for situations, where the number of particles is allowed to vary. That is why one has to introduce chemical potentials  $\mu_i$ ; i.e.  $\mu_i$  denotes the energy cost of adding or removing a particle  $i$  from the system.

The sums in table 2.1 are over all possible states of the system allowed by the constraints. The sums depend upon the size of the system and the number of degrees of freedom for each particle.

The transition rates  $W(i \rightarrow j)$  appearing in the master equation Eq. (2.40) take particular values which arise out of the thermal nature of the interaction between the system and the thermal reservoir. It is important that they are chosen in a way that mimics the interactions with the thermal reservoir correctly [48]. The important point is that the equilibrium values of finding the system at configuration  $i$  are known a priori. These equilibrium values are known as equilibrium occupation probabilities and are denoted by

$$P_i = \lim_{t \rightarrow \infty} P(i, t). \quad (2.45)$$

The nature of the system and its surroundings determines its equilibrium occupation probabilities  $P_i$ . For a system in the microcanonical ensemble  $P_i = 1/\Omega$  (i.e. the microcanonical distribution function), the equilibrium distribution of electrons (Fermions) is given by the Fermi-Dirac distribution function, that of a non-interacting Bose gas (Bosons) is given by the Bose-Einstein distribution function. In general the distribution function of a quantum system is given by  $|\psi|^2$ , i.e. the probability associated with the wave function solution of the Hamiltonian under investigation [19].

In a particular problem, the choice of ensemble depends on the characteristics of the system under study. In principle, all ensembles are equivalent, and they lead to the same results; however, an appropriate choice of ensemble can simplify a statistical mechanics calculation considerably.

The experimental measurement of two-dimensional adsorbate phase diagrams is mostly carried out through LEED experiments [49]. Those experiments are carried out at  $(N, V, T)$  approximately constant and the adsorbate overlayer can usually be assumed to be a classical system. Thus, in order to mimic the experimental situation, the canonical ensemble is the appropriate choice to numerically simulate the two-dimensional phase transitions of adsorbates. In the following, the canonical partition function  $Z$  is used in the formulas; however, they are valid for all the ensembles, provided the right partition function is used.

The probability  $P(i, t)$ , of finding the system in configuration  $i$  at time  $t \rightarrow \infty$  (i.e. the equilibrium occupation probability  $P_i$ ) is given by the Boltzmann distribution [50]

$$P_i = \lim_{t \rightarrow \infty} P(i, t) = \frac{1}{Z} e^{-E_i/k_B T}, \quad (2.46)$$

where  $E_i$  is the energy when system is in the  $i$ th state.

From Eq. (2.42) and (2.46) the expectation value of any observable  $Q$  for a system in equilibrium at temperature  $T$  is

$$\langle Q \rangle = \sum_i Q_i P_i = \frac{1}{Z} \sum_i Q_i e^{-E_i/k_B T}. \quad (2.47)$$

For example, the expectation value of the energy  $\langle E \rangle$ , which is also the quantity known in thermodynamics as the internal energy  $U$ , is given by

$$U = \frac{1}{Z} \sum_i E_i e^{-E_i/k_B T}. \quad (2.48)$$

The only information needed to apply Eq. (2.42) is the knowledge of the microstate energies  $E_i$ . In principle, those can be obtained from quantum mechanics at  $T = 0K$ . Thus, statistical mechanics allows calculation of the thermodynamical properties of the system at any temperature  $T$  from the knowledge of the energetics of the system at  $T = 0K$ . In fact, in the absence of work, the energy levels of a system remain fixed when heat is added to the system. The energy levels are functions of the external parameters alone (e.g. volume, magnetic and electric fields). It is the occupancy of the levels, i.e. the Boltzmann probability distribution, that changes when heat is added to the system. Statistical mechanics prescribes the way the changes in probabilities determine the thermodynamic properties of the system at temperature  $T$ . If work is done on the system, but no heat is added to it, the Boltzmann probability distribution remains constant, but the energy levels change. In this case, the quantum mechanical reference system at  $T = 0K$  has to be modified in order to work out the corresponding energy levels.

For a system consisting of only a few interacting particles, the partition function can be written down exactly with the consequence that the properties of the system can be calculated in closed form. However, in general, for large systems of interacting particles the partition function cannot be evaluated exactly. One has to resort to Monte Carlo methods to numerically evaluate the partition function.

Before getting into the details of Monte Carlo algorithms, it is convenient to introduce a simple statistical model through which the algorithms will be explained.

Ising model	Lattice-gas model
Canonical ensemble	Grand canonical ensemble
Coupling constant $J$	Interaction energy $\epsilon$
External field $B$	Chemical potential $\mu$
Magnetization $M$	Coverage $\Theta$
Susceptibility $\chi$	Compressibility $\alpha$
Curie point	Critical point

Table 2.2: Correspondence between the Ising model and the Lattice-gas model

### 2.4.3 The Ising and Ising-like models

The Ising model [51] is one of the simplest and most fundamental models of statistical mechanics. It can be used to describe such diverse phenomena as magnets, liquid-gas coexistence, alloys, adsorbates on metals, and many others. The particular form of this model considered here is that of an infinite regular square lattice in two-dimensions only. Each site in the lattice contains an elementary variable  $s$  called spin with possible values  $s = \pm 1$  (see 2.5). The spin at each lattice site  $i$  interacts with its four nearest sites such that the overall Hamiltonian for the system is

$$H_{Ising} = -J \sum_{\langle i,j \rangle} s_i s_j, \quad (2.49)$$

where the sum over  $\langle i, j \rangle$  represents a sum over the nearest neighbors of all the lattice sites, and  $J$  is the nearest sites interaction energy. Each state of the system, i.e. each configuration of spins  $s$  occurs with probability given by Eq. (2.46). Even though the Ising model is a drastic simplification compared to realistic situations, it is able to describe the occurrence of order at low temperatures and disorder at high temperatures, and especially the phase transition between those situations, in which spin correlations over very large length scales become essential. The lattice-gas model (LG) is isomorphic with the Ising model. The only difference is that each cell can be either occupied by a particle ( $n_i = 1$ ) or unoccupied ( $n_i = 0$ ). The variables  $n$  are usually called point or occupation variables. The correspondence with the Ising model is established by making the change of variables

$$s_i = 2n_i - 1. \quad (2.50)$$

The interaction of a lattice-gas model model can then be expressed as an Ising-like hamil-

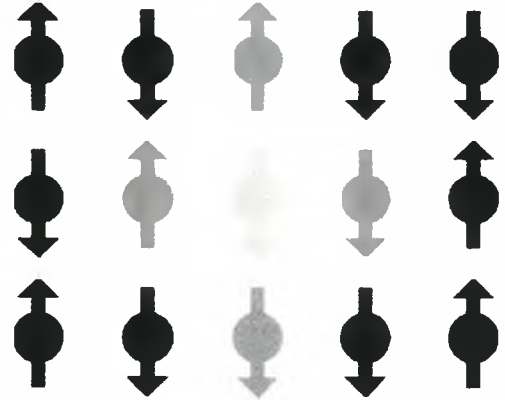


Figure 2.5: One possible arrangement of Ising spins on a lattice. Each spin is either up or down. The nearest states of the spin in the center have been highlighted

tonian

$$H_{LG} = -\varepsilon \sum_{\langle i,j \rangle} n_i n_j. \quad (2.51)$$

The correspondence between the Ising model and the lattice-gas model up to a constant or a factor is summarized in table 2.2[50].

The Ising model is important because similar (more sophisticated) models, like the lattice-gas model, can be constructed by generalizing the nature of the lattice and the number of components and states. The Ising model can be extended by:

- Letting  $s_i$  have several values (Potts model)
- Introducing vectors  $s_i$  and writing the interactions as  $(s_i \cdot s_j)$  (Heisenberg model).
- Introducing complex lattices (fcc, bcc, trigonal, hexagonal...)
- Introducing several sub-lattices (decorated lattices)
- Introducing interaction of more distant neighbors and multisite interactions (cluster expansion technique)
- Making J random (glass models)
- Extending the model to three dimensions (three dimensional Ising model)
- Introducing kinetics and making the model time-dependent (non-equilibrium simulations, cellular automata)

The Ising model can be solved exactly only in the simplest cases (in one spatial dimension, and on a two-dimensional square lattice [52]). In most cases of practical interest, one has to resort to numerical techniques like Monte Carlo simulations, or use approximate analytical techniques.

#### 2.4.4 Monte Carlo Methods

Monte Carlo [48] is a numerical technique that makes use of random numbers to solve a problem. Monte Carlo methods are used in statistical mechanics for the calculation of thermal averages according to the principles of statistical mechanics in a given equilibrium ensemble.

In a Monte Carlo simulation, a set of random numbers is used to determine the sequence of states through which the system evolves. Consequently, the changes in the system do not occur in a predefined fashion, i.e. deterministically, but in a stochastic manner such that the average quantities obtained from two independent runs agree within some statistical error. The time in connection with Equilibrium Monte Carlo simulations is referred to as the "Monte Carlo time" and it is not directly related to the real physical time [48]. In contrast, the Kinetic Monte Carlo method [53] has been specifically designed to describe the dynamical evolution of the system, and therefore it can be used to study time-dependent physical properties.

Since in this thesis we are interested in equilibrium properties of Ising-like systems (Section

2.4.3), we concentrate here on the theoretical foundation behind the standard application of Monte Carlo methods (e.g. Metropolis and Wolff algorithms) to the simulation of thermal equilibrium systems.

The usual goal in such Monte Carlo simulations of thermal systems is the calculation of the expectation value  $\langle Q \rangle$  of some observable quantity  $Q$ . The ideal route of calculating such an expectation value is averaging the quantity of interest over all states  $i$  of the system, weighting each with its own Boltzmann probability, i.e. Eq. (2.47). However, complete enumeration of configuration space in medium size systems is impossible with present day computers, let alone that it is inefficient and unnecessary.

In Monte Carlo simulations this difficulty is solved by replacing the set of all configurations in Eq. (2.47) by a representative tractable subset of  $M$  configurations, where  $M$  is much smaller than the total number of configurations,  $N$ . An estimate for the thermal average, is then obtained by

$$Q_M = \frac{\sum_{i=1}^M Q_i e^{-E_i/k_B T}}{\sum_{i=1}^M e^{-E_i/k_B T}}. \quad (2.52)$$

It is clear that the accuracy of the estimate will depend directly on the quality of the representative subset of  $M$  configurations. In a simple sampling method, for example, where the  $M$  configurations are chosen randomly, the immense majority of the configurations will have energies very different from the average energy of the system at temperature  $T$  and their contribution to the estimate will be insignificant due to the small Boltzmann factor. The estimate obtained by simple sampling would be, therefore, very inaccurate, unless  $M$  becomes as big as  $N$ , or even larger.

The idea of importance sampling in MC simulations is to choose the representative set of configurations not completely at random, but in such a way that the selection is somehow biased towards configurations that are significantly populated at equilibrium. In general, if the probability that a given configuration appears in the sample representative of configurations is  $P'_i$ , then one should weight the contribution of configuration  $i$  by the inverse of the sampling probability [53], i.e. Eq. (2.52) becomes

$$Q_M = \frac{\sum_{i=1}^M \frac{Q_i e^{-E_i/k_B T}}{P'_i}}{\sum_{i=1}^M \frac{e^{-E_i/k_B T}}{P'_i}}. \quad (2.53)$$

The real system is not sampling all states with equal probability, but instead sampling them according to the Boltzmann probability distribution, Eq. (2.46). If one can mimic this effect in the simulations, one can exploit these narrow ranges of sampling to make estimates of such quantities very accurate. Thus, if the configurations are chosen with sampling probability  $P'_i \propto e^{E_i/k_B T}$ , then the Boltzmann factors cancel out and the estimate for the thermal average just becomes

$$Q_M = \frac{1}{M} \sum_{i=1}^M Q_i. \quad (2.54)$$

The only remaining question is how exactly to pick the states so that each one appears with its correct Boltzmann probability. One cannot simply choose states at random and accept or reject them with  $P'_i \propto e^{E_i/k_B T}$ . That would be no better than the original scheme of

sampling states at random. Instead, almost all Monte Carlo schemes rely on Markov chains as the generating engine for the set of states used. Concerning Monte Carlo applications, a Markov chain is a mechanism which, given a system in one state  $i$ , generates a new state of that system  $i + 1$ . It does so in a random fashion; it will not generate the same new state every time it is given the initial state  $i$ . The probability of generating the state  $i + 1$  given  $i$  is called the transition probability  $P(i \rightarrow i + 1)$  for the transition from  $i$  to  $i + 1$ . Thus the Markov chain

$$a_i \rightarrow a_{i+1} \rightarrow a_{i+2} \rightarrow a_{i+3} \cdots \rightarrow a_{i+n-1} \rightarrow a_{i+n}, \quad (2.55)$$

has the following properties [48]:

- Each "link" in the chain depends only on the configuration of the "link" immediately before it.
- Links from further in the past are irrelevant for determining the next configuration, i.e. the probability of transitions between states is independent of history
- The transition probabilities do not vary over time

The transition probabilities from state  $i$  to state  $j$  (i.e.  $i + 1$ ) in the Markov chain must also satisfy the constraint

$$\sum_j W(i \rightarrow j) = 1, \quad (2.56)$$

since the Markov chain must generate some state  $j$  when handed a system in state  $i$ .

In order to achieve an equilibrium distribution, the Markov chain must obey two requirements [48]:

- It must be ergodic, i.e. there must be a "path" from every state  $i$  to every state  $j$
- It must obey detailed balance, (i.e. microscopic reversibility)

The condition of ergodicity implies that one is allowed to set some of the transition probabilities  $P(i \rightarrow j)$  of the Markov chain to zero, but that there must be at least one path of non-zero transition probabilities between any two states picked at random. This is necessary to achieve the stated goal of generating states with their correct Boltzmann probabilities. Every configuration  $j$  appears with some non-zero probability  $P_j$  in the Boltzmann distribution. If that state was inaccessible from another state  $i$ , no matter how long the Markov process continues, the goal is thwarted if one starts in state  $i$ .

The condition of detailed balance ensures that the system converges to the selected equilibrium probability distribution. It also allows free choice of the equilibrium probability distribution of configurations [48]. For a system in the canonical ensemble at thermal equilibrium this probability distribution function is given by the Boltzmann distribution.

Thus, substituting Eq. (2.46) into Eq. (2.44) leads to the following form of the detailed balance condition

$$\frac{W(i \rightarrow j)}{W(j \rightarrow i)} = \frac{P_j}{P_i} = e^{-(E_j - E_i)/k_B T}. \quad (2.57)$$

Note that the partition functions cancel out in the ratio  $P_j/P_i$ . The transition probabilities can also be written as

$$W(i \rightarrow j) = g(i \rightarrow j)A(i \rightarrow j), \quad (2.58)$$

where the quantity  $g(i \rightarrow j)$  is the selection probability, which is the probability, given an initial configuration  $i$ , that the algorithm will generate a new target configuration  $j$ , and  $A(i \rightarrow j)$  is the acceptance probability of the new configuration. Writing the transition probabilities in this way gives us complete freedom about how to choose the selection probabilities  $g(i \rightarrow j)$ , since the constraint Eq. (2.59) only fixes the ratio

$$\frac{W(i \rightarrow j)}{W(j \rightarrow i)} = \frac{g(i \rightarrow j)A(i \rightarrow j)}{g(j \rightarrow i)A(j \rightarrow i)} = e^{-(E_j - E_i)/k_B T}. \quad (2.59)$$

The constraints on the choice of transition probabilities  $W(i \rightarrow j)$  are given by Eq. (2.59). Satisfying such constraints and the condition of ergodicity ensures that the equilibrium distribution of configurations generated by the Markov process will be the Boltzmann distribution.

### The Metropolis Monte Carlo algorithm

The Metropolis algorithm [55] is the workhorse of stochastic simulations. Its simplicity, range of application, and power make it the algorithm of choice in Monte Carlo simulations. In the following, we discuss the derivation of the Metropolis algorithm based on the general theory of Monte Carlo methods (Section 2.4.4). The derivation is more transparent if it is applied to a specific system. For that purpose, we use the Ising model (Section 2.4.3), since it is the generic model used later to describe adsorbed overlayers on surfaces in this study.

The derivation of the Metropolis algorithm consists of choosing selection probabilities  $g(i \rightarrow j)$  and acceptance probabilities  $A(i \rightarrow j)$  such that Eq. (2.59) satisfies the condition of detailed balance. The algorithm works by repeatedly choosing a new configuration  $j$ , and then accepting or rejecting it at random with the chosen acceptance probability. If the configuration is accepted, the system changes to the new configuration  $j$ . If not, it just leaves it as it is. Then, the process is repeated again and again.

The selection probabilities  $g(i \rightarrow j)$  should be chosen so that the condition of ergodicity, i.e. the requirement that every state be accessible from every other in a finite number of steps, is fulfilled. Besides, since the real system in thermal equilibrium spends most of its time in a subset of configurations with a narrow range of energies [48], the algorithm should avoid configurations whose energy is very different from the energy of the present configuration. The simplest way of achieving this in the Ising model is to consider only those states which differ from the present one by the flip of a single spin, i.e. single-spin-flip dynamics. For a  $N$  spin system, there are then  $N$  different spins that one could flip, and hence  $N$  possible states  $j$  that one can reach from a given state  $i$ , i.e.

$$g(i \rightarrow j) = \frac{1}{N}. \quad (2.60)$$

Using single-spin-dynamics also ensures that the algorithm obeys ergodicity, since it can get from any state to any other on a finite lattice by flipping one by one each of the spins by which the two states differ.

With the selection probabilities given by Eq. (2.60), the condition of detailed balance Eq.

(2.59) takes the form

$$\frac{A(i \rightarrow j)}{A(j \rightarrow i)} = e^{-(E_j - E_i)/k_B T}. \quad (2.61)$$

It remains only to choose the acceptance probabilities  $A(i \rightarrow j)$  and  $A(j \rightarrow i)$  to satisfy this equation. The only constraint is that both acceptance probabilities remain between zero and one.

To make the algorithm as efficient as possible, the acceptance ratio should be as large as possible (i.e. the algorithm should move freely about configuration space and sample a wide selection of configurations according to the Boltzmann distribution). The way to maximize the acceptance ratio (and therefore produce the most efficient algorithm) is always to give the larger of the two acceptance probabilities the largest value possible, namely 1, and then adjust the other to satisfy the constraint [48]. For example, suppose that of the two states (i.e.  $i$  and  $j$ )  $i$  has the lower energy and  $j$  the higher (i.e.  $E_j > E_i$ ); then the larger of the two acceptance probabilities is  $A(j \rightarrow i)$ , because  $e^{-(E_j - E_i)/k_B T} < 1$  in Eq. (2.61). Thus, one sets  $A(j \rightarrow i) = 1$ ; and, in order to satisfy Eq. (2.61),  $A(i \rightarrow j)$  must take the value  $e^{-(E_j - E_i)/k_B T}$ . Thus the optimal algorithm is one which satisfies

$$P(E_1 \rightarrow E_2) = \min[e^{-(E_2 - E_1)/k_B T}, 1]. \quad (2.62)$$

In other words, if a configuration is selected with an energy lower than or equal to the present one, the transition to that state should always be accepted. If it has a higher energy, then the new configuration might be accepted with the probability given by  $e^{-(E_j - E_i)/k_B T}$ . This is the acceptance rule which characterizes the Metropolis algorithm. There are actually many ways to choose acceptance probabilities which satisfy the condition of detailed balance Eq. (2.61); however, the Metropolis acceptance rule appears to date to be by far the most efficient one[48].

Any Monte carlo algorithm, applied to any model, which chooses acceptance probabilities according to the rule Eq. (2.62) can be said to be a Metropolis algorithm [48]. The explicit rules for the Metropolis algorithm applied to the simple Ising model of Section 2.4.3 are:

1. Start with an arbitrary spin configuration  $\alpha_k = \{s_1, s_2, \dots, s_N\}$
2. To generate a new configuration  $\alpha_{k+1}$ 
  - (a) Pick a particle  $i$  randomly
  - (b) Reverse  $i$ 's spin direction to create a trial configuration  $s_{tr}$
  - (c) Calculate the energy  $E(\alpha_{tr})$  of the trial configuration
  - (d) If  $E(\alpha_{tr}) \leq E(\alpha_k)$ , accept the trial; that is, set  $\alpha_{k+1} = \alpha_{tr}$
  - (e) if  $E(\alpha_{tr}) > E(\alpha_k)$ , accept with probability  $P = e^{-\beta(E_{tr} - E_k)}$ 
    - i. Choose a uniform random number  $0 \leq r \leq 1$

The Metropolis algorithm generates a random walk of points distributed according to the Boltzmann distribution Eq. (2.46). From an initial "position" in phase or configuration space, a proposed "move" is generated and the move is either accepted or rejected according to the Metropolis algorithm. By taking a sufficient number of trial steps all of the



relevant phase space is explored and the Metropolis algorithm ensures that the points are distributed according to the Boltzmann distribution.

Note that the temperature  $T$  enters into the simulation through the Boltzmann factor  $e^{-E/k_B T}$ , i.e. the properties of the system can only be calculated at the specific temperature  $T$  of the simulation. To study how the system depends on  $T$ , it is necessary to carry out simulations at different temperatures. After equilibration at a specific temperature, any macroscopic quantity of interest can be averaged over different configurations generated by the Metropolis algorithm. Observables are evaluated by sampling the system at different configurations  $M$  belonging to the Boltzmann distribution, i.e. observables are calculated from the statistical average Eq. (2.54).

Thus, rather than finding an exact solution, Metropolis Monte Carlo allows one to stochastically sample a probability distribution  $P$  (in this case the Boltzmann probability distribution) and obtain an ensemble of configurations  $i$  which conform to  $P$ . Ensemble averages over that distribution may then be obtained to within arbitrary precision by increasing the number of states sampled.

The Metropolis algorithm is also useful in combinatorial optimization problems. By permitting the system to accept sometimes configurations with higher energy (i.e. go "uphill" for a while), this technique is successful at finding a global extremum for situations in which other techniques stick in local ones. Its success relies on imposing a slow cooling schedule to the combinatorial problem. This optimization technique is known as simulated annealing [56].

Even though simple and powerful, the Metropolis algorithm has some limitations, especially near phase transitions. Those limitations will be explained in Chapter 5, when discussing the calculation of thermodynamic properties from Metropolis Monte Carlo simulations. Here, we discuss a different approach to Monte Carlo simulations that avoids the problem of the Metropolis algorithm near phase transitions.

### The Wang-Landau Monte Carlo algorithm

A class of Monte Carlo methods, called the generalized ensemble algorithms [57] have been conceived in order to overcome the multiple-minima problem of the standard Metropolis algorithm. In a generalized ensemble simulation, each state is weighted by a non-Boltzmann probability weight factor so that a random walk in potential energy space may be realized. These methods (e.g. multicanonical method [53], flat histogram method [53], the broad histogram method [53], Wang-Landau method [58-62]) have been developed based on re-writing the partition function as a sum over energies

$$Z(T) = \sum_i e^{-E_i/k_B T} \equiv \sum_E \Omega(E) e^{-E/k_B T}, \quad (2.63)$$

where  $\Omega(E)$  is the configurational density of states (CDOS), i.e. the number of possible configurations for an energy level  $E$ . thus, the partition function  $Z$  is reduced from a sum over all configurations  $i$  to a sum over all energy levels. The partition function would be tractable if the configurational density of states  $\Omega(E)$  could be evaluated.

The Wang-Landau algorithm is designed to calculate an estimate of  $\Omega(T)$ . In practice, this estimate is so close to the true density of states that thermodynamic quantities can

be accurately derived from it. The Wang-Landau algorithm has its origin in the entropic sampling method [63], the difference being only the update rule of the CDOS estimate. The basic idea is to sample from a distribution other than the Boltzmann distribution. In principle, one can sample configurations from any probability distribution  $P'_i$ , as expressed be Eq. (2.53), and still get an estimate  $Q_M$  of the observable  $Q$ . In the entropic sampling and Wang-Landau methods, instead of sampling configurations with  $P'_i \alpha e^{-E_i/k_B T}$  as in the Metropolis algorithm, one samples configurations with  $P'_i \alpha e^{1/\Omega(E)}$ , i.e. the reciprocal of the density of states. In other words, states in the ranges of  $E$  where there are many configurations, so that the density of states is high, are sampled with lower probability than those in ranges where there are few configurations.

With a probability  $P'_i$  for a single configuration of energy  $E$ , the probability of sampling an arbitrary configuration with energy  $E$  is given as

$$P_E = \Omega(E)P'_i, \quad (2.64)$$

where the density of states  $\Omega(E)$  counts the number of configurations with energy  $E$ . Upon choosing  $P'_i \alpha 1/\Omega(E)$  instead of the canonical weight  $P(E) \alpha e^{-E/k_B T}$  one obtains a constant probability  $P_E$  for visiting each energy level  $E$ , and hence a perfectly flat histogram. With this sampling selection, the estimation of the observables, Eq. (2.52), becomes

$$Q_M = \frac{\sum_{i=1}^M Q_i \Omega(E_i) e^{-E_i/k_B T}}{\sum_{i=1}^M \Omega(E_i) e^{-E_i/k_B T}}. \quad (2.65)$$

This formula applies for a sample of size  $M$ . However, if one has knowledge of the complete density of states  $\Omega(E)$ , observables are better calculated from:

$$Q = \frac{\sum_E Q_i \Omega(E_i) e^{-E_i/k_B T}}{\sum_E \Omega(E_i) e^{-E_i/k_B T}}. \quad (2.66)$$

Implementation of entropic sampling is straightforward. One only has to employ the condition of detailed balance

$$\frac{W(i \rightarrow j)}{W(j \rightarrow i)} = \frac{P_j}{P_i} = \frac{\Omega(E_i)}{\Omega(E_j)}, \quad (2.67)$$

which, using the same arguments as in the Metropolis algorithm, can be reduced to an acceptance probability ratio

$$\frac{A(i \rightarrow j)}{A(j \rightarrow i)} = \frac{\Omega(E_i)}{\Omega(E_j)}. \quad (2.68)$$

To make the algorithm as efficient as possible, the acceptance ratio should be taken as large as possible. Thus, similar to the Metropolis algorithm, the optimal entropic sampling algorithm is one which satisfies

$$P(E_1 \rightarrow E_2) = \min \left[ \frac{\Omega(E_1)}{\Omega(E_2)}, 1 \right]. \quad (2.69)$$

The condition of ergodicity is satisfied, because through single spin flipping dynamics (in the context of the Ising model, Section 2.4.3) and a random walk in energy space (due to

the flat energy distribution), the entropic sampling algorithm is able to find a path from every state  $i$  to every state  $j$ .

The only major problem left is that the density of states  $\Omega(E)$  is not known a priori and has to be calculated by the simulation algorithm. Most of the generalized ensemble methods estimate  $\Omega(E)$  based on the accumulation of histogram entries in energy space  $H(E)$ , i.e. the quantity which keeps track of the number of visits at each energy level  $E$  [48,53]. Due to the exponential growth of the density of states in energy space, this process is not efficient because the histogram is accumulated linearly. The Wang-Landau algorithm iteratively modifies the density of states using a carefully controlled modification factor. The histogram entries  $H(E)$  are accumulated during the random walk, but  $H(E)$  is only used to check whether the histogram is flat enough to go to the next level random walk with a finer modification factor.

The Wang-Landau algorithm for the simple Ising model of Section 2.4.3 has the following steps:

1. Start with an arbitrary spin configuration  $\alpha_k = \{s_1, s_2, \dots, s_N\}$
2. Create a flat initial density of states  $\Omega(E) = 1$  and take an initial modification factor  $f_i = f_0 = e^1$  (greater than 1)
3. Flip random spin and calculate the new energy  $E_2$
4. Accept spin flip with probability  $P(E_1 \rightarrow E_2) = \min \left[ \frac{\Omega(E_1)}{\Omega(E_2)}, 1 \right]$
5. Update energy histogram  $H(E_j) \rightarrow H(E_j) + 1$  (in either of both cases, i.e.  $E_j = E_1$  or  $E_j = E_2$ )
6. Update density of states according to  $\Omega(E_j) \rightarrow f_i \Omega(E_j)$  (in either of both cases, i.e.  $E_j = E_1$  or  $E_j = E_2$ ) [15]
7. Continue doing step 3-6 until a flat energy histogram is created. In practice this means until  $H(E) > c \langle H(E) \rangle$  where  $c$  is the flatness criterion parameter, typically  $0.6 < c < 0.9$
8. Enhance the modification factor  $f_{i+1} = (f_i)^a$  where exponent  $a < 1$  defines the smoothness of the iteration ( $a = 1/2$  has been recommended [58], however any  $a < 1$  will do). Reset  $H(E) = 0$  for all  $E$
9. Do steps 3-8 until  $f_n < f_{final}$ , where  $f_{final} = e^{10^{-8}} \approx 1.00000001$  (i.e. when the modification factor is essentially equal to 1)
10. Finally make the generated relative density of states  $\Omega(E)$  absolute using the knowledge of the ground state  $\Omega(E_0)$  or the total number of states  $\sum_E \Omega(E)$

Since the density of states  $\Omega(E)$  does not depend on the temperature  $T$ , only one simulation is necessary for the whole range of  $T$ . Thermodynamic properties can then be determined from averages in the form of Eq. (2.66).

Because the running estimate of the density of states  $\Omega(T)$  changes at every state in the

simulation, the Wang-Landau algorithm does not satisfy the condition of microscopic detailed balance Eq. (2.68). However, over the course of the iteration, the magnitude of the density of states modification factor  $f$  is decreased until changes are just within the precision of the computer (i.e. until  $f \approx 1$ ). At this point, the detailed balance is essentially satisfied.

Various questions about the Wang-Landau algorithm remain unanswered. For example, what determines the rate of convergence to the true energy of states?, How is flatness of the algorithm related to the accuracy?, What is the relation between the modification factor and error?, and How does the simulation actually find out the density of states? As a result, the algorithm is sometimes regarded as an empirical method [64]. Nevertheless, the standard version of the method and tuning parameters (e.g. modification factor  $f$ , energy histogram flatness criteria [58]) have proven to be very effective in calculating accurate estimates of the density of states for a great variety of systems [62]. Efforts are currently underway in order to study these important aspects of the algorithm [64-66].

## 2.5 Multiscale modelling: bridging the regimes

Statistical mechanics provides a way of evaluating the properties of large ensembles of particles. Central to this description is the partition function, see Table 2.1. In practice, one often evaluates the partition function numerically using e.g. Monte Carlo methods, as described in Section (2.4.4).

Monte Carlo methods sample the configuration space of the system under study in order to estimate quantities of interest (e.g. energy  $E$ , entropy  $S$ , heat capacity  $C$ , transition temperatures  $T_C$ ). Such sampling schemes require many evaluations of the system Hamiltonian, i.e. the energy of many different configurations. The straightforward matching with electronic structure theories would thus be to determine with DFT the energetics of all system configurations generated in the course of a Monte Carlo Simulation. Unfortunately, this direct link is currently and also in the foreseeable future computationally unfeasible. The exceedingly large configuration space of most materials science problems requires a prohibitively large number of energy evaluations (which can easily go beyond  $10^6$  for moderately complex systems), making the direct matching impossible.

A multiscale modelling approach in this context would evaluate the energy of the system from first-principles, yet this approach is not possible in view of Monte Carlo simulations. The solution to this dilemma is to map the properties of the system under study onto a simpler model that preserves the essential features of the system, i.e. to carry out a coarse-graining of the system. The model should allow for a fast and flexible way of calculating the total energy of the system; yet it should preserve the most important characteristics of the real system giving rise to the properties one is interested in. Such an approach (i.e. replacing a part of the real world under investigation by a simpler model) is nothing but an example of scientific abstraction, an approach which lies on the very foundations of modern science.

### 2.5.1 The lattice-gas model

Single crystal surfaces exhibit variations in the surface electron density that reflect the symmetry of the surface atom arrangement. The ability of different regions of the surface to exchange electrons with adsorbates, and thereby form chemical bonds, is strongly influenced by the coordination number of the various sites on the surface. More fundamentally, the ability of various surface sites to enter into bonding is related to the symmetry, nature and energy of the electronic states found at these sites [67].

Thus, the heterogeneity of single-crystal surfaces presents an adsorbate with a regular array of different sites. Similarly, the strength of the interaction varies in a regular fashion that is related to the underlying periodicity of the surface atoms and the electronic states associated with them. These variations (geometric and electronic) are known as corrugations and its corresponding PES is called corrugation potential [67]. A corrugation of zero corresponds to a completely flat surface. A high corrugation corresponds to a mountainous topology.

For chemisorbed adsorbates, the wells of the corrugation potential are steep and high. The locations of the minima of the corrugation potential thus form a well-defined lattice, at which the occupation probability density of adsorbates is sharply peaked. Then, in the study of equilibrium properties of adsorbed overlayers, one can neglect deviations of the adsorbate positions from the sites of this "preferred lattice" altogether, introducing the lattice gas model. This model has a single degree of freedom, namely an occupation variable  $n_i$  for lattice site  $i$ , with  $n_i = 1$  if at site  $i$  there is a particle, and  $n_i = 0$  if site  $i$  is empty (multiple occupancy of the lattice sites being forbidden).

In the Lattice-Gas model, the complex many-body interactions in the adsorbate/substrate system are coarse grained to lateral interactions among the adsorbates on the surface. The energy of the system is then given by a Lattice-Gas Hamiltonian of the form of Eq. (2.51). Thus, what is preserved in the model is the energy dependency on the lateral interactions among the atoms. These are the main, relevant physical quantities that enter from the real system and that are responsible for the collective behavior of atoms on surfaces. In this way, one is able to study the system by means of a simplified model that exhibits the most important features of the real system.

A quantitative description of adsorbed overlayers on metal surfaces usually requires more lateral interactions than the simple nearest neighbors interactions of Eq. (2.51), e.g. next-nearest neighbors, trios [49]. Besides, the value of the lateral interaction energies are an input to the model rather than an output. As a result, the application of the lattice-gas model faces two main problems:

- How to determine the value of the lateral interaction energies?
- How to determine how many and which type of interactions to include in the Hamiltonian?

Traditionally, in the application of the lattice-gas model in surface science, the interaction parameters have been assumed to be just close range pairs and trios, and the interaction energies were obtained by simply fitting to experimental data (e.g. phase diagrams, TPD spectra) [22,49,68,69]. This procedure obviously results in "effective parameters" with an

unclear microscopic basis, "masking" the possible effect and importance of higher order interactions. The Hamiltonian obtained in this way is unlikely to be transferable to calculation of other properties of the system.

An alternative approach is to derive the interaction parameters from electronic structure theory instead of fitting them to experiment. The appealing aspect of determining the interaction parameters in this way is that there is a "microscopic" meaning to the parameters. Earlier applications of this approach used the embedded cluster model [70] and tight binding theory [71] in order to derive interaction parameters. The predictive power of such parameters has been limited by the level of approximations to describe the electronic structure of the adsorbate/surface systems.

The development of computer power and high level first principles methods such as DFT has made it possible to derive interaction parameters with increased predictive power [2-4,6,7,72-74]. Since the parameters are determined from first-principles, the approach has been called ab-initio lattice-gas Hamiltonian method [6], in the surface science context. On the other hand, improvements in electronic structure methods have also been exploited in the study of alloy composition and phases. Here, the system interactions are usually mapped onto three dimensional lattices instead of two dimensional ones as in surfaces. The energy of the system is also given by an Ising-like hamiltonian as in the lattice-gas model. This approach in alloy theory is known as the cluster expansion method [5].

Both approaches, ab-initio lattice-gas Hamiltonian method and cluster expansion method, are essentially the same: they express the energy of the system in the form of an Ising-like expansion. The interaction parameters of the expansion are best derived from its first-principles calculations, so that the parameters have a firm microscopic basis.

Thus, the problem of how to determine the value of lateral interactions seems to have been solved by the use of first-principles methods. However, there still exists the problem of deciding upon the number and kind of interaction parameters to include in the Hamiltonian. This problem is by no means trivial and it is a very important one, because it determines how systematic the approach is.

One of the main purposes of this work is to systematically study the different approaches which have been suggested in order to derive the lateral interaction parameters from first-principles. To that end, it is convenient to couch the discussion of lateral interaction energies in terms of the cluster expansion method. However, we have to bear in mind, that the concepts apply to the ab-initio lattice-gas Hamiltonian method as well.

## 2.5.2 The cluster expansion method

The cluster expansion (CE) is a generalization of the Ising Hamiltonian in Eq. (2.49). In the common case of an adsorbed monolayer on a surface, the Ising model consists of assigning a spin-like occupation variable  $\sigma_i$  to each site  $i$  of the lattice. The spin variable  $\sigma_i$  takes the value +1 if the site is occupied and -1 corresponds to a vacancy at that site. Recall that point variables (1,0) are also possible. If the surface lattice contains  $N$  sites, each configuration of ad-atoms is characterized by a configuration vector  $\sigma = (\sigma_1, \sigma_2, \dots, \sigma_N)$ . A particular arrangement of spins of the parent lattice is called a cluster figure (see Fig. 2.6) and can be represented by a vector  $\sigma_\alpha$  containing the value of the occupation variable for each site

belonging to a determined cluster figure. The energy  $E(\sigma)$  can be described by a infinite sum over contributions arising from all possible spin clusters  $\alpha$  on the surface lattice[75].

$$E(\sigma) = \sum_{\alpha} J_{\alpha} \Pi_{\alpha}(\sigma), \quad (2.70)$$

where the index  $\alpha$  labels the various different cluster figures, i.e. isolated atoms, nearest-neighbor pairs and further distant pairs, triples of different shapes, quartets, and so on (Fig. 2.6). The  $\Pi_{\alpha}$  are given by products of the spin variables that make up the clusters  $\alpha$ , i.e.

$$\Pi_{\alpha} = \prod_{i \in \alpha} \sigma_i. \quad (2.71)$$

The coefficients  $J_{\alpha}$  are the corresponding interaction energy parameters which do not depend on the configuration  $\sigma$  and are called the effective interactions (ECI). When expanded, Eq. (2.70) and (2.71) take the Ising-like Hamiltonian form

$$H \equiv E(\sigma) = J_0 + \sum_i \sigma_i J_i + \sum_{ij} J_{ij} \sigma_i \sigma_j + \sum_{ijk} J_{ijk} \sigma_i \sigma_j \sigma_k + \dots \quad (2.72)$$

When all clusters  $\alpha$  are considered in the sum Eq. (2.70), the cluster expansion is able to represent any function  $E(\sigma)$  of configuration  $\sigma$  by an appropriate selection of the values of  $J_{\alpha}$ . However, it is not practical to consider all the terms in the sum and the expansion has to be truncated. In general, one could expect that the expansion would converge rapidly after keeping only clusters  $\alpha$  that are relatively compact (e.g. short-range pairs or small triplets). The accuracy of the truncated expansion is then hopefully enough to calculate properties of the system (e.g. ground state configurations, phase diagram, TPD spectra) from Monte Carlo simulations. The big advantage of the CE is its ability to rapidly calculate the energy  $E(\sigma)$  for any configuration  $\sigma$ , which renders the technique useful for sampling the configuration space in Monte Carlo simulations. The unknown parameters of the cluster expansion,  $J_{\alpha}$ , can be determined by fitting them to the energy of a relatively small number of configurations obtained, for instance, through first-principles computations. This approach is known as the structure inversion method (SIM) or the Connolly-Williams method [76].

The expansion of the energy of a determined configuration of adatoms  $\sigma$  in terms of cluster figures  $\sigma_{\alpha}$  requires one to find the  $\pi_{\alpha}$ 's in Eq. (2.70) and Eq. (2.71). One then obtains the multiplicity  $\pi_{\alpha}$  of a determined cluster figure  $\sigma_{\alpha}$ , i.e. how often a determined cluster figure  $\sigma_{\alpha}$  (e.g. one of the cluster figures in Fig. 2.6) appears in a configuration  $\sigma$ . If such counting is done inside a periodic unit cell, care has to be taken so that the counting considers not only the interactions with ad-atoms inside the unit cell, but also with their periodic images. In that way, the coefficients of  $J_{\alpha}$ , i.e. the  $\Pi_{\alpha}$ 's, are found and one ends up with a linear expression of the form of Eq. (2.72) for every configuration  $\sigma$ . The known quantities in Eq. (2.72) are the  $E(\sigma)$  (from first principles calculations) and the unknown quantities are the ECI's  $J_{\alpha}$ .

Another way of determining the ECI's in Eq. (2.72) would be to carry out expansions for isolated cluster in infinite (very big) lattices. This would allow us to isolate the energetic contribution of every cluster figure  $\sigma_{\alpha}$  and unambiguously determine its  $J_{\alpha}$  value. This approach is unfortunately incompatible with the supercell approach (Section 2.2.2), required

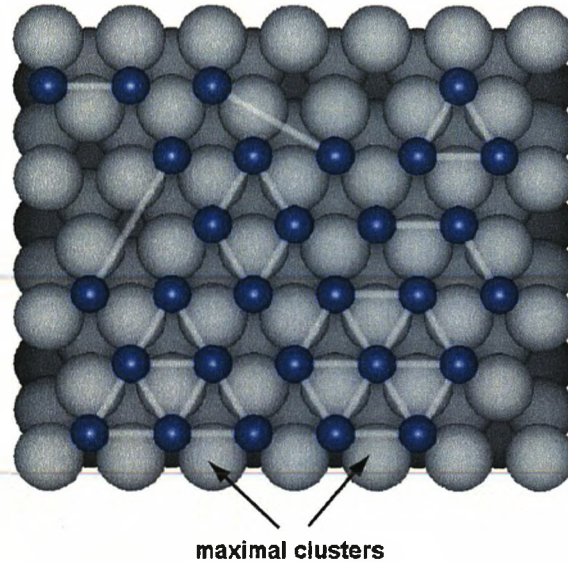


Figure 2.6: Some cluster figures between adsorbates atoms on the fcc sites of a (111) metal surface. two possible choices of maximal clusters are also shown.

to accurately describe metallic surfaces, because very big unit cells would be needed, which are very expensive to calculate from first principles.

Thus, the application of the cluster expansion technique comprises the following steps:

- First principles energy calculations for periodic configurations  $\sigma$
- Expansion of the energy in cluster figures  $\sigma_\alpha$ , i.e. application of Eq. (2.72)
- Set up of a system of linear equations where the known quantities are the energies  $E(\sigma)$  (from first principles calculations) and the unknown quantities are the ECI  $J_\alpha$  (from the cluster expansion)
- Inversion of the system of equations to obtain the ECI's

Since the cluster expansion is truncated and therefore approximate (small contributions from far-reaching interactions are mixed in an uncontrolled way) and the  $E(\sigma)$  have numerical errors due to the approximations in the first principles approach (Section 2.2) it is advisable to use more configurations (equations) than ECI's (unknowns) in order to derive the value of the ECI's. By doing so, one expects to have some error cancellations and to obtain (through least squares fits) the set of optimum parameters which are able to reproduce the set of given DFT energies.

The cluster expansion should accurately reproduce not only the DFT energies of the configurations used in the fitting procedure, but also the DFT energies of any configuration. In this context, the Monte Carlo simulation results using a cluster expansion should be the same as if the energies would have been calculated directly from DFT (Something that is still impossible due to the enormous computational burden). In this way, one is able to



study the energetic properties of large systems with the accuracy of first-principles calculations. Thus, the more DFT energies are used in the fitting procedure, the better the cluster expansion can be tuned to reproduce any DFT energy.

### **Optimal cluster expansion construction**

Deciding which ECI's  $J_\alpha$  are retained in the cluster expansion and which structural energies are used in the fit is still largely a process of trial and error, based on the experience of the researcher, making an automated procedure difficult. The algorithms used a range from a set of heuristic rules [77-82] to the use of genetic algorithms [83,84]. Even though the process of obtaining a reasonable CE still requires a lot of skillful human decisions "on the fly", the rules do provide at least some guidance on the task of extracting ECI's from first principles calculations.

Obtaining a reasonable CE from first-principles calculations implies addressing the following questions:

- Which cluster  $\alpha$  should be included in the cluster expansion (nearest neighbour pair, second nearest neighbour pair, triplets, quadruplets, etc...)?
- Which atomic arrangements should be used in order to determine the unknown ECI  $J_\alpha$ ?

### **ECI selection**

The selection of ECI's to be included in the CE is based on the concept of a maximal cluster (see Fig. 2.6). The maximal cluster is generated by the principle of a complete set of most compact clusters that are found within a circle of a given radius. Thus, one selects a distance  $d$  and identifies the most compact clusters that have atoms separated by a distance no larger than  $d$ . In (Fig. 2.6), for instance, a distance corresponding to the third nearest neighbour (adsorption only on fcc places) leads to the centered triangle and the hexagon depicted in (Fig. 2.6) as maximal clusters. All the sub-clusters included in the maximal cluster are available as ECI's. One ends up with a hierarchy of pairs, triplets, quadruplets, etc. that should be included in the CE.

After establishing a hierarchy of available cluster figures, the following three rules determine which ECI should be considered in the CE[79]:

- If an n-body cluster is included, then include all n-body clusters of smaller spatial extent (e.g. third nearest neighbor clusters can only be included if second and first nearest neighbors have been included)
- If a cluster is included, include all its sub-clusters (e.g. a triplet can only be included if all its pairs have been included)
- To prevent both under-fitting and over-fitting minimize the so-called cross-validation score ( $CV$ )

The first two rules are based on "physical intuition" [79]. The CE should decay with increasing separation and number of sites involved, i.e. ECI's associated with clusters consisting of many sites should be much smaller than those associated with effective pair interactions.

The last rule is aimed at evaluating the predictive power of a CE using the so-called *CV* score

$$CV^2 = \frac{1}{N} \sum_{i=1}^N (E_{DFT}^i - E_{CE}^{(i)})^2, \quad (2.73)$$

where  $E_{CE}^{(i)}$  is predicted by a least squares fit to  $(N - 1)$  DFT energies excluding  $E_{DFT}^i$ . While a least squares fit using  $N$  DFT energies measures the error in reproducing known values of  $E_{DFT}^i$ , the CV score estimates an uncertainty of predicted values. Both too few (under-fitting) or too many (over-fitting) parameters give poor prediction. Thus the CV score is designed as a statistical criterium to select the best set of cluster figures given a set of  $E_{DFT}$ .

Although this way of ECI selection is frequently used when deriving Ising-like Hamiltonians from first-principles for alloys, there is no proof that this is really the best way of selecting ECI's. They are just heuristic rules that guide in the selection process.

There are additional tools in order to find out a good set of cluster figures; e.g. linear programming techniques to reproduce the ground state and relative values of  $E_{DFT}$  [77], penalty functions to ensure that long range and multi-site parameters decrease to zero [78,80], leave-many-out CV scores [178]. The need of using such additional tools and their suitability depends on the problem at hand.

### Structure selection

The main criterium to select structures for the CE is the ground state search, i.e. the CE has to reproduce the same ground state configurations as predicted by the first-principles calculations. In practice, this, of course, is limited by the size of the structures one is able to directly calculate using first-principles methods.

The implementation of this criterium commences by calculating an initial set of configurations by DFT. Such configurations are typically chosen according to the symmetry of the lattice. Subsequently, ECI's are calculated from this initial set and used to search for ground state structures. The ground state search can be done either by a direct enumeration scheme, where the energy of all possible structures with a limited number of adsorbates per unit cell is computed [78,81]; or by simulated annealing runs. Usually, such a ground state search predicts new ground states different from the ones computed so far from first-principles. These new ground state configurations are computed from first-principles and new ECI's are derived in order to follow up the ground state search. The procedure is repeated until the first-principles and CE ground states are the same. Recently, a variance reduction scheme [79] has been proposed in order to select structures for the CE. It is based on the idea of selecting the structure that yields, for a given amount of computational time, the largest reduction in the prediction error of the least-squares fit. Even though such an approach has potential applications in CE, it is particular characteristics of the problem at hand that determines its applicability (e.g. the size of unit cells that can be calculated

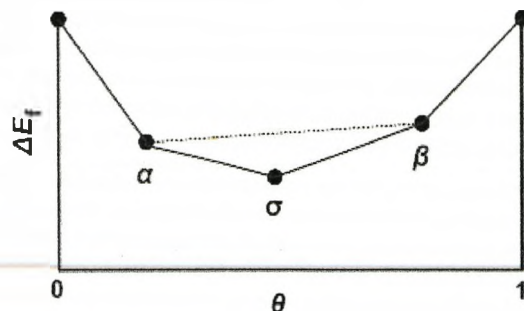


Figure 2.7: **Schematic ground state** diagram for an adsorbed layer. Besides the full monolayer  $\Theta = 1$  ML, the ground state line is formed by three structures  $\alpha$ ,  $\sigma$ , and  $\beta$ . If  $\sigma$  would lie energetically above the broken straight line between  $\alpha$  and  $\beta$ , a mixture of both would be more stable than  $\sigma$  (from Ref. [81])

imposes practical limitations).

### Formation energy

In general, when studying ground states and phase stability, the central energetic quantities used in the theoretical discussion are the formation enthalpy  $\Delta H_f$  or the mixing enthalpy  $\Delta H_{mix}$  [5]. These are defined as the excess energies taken with respect to the equivalent amounts of pure constituents.

In the case of two-dimensional phases, the situation does not change: the energy of the system has to be defined as an excess energy

$$\Delta E_f = \frac{1}{N} \left[ E_{slab}^{total} - (1 - \Theta)E_{clean}^{total} - \Theta E_{(1 \times 1)}^{total} \right], \quad (2.74)$$

here  $\Delta E_f$  is the formation energy,  $E_{slab}^{total}$  is the total energy for a specific adsorbate configuration with the coverage  $\Theta$ ,  $E_{clean}^{total}$  is the total energy of the clean surface,  $\Theta E_{(1 \times 1)}^{total}$  is the total energy of a full monolayer of adsorbate and  $N$  is the total number of adsorption sites per unit cell. Thus  $\Delta E_f$  reflects the relative stability of a particular configuration with respect to phase separation into a fraction  $\Theta$  of the full monolayer configuration ( $1 \times 1$ ) and a fraction  $(1 - \Theta)$  of empty sites (clean surface).

The formation energies  $\Delta E_f$  allow us to determine the ground-state energy versus composition curve by constructing a convex hull (Fig. 2.7). The convex hull is the set of straight lines that connects all the lowest-energy ordered phases [53]. When the energy of a particular ordered structure is above a straight line, it is unstable with respect to a mixture of the two structures that define the end points of the straight line. This is schematically shown in (Fig. 2.7): an individual structure  $\sigma$  only contributes to the ground-state line if the linear energy average between the stable structures at the next highest and lowest concentration is energetically less favorable than the formation energy of  $\sigma$ . More precisely, for three calculated structures  $\alpha$ ,  $\sigma$ , and  $\beta$  with  $\Theta(\alpha) < \Theta(\sigma) < \Theta(\beta)$ , which are the lowest in

energy for their individual coverage, the structure  $\sigma$  has to fulfil the condition

$$\Delta E_f(\sigma) < \frac{\Theta(\sigma)\Theta(\beta)}{\Theta(\alpha)\Theta(\beta)}\Delta E_f(\alpha) + \frac{\Theta(\sigma)\Theta(\alpha)}{\Theta(\beta)\Theta(\alpha)}\Delta E_f(\beta), \quad (2.75)$$

in order to be the ground state at  $\Theta(\sigma)$ . If Eq. (2.75) holds, a mixture of the phases  $\alpha$  and  $\beta$  would be higher in energy than structure  $\sigma$  [81].

The formation energy  $\Delta E_f$  is not the same as the adsorption energy  $E_{ads}$ . The last one measures the gain in energy of the adsorbate-substrate system with respect to the free substrate (clean surface) and the free molecule, i.e.

$$E_{ads} = \frac{1}{n} \left[ E_{slab}^{total} - E_{clean}^{total} - n \left( \frac{1}{2} E_{molec}^{total} \right) \right], \quad (2.76)$$

where  $E_{ads}$  is the adsorption energy per ad-atom,  $E_{slab}^{total}$  is the total energy for a specific adsorbate configuration,  $E_{clean}^{total}$  is the total energy of the clean surface,  $E_{molec}^{total}$  is the energy of the free molecule (formed by its respective ad-atoms) and  $n$  is the number of ad-atoms in the surface unit cell.  $E_{ads}$  indicates if the dissociative adsorption of a molecule is exothermic or not with respect to the binding energy of the molecule in the gas phase.  $E_{ads}$  cannot be used in order to compare the relative stability of different phases.

The formation energy  $\Delta E_f$  can also be calculated from the adsorption energy  $E_{ads}^\Theta$  at coverage  $\Theta$  by

$$\Delta E_f = \Theta(E_{ads}^\Theta - E_{ads}^{\Theta=1ML}). \quad (2.77)$$

## 2.6 Summary

Due to their reactive properties, metallic surfaces are the place of many reactions of industrial importance (heterogeneous catalysis). Typically, metals are used in industrial applications in a polycrystalline form and interact with a multitude of particles on their surfaces. The study of such systems is very complicated due to the microscopic nature of the processes taking place (e.g. adsorption, reaction, desorption). Since the metal surface consists of many single-crystal surfaces, understanding of the metal surface properties can be gained by studying microscopic processes on single-crystal surfaces. The collective behaviour of adsorbates on the metal can conveniently be studied by adopting a multiscale approach. Such an approach, in the context of this work, uses modern electronic structure methods, i.e. first-principles methods, to provide information used to parameterize interactions, which are then used as input to mesoscopic simulations of the system.

The microscopic description of the system is based on quantum mechanics and its mesoscopic description on statistical mechanics. The most important equations for both types are the Schrödinger equation (contains all information about the system) and the partition function (contains all thermodynamic information about the system), respectively.

Metal and semi-conductor surfaces are conveniently modelled using the supercell approach within density functional theory (DFT). By focusing on the electronic density instead of the wave function of the system, DFT considerably reduces the dimensionality of the many-body problem posed by the Schrödinger equation. Due to the unique characteristics of the

electronic structure of transition metals, elaborate DFT implementations are needed in order to obtain accurate ground state energies for those systems. The statistical mechanics description renounces the need to keep track of every single particle in the system, in favor of a probabilistic treatment. Thus, equilibrium systems are studied through probability distribution functions. Temperature effects are reflected by changes in the occupation of microscopic states. Those changes are governed by the probability distribution functions. The equivalence of time and ensemble averages postulated by statistical mechanics, allows practical implementation of many statistical mechanics concepts.

The application of Monte Carlo methods to systems in thermal equilibrium is based on the conservation of microscopic probabilities (i.e. the Master equation). Through the ergodic hypothesis and the detailed balance condition it is possible to design importance-sampling Monte Carlo methods that converge to an arbitrary probability distribution. The thermal equilibrium of classical systems is governed by the Boltzmann probability distribution.

The Metropolis Monte Carlo algorithm calculates thermodynamic properties by sampling the Boltzmann distribution of the system at equilibrium and averaging over multiple measurements. Because of its random walk in energy space the Wang-Landau algorithm is expected to perform better than the Metropolis algorithm near phase transitions.

The direct coupling of the micro and mesoscopic regimes (i.e. the quantum mechanics and statistical mechanics descriptions) is not possible because many calculations would be needed in the mesoscopic regime, while the first principles calculations are very expensive. Thus, a physically sound model of the system is needed that retains the most important microscopic parameters responsible for the collective behavior of adsorbates in the mesoscopic regime. This model is the lattice-gas model and the most important microscopic parameters, in this context, are the lateral interactions between adsorbates.

Using first-principles methods, the lateral interactions of the lattice-gas model can be calculated and Monte Carlo simulations can be carried out in order to study important properties of the adsorbate/surface system. This expansion of the energy by means of an Ising-like Hamiltonian and derivation of the Hamiltonian interactions from its first principles is known as the ab-initio lattice-gas Hamiltonian method in surface science, and the cluster expansion method in alloy theory. They are actually different names for the same approach. Unfortunately, there is currently no satisfactory systematic procedure to derive interaction parameters from first-principles calculations. The principal questions are which and how many interactions should be included in the lattice-gas Hamiltonian. Some heuristic rules and optimization methods have been proposed within the cluster expansion method and will be applied to the tartaric acid/Cu(110) system.

## Chapter 3

### Self-assembled corrals on Si (111)-(7 × 7)

The fabrication and electronic properties of nano-corrals[121-123], are of interest as building blocks in molecular electronics[124,125]. The favored substrate is a semiconductor surface[126]. Although a Scanning Tunneling Microscope (STM) can be used to manipulate any type of adsorbates at these surfaces[127,128,108], this has not provided a ready path to the construction of corrals. It is, moreover, recognized that self-assembly is preferable to atom-by-atom fabrication. Molecular adsorbates have been shown to self-assemble to yield a variety of patterns, though not previously nano-corrals, at semiconductor surfaces.

Here we describe a different approach to corral formation, with the desirable attributes of (a) self-assembly, (b) a semiconductor substrate, and (c) stability at elevated temperatures. Physisorbed haloalkane molecules such as chlorododecane self-assemble on Si(111)-(7×7) to form dimers stable up to 400K, which corral silicon adatoms. The corral size is determined by the haloalkane chain-length. Spectroscopic and theoretical evidence is presented to show that the haloalkane dimer induces electron transfer to the corralled adatom, shifting its energy levels. Isolation of a labile pre-cursor suggests a model for corral formation in which monomers diffusing in a vertical state meet and convert to the observed immobile horizontal dimers, forming corrals. Variations in the alkane chain-length and dipolar substituent suggest a means for the self assembly of nano-corrals and dots of defined size and electronic properties.

In this chapter we focus on the properties of a type of corral formation featuring two chlorododecane molecules bending over a silicon adatom, which darkens under the molecular effect, since the experiments examined previously the effect of this corral on its single enclosed adatom. The adsorption of chlorododecane molecules at Silicon (111) – (7 × 7) has been studied by Scanning Tunneling Microscopy.

#### 3.1 Experimental methods and research

This section displays the principle methods of measurements carried out to study different haloalkanes on a silicon(111)-(7 × 7) surface. The results are presented step by step reflecting the history of how the different phenomena were understood by the experimentalists. Similar measurements were carried out with different molecules such as Di-haloalkanes or

small carbon chained haloalkanes which are not presented here. Only the halododecanes were studied by DFT and STM simulations.

The main device for imaging is the Scanning Tunneling Microscope (STM). All surface deposition took place under Ultra High Vacuum conditions. The haloalkanes in question are halododecanes studied with different halogens to observe different behaviors with respect to their electronegativity. Bromide (Br), Chlorine (Cl) and Fluorine (F) atoms are the main terminations of these halododecane molecules. The surface deposition is performed at 50K. Some scans were carried out to study the low temperature behavior and the kinetic mechanism of the physisorbed molecules below room temperature. Then static STM measurements were done at room temperature up to 400K, to observe the features of halododecane on silicon(111). The bias voltages did not exceed 2.5V.

### **3.1.1 STM imaging**

The Observations were carried out by Scanning Tunneling Microscopy (STM) in a Ultra High Vacuum (UHV) chamber using phosphorus n-doped silicon ( $0.02 - 0.5\Omega$  cm). Three STM instruments were used to perform the measurements, an Omicron-VT, a RHK300, and the RHK400 STM.

### **3.1.2 Halododecane molecules**

The following part presents the research on Halododecane by Scanning Tunneling Microscopy (STM). Three halogens were considered in this research, Chlorine (Cl), Bromide (Br), and Fluorine (F) giving: Chlorododecane, Bromododecane and Fluorododecane. These three molecules, once deposited on the silicon surface, are physisorbed to form different types of adsorbates containing one to three molecules. One configuration containing a single molecule on the surface called a monomer, two or three molecules forming reproducible and stable configurations are called dimers and trimers.

### **Quantum Corrals and Molecules**

The idea was to imitate the atomic quantum corral using molecules with the possibility to cover several adatoms of a metal or semiconductor surface. The electronic properties of the corral are then extended to three or more adatoms for better control of a spatial and spectral distribution of surface electrons. The 1-Chlorododecane molecule, for example, has a carbon chain of twelve atoms, fully saturated with hydrogen and terminated with chlorine. Such a molecule has no asymmetrical carbons but the carbon chain can bend in different directions leading to different conformations in two dimensional or three dimensional space. The length of the molecule is close to 15 angstroms, it can theoretically cover 3 adatoms on a silicon(111) surface.

### **3.1.3 Halododecanes on Silicon(111)-(7 × 7)**

Bromododecane, Chlorododecane, and Fluorododecane, once physisorbed at the Si(111)-(7 × 7), give very specific and reproducible patterns at room temperature, stable up to 400K.

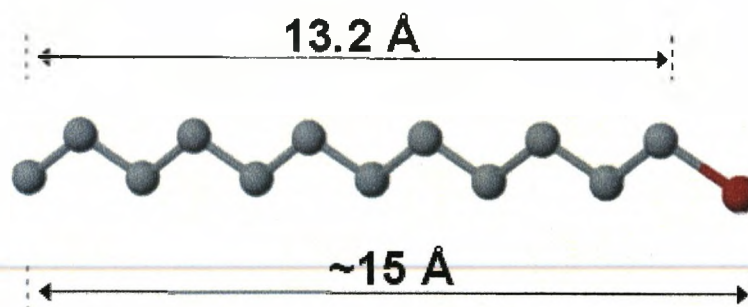


Figure 3.1: Chlorododecane lengths

One observes very rarely the presence of monomers. They tend to form dimers or trimers as stable configurations especially at room temperature. With respect to the very specific shape of the Si(111)-(7 × 7) surface, the features of molecules bend quite substantially around the corner holes of the silicon surface or around silicon adatoms. No STM image shows straight molecules at 300K.

Fig. (3.2(a)), Fig. (3.2(b)) and Fig. (3.2(c)) show the STM images of Chlorododecane, Bromododecane and Fluorododecane at Si(111)-(7 × 7). The STM measurement were carried out in identical conditions and at room temperature. The bias voltage in each case is 1.5V. The same dosing (1L) was used in all three cases. As one can see easily the adsorbates are

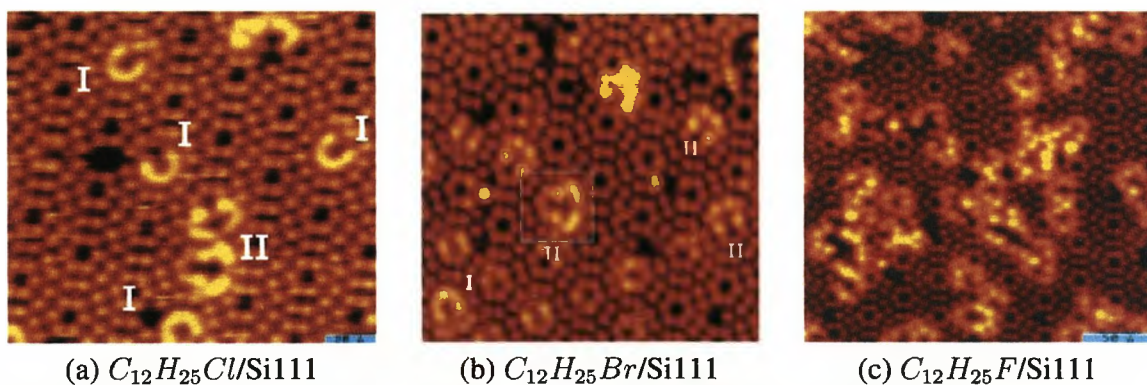


Figure 3.2: STM measurements at room temperature for a Bias voltage of 1.5V. For the same dosing, one observes a very low coverage of chlorododecane and bromododecane compared to the fluorododecane. The types are mainly type I and type II for the first two cases and different types for the fluorododecane

represented by brighter features in the images. These bright features have different shapes called types, each type can be oriented in different directions retaining the same shape. One observes that the coverage is very low for the three different halogens. The images show that the coverage is 4 times higher for Fluorododecane than for Chlorododecane or Bromododecane. The reason is that Fluorododecane has a higher sticking coefficient than the two other halogenated molecules. This may be due to the strong electrostatic interaction between Fluorine and the silicon substrate compared to Chlorine and the Bromide.



On Fig. 3.3 (a),(b), and (c)), one observes very low rates of Type I and Type II (see Fig. 3.4) configurations for Fluorododecane, while for Bromo- and Chlorododecane these two types are dominant. The relative number of type I and II configurations depend on the molecules: in the case of Chlorododecane one finds  $TypeI/TypeII = 1.9$ . For Bromododecane,  $typeI/typeII = 0.52$  which is almost exactly the opposite relative occurrence. The type I and type II configurations represent 80% of the adsorbate types for Bromododecane and Chlorododecane. For Fluorododecane these two configurations amount to only 20% while the type III, IV, V, VI (see Fig. 3.4) represent together 80% of the configurations (see Fig. 3.3 (a),(b), and (c)). Due to the specific structure of a halododecane, one may infer that

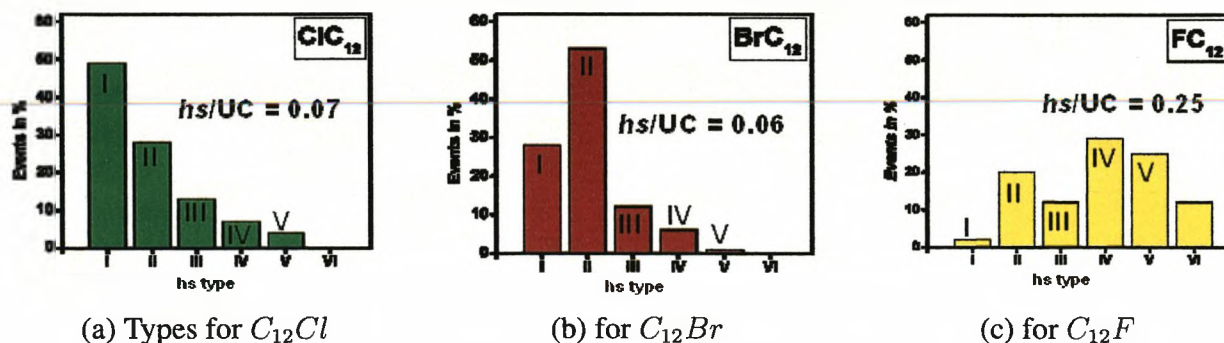


Figure 3.3: For the same dosing (1L) of halododecane onto silicon, these diagrams show the different rates of appearance of the types of adsorbates registered by the experimentalists. (a) For Chlorododecane, the type I and type II have the highest probability of appearance, Type I appears twice as much as the Type II. Some residue of Type III, IV and V exist (b) For Bromododecane, Type II and type I are the most probable; Type II appears twice as often as the type I. Some residue of Types III, IV and V also exist (c) For the Fluorododecane, types I and II are residual. Some undefined types represent 10 percent of appearance. Types III, IV and V have the highest probability for this molecule

each type of adsorbate configuration contains more than a single molecule. One finds from the shape and size of the structure that Type I, Type II, and Type III contain two molecules. Type IV and V contain between two and four molecules.

Fig. (3.4) shows three unit cells of the silicon (111) surface with the corner holes (ch) and the silicon adatoms (orange spheres). Distances are indicated, to determine the adsorbate position and calculate the number of chlorododecane molecules contained in each type of configuration. The distance between the corner holes is roughly  $26.9\text{\AA}$ . The smallest distance between two silicon adatom is close to  $5\text{\AA}$ . The closest adatoms in this case are the 6 adatoms located around the corner holes (ch). This diagram also shows the distances between the silicon adatom corralled after the deposition of the chlorododecane. Note that no corral is larger than the distance between two corner holes, or  $26.9\text{\AA}$ . The average extension of a corral is between  $10\text{\AA}$  and  $20\text{\AA}$ . With respect to the position of the silicon adatoms and the corner holes, the different configurations can be characterized as follows:

- **Type I:** This type is around a corner hole (ch). It covers 5 silicon adatoms. One silicon adatom around the corner hole remains unoccupied, with very characteristic properties as it is influenced by the molecules forming the adsorbate. Considering the

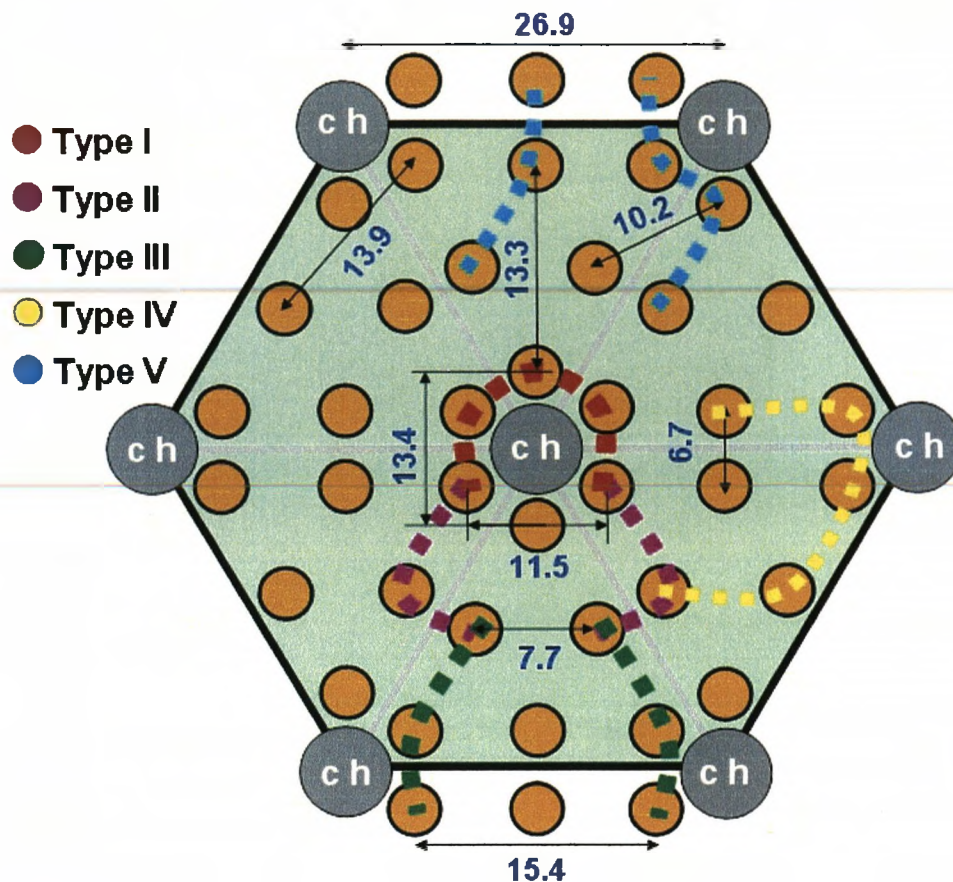


Figure 3.4: Main structures on the silicon surface. (red dashed line) shows the Type I configuration. (pink dashed lines) show the Type II configuration positioned onto its corresponding silicon adatoms. (green dashed lines) show the Type III configuration. (yellow dashed line) shows Type IV. (light blue dashed line) shows Type V.

length of the Chlorododecane molecule (around  $15\text{\AA}$ ), the Type I adsorbate should contain two molecules with their Chlorine atoms next to the free silicon adatom.

- **Type II:** This configuration encloses a silicon adatom (orange sphere). It covers 6 silicon adatoms. The corralled silicon adatom is darkened by the presence of such a feature. One expects the Type II adsorbate configuration to contain 2 molecules, with their Chlorine atoms at the same positions as the chlorine atoms of Type I, but corralling a silicon adatom, instead of corralling a corner hole.
- **Type III:** It covers 6 silicon adatoms around two free adatoms of the silicon surface. The two corralled adatoms are darkened by its presence, like the silicon adatom in the type II configuration. Type III contains 2 molecules. The start and end point of the chlorododecane molecules is undetermined. This configuration is not studied in the following sections.
- **Type IV:** It covers 5 silicon adatom close to a corner hole with a free silicon adatom

in between. The adatom is darkened by the presence of the corral as the silicon adatom in type II. 3 chlorododecane molecules form this type which is not studied in the following sections

- **Type V:** This adsorbate covers 7 silicon adatoms with one silicon adatom in between. This adatom is darkened by the presence of the corral like the silicon adatom in Type II. 3 to 4 chlorododecane molecules are contained in this type which is not studied in the following sections.

### 3.1.4 Type-II configuration of Chlorododecane

One can observe, from the relative appearance of halododecane dimers on the surface that the Type-II halododecane configuration exist for all three halogen terminations molecules, respectively, Bromide, Chlorine and Fluorine. It seems to be the most stable configuration for twelve-carbon Haloalkanes on silicon. The configuration is stable up to 400K. Beyond this temperature it breaks apart into carbon chains separated from halogen atoms.

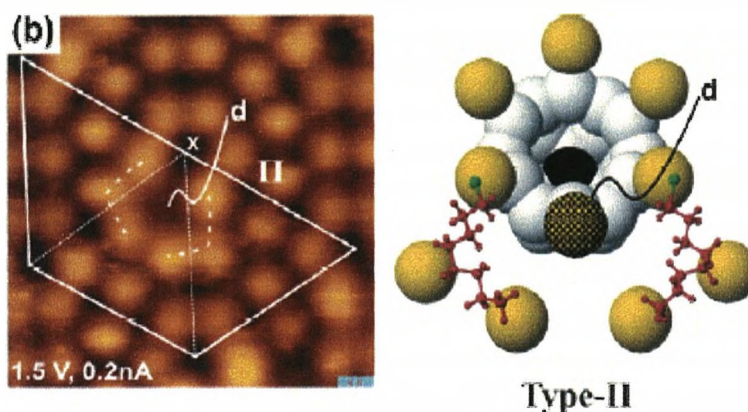


Figure 3.5: STM picture of a Chlorododecane molecule physisorbed on silicon(111). (1.5V, 0.2nA). This configuration contains two molecules corraling a darkened silicon adatom.

### 3.1.5 Experimental results on TypeII-Chlorododecane

Here we focus on the properties of the type-II corral of 1-Chlorododecane on Si(111)-(7 × 7), since experiments revealed a clear effect of this corral on the single enclosed adatom. The dissociation of one molecule of the dimer (corral) above 400K was always accompanied by desorption of the other molecule, showing that interaction between the molecules is vital for the stability. At elevated temperatures, in addition to the dissociation,  $(C_{12}H_{25}Cl)_2$  corrals were also observed to desorb leaving no residue. This, indicates that  $(C_{12}H_{25}Cl)_2$  has physisorbed intact at room temperature. Since it is unlikely that both molecules desorb simultaneously, one can conclude that the desorption of the first molecule triggers the desorption of the second. Again, this indicates that the dimer is stabilized by the interaction between its component molecules.

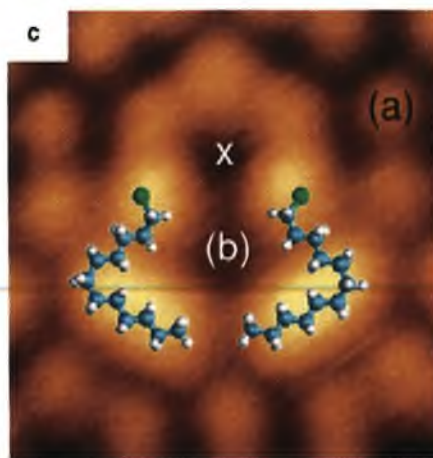


Figure 3.6: High resolution STM image of a single type-II corral ( $30 \times 30 \text{ \AA}$ ,  $+1.4 \text{ V}$ ,  $230 \text{ pA}$ ) with two 1-chlorododecane molecules, drawn to scale, superimposed; blue atoms are carbon, white hydrogen and green chlorine; (a) marks an uncorralled Si adatom (bright), (b) the corralled Si adatom (dark) and (x) a corner-hole surface site

At room temperature bromo and fluorododecane molecules form similar dimer structures to 1-chlorododecane, corralling a corner hole (type-I) or a single adatom (type-II). Experimentally the sticking probability increases with the electronegativity of the halogen atom. Dodecane, without a terminal halogen atom, does not stick to a room-temperature surface. Dosing 1-chlorododecane onto a cold surface, around  $210 \text{ K}$ , prevents the formation of corrals, instead forming exclusively curved monomeric adsorbates. Such semi-circular monomers, were observed as a lesser constituent at room temperature. From this effect of cooling we infer that corral formation involves diffusion of single molecules across the surface to form pairs. Yet the monomeric features does not diffuse even at elevated temperatures around  $400 \text{ K}$ . Corral (dimer) formation, it thus appears, is due to the diffusion of a mobile state of the monomer different from the strongly-physisorbed multiply-attached horizontal states, monomer or dimer. Such a mobile state has been observed in the present work, at  $50 \text{ K}$ , as indicated below. Fig. (3.7) shows an STM image of 1-chlorododecane at  $50 \text{ K}$ . One finds two molecular features, both mobile and markedly different from those obtained at higher temperature. These comprise a single bright feature on top of an adatom, stable for up to five minutes, and mobile lines of bright features along the  $\text{Si}(111)-(7 \times 7)$  dimer-rows joining corner holes. Some molecules (not shown) exhibit streaking under these scanning conditions indicating mobility. Successive imaging at intervals of 1 minute show the bright lines increasing in length at one end due to addition of single adsorbed molecules, or decreasing in length due to loss of single molecules. The overall effect is that the bright features appear to be moving across the viewed area.

With increasing temperature the bright single-atom features (vertical chlorododecane), seen at  $50 \text{ K}$ , are no longer observed. Instead, half-corrals (horizontal molecules) and, at still higher temperatures ( $220 \text{ K}$ ), full dimeric corrals appear. These changes have been modeled kinetically, leading to an energy barrier of several kcal/mol for conversion from the vertical state of chlorododecane to the horizontal state.

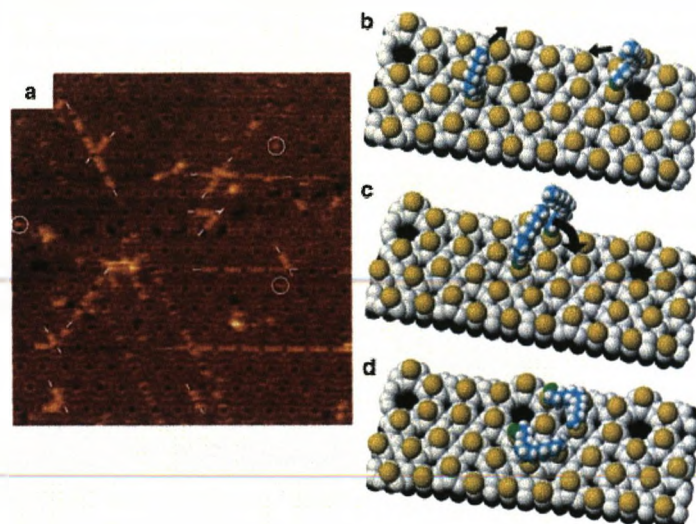


Figure 3.7: Mechanism for corral formation. (a) STM image taken at 50K ( $400 \times 400 \text{ \AA}$ , +1.5V, 200pA) showing two types of 1-chlorododecane precursor on Si(111)-( $7 \times 7$ ), one type on top of an adatom (circled) and the other forming lines along silicon-dimer rows (the latter are marked at either end by a dash); (b)-(d) schematic of corral formation: (b) molecules in vertical pre-cursor states diffusing along silicon-dimer rows; (c) a pair of molecules meeting one another and (d) molecules stabilized by lying down to form a horizontal corral-structure of type-II.

Since adsorption of the mobile structure is at single-adatom sites (cf. the multiple-site adsorption of Fig. 3.6), one proposes a mechanism whereby gas-phase molecules first form mobile vertical pre-cursor states on top of an adatom and then diffuse to a silicon-dimer row which acts as a conduit for transport across the surface (e.g., Fig. 3.7(b)). If a pair of molecules become attached to another one (Fig. 3.7(c)) they stabilize forming the observed horizontal corral structure (Fig. 3.7(d)). This process is in competition with desorption, and also in competition with forming stable monomers. The mechanism, which we find to be general for these and non-halogenated alkanes is noteworthy since it provides a means to mobility (due to single-point attachment) and subsequent immobility (due to multiple attachment); a mechanism known also to skiers, who are only mobile when upright.

A significant feature of type-II 1-chlorododecane corrals is the invariable presence of a darkened corralled adatom. This darkening, evident at 'b' in (Fig. 3.6), consists of a  $0.4 \pm 0.1 \text{ \AA}$  lowering in the image relative to an unperturbed adatom 'a' in (Fig. 3.6), for a bias near +1V (surface voltage, relative to the tip) and a tunneling current near 100pA. (The z-piezoelectric  $\text{\AA V}^{-1}$  was calibrated by measuring a single step on a clean Si(111)-( $7 \times 7$ ) surface with tunneling parameters of +1.5V and 150pA). The observed lowering is not due to a missing adatom, since the measured height at 'b' return to normal when a corral desorbs ( $> 400\text{K}$ ). For this measurement a particular corral was imaged at high temperature, (400K), until it desorbed leaving behind a clean area of silicon. Moreover, were corrals to form only around naturally occurring defects (typically  $< 0.2 \%$  defects) corraling would halt at this coverage; in the experiments one does not find such limit.

From the darkening of the corralled adatom one concludes that its dangling bonds states (at +0.5 and -0.3eV with respect to the Fermi level for clean Si(111)-(7 × 7) [137-139]) are no longer available for tunneling. The loss of both of the dangling-bond states is analogous to covalent bonding. The corral has caused the enclosed adatom to behave as if it had an adsorbate attached[140].

To characterize the effect of the corral on the adatom's electronic states, scanning tunneling spectroscopy (STS) I-V curves were taken over a clean adatom (Fig. 3.8a(a)) and over a corralled adatom (Fig. 3.8a(b)). The +0.5eV adatom state was present for (a) the clean adatom, but missing for (b) the corralled adatom (Fig. 3.8a). The absence of this state is also clear in the STM inset image taken at +0.5eV. Owing to the low tunneling current in the band gap, the state at -0.3eV is absent from both spectra of (Fig. 3.8a), but the difference between the clean and the corralled adatom can be seen in the inset STM image taken at -0.6V. Below -1.6V the corralled adatom shows a large increase in tunneling current not seen for the clean adatom, suggesting a new (or shifted) state at the corralled adatom site at large negative bias. Difference-current-imaging tunneling spectroscopy ( $\Delta$ CITS [137]) can

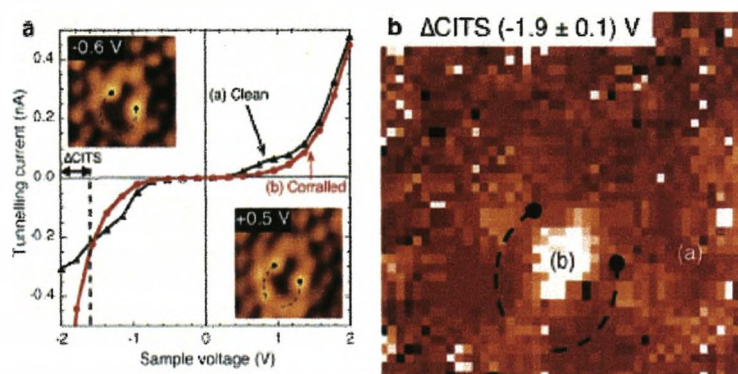


Figure 3.8: Electronic properties of the corralled adatom. (a) I-V spectra taken over (a) a clean (unperturbed) silicon adatom and (b) a corralled adatom (both with set-points +2V, 500pA). Inset STM images ( $40 \times 40 \text{ \AA}$ , 230pA) show a type-II corral at bias voltages of +0.5 and -0.6V and panel (b)  $\Delta$ CITS from the difference between CITS images taken at -2.0V and -1.8V; dashed black curves indicate the 1-chlorododecane dimer, (a) marks an uncorralled adatom and (b) marks the corralled adatom. The set-point used in the CITS images was +2V,500pA.

isolate a state between two voltages (energies) giving a map of the total density of states (DOS) between these voltages. (Fig. 3.8b) shows a  $\Delta$ CITS map between -1.8V and -2.0V taken over a corral, as indicated. The bright feature over the corralled adatom, '(b)', gives evidence of a large density of states at this site at -1.9V, not seen at other atomic sites, e.g. '(a)'. The corral is inducing electronic change only at the corralled adatom.

## 3.2 TypeII-Chlorododecane adsorption energies and geometries

Different conformations of chlorododecane molecules have to be determined in such a way that can fit the Type-II on  $Si(111) - (7 \times 7)$  surface. As shown above, the chlorododecane molecules fits three silicon adatom in variable orientation on the silicon surface, from room temperatures up to 400K. In the case of the Type-II configuration, one expects two Chlorododecane molecules to corral the surface by physisorption around the dark silicon adatom symmetrically, as six silicon adatoms are covered with respect to the bright feature shown by the STM pictures. Here, two questions arise. The first one is which carbon of the 12 carbon-chained molecule is bending. The second is to determine which part of the molecule is terminated by the Chlorine atom.

To do so, the calculations of the different conformations of  $ClC_{12}$  were performed in vacuum. We calculate the different geometries by bending the carbon chain of the molecules at different carbon positions.

The adsorbate/substrate system, Chlorododecane at  $Si(111) - (7 \times 7)$ , is the third part of the calculations. First, we need to obtain the ground-state of this system. The fully converged  $ClC_{12}/Si(111) - (7 \times 7)$  is then studied by STM simulations. The ground state of such a system is calculated by DFT, STM simulations are performed by bSKAN[103,104]. Individual slabs in the supercell periodic geometry were separated by 20Å of vacuum, sufficient to accurately describe the exponential decay of surface wave functions and exclude coupling in the z-direction. One corrected for dipole interactions between adjacent unit cells. Ionic cores were represented by ultrasoft pseudopotentials. Exchange correlation functionals were parameterized within the general gradient approximation (PW91 [141]). Given the large system-size of more than three hundred atoms per unit cell, the simulation had to be performed with a single k-point at the centre of the Brillouin zone.

### 3.2.1 Computational details

In this work, the structure optimization is carried out with the Vienna ab-initio Simulation Package (VASP)[101,102], a density functional theory code for systems with periodic boundary conditions. After the calculation of the electron ground state and the creation of the input for the STM simulation, we calculate the tunneling current in a perturbation model of tunneling. The STM images are produced with bSKAN[103,104]. The tip used in all the simulations was the tungsten tip.

### 3.2.2 Chlorododecane molecules in Vacuum

Many conformations of the Chlorododecane molecule can fit geometrically the three silicon adatom positions of the Type-II configurations of Chlorododecane on the silicon surface. We find the best match with STM experiments by bending the carbon chain from the first carbon atom to the 12th. The first logical step is to consider a molecule bent on the 5th, 6th or 7th carbon atoms, which are roughly located at the middle of the molecule. The ground state conformation of Chlorododecane molecules, in vacuum, retaining the shape

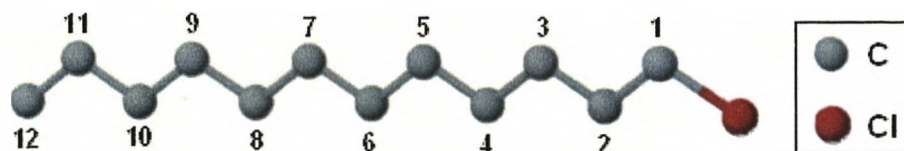


Figure 3.9: Chlorododecane molecule in the vacuum

of the two molecules found in STM experiments, can be determined from the known interatomic distances and bond angles. A carbon-carbon bond length of  $1.20 - 1.54 \text{ \AA}$ , a carbon-hydrogen bond has a length of  $1.4 \text{ \AA}$ , and a carbon-chlorine bond a length of  $1.06 - 1.20 \text{ \AA}$ . The  $C - \overline{C} - C$  bond angle is  $110^\circ$ . Fig. (3.10) shows the different conformation of the chlorododecane molecule in vacuum from the straight conformation to the most bent fitting the type II adsorbate on both sides. The following step of the study is to calculate the

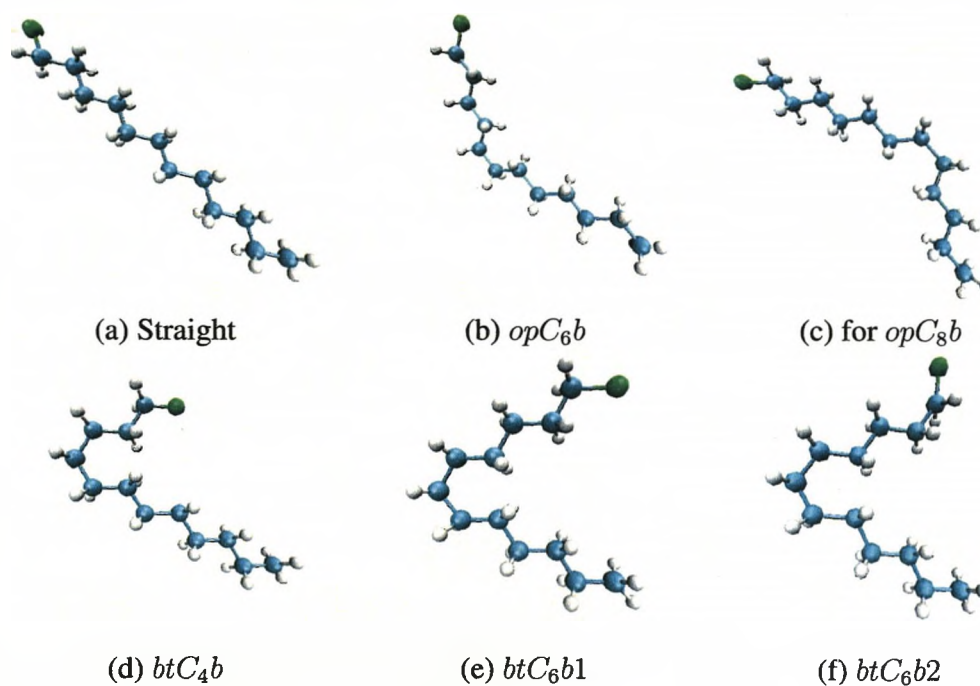


Figure 3.10: Different conformations of chlorododecane molecules in vacuum

ground state energies of such molecules in the vacuum. The set up is the same for each conformation, the fully relaxed state is calculated within the same volume. One observes that the conformation *btC<sub>6</sub>b2*, fitting the type II adsorbate, is the least stable in the vacuum. This information shows that the molecule is forced to have this shape due to the interactions with the silicon surface at the adsorbed state.



Conformation in vacuum	Ground state energies
Straight	$E(\text{tot}) = -203.040 \text{ eV}$
opC6b	$E(\text{tot}) = -203.160 \text{ eV}$
opC8b	$E(\text{tot}) = -203.668 \text{ eV}$
btC4b	$E(\text{tot}) = -203.060 \text{ eV}$
btC6b2	$E(\text{tot}) = -202.730 \text{ eV}$
btC6b1	$E(\text{tot}) = -203.664 \text{ eV}$

Table 3.1: In vacuum, the ground state energies of the 6 Chlorododecane molecules are roughly the same at -203eV. However for the *btC6b2* molecule, which fits the type II adsorbate, the ground state is lower by about 70meV compared to all other configuration.

### 3.2.3 Chlorododecane on Si(111)-(7 × 7)

DFT calculations on silicon(111) were performed with a (7 × 7) of 249 atoms. This number contains two types of atoms:

- Silicon atoms: forming 4 layers of the (111) arrangement. The total number of silicon is 200 atoms. This unit cell has 12 adatoms and 188 restatoms. The bottom of the silicon surface is fully passivated by hydrogen
- Hydrogen atoms: these atoms passivate the bottom of the silicon surface. There is a total number of 49 hydrogen atoms, which passivate the dangling Si-bonds in order to avoid charges up effects.

The chlorododecane molecule (38 atoms) has 12 carbon atoms passivated by hydrogen (25 atoms) and terminated with a chlorine atom. Once the molecule is deposited onto the

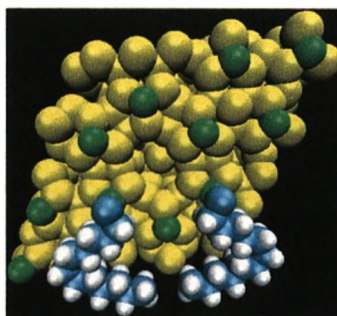


Figure 3.11: The two chlorododecane molecules, the silicon atoms (green) onto which they are deposited, the silicon adatom (green) between the molecules, and the rest of the silicon adatoms (green) are free to move during the DFT calculation. The hydrogen at the bottom of the unit cell and the silicon restatoms (yellow) are frozen

silicon surface for a DFT calculation, the total system contains 287 atoms. For the system including 2 Chlorododecane molecules the corresponding number of atoms is 325. In all

simulations the molecules and the silicon adatoms were fully relaxed.

$$E_{ads} = E_{tot} - (E_{surf} + E_{mol}) \quad (3.1)$$

$$E_{ads}(C_{12}Cl/Si111) = E_{tot}(C_{12}Cl/Si111) - (E_{Si111} + E_{C_{12}Cl}) \quad (3.2)$$

$$E_{ads}(2C_{12}Cl/Si111) = E_{tot}(2C_{12}Cl/Si111) - (E_{Si111} + 2E_{C_{12}Cl}) \quad (3.3)$$

The adsorption energies of one and two molecules on the silicon surface can be calculated using the ground state energy differences described above. Eq. (3.1), Eq. (3.2), Eq. (3.3) gives the general equations for determining the adsorption energy of a system (adsorbate/substrate). The total energies obtained are: Table 3.2 displays the DFT ground state

System	TOT/ADS energies
Silicon surface	E(tot) = -1179.30 eV
Chlorodod.(vacuum)	E(tot) = -202.73 eV
1Chlorodod./Si111	E(tot) = -1383.97 eV
1Chlorodod./Si111	E(ads) = -1.94 eV
2Chlorodod./Si111	E(tot) = -1588.60 eV
2Chlorodod./Si111	E(ads) = -3.84 eV

Table 3.2: Ground state energies and adsorption energies of the clean silicon surface, the  $C_{12}Cl$  in the vacuum, the system  $C_{12}Cl/Si111$ , and the system  $2C_{12}Cl/Si111$

values of the systems and the results for the adsorption energies for the two interesting adsorbate/substrate systems: the  $C_{12}Cl/Si111$  and  $2C_{12}Cl/Si111$ . The adsorption energy of the adsorbate/substrate system  $C_{12}Cl/Si111$  is -1.94eV. The adsorption energy of the Type II corral at Silicon(111) is -3.84eV. This system is now studied by STM simulations.

### 3.3 STM Simulations of Chlorododecane/Si111 systems

#### 3.3.1 STM simulations using bSKAN

Fig. 3.12 shows a charge density contour map of the surface for comparison with the STM image (Fig. 3.6). Owing to numerical limitations the molecules of adjacent unit cells were in close proximity, making an STM simulation including the tip-structure unreliable[142]. Instead we used a charge density contour of the surface for states in the unoccupied range from the Fermi level to +1.2eV (Fig. 3.12). The apparent height of the molecule was 1.5Å. The contour, at a maximum distance of 7Å from the silicon surface, showed that the adatom in the corral was depressed (black cross) compared with the equivalent adatoms outside the corral (white cross). The difference in apparent height between the corralled and the uncorralled adatom is about 0.4Å, matching experiments. Fig. 3.13 shows the computed density of states at three locations: (a) the position of the corner adatom on a clean silicon surface (yellow line), with only one adsorbate molecule present (dashed yellow line), and

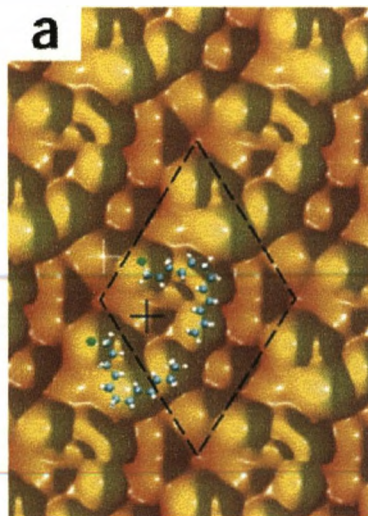


Figure 3.12: Simulation of the electronic ground-state of a corral . (a) charge density contour of electronic states integrated from the fermi level to  $+1.2\text{eV}$ . The position of a dimer-pair of molecules is indicated by a ball-and-stick model. The apparent height of the molecules is  $1.5\text{\AA}$ . The difference in apparent height between the corralled adatom (black cross, lower) and an uncorralled adatom (white cross, higher) is  $0.4\text{\AA}$

(b) within the dimer-corral (red line).

A single molecule gives rise to a minor perturbation in the electronic states, whereas the corral comprising two molecules, shifts the corralled adatom's electronic states by  $-1\text{eV}$ . This indicates that the potential in the vicinity of the corralled adatom has changed by about this amount. The steep onset of the density of states of the corralled adatom below  $-1.7\text{eV}$  is in agreement with our spectroscopic measurements (Fig. 3.8)

### 3.3.2 Dipole moments

The corral's electronic properties originate from induced dipoles in the silicon surface. Figs. 3.14 show the dipole moments induced by the two molecules (d and e), and by the corral (f). Adding the individual dipole moments induced by the two molecules does not produce the dipole moment computed for the corral. The corral has therefore induced an extra dipole (red arrow). This is due to charge-transfer into the corralled adatom. The computed surplus charge of about 0.6 electrons on the corralled adatom is thought to originate from the shift of its valence-band to a lower energy (Fig. 3.13), placing additional states within the occupied range. This accounts for the observed darkening of the corralled adatom in the STM images both for positive bias, as the dangling bond state is now filled, and negative bias, as the state has been lowered by  $-1\text{eV}$ .

Variation in chain length and chain substituents could provide a means to self-assembly of nano-corrals and filled corrals (nano-dots) of varied but defined size and electronic properties.

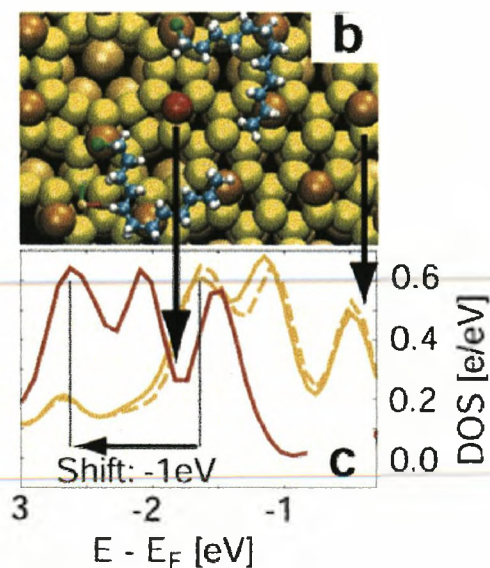


Figure 3.13: Density of states (DOS) of an uncorralled adatom (yellow curve) corresponding to position (a): red silicon adatom, and of corralled adatom (red curve, corresponding to position (b): dark yellow silicon adatom

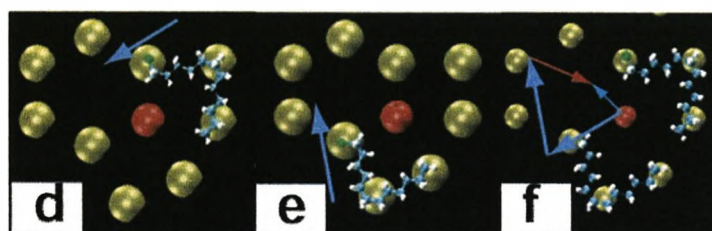


Figure 3.14: (d)-(f) Induced surface dipoles due to the adsorbed molecule(s); (d) and (e) Single molecules and induced dipoles (blue arrow) and (f) corrall and induced dipole (light blue arrow); dipole due to additional charge-transfer in the corrall (red arrow)

### 3.3.3 Summary

The STM simulations show a direct influence of the two chlorododecane molecules, forming the type-II configuration, on the corralled silicon adatom which darkens in the STM images. This phenomenon is described by a decrease of the apparent height of the silicon adatom.

The dipole moments finally show that two molecules on the Si(111)-(7 × 7) surface form a very stable system which is qualitatively different from single molecules.

## Chapter 4

# Electronic Switching of Single Silicon Atoms by Molecular Fields Effects

Single-molecule switches have been the subject of numerous experimental and theoretical studies aimed at understanding their behaviour and engineering their properties. Molecular conductance has been controlled largely by conformational change in the conducting molecule[90-92], by external electric fields[93-95], and subsidiarily by structural changes in the embedding environment[96]. A recent study demonstrated changes in molecular conductivity due to a local electric field, namely, a single negatively charged silicon dangling bond[97]. A critical next step is to find a more general means of varying the local electrostatic field. Here, this is accomplished by surrounding a conducting atom by dipolar molecules that switch their configuration. The field from the fixed point charge is thus replaced by a variable field. The dipolar molecules consist of a self-assembled halododecane dimer[98] that abuts a single silicon adatom on either side. These dimers are shown here to be bistable; they have a high and a low conductance state of the single corralled adatom. A small shift in the dimer's dipolar end groups changes the induced electric field at the corralled adatom by 1V, leading to an order of magnitude conductance change of the corralled adatom. This effect is comparable in size to that generated by semiconductor doping. The following study demonstrates that small changes in molecular configuration can have substantial effects on the surrounding medium, a finding relevant for molecular electronics and also biochemistry, where links between molecular conformation and function are of importance[99].

### 4.1 Experiments

#### 4.1.1 Experimental methods and results

##### STM imaging

The experiments were carried out in ultrahigh vacuum (UHV) using an RHK room temperature scanning tunneling microscope (STM) or an Omicron variable-temperature STM. All STM bias voltages are sample voltages. Samples were cut from n-type (phosphorus-doped) silicon (111) wafers and were resistively flashed in UHV to produce large terraces

of Si(111)-(7 × 7). Liquid chlorododecane was repeatedly freeze/pumped/thawed to remove contamination. STM tips were electrochemically etched from 0.38-mm diameter polycrystalline tungsten wire, using a drop-off technique[100].

#### 4.1.2 Type-I corral formation mechanism

In this section, we report the distinctive mechanism for self-assembly by vertical molecules that glide across the surface loosely attached at a single halogen atom, and thereafter lie down to contact the surface at multiple points and become immobilized. The most facile glide path across the surface appears to be the dimer row on Si(111), joining corner holes.[179]

At low temperature, as it has been illustrated previously for 12-carbon-chain haloalkanes (see chapter 3), we have been able to observe vertical molecules progressing along dimer rows for two- and three-carbon alkyl bromides [98,119,120]. The existence of these lines, rather than isolated molecules, even at low coverage is evidence of their affinity for one another even for two- and three-carbon chains. One attributes this, most probably, to hydrogen bonding entanglement between even short adjacent hydrocarbon tails.

Significantly experimentalists have been unable to observe rows of methyl bromide lining up on our 50K silicon surface. The presence of even a two- or three-carbon chain appears to be enough to give rise to the adsorbate-adsorbate attraction necessary for the (occasional) formation of such lines of ethyl bromide or propyl bromide, though not for methyl bromide. Similar topographs have been obtained for ethyl bromide at 50K.

With this vertical precursor state confirmed by the observation of physisorbed rows of adsorbates at individual Silicon atoms, an analogy with earlier kinetic studies of dodecyl halide[120], it has been proposed a simple mechanism for the formation of dimeric corrals of octyl chloride and octyl bromide. The principal mechanism for corral formation proposed, as in the visualization of Fig. 4.1, involves a deceleration of motion of the vertical,  $v$ , molecules in their vertical encounters with corner holes, followed by attractive hydrogen bond interaction between pairs of alkane chains as for the nested lines of vertical molecules at low temperature.

At room temperature a loosely bound molecular pair, after leaving the dimer row, topples into the observed horizontal dimeric configurations; type I if they fall in one direction around the corner hole, and type II if they fall in the other direction around an adatom.

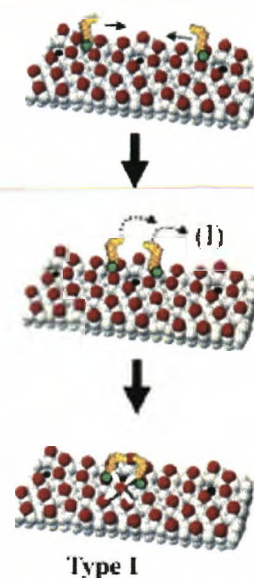


Figure 4.1: Schematic diagram showing Type I corral formation at the Si(111)-(7 × 7) surface. Two mobile physisorbed vertical monomers proceeding along dimer rows meet at a corner hole. Following migration to an adjacent corner adatom they 'fall' ( $2v \rightarrow h_2$ ) to form a type I (around a corner hole). The corralled atom switches on and off (white rays) as the corral opens and closes.

Earlier work[98,119,120] showed evidence of a significant gain in stability for the horizontal pair ( $h_2$ ) as compared with the horizontal monomer ( $h$ ). This was evidenced by the fact that if one half of  $h_2$  was removed from the surface by breaking its C-X bond by electron impact, the other half of the dimer desorbed. The dimer  $h_2$  at the surface is stabilized relative to the monomer by the observed charge transfer to its centre. The importance of this is highlighted by recent experiments that have shown that interference with this charge-transfer process by co-adsorption of a sub-monolayer of sodium causes all  $h_2$  to separate into  $2h$ . [179]

### 4.1.3 Type-I configuration of Chlorododecane

We can observe, from the appearance of halododecane dimers on silicon, that the Type-I halododecane configuration exists for three different halogen terminated molecules: Bromide, Chlorine and Fluorine. It seems to be the most stable configuration for twelve-carbons Haloalkanes once physisorbed on the silicon surface. Such a configuration is stable from room temperature up to 400K. Beyond this temperature it breaks apart into carbon chains separated from the halogen atoms. For this chapter, we study the type-I Chlorodo-

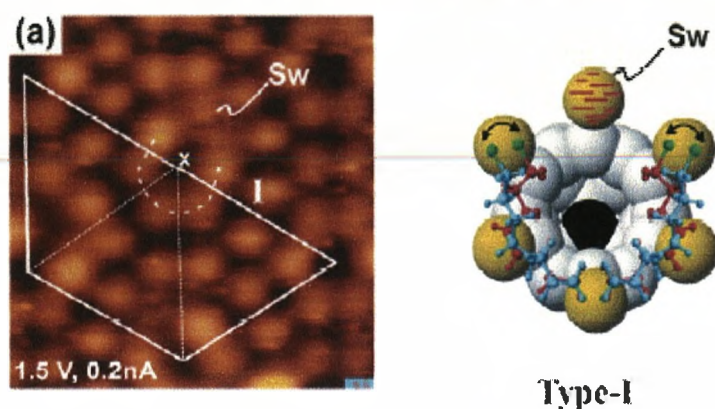


Figure 4.2: STM image of the Chlorododecane molecule physisorbed at silicon(111) (1.5V, 0.2nA). This configuration contains two molecules corraling a corner hole and switching the states of a silicon adatom.

decane dimer configuration(Fig. 4.2). As said above, two chlorododecane molecules are part of this specific configuration. The corral bends over a corner hole of the silicon surface and switches the states of the next silicon adatom following the hole and the dimer.

### 4.1.4 TypeI-Chlorododecane corral study

Fig. 4.3 shows an STM image of a Si(111)-(7 × 7) surface after exposure to chlorododecane molecules self-assembled through non-covalent bonds into two types of dimer structures, type I (around a corner hole) and type II (around a corner adatom). The circles in Fig. 4.3 indicate type I, and the square indicates type II. The type-I structure leaves only one of the six corner adatoms uncovered (Fig. 4.2). This uncovered adatom, located between the jaws of the corral, images as a streaky feature. We now show that the adatom switches repeatedly between conductance states, leading to its streaky appearance. This adatom, the corralled adatom, is the focus of this section. Type II corrals form around a central adatom which undergoes charge transfer induced by the corral to create, instead, a stable darkened adatom[98]. The invariable presence of a streaky corralled adatom only for type I corrals implies that this effect is associated with the corral and is not a tip effect[105,106]. A chemical change such as C-Cl bond breaking could explain the observed conductance change but the energies of the tunneling electrons (< 2.5eV) are insufficient to break the C-Cl covalent bond of chlorododecane, we therefore discount this possibility[98,107,108]. We also rule out extensive changes in the molecular adsorption geometry[109] required



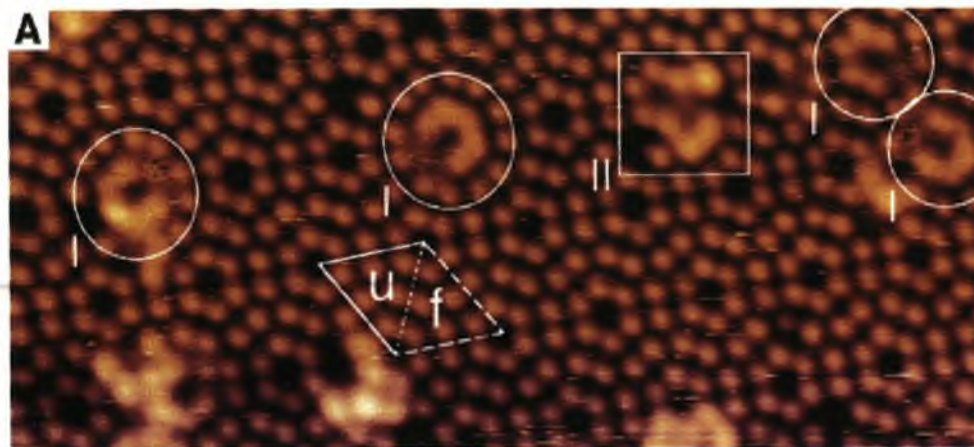


Figure 4.3: (A) large-area STM image of a Si(111)-(7 × 7) surface at room temperature after exposure to chlorododecane molecules (230 × 100 Å, +2V, 0.1nA). Two types of dimer corral are present: those that surround a corner hole (indicated by circles, labelled type I) and those that surround a corner adatom (indicated by squares, labelled type II). Also marked is a unit cell of the surface indicating the faulted (f) and unfaulted (u) halves.

to bring the halogen atom(s) of the intact alkane halide to within bonding distance of the corralled adatom, as the bright features associated with the adsorbed molecules extend far from the corralled adatom and show little or no change (noise) during imaging. Instead, as discussed below, a more subtle change in the molecular dimer at a distance from the corralled adatom appears to be responsible for the conductance switching.

We also considered the possibility that a mobile impurity hopping between tip and adatom could be the cause of the observed switching, but discounted it on the grounds that when switching is halted by cooling there is no detectable (immobilized) impurity, as well as on the grounds that an alteration in current has no effect on switching rate, and, finally, on the grounds that (in three different UHV machines) switching is invariably present for type I configuration corrals but always absent for type II configuration corrals.

The Si(111)-(7 × 7) unit cell has two electronically distinct halves, faulted and unfaulted (see Fig. 4.3), that result from the stacking fault layer of silicon atoms. There are therefore two kinds of type I corralled adatom: faulted (Fig. 4.4B) and unfaulted (Fig. 4.4F). Experimentally it is found that these two kinds exhibit different STM imaging properties. A faulted corralled adatom had long streaks while an unfaulted one has short streaks. We show below that this difference is due to slow conductance switching and fast conductance switching, respectively. Measurements of the tunneling current into the corralled adatom give time-resolved information with respect to both, the slow and the fast switch.

During an image scan of a type I corral, the raster motion was stopped at preset locations and the feedback loop was disabled. Before resuming the scan, the tunneling current was measured every 25 μs over 0.4s, building up a time trace of the tunneling current. Fig. 4.4C shows a time trace taken over a faulted corralled adatom, the Fig. 4.4G shows a time trace taken over an unfaulted corralled adatom. The difference in switching rates is apparent. For the faulted corral, the distribution of tunneling currents in the time trace

is clearly bimodal (Fig. 4.4D); the corralled adatom was repeatedly switching between two conductance states. One labels the high-current state "on" and the low-current state "off". In the STM images of Fig. 4.4B, Fig. 4.4F, the on-state corresponds to the corralled adatom's bright streaks and the off-state corresponds to the dark streaks. Two pairs

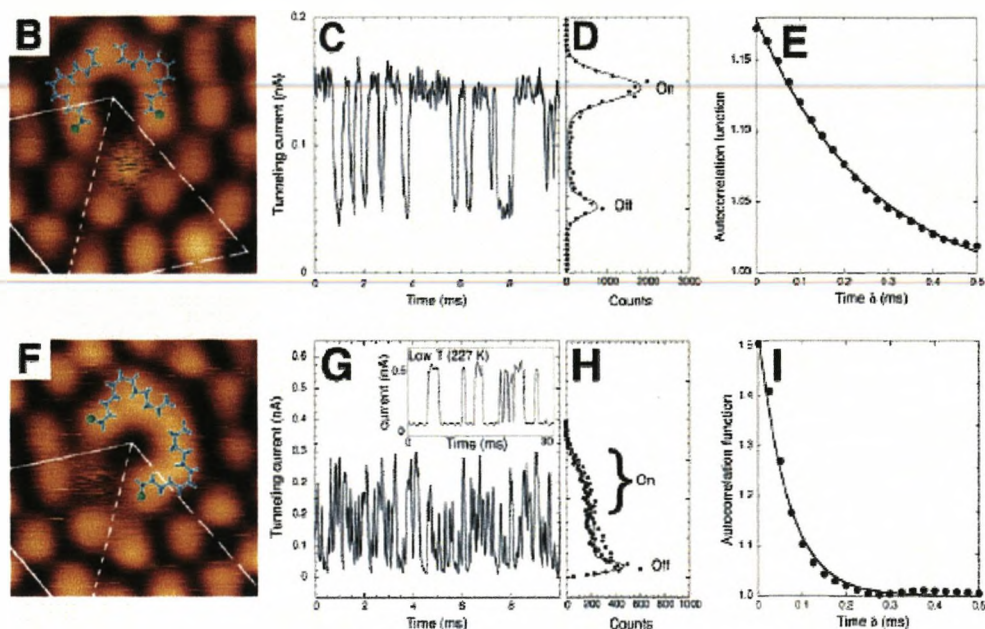


Figure 4.4: (B and F) High-resolution STM images of a type I corral with the corner adatom that lies in the jaws of the corral belonging to the faulted half of the unit cell (B) and the unfaulted half of the unit cell (F). Each image has two chlorododecane molecules, drawn to scale and superimposed. Chlorine atoms are shown in green, and the alkane chain is blue. (B)  $30 \times 30 \text{ \AA}$ ,  $+2.5\text{V}, 0.4\text{nA}$ ; (F)  $30 \times 30 \text{ \AA}$ ,  $+2\text{V}, 0.15\text{nA}$ . (C and G) Tunneling current versus time measurements over (B) a faulted corralled adatom at  $-2.5\text{V}$  and (F) an unfaulted corralled corner adatom at  $+2.4\text{V}$ . (G, inset) Low temperature ( $227\text{K}$ ) tunneling current versus time measurements over an unfaulted corralled corner adatom at  $+2\text{V}$ . (D and H) The corresponding tunneling current distributions with a pair of Gaussian functions fitted in each case; high-current (on) and low-current (off) states are labelled. (E and I) The autocorrelation of the tunneling current time traces of C and G. The fitted functions are exponential decays (see Method for details).

of parameters characterize conductance switching: the on-state and off-state tunneling currents, and the on-state and off-state lifetimes. Gaussian functions fitted to the distribution of tunneling currents determined the on-state and the off-state tunneling currents, whereas auto-correlation of the time traces determined the lifetimes. The Gaussian fits in fig. 4.4D for the faulted corral gave an on-state tunneling current of  $150 \pm 20\text{pA}$  and an off-state tunneling current of  $50 \pm 15\text{pA}$  (errors are the full width at half-maximum). This yields a  $3 \pm 1$  ratio for on-current to off-current for this particular time trace. A similar analysis for the unfaulted corral (fig. 4.4H) gave only one fully defined state, the off-state at  $30 \pm 15\text{pA}$ . Yet, when cooled, the unfaulted corrals showed two well-resolved

states in their time traces (Fig. 4.4G, inset). The unresolved on-state of Fig. 4.4H therefore resulted from the room-temperature unfaulted corrals' rapid switching near the limit of time resolution. To allow these fast switching corrals to be examined, the experimentalists increased the effective time resolution by analyzing the time traces using the auto-correlation technique, as follows.

Auto-correlation is commonly used to study time-resolved measurements of fluorescence blinking [110,111]; here it is used to measure the fluctuation in the tunneling current. The maximum correlation occurs at zero delay; at long delay times there is no correlation and the auto-correlation tends to unity. Fig. 4.4E-Fig. 4.4I show the auto-correlated time traces of the faulted corral and the unfaulted corral. Both auto-correlation plots displayed an exponential decay. The exponential fits to the auto-correlation yielded the lifetimes of the on-state and the off-state for both the (slow switching) faulted corral and the (fast switching) unfaulted corral. The average on-state lifetime, over a range of tunneling currents,

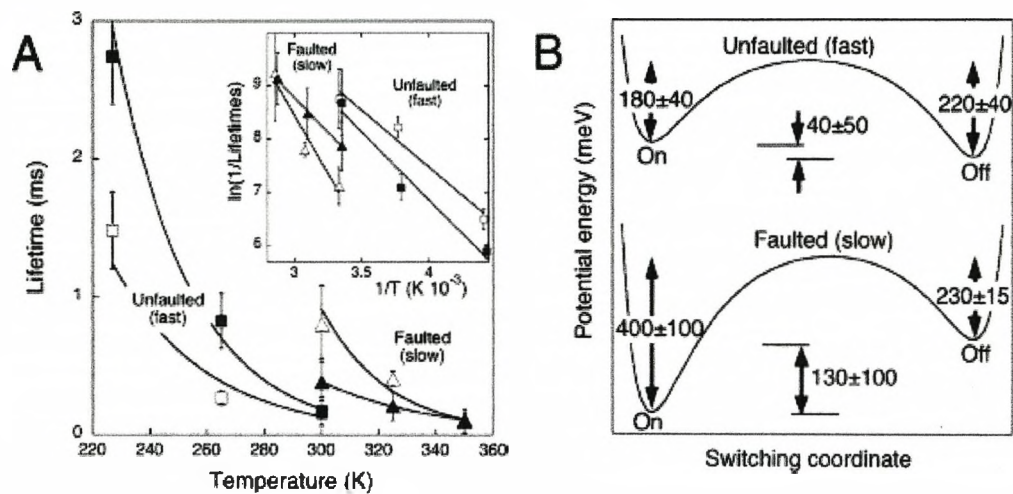


Figure 4.5: (A) Lifetime as a function of the sample temperature of the faulted on-state and off-state and the unfaulted on-state and off-state. Fits are exponential. (inset) Arrhenius plot with linear fits. (B) Schematic of the potential energy, derived from the Arrhenius fits, for the faulted and unfaulted corralled adatoms.

bias voltages, and 11 different type I corrals, was  $930 \pm 50 \mu s$  for the faulted corral. For the off-state lifetime it was  $310 \pm 20 \mu s$ . The faulted corral adatom preferred the on-state. The average on-state lifetime for the unfaulted corral was  $150 \pm 6 \mu s$ , and for the off-state lifetime it was  $215 \pm 16 \mu s$ . The unfaulted corral marginally preferred the off-state. The ratio of on-current to off-current for the faulted corral was  $3.8 \pm 0.1$ , which corresponds to a change in the tip height of  $0.67 \pm 0.01 \text{ \AA}$  (with the decay constant  $k = 1 \text{ \AA}^{-1}$ ). For the unfaulted corral, the tunneling current ratio is  $8.7 \pm 1.1$ , corresponding to a tip height change of  $1.08 \pm 0.06 \text{ \AA}$ .

One now considers the controlling factors for the conductance switching of the corralled adatom. The exponential decays of the auto-correlations imply that the switching rates (on-to-off and off-to-on) are both stochastic. Two possible sources of excitation that could

produce stochastic switching rates are the tunneling current and thermal fluctuations.

A process driven by the tunneling current will have a dependence on the tunneling current and a threshold voltage[112,113]. Over a range of tunneling currents from 0.1 to 1.2nA, no change was found for any of the lifetimes. Equally no threshold behavior was found for the bias dependence of the lifetimes (+2.5 to +0.7 and -0.7 to -2.3V)[114,115]. Furthermore, within the scatter of the experimental results, the tunneling ratios were also found to be independent of either tunneling current or bias voltage. It follows that STM-induced electronic effects do not drive the switch. By contrast, heating the sample above room temperature, as fig. 4.5A shows, reduced the on-state and off-state lifetimes, while cooling the sample increased their lifetimes. Therefore, thermal fluctuations at constant temperature drive the switch.

By fitting the Arrhenius equation to the temperature dependence of the lifetimes (Fig. 4.5A, inset), we can calculate the activation energies and pre-exponential A-factors for the switching processes. Fig. 4.5B presents the activation energies as two schematic potential energy curves. The average pre-exponential A-factor was  $10^{7.5 \pm 0.5} s^{-1}$ , much lower than the standard value of  $10^{13} s^{-1}$ [116,117]. Reduced A-factors have been associated with thermally induced charge transfer from the substrate to adsorbate. To determine if such processes are involved in the switching, further experiments with different surface doping would be required; these lie outside the scope of the present study.

To probe the molecular properties that govern the conductance switching, type I corrals were built from different halogenated alkanes. Changing the length of the alkane chain from 12 carbon atoms (chlorododecane) to 10 carbon atoms (chlorodecane) did not measurably affect the on-state and off-state lifetimes. Similarly, changing the halogen atom from Cl to F did not significantly change the on-state lifetime:  $200 \pm 60 \mu s$  for a fluorododecane corral and  $150 \pm 6 \mu s$  for a chlorododecane corral. However, this change of halogen, Cl to F, increased by more than a factor of three the off-state lifetime:  $710 \pm 130 \mu s$  for a fluorododecane corral compared to  $215 \pm 16 \mu s$  for a chlorododecane corral. It appears that the conductance switching of the corralled adatom is controlled by atoms toward the halogen end of the corralling molecules.

The surface itself, faulted and unfaulted, also affected the conductance switching. As already noted, the two halves of the Si(111)-(7 × 7) unit cell give different switching rates. To explore this surface effect, one combines time-resolved measurements with the spatial resolution of the STM to form a map of the ratio of on-state to off-state tunneling currents, that is, the switching amplitude. These maps are presented in Fig. 4.6A for a faulted corral and Fig. 4.6B for an unfaulted corral. The faulted map contains data from 234 time traces taken over 35 different faulted corrals. Similarly, the unfaulted map contains data from 348 time traces taken over 47 different unfaulted corrals. The symmetry of the corral/substrate system imposes a vertical mirror plane in the switching maps. Most striking is the location of the switch; for the unfaulted corral (Fig. 4.6B) the switch is centrally located between the corralled adatom and its neighboring rest atom; the faulted corral (Fig. 4.6A) also has a large switching ratio at the equivalent location of the corralled adatom. This result mirrors the location of the switching effect observed in high-resolution STM imaging (Fig. 4.6C, 4.6D).

The difference between faulted and unfaulted regions is the location of the substrate silicon atom in the stacking fault layer. For the faulted section, the stacking fault atom is

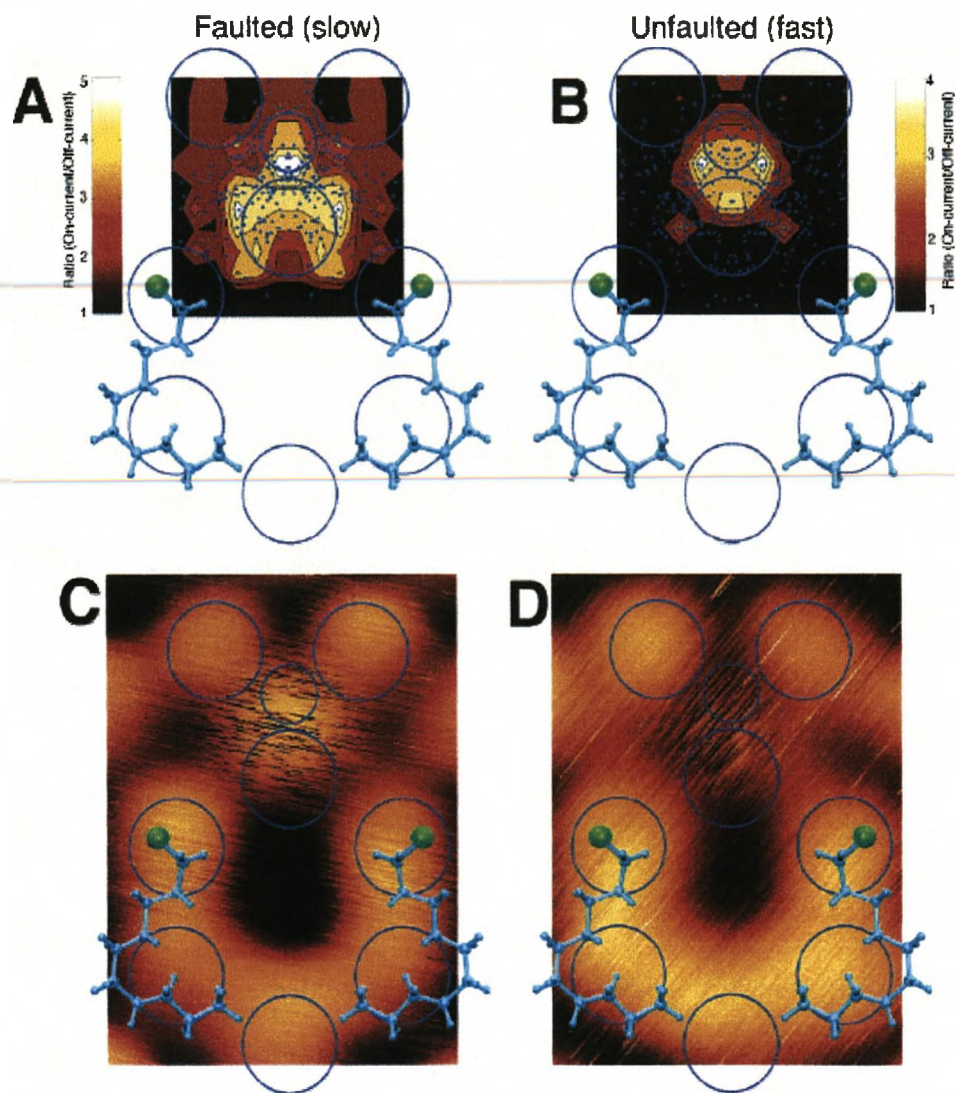


Figure 4.6: (A and B) Plane view spatial maps of the ratio of on-state tunneling current to off-state tunneling current for chlorododecane type I corrals with (A) a faulted corralled adatom and (B) an unfaulted corralled adatom (see side bar for color code). Large blue circles represent silicon adatoms, and the smaller blue circle represents a rest atom. Blue dots indicate the position of individual time-trace measurements. A vertical plane of symmetry exists in the dimer/surface system, and the symmetry was imposed in the switching maps. (C and D) STM images of Fig. 4.4B, 4.4F shown with adatoms and rest atoms indicated to allow easy comparison

directly below the corralled atom, whereas for the unfaulted section it is halfway between the corralled adatom and the neighboring rest atom. Therefore, there appears to be some correlation between the location of the stacking fault atom and the location of the switch. One tentatively proposes that the stabilization energy of the on-state is dependent on the stacking fault atom, so that when this atom is close to the corral (faulted) the on-state

potential is twice as deep than when it is further away (unfaulted); 400meV rather than 200meV.

## 4.2 Type-I Chlorododecane adsorption energies and geometries

Different conformations of chlorododecane molecules have to be determined in such a way that they fit the type-I adsorbate at a  $Si(111) - (7 \times 7)$  surface. As shown in chapter 3, the chlorododecane molecule fits three silicon adatom in any orientation. In case of the Type-I corral, the two Chlorododecane molecules corral 5 silicon adatoms around the corner hole symmetrically. The two chlorine atoms lie on different silicon adatoms. Then the molecules terminate with the carbon chains joining each other on the last silicon adatom of the corral. Successive DFT calculations of these different conformations of  $ClC_{12}$  have to be done in the vacuum. Here we calculate the different geometry possibilities by bending the carbon chain of the molecules at different carbon positions.

The adsorbate/substrate system Chlorododecane at  $Si(111) - (7 \times 7)$  is the second part of the calculations. The fully converged  $2ClC_{12}/Si(111) - (7 \times 7)$  is then studied by STM simulations. The ground state of such a system is calculated by DFT and STM simulations are performed with bSKAN[103,104].

### 4.2.1 Computational details

Density functional theory simulations on a full unit cell were carried out using the Vienna ab-initio Simulation Package (VASP)[101,102]. The switching adatom was chosen to be in the faulted half of the unit cell. The molecules were suspended above the silicon  $7 \times 7$  unit cell, and the whole system was fully relaxed until the forces on individual atoms were less than  $0.02eV/\text{\AA}$ . The initial position of the chlorine atoms was selected by placing them either above or below the alkane chain in the initial configuration. The Brillouin zone was sampled at the  $\Gamma$ -point only. STM simulations were performed using bSKAN[103,104], and the tip model in this case was the tungsten film in (110) orientation with a tungsten pyramid of two layers at the apex.

### 4.2.2 Chlorododecane molecules in vacuum

Many conformations of the Chlorododecane molecule can fit geometrically the three silicon adatom positions of the Type-II configuration on the silicon surface. With respect to the specific geometry of type-I, the degree of freedom is more limited than for the type-II corral, as both ends of the carbon chains of the two chlorododecane molecules lie on the same silicon adatom. Two specific conformations fit the type-I corral with the same carbon chain conformations. The difference between these molecule comes from the chlorine atom oriented into different directions. Fig. 4.7 shows the three different conformations. If the chlorine atom are facing the silicon surface at different angles the carbon chain lies differently on the surface, and still matches STM images. The first step of the study is to

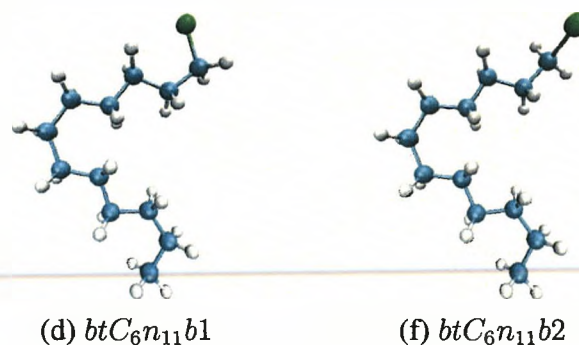


Figure 4.7: By rotating the chlorine atom around nearest carbon, one obtains two different conformations of Chlorododecane. The Chlorine of the  $btC_6n_{11}b2$  molecule is the only one facing the silicon surface

calculate the ground state energies of the molecules in vacuum. The set up is the same for each conformation, the fully relaxed state is calculated within the same volume. We observe three conformations, matching the type II corral, with similar ground states energies. The lowest energy state (see Table 4.1) is 0.4eV more favorable than other states.

Conformation in vacuum	Ground state energies
C6n11b1	$E_{tot} = -203.651 \text{ eV}$
C6n11b2	$E_{tot} = -203.524 \text{ eV}$

Table 4.1: In vacuum, the ground state energies of the 2 conformations of the chlorododecane molecule are close to -203.5eV.

### 4.2.3 Type-I Chlorododecane/Si111 systems calculated by DFT

By depositing the three different conformations of chlorododecane molecules on the silicon surface, we expect to determine the molecular ground state. Here, it is necessary to also relax Si atoms of subsurface layers. The top layers of the silicon surface have been fully relaxed in our simulations. Equally, we have also relaxed the two molecules. The forces on the ionic cores at the final iterations were less than  $0.02\text{eV}/\text{\AA}$

$$E_{ads} = E_{tot} - (E_{surf} + E_{mol}). \quad (4.1)$$

The adsorption energies of an adsorbate on a silicon surface can be calculated using the ground states energies of the systems described above. Eq. 4.1 gives the general relation for determining the adsorption energy of a system (adsorbate/substrate), in this case the adsorption energy of a type I corral of chlorododecane on silicon. Table 4.2 displays the DFT ground state values of the two calculated systems and the results of the calculations of adsorption energies for the adsorbate/substrate system. The  $btC_6n_{11}b2$  chlorododecane molecule shows the highest adsorption energy with -2.08eV while the other molecules,  $btC_6n_{11}b1$  have got lower adsorption energies around -1.54eV. The two systems are now to be studied by STM simulations.

System	TOT/ADS energies
Silicon surface	$E(\text{tot}) = -1179.30 \text{ eV}$
$2C_6n11b1/Si111$	$E(\text{tot}) = -1588.14 \text{ eV}$
$2C_6n11b1/Si111$	$E(\text{ads}) = -1.54 \text{ eV}$
$2C_6n11b2/Si111$	$E(\text{tot}) = -1588.42 \text{ eV}$
$2C_6n11b2/Si111$	$E(\text{ads}) = -2.08 \text{ eV}$

Table 4.2: Summary of the ground state energies and adsorption energies of the clean silicon surface, the  $C_{12}Cl$  in the vacuum, and the systems  $2C_{12}Cl/Si111$

### 4.3 STM Simulations on the TypeI-Chlorododecane/Si111 system

To determine whether conformation changes could account for the conductance switching of the corralled adatom, we performed electron transport (STM) simulations on a chlorododecane corral with a faulted corralled adatom (see computational details). In the calculations, two stable adsorption configurations have been identified, shown in Fig. 4.8. The two configurations below correspond to an on-state (blue molecules of Fig. 4.8) and an off-state (red molecules of Fig. 4.8) of the corral. Given the size of the molecules, one cannot be certain that these configurations are unique. In accord with the interpretation of the experiments given above, the main geometric difference between the pair of configurations is the position of the chlorine end of the molecule; the terminal chlorine ends of the molecules are either closer (off-state) or more distant (on-state) from the corralled adatom. The calculated energy difference between the two configurations was 270meV per

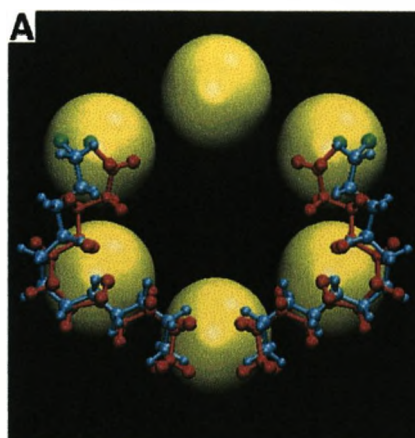


Figure 4.8: Molecular configurations: on-state (blue molecule) and off-state (red molecule).

molecule. However, it should be noted that owing to the large size of the simulated unit cell



the precision of the calculation, which is satisfactorily small at 1 meV per atom, amounted to a total energy uncertainty of 300 meV. For this reason, we had to consider the energies of the two configurations equal to within the limits of the calculation. Nonetheless, the simulations establish that the molecular arrangements have a small enough energy difference so that they can be changed in a thermally driven process. In this process, the chlorine ends of the molecules alternate their distance from the corralled adatom. In neither configurations, however, is the chlorine nearer than 6 to 7 Å from the corralled adatom; too far even for weak chemical bonding.

While the computed configuration changes from the on-state to the off-state appear to be minor, they have a substantial effect on the electron states at the position of the corralled adatom. Figs. 4.9B, 4.9C reveals that the height of the calculated charge density contour at the corralled (top) adatom changes by more than 0.5 Å. Successive contour lines in these plots describe a height variation of 0.5 Å. To compute the changes in the tunneling cur-

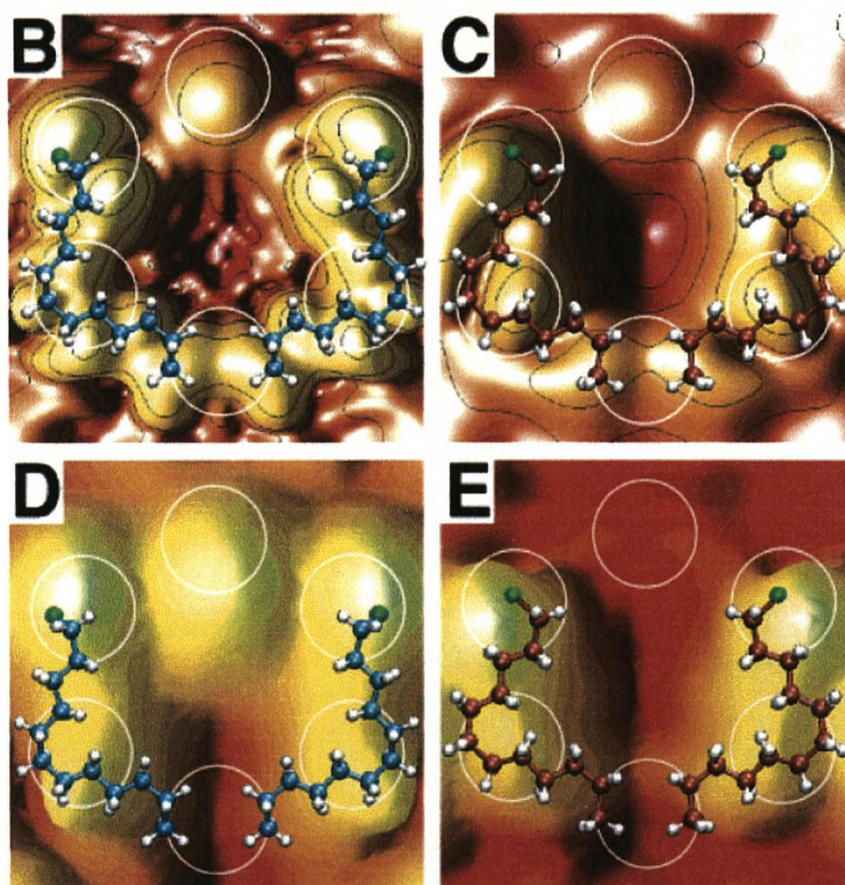


Figure 4.9: (B and C) Density contours from  $E_F$  to  $E_F + 2eV$ , value  $10^{-5} e/\text{Å}$ [92]. The contour lines correspond to a vertical distance of 0.5 Å. White circles indicate the silicon adatoms at the corner hole. (D and E) Simulated STM constant current contours (+2V, 50 pA). (D) On-state. (E) Off state. The difference in apparent height measured at the top of the adatom is 1 Å

rent flowing into the corralled adatom, we performed STM simulations with a (theoretical)

tungsten tip. Fig. 4.9D, Fig. 4.9E present the simulated STM images of the two molecular geometries shown in Fig. 4.8A. It can be seen that depending on the configuration of the molecules the corralled adatom appears either as a distinct protrusion (Fig. 4.9D) or as a "missing" feature (Fig. 4.9E). The computed height difference between the two states of the corralled adatoms is  $1\text{\AA}$ , comparable to the experimental height difference of  $0.7\text{\AA}$ . These two states of the molecules thus correspond to the on-state and off-state of the corral. The switching behavior is established as being dependent on small changes in the position of the polar end of the molecules.

We note the absence of tunneling current in the theoretical STM images of Fig. 4.9D, Fig. 4.9E to the adatom at the bottom of the corral. This is despite the fact that Fig. 4.9B, Fig. 4.9C shows a high DOS at this location. We attribute this to a numerical artifact stemming from the finite size of the simulated STM tip.

It was found previously that the molecular chlorododecane type I corral induces lateral surface dipoles in the silicon surface, which are accompanied by substantial charge transfer along the surface[98]. The occurrence of surface dipoles due to the formation of a corral. Here, we find that the type I induced surface dipoles are switched on and off by a change of the conformation of the molecules. This can be seen in the analysis of the density of states (DOS) at the position of the corralled adatom. Fig. 4.10F shows that the off-state

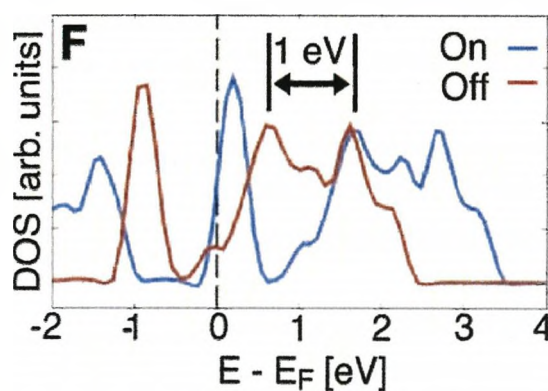


Figure 4.10: (F) DOS integrated over a silicon adatom. The DOS is bodily shifted by  $1\text{eV}$ , indicating the change of the dipole field due to molecular configurations

of the molecules corresponds to a bodily downward shift of the DOS, relative to on-state, at the corralled adatom by about  $1\text{eV}$ . The DOS also reveals that the main contribution to the tunneling current originates from the lowest unoccupied state at the position of the adatom(see the distinct peak at low positive energy). This state is shifted below the Fermi level in the "off" configuration, which means that in this case it carries additional electron charge. A similar shift to lower energies has been observed for the type II corral in the previous chapter[98].

This type of DOS shift is only observed if an electrostatic field is applied to the surface at this location. From the simulated STM images and the corresponding changes in configuration, we therefore conclude that the small configuration changes induces electric fields in the vicinity of the corral, which amount to an electrostatic potential of about  $1\text{V}$ . Given that defect atoms in semiconductors (e.g. dopants) show effects of a similar magnitude, we

conclude that modest molecular configuration changes can produce effects equal in magnitude to the effects of chemically doping a semiconductor. However, the effect in this case is not due to localized charges, but due to a substantially enlarged dipole field in the "off" configuration. We find that the lateral dipole moment in the off-state is increased by a factor of 7. Due to decay characteristics of dipole fields, proportional to the inverse square of the distance, the effect is limited to a very small region of the surface, in contrast to charges at dangling bonds[97], where the Coulombic field decays with the inverse distance.

In summary, we have shown a single-atom electronic switch in silicon due to molecularly induced field effects. Small changes in the configuration of a self-assembled pair of dipolar adsorbate molecules surrounding a silicon atom are shown to have a large electronic effect characterized by a high and a low conductance. The finding that small changes in conformation of molecules can have substantial external electronic effects should be of interest in contexts ranging from nanoscale electronics to molecular biology.

## Chapter 5

# Monte Carlo and statistical mechanics for a simple model

This chapter presents a visualization of the Monte Carlo simulation and the statistical mechanics theories, using a simple model. The combination of the Monte Carlo/Metropolis algorithm and statistical mechanics parameters is a key to determining the evolution of the physical states of a complicated system such as Tartaric Acid molecules adsorbed at Copper(110). Thus, it is quite important to study the accuracy of the information entered into or received from a Monte Carlo simulation, performed in the Canonical ensemble.

There are different states during the run of a Monte Carlo program which can be verified and determined by use of statistical mechanics. These are the initial states and the final states for a single Monte Carlo simulation, analyzing exactly what one expects a Monte Carlo simulation to render. In the case of Monte Carlo simulations performed with the evolution of the size of the cell of the system, one can sort out the accuracy of the thermodynamic information, following the evolution of statistical mechanics parameters from two initial cases such as the perfect ordered state and the full disorder state. Monte Carlo simulations performed at successive and increasing temperatures give an evidence of the reliability of the order parameter and the heat capacity parameter with respect to the state of the system especially at low temperatures, at the temperature of the critical phase, and at high temperatures.

To do so, a simple cubic surface at the (100) face is used as a reference. This surface admits a lattice parameter  $a$  of an undefined value. The supercell of the following simulation is squared of the following dimensions  $(10 \times 10)$ ,  $(20 \times 20)$ ,  $(30 \times 30)$  and  $(40 \times 40)$ . A particle  $p$ , once adsorbed at the cubic surface sits, at a hollow site of the cubic (100) face and has a repulsive interaction of  $+0.1eV$  at the smallest distance of  $d = a$  to the next particle. For simplicity no other particle-particle interaction is considered in the simulations. The ordered structure of such a Monte Carlo set-up for  $\Theta = 0.5$  ML is  $c(2 \times 2)$  at low temperatures.

## 5.1 Order parameter

Surface phase transitions are usually discussed in terms of an order parameter  $\Psi$  [68,83,84]. It can be a scalar, a vector, or a tensor of a higher rank. The order parameter is defined to be zero above  $T_C$ , when there is no long-range order, and it is usually normalized to unity for a fully ordered state. In a second-order phase transitions,  $\Psi$  increases continuously from zero as T decreases below  $T_C$ , while in a first-order transition, it changes discontinuously. One can choose as an order parameter the low-energy-electron-diffraction (LEED) intensity of a suitable diffraction spot. Thus, as in LEED intensity measurements, the critical temperature of the order-disorder transition can be estimated from the inflection point of the curve  $\Psi$  versus T for constant  $\Theta$ .

The order parameter  $\Psi$  is supposed to measure the periodicity of a determined surface structure with a defined symmetry. As such, it can conveniently be evaluated by Fourier transform techniques. The information in real space is transformed into frequency space and patterns in real space can then be effectively measured.

### 5.1.1 Discrete Fourier transform

The configurations of particles in a lattice can be represented as matrices. Thus, a specific ordering behavior can be measured by applying a discrete fourier transform to the matrix representation and extracting the Fourier coefficients that correspond to the frequency of the ordered configuration.

The discrete Fourier transform of a vector  $\mathbf{x}$  is given by [82]

$$\begin{bmatrix} w_n^{1-1} & w_n^{1-2} & \dots & w_n^{1-n} \\ w_n^{2-1} & w_n^{2-2} & \dots & w_n^{2-n} \\ \vdots & \vdots & \ddots & \vdots \\ w_n^{n-1} & w_n^{n-2} & \dots & w_n^{n-n} \end{bmatrix} \begin{bmatrix} x_0 \\ x_1 \\ \vdots \\ x_{(n-1)} \end{bmatrix} = \begin{bmatrix} c_0 \\ c_1 \\ \vdots \\ c_{(n-1)} \end{bmatrix} \quad (5.1)$$

where  $w_n^{r-s} = e^{\frac{-2i\pi(r-1)(s-1)}{n}}$  and  $\mathbf{c}$  is the vector of Fourier coefficients; Eq. 5.1 can be also expressed in matrix notation as

$$\mathbf{F}\mathbf{x} = \mathbf{c}, \quad (5.2)$$

where  $\mathbf{F}$  is called the Fourier matrix. Note that  $\mathbf{F}$  is a symmetrical matrix.

Since the ordering on a surface takes place in 2 dimensions, the discrete Fourier transform has to be applied in 2 dimensions. Two dimensional Fourier transforms simply involve a number of one dimensional Fourier transforms. More precisely, a two-dimensional transform of a matrix is achieved by first transforming each row, replacing each column with its transform. The two-dimensional fourier transform of a  $(n \times n)$  matrix  $\mathbf{A}$  is given by

$$\mathbf{F}(\mathbf{F}\mathbf{A}^T)^T = \mathbf{c}, \quad (5.3)$$

where the transpose, T symbol, refers to the transpose without conjugate.

### 5.1.2 The $(2 \times 2)$ ordering

The ordering corresponding to the  $(2 \times 2)$  symmetry is illustrated in Fig. 5.1(a). Two types of structures are possible:  $c(2 \times 2)$  corresponding to  $\Theta = 1/2 \text{ ML}$  and  $p(2 \times 2)$  corresponding to  $\Theta = 1/4 \text{ ML}$ . The structures have respectively one and two atoms per unit cell. Usually, spin variables (+1 if the site is occupied, -1 if the site is empty) are used when calculating order parameters. However, the calculation with point variables (+1 if the site is occupied, 0 if the site is empty) is readily carried out. One only need to convert every element of the point configuration (usually given as a matrix of +1 and 0) to a spin configuration through the relationship:

$$S_i = 2n_i - 1. \quad (5.4)$$

The direct calculation with point variables is also possible. However, additional normalization factors should be found in order to ensure that  $\Psi = 1$  for a fully ordered state. In a point variable configuration, the coverage  $\Theta$  is given by

$$\Theta = \frac{1}{N} \sum_{i=1}^N n_i, \quad (5.5)$$

where  $N$  is the number of lattice sites. The equivalent quantity configurations is called

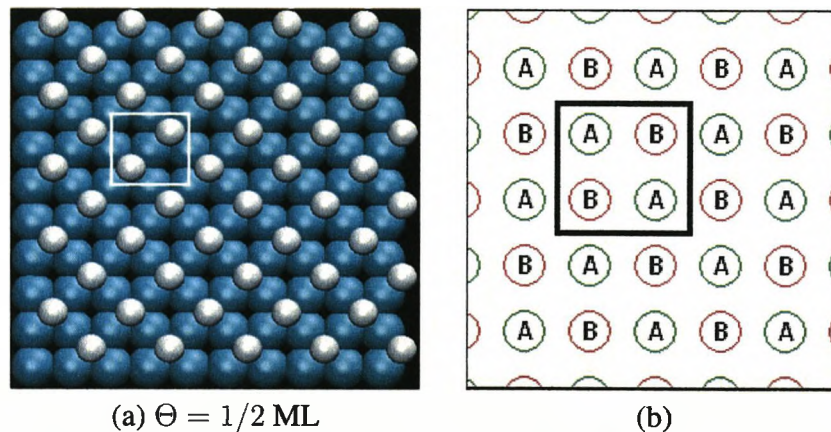


Figure 5.1: (a) Ordered  $c(2 \times 2)$  phase in a square lattice, i.e. a (100) surface. The  $c(2 \times 2)$  unit cell is sketched as well. Note that the coverage has two atoms per unit cell (b) Division of the square lattice into sublattices

magnetization. it is given by

$$M = \sum_{i=1}^N s_i. \quad (5.6)$$

Note the magnetization can be positive or negative. The magnetization per spin is given by

$$m = \frac{1}{N} \sum_{i=1}^N s_i. \quad (5.7)$$

The coverage  $\Theta$  then is simply related to the magnetization per spin  $m$

$$\Theta = \frac{1}{2}(1 + m). \quad (5.8)$$

The  $(2 \times 2)$  configuration can be described by decomposing the original lattice into two sublattices made up of sites connected by next nearest-neighbour bonds.

The total magnetization of every sublattice is given by

$$M_\alpha = \sum_{i \in \alpha} s_i, \quad (5.9)$$

with  $\alpha = A, B, C, \dots$ . The order parameter can be written in term of the magnetizations  $M_\alpha$ . In order to do so, one has to express the  $p(2 \times 2)$  ordering in term of  $M_\alpha$ . This is accomplished by writing the  $c(2 \times 2)$  configurations in matrix notation. The possible  $c(2 \times 2)$  configurations can be expressed in matrix notation using a  $(2 \times 2)$  matrix. The degenerate matrix representations of the  $c(2 \times 2)$  configurations in terms of spin variables are:

$$\begin{bmatrix} 1 & -1 \\ -1 & 1 \end{bmatrix}, \begin{bmatrix} -1 & 1 \\ 1 & -1 \end{bmatrix}$$

Thus one can set up a general matrix for the  $p(2 \times 2)$  configurations in term of the magnetizations  $M_\alpha$  according to the sublattices in Fig. 5.1(b).

$$M = \frac{1}{2} \begin{bmatrix} M_A & M_B \\ M_B & M_A \end{bmatrix}. \quad (5.10)$$

The next step is to Fourier transform the  $(2 \times 2)$  matrix  $M$ . For that purpose, one needs the  $(2 \times 2)$  Fourier matrix. From the definition in Eq. (5.1).

$$F_2 = \begin{bmatrix} 1 & 1 \\ 1 & -1 \end{bmatrix}. \quad (5.11)$$

By applying Eq. (5.3) to Eq. (5.10) and taking the absolute value of the Fourier coefficients, one arrives at:

$$|c| = \begin{bmatrix} M_A + M_B & 0 \\ 0 & M_B - M_A \end{bmatrix}. \quad (5.12)$$

From this Fourier transform it is possible to derive the order parameter for the  $c(2 \times 2)$  configuration. The matrix component  $M_A + M_B$  is not suitable as the order parameter because it is constant for all the configurations, i.e.  $M_A + M_B = M$  where  $M$  is the total magnetization given by Eq. (5.7). The remaining nonzero matrix elements measure the frequency of the  $c(2 \times 2)$  configuration. They are degenerate and their algebraic expression can be used as order parameter

$$\Psi' = M_A - M_B. \quad (5.13)$$

The expression in Eq. (5.13) can be conveniently normalized to 1 by finding its maximum value. Since  $\Psi'$  measures the frequency of the  $c(2 \times 2)$  configuration, its value must be maximum when the surface exhibits such a configuration. If this is the case, then  $|M_A| =$

$M_B$  |, because of the twofold degeneracy of the  $c(2 \times 2)$  configuration. Assuming  $M_B = -M_A$  one can simplify to

$$\|\Psi'\| = 2M_A, \quad (5.14)$$

$\|\Psi\|$  is the factor by which Eq. 5.13 should be divided in order to normalize  $\Psi'$  to 1.  $\|\Psi\|$  can be conveniently expressed in terms of the number of the lattice sites  $N$ . For the assumed  $c(2 \times 2)$  configurations  $M_A = \frac{N}{2}$ , so that

$$\|\Psi'\| = N. \quad (5.15)$$

The normalized order parameter is given by

$$\Psi = \frac{1}{N} \sqrt{(M_A - M_B)^2}. \quad (5.16)$$

The computational implementation of the order parameter given by Eq. (5.16) is straightforward. One only needs to count the sublattice magnetizations  $M_A$  and  $M_B$  from a given matrix and evaluate  $\Psi$ . For disordered states  $\Psi = 0$  and for ordered states with  $c(2 \times 2)$  symmetry  $\Psi = 1$ . By cooling down the system near the critical temperature  $T_C$ , the order parameters  $\Psi$  rapidly increase from values near zero (disorder) to one (order). The measurements point of  $\Psi$  versus  $T$  for constant  $\theta$  can be fitted by sigmoidal curve. The inflection point of the curve corresponds to the order-disorder transition temperature for a given  $\theta$ .

The order parameter  $\Psi$  can be confirmed to accuracy, for that purpose, thermodynamic methods (e.g. heat capacity measurements) are necessary.

## 5.2 Thermodynamic approach

### 5.2.1 Thermodynamics

Thermodynamics establishes the relationships between the different macroscopic thermodynamic properties of a system. The corresponding mathematical framework is based on the laws of thermodynamics. The first law of thermodynamics states that the total energy of a system is conserved, i.e. the energy is invariant, it remains the same going forward and backward in time (time symmetry). The energy  $U$  of a system (associated with its capacity for doing work) can only be transferred, but not destroyed, i.e. for an infinitesimal process [19]

$$dU = \delta Q + \delta W. \quad (5.17)$$

The differential heat flow into the system  $\delta Q$  and the differential work done on the system  $\delta W$  represent ways that energy can be transferred from one system to the other. They are dependent upon the path followed in making the transfer (i.e.  $\delta Q$  and  $\delta W$  are inexact differentials, since their value depends upon the path taken by the system). Though  $\delta Q$  and  $\delta W$  change with the path, their sum produces always the same  $dU$ , since  $U$  is a state function and  $dU$  is independent of the path (an exact differential). The work term, has the general form

$$\delta W = \mathbf{f} \cdot d\mathbf{X}, \quad (5.18)$$



where  $\mathbf{f}$  is the applied "force", and  $\mathbf{X}$  stands for a mechanical extensive variable. The variables  $\mathbf{f}$  and  $\mathbf{X}$  are called conjugate variables. The work done in changing an extensive thermodynamic variable  $\mathbf{X}$  is the product of the change in that variable and its conjugate intensive variable  $\mathbf{f}$ . For the type of closed (constant mass) systems we are interested in, the work term takes the form

$$\delta W = -pdV, \quad (5.19)$$

where  $V$  is the volume of the system and  $p$  is the pressure on the system.

The first law establishes the equivalence of the different forms of energy (radiant, chemical, physical, electrical, and thermal), the possibility of transformation from one to another, and the laws that govern these transformations. The first law considers heat and energy as two magnitudes of the same physical nature.

While the first law of thermodynamics says that the total quantity of energy in a closed system remains constant (this is the principle of the conservation of energy), the second law of thermodynamics states that the quality of this energy (its ability to do work) is degraded irreversibility (this is principle of the degradation of energy) [85].

The quantity which measures the extent to which the energy of a system is available for conversion to work is the entropy  $S$ . If a system undergoing an infinitesimal reversible change takes in a quantity of heat  $\delta Q$  at absolute temperature  $T$ , its entropy increased by

$$dS = \delta Q/T. \quad (5.20)$$

The second law thus states that the total entropy change of a closed system is always positive and the amount of energy not available for doing work,  $TdS$ , increases continually. The increase in entropy defines the thermodynamic arrow of time.

The fundamental thermodynamic relationship that applies to any process in a closed system (where only  $pdV$  work is present) can be obtained from Eq. (5.17), Eq. (5.19), Eq. (5.20), i.e.

$$dU = TdS - pdV. \quad (5.21)$$

Eq. (5.21) can be applied to any differential change in both reversible and irreversible processes, because it states a relationship between functions of state only, i.e. their values depend only on the state of the system and not on the path to reach that state [86].

The equilibrium state of a system can be characterized by the variational statement of the second law [50]. For small displacements away from the equilibrium manifold of the states, the entropy remains constant or decreases

$$(\delta S)_{U,V} \leq 0. \quad (5.22)$$

It means that, for a system in thermodynamic equilibrium with a given energy, the entropy is greater than that of any order state with the same energy. This entropy maximum principle has a corollary that is an energy minimum principle [50], i.e. for small displacement away from the equilibrium state

$$(\delta U)_{S,V} \geq 0. \quad (5.23)$$

The fundamental thermodynamic relationship Eq. (5.21) and the variational statement of the second law, Eq. (5.22) and Eq. (5.23), are the principles necessary for analyzing the macroscopic thermodynamics of systems at equilibrium. However, the characterization of

the system is greatly facilitated by changing the independent variables of the fundamental relationship.

The variational principle in Eq. (5.23) tells us facts about equilibrium states characterized by  $S$  and  $V$ , i.e.  $U$  is a natural function of  $S$  and  $V$  (see Eq. (5.21)). Now, suppose we want to construct a natural function of  $T$  and  $V$  to characterize the equilibrium states of a closed system (in fact,  $T$  is experimentally more accessible than  $S$ ); but the new function must contain not more or less information than  $E$ . The way to achieve this is a Legendre transformation [50]. To construct a natural function of  $T$  and  $V$  for a closed system, one has to subtract from  $dU$  the quantity  $d(TS)$ , i.e. the extensive variable  $S$  times its conjugate  $T$ , to obtain

$$d(U - TS) = -SdT - pdV. \quad (5.24)$$

This quantity,  $U - TS$ , is called the Helmholtz free energy, or simply the free energy

$$F = U - TS. \quad (5.25)$$

Similar transformations are possible by selecting different (non-conjugate) pairs of independent variables, i.e. the independent variables describing the system have to be non-conjugate [50]. The resulting state functions: energy  $U(S, V)$ , enthalpy  $H(S, p)$ , Helmholtz free energy  $F(T, V)$ , and Gibbs free energy  $G(T, p)$ ; are called thermodynamic potentials [19]. All of them can be used to characterize equilibrium states through the use of variational principles of the form of Eq. (5.23).

Since heat flow and temperature changes are intimately related, it is useful to quantify their connection by introducing heat capacities. The heat capacity at constant volume is given by

$$C_V = \left( \frac{\delta Q}{dT} \right)_{N,V} = T \left( \frac{\partial S}{\partial T} \right)_{N,V} = \left( \frac{\partial U}{\partial T} \right)_{N,V}. \quad (5.26)$$

The last equation provides a way for evaluating the entropy  $S$  of the system from  $C_V$  measurements, i.e. integrating Eq. (5.26).

$$S(T) = S(T_0) + \int_{T_0}^T \frac{C_V}{T} dT. \quad (5.27)$$

However, the result given by Eq. (5.27) is not reliable, because the specific heat itself is not easy to determine, particularly in view of its divergence at a phase transition. In the case of theoretical Monte Carlo simulations, where the Hamiltonian of the system is known and its energy  $U$  is usually a direct result of the simulation, one can calculate the entropy from the thermodynamic relationship

$$\left( \frac{\partial S}{\partial T} \right)_{N,V} = \left( \frac{\partial U}{\partial T} \right)_{N,V}. \quad (5.28)$$

Integrating Eq. (5.28)

$$S(T) = S(T_0) + \int_{T_0}^T \frac{dU}{T}. \quad (5.29)$$

These last equations illustrate the practical utility of thermodynamics. It makes inferences about unmeasurable quantities from observable ones (e.g. the Maxwell relations [50]).

However, thermodynamics says nothing about the actual value of the thermodynamic properties. For that, we need to carry out experiments or run simulations using statistical mechanics.

### 5.3 Statistical mechanics approach

Statistical mechanics was developed to obtain averages of the mechanical variables of the molecules in a system and to provide the coarse features of the system. These coarse features turn out to be, precisely, the macroscopic thermodynamic properties. Thus, statistical mechanics anchors thermodynamics to mechanics.

The statistical mechanics description of thermodynamic equilibrium considers a manifold of microscopic states consistent with the constraints imposed on the system. The basic idea is that during a measurement every microscopic state or fluctuation that is possible does in fact occur, and observed properties are actually the averages from all the microscopic states (the fundamental postulate) [50].

Thus, if the value of some quantity  $X$  in the  $i$ -th microstate is  $X_i$ , and the probability that the system is in that microstate is  $P_i$ , then the value of  $X$  in the macrostate is given by the ensemble average

$$\langle X \rangle = \sum_i P_i X_i. \quad (5.30)$$

This is crucial link from microscopic to macroscopic properties. In the molecular interpretation, the energy  $E$  is the energy stored within the molecules of a system. It is related to the macroscopic internal energy  $U$  by

$$U \equiv \langle E \rangle = \sum_i P_i E_i. \quad (5.31)$$

The temperature is a measure of the molecular activity of a substance. The greater the movements of the molecules (kinetic energy), the higher the temperature, and the more microstates the molecule can populate. The physical constant relating temperature to energy is the Boltzmann constant  $k_B$ .

For an isolated system with a fixed total number of particles  $N$ , fixed volume  $V$ , and fixed energy  $E$ , statistical mechanics assumes that all attainable microscopic states are equally likely at thermodynamic equilibrium (ergodic hypothesis). If the number of such microstates is  $\Omega$ , the probability that the system is in any one microstate will be:

$$P_i = \frac{1}{\Omega} \quad \text{and} \quad \sum_{i=1}^{\Omega} P_i = \Omega \frac{1}{\Omega} = 1. \quad (5.32)$$

The statistical definition of entropy  $S$  for a macroscopic state composed of  $\Omega$  microscopic states is given by [172]

$$S = k_B \ln \Omega, \quad (5.33)$$

where  $k_B$  is the Boltzmann constant. Thus, according to the statistical mechanics interpretation, entropy increase (or a molecular basis) means that a system changes from having fewer accessible microstates to having a larger number of accessible microstates.

The increase in entropy in a closed system to a maximum at equilibrium is the consequence of the trend from a less probable to a more probable state. At equilibrium, the system will be in the manifold of microstates corresponding to the macrostate having the highest number of microstates.

From Eq. (5.21) and Eq. (5.33) we obtain the statistical mechanics definition of temperature

$$\left(\frac{\partial \ln \Omega}{\partial E}\right)_{N,V} = \frac{1}{k_B T}, \quad (5.34)$$

which relates the temperature to the change in the logarithm of the microscopic degeneracy with energy. Since the degeneracy increases with the energy, the temperature is a positive quantity.

The Boltzmann entropy in Eq. (5.33) is defined for a macroscopic state, whereas the Gibbs entropy is defined over a statistical ensemble. That is, over the probability distribution of macrostates [87]

$$S = -k_B \sum_i P_i \ln P_i. \quad (5.35)$$

For one macrostate (i.e. the microcanonical ensemble) all probabilities are equal and are given by Eq. (5.32). Then Eq. (5.35) reduced to Eq. (5.33)

$$S = -k_B \sum_{i=1}^{\Omega} \frac{1}{\Omega} \ln \frac{1}{\Omega} = k_B \ln \Omega. \quad (5.36)$$

By using the variational formulation of the second law Eq. (5.22) and the Gibbs entropy formula Eq. (5.35), one is able to derive the equilibrium distribution functions for other ensembles [50]. According to the second law, at equilibrium

$$(\delta S)_{E,V,N} = 0. \quad (5.37)$$

That is, the partitioning of microscopic states at equilibrium is the partitioning that maximizes the entropy. Thus, the equilibrium distribution of the canonical ensemble (table 2.1) can be obtained by maximizing Eq. (5.35) subject to the canonical ensemble constraints

$$\langle E \rangle = \sum_i E_i P_i \quad \text{and} \quad \sum_i P_i = 1. \quad (5.38)$$

By combining Eq. (5.35), and Eq. (5.37), and Eq. (5.38) one obtains

$$\delta \left( -k_B \sum_i P_i \ln P_i - \lambda \sum_i E_i P_i - \gamma \sum_i P_i \right), \quad (5.39)$$

where  $\lambda$  and  $\gamma$  are Lagrange multipliers. When the extremum is obtained [50], the canonical probability (Boltzmann distribution function) is given by

$$P_i = \frac{e^{-E_i/k_B T}}{\sum_i e^{-E_i/k_B T}}. \quad (5.40)$$

The sum in the denominator of Eq. (5.40) is over all states and normalizes the distribution. It plays a central role in statistical mechanics and is called the canonical partition function

$$Z = \sum_i e^{-E_i/k_B T}. \quad (5.41)$$

The partition function encodes all thermodynamic information of the system. The connection of  $Z$  to thermodynamics is obtained by writing Eq. (5.40) as

$$\ln P_i = \frac{E_i}{k_B T} - \ln Z, \quad (5.42)$$

and substituting in Eq. (5.35). Recognizing that the energy  $U$  is given by Eq. (5.31), one obtains [86]

$$S = \frac{U}{T} + k_B \ln Z, \quad (5.43)$$

which, from the definition of the free energy in Eq. (5.25), can be written in compact form as

$$F = -k_B T \ln Z. \quad (5.44)$$

This is an important result. It shows that the free energy  $F$  is the bridge between the canonical partition function and thermodynamics. All other thermodynamic quantities can be calculated by appropriate differentiation of Eq. (5.44) [143].

The internal energy  $U$  can be obtained from the free energy via

$$U = -T^2 \left( \frac{\partial(F/T)}{\partial T} \right)_{N,V}, \quad (5.45)$$

the entropy  $S$  from

$$S = - \left( \frac{\partial F}{\partial T} \right)_{N,V}, \quad (5.46)$$

and the heat capacity  $C_V$  from

$$C_V = \left( \frac{\partial U}{\partial T} \right)_{N,V}, \quad (5.47)$$

Statistical mechanics also relates the size of the spontaneous fluctuations in the energy to the heat capacity  $C_V$  [50]

$$\langle (\delta E)^2 \rangle = \langle (E - \langle E \rangle)^2 \rangle = \langle E^2 \rangle - \langle E \rangle^2 = k_B T^2 C_V, \quad (5.48)$$

which is a remarkable result relating the size of spontaneous fluctuations  $\langle (\delta E)^2 \rangle$  to the rate at which energy will change due to alterations in the temperature. This result could never have been derived within the framework of thermodynamics, since it depends on microscopic insight in statistical mechanics.

The microscopic insight contained in statistical mechanics can be illustrated by considering the Ising model near the critical region (Phase transition). The system tends to form into large clusters (spins in the same direction). These clusters contribute significantly to the energy of the system. They form and disappear, producing large fluctuations in  $E$ , called "critical fluctuations". As the typical size  $\xi$  of the clusters diverges as  $T \rightarrow T_C$ , the size of the fluctuations does too, and, consequently, the heat capacity  $C_V$ . This is the microscopic origin of the abrupt change in the heat capacity during a continuous phase transition in the Ising model [50].

Similar to the canonical ensemble, it is possible to derive the probability distribution for

other ensembles from the variational form of the second law Eq. (5.22) and the Gibbs entropy formula Eq. (5.35). Likewise, the bridge to thermodynamics is given by an appropriate thermodynamic potential as illustrated in Eq. (5.44) for the canonical ensemble [50].

## 5.4 Theory of phase transitions

A phase is a region of a system with uniform properties. Equivalently, two states of a system are in the same phase if they can be transformed into each other without abrupt changes in any of their thermodynamic properties [19].

The transition from one phase to another is marked by sudden alterations in the thermodynamic properties of a substance. It is thus, a transition of a thermodynamic system from one phase into another. A phase transition occurs when there is a singularity in the free energy or one of its derivatives. What is often visible is a sharp change in the properties of a substance. This non-analytical behavior generally stems from the interaction of an extremely large number of particles in the system, and does not appear in systems that are too small.

During a phase transition, the heat capacity dramatically increases as the transition temperature is approached, because due to the cooperative nature of the transition it is increasingly easy for the heat supplied to drive the phase transition rather than to be stored as thermal motion.

A phase transition is classified by the type of its singularity. The first attempt at classifying phase transitions was the Ehrenfest classification scheme [88] which grouped phase transitions based on the degree of non-analytical behavior involved. Ehrenfest classified transitions with a discontinuity in the first derivative of the free energy as first order (for which the Clausius-Clapeyron equation holds [19]). In a first-order transition the free energy is a continuous function that has a kink at the transition point, so that the first (and higher) derivatives are discontinuous. Examples of first-order phase transitions are melting, freezing, and vaporization. In the same way, transitions where the first derivative is continuous, but the second derivative is discontinuous are called second-order. In a second-order transition, there is a kink in the first derivative of the free energy. Typical examples of second-order transition are the critical vaporization of a liquid or the phase transition of an Ising model. Third-order phase transitions are identified by discontinuity in the third derivative of the free energy, and so on. Later, it was shown that this was an inappropriate scheme of classification [19], because in these higher order phase transitions what identifies the transition is a divergence in one or more of the derivatives, rather than a discontinuity. In view of this, although first-order transitions continue to be classified as "first-order", higher order transitions are best termed "continuous", though they are often called critical transitions. Also, the term second-order transition still appears quite often, and synonymous with "continuous transition".

The number of phases which can coexist at equilibrium is given by the Gibbs phase rule [19]. However, the rule does not apply to continuous phase transitions, since there is no phase separation; both phases are critically identical.

The nature and general characteristics of first and continuous phase transition in three and

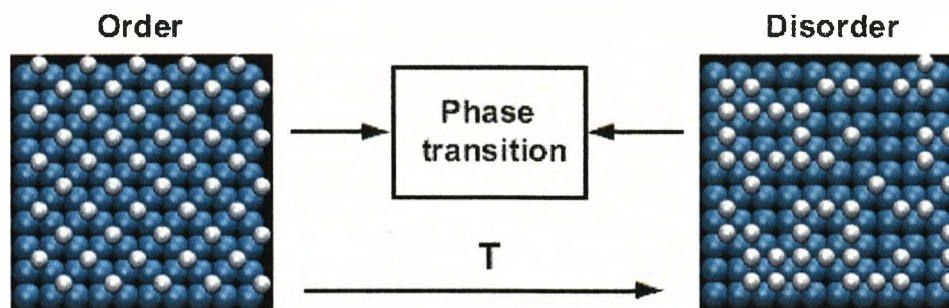


Figure 5.2: Order-disorder phase transition in a square lattice. The ordered phase at low temperature has  $c(2 \times 2)$  symmetry and corresponds to  $\Theta = 1/2$  ML

two dimensions are very similar, independent of the type of substances involved. This behavior is an example of universality, i.e. at a phase transition systems exhibit the same microscopic behavior, independent of their interatomic interactions [19].

### 5.4.1 Two-Dimensional phase transition

The molecular theory of 2D phase transition was discussed in Chapter 2. Here, we proceed to discuss general thermodynamic aspects related to order-disorder phase transitions in chemisorbed layers. 2D phase transitions, which are the subject of the present discussion, are illustrated in Fig. (5.2).

The experimental measurement of phase transitions of adsorbates on metal surfaces, e.g. through LEED intensity measurements [25], often takes place at constant temperature  $T$ , number of particles  $N$  and volume  $V$ . In such cases it is thus appropriate to use the canonical ensemble (table 2.1) in order to carry out Monte Carlo simulations of the system. The canonical ensemble imposes constraints on  $(N, V, T)$  and therefore mimics the experimental conditions.

The thermodynamic potential which determines the phase behavior of the system in the canonical ensemble is the free energy  $F$  - see Eq. (5.44). The free energy shows that there is a competing tendency between energy and entropy ( $F = U - TS$ ). The equilibrium state between the two is determined by the temperature. At low temperature, energy dominates and we see the emergence of ordered (weak-entropy) and low energy states. However, at high temperature, entropy prevails, and it is usually expressed in molecular disorder.

Microscopically, as the temperature increases, the particles (atoms or molecules) acquire enough thermal energy to populate higher energy microstates. As more microstates are energetically accessible to the particles, the entropy of the system increases. Thus, the microscopic entropy is a measure of the degree of spreading and sharing of thermal energy within the system.

It is also possible to carry out Monte Carlo simulations of chemisorbed systems in the grand canonical ensemble, i.e. by constraining  $(\mu, V, T)$  (table 2.1). If it is done properly, both ensembles should lead to the same results. In fact, simulation results in the grand canonical ensemble, in the form of adsorption isotherms  $(\mu, \Theta)$ , can be readily translated back to the canonical ensemble, in the form of phase diagrams  $(\Theta, T)$ [49].

Even though the results of simulations in different ensembles should be the same, there are sometimes computational advantages in choosing a particular ensemble. It turns out, for example, to be rather difficult in the grand canonical ensemble to tune to a coverage that deviates significantly from ideal coverage, i.e. those that correspond exactly to a determined symmetry. In a grand canonical Monte Carlo run, the system tends to jump between the competing ideal structures, and very long runs are necessary to achieve accurate statistics [89]. One can get rid of such problems by carrying out simulations in the canonical ensemble.

On the other hand, first order phase transitions are generally better simulated in the grand canonical ensemble. First-order phase transitions show up as two-phase coexistence regions. Each of these phases has a different coverage  $\Theta$ , and the phase transition from one phase to the other is best simulated at constant temperature by letting the number of particles in the system  $N$  vary according to the chemical potential  $\mu$  of the system [49].

In order to obtain a detailed picture of the phase transitions of a system, it may often be convenient to carry out simulations in both: the canonical ensemble and the grand canonical ensemble.



## 5.5 Metropolis/Monte Carlo approach

Different molecular simulation algorithms are required for different choices of the dependent and independent state variables. Common choices for the independent variables are EVN (the microcanonical ensemble), TVN (canonical ensemble), TPN (isothermal-isobaric ensemble) and  $TV\mu$  (grand canonical ensemble) (see Table 5.1). Other choices are possi-

Extensive variable	Conjugate field
Internal energy $E$	Temperature $T$
Volume $V$	Pressure $P$
Number of molecules $N$	Chemical potential $\mu$

Table 5.1: Physical quantities in statistical mechanics

ble, but note that there must always be at least one extensive variable in the set; otherwise there is nothing to specify the absolute size of the system, and the state is not well defined (violation of the Gibbs phase rule). The Monte Carlo simulation using the Metropolis algorithm is performed in the canonical ensemble (See Fig. 5.3), which means that the number of particles  $N$ , the volume  $V$  and the temperature  $T$  are constant. As the whole system is closed and stable, one can represent it in terms of diagrams. Diagrams take into account the physical parameters to perform the simulation, as well as the initial state to study. The conditions of calculation must be defined at the beginning of the simulation. The system admits some constants as it performs Monte Carlo simulation in the canonical ensemble. As stated above, the temperature and the volume remain constant during the calculation. This state needs to be defined in the first step of the simulation so to say the "choice of parameters and conditions". The number of Monte Carlo steps has also to be defined in the first step of the simulation. The second step is to construct the size of the cell and the initial configuration of the particles pre-adsorbed on the surface as it is known that Monte Carlo simulations do not provide any kinetic information on the system. This initial state comes from experiments enforced to study its stability, or is defined as a random configuration. Then a Monte Carlo cycle begins the simulation of the defined system. A loop of the Monte Carlo simulation contains displacements, or rotations of the particles, the Metropolis algorithm, and the possibility to save the new system if a time-step is accepted. The degree of freedom of the system and the accuracy of a simulated result depend directly on the number of Monte Carlo steps defined initially. An infinite number of Monte Carlo steps leads to optimum convergence of the system. As this is not feasible, the highest number of Monte Carlo steps has to be defined. In this case, the accuracy of the simulated results is related to the size of the cell.

The derivation of thermodynamic properties from the free energy (Section 5.3) is elegant and compact. However, the actual calculation of thermodynamic properties of (two-dimensional) systems is the Metropolis algorithm used in the simulations.

The algorithm has been discussed previously. Here, we proceed to discuss the way how thermodynamic properties are calculated from Metropolis Monte Carlo Simulations. The discussions are confined to the canonical ensemble and two dimensional phase transition in chemisorbed layers, i.e. of lattice-gas models.

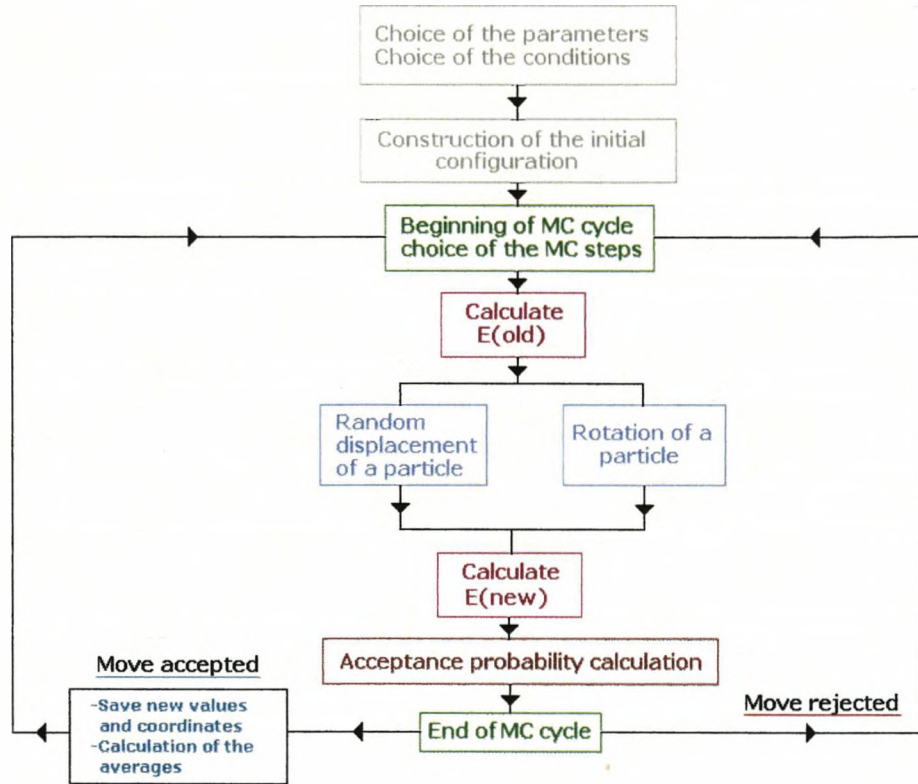


Figure 5.3: Monte carlo simulation in the canonical ensemble

Essentially, what the Metropolis algorithm does, is to generate an unnormalized canonical distribution of microstates

$$P(E, T) = \Omega(E)e^{E/k_B T}, \quad (5.49)$$

corresponding to the thermodynamic equilibrium of the system. Microstates belonging to this distribution are then sampled  $M$ -times and the thermodynamic properties of interest,  $Q_i$ , are measured. Since the microscopic thermodynamic properties fluctuate according to the canonical distribution, the macroscopic properties  $Q_M$  are obtained from the ensemble average

$$Q_M = \frac{1}{M} \sum_{i=1}^M Q_i, \quad (5.50)$$

whereby

$$Q = \lim_{M \rightarrow +\infty} Q_M. \quad (5.51)$$

If the Hamiltonian of the system is known (i.e. the energy function of every microstate), the internal energy of the system can be calculated from

$$U \equiv \langle E \rangle = \frac{1}{M} \sum_{i=1}^M E_i. \quad (5.52)$$

The heat capacity  $C_V$  can, in principle, be calculated from Eq. (5.47) However, given that the energy  $U$  from Eq. (5.52) is an estimate of the energy of the system and is only known

at discrete points (i.e. at the temperature  $T$  of the simulations), the derivative cannot be analytically determined and its numerical estimate is prone to errors. It turns out that it is much better to calculate  $C_V$  from the energy fluctuations of the system, i.e.

$$C_V = \frac{\langle E^2 \rangle - \langle E \rangle^2}{k_B T^2}, \quad (5.53)$$

where  $\langle E^2 \rangle$  is given by

$$\langle E^2 \rangle = \sum_{i=1}^M E_i^2. \quad (5.54)$$

After reaching thermal equilibrium and measuring the properties of interest, the system is brought to equilibrium at another temperature and equilibrium properties are calculated at the new equilibrium temperature. After repeating this for a range of temperatures, one obtains a discrete set of thermodynamic properties as functions of temperature.

The entropy  $S$  can be calculated by integrating the  $C_V$  data according to Eq. (5.27). However, as pointed out in Section 5.2, the numerical evaluation of the integral in Eq. (5.27) is not reliable, because the specific heat itself is not easy to determine accurately, particularly considering its divergence at a phase transition. A better way to calculate the entropy is from the  $U(T)$  data and the thermodynamic relation Eq. (5.28), i.e.

$$S(T) = S(T_0) + \int_{T_0}^T \frac{dU}{T}. \quad (5.55)$$

This expression allows a better estimate of the entropy, because the integral can be accurately estimated from Monte Carlo simulation data of  $U(T)$ .

In practice, the  $U(T)$  is spline-fitted and numerically integrated. This way of obtaining thermodynamic quantities from integrations is known as the thermodynamic integration method.

If one is only interested in how  $S$  varies with  $T$ , then it is not necessary to know the value of the integration constant  $S(T_0)$  and one can give it any arbitrary value. If the absolute value of  $S$  is needed, then one has to fix  $S(T_0)$  by choosing  $T_0$  to be some temperature at which the value of the entropy is known (e.g., for perfect crystals,  $S = 0$  at  $T = 0$  according to the third law of thermodynamics).

Once the entropy is known, the free energy of the energy of the system is readily calculated from

$$F = U - TS. \quad (5.56)$$

The thermodynamic properties discussed before, i.e.  $U$ ,  $C_V$ ,  $S$ ,  $F$  are general and can be used to identify phase transitions of any type in any system. The transition is triggered when a thermodynamic parameter, e.g. the temperature, is varied and leads to a sharp change in the thermodynamic properties of the substance.

Additionally, depending on the type of phase transition under study, additional parameters can be defined which identify a phase transition. Such parameters are known as order parameters and defined as normalized parameters that indicate the degree of a system. An order parameter of 0 indicates disorder; the absolute value in the ordered state is 1. Thus, for the familiar cases of a liquid-vapor phase transition or a ferromagnet, appropriate order

parameters are the normalized density difference between the liquid and the vapor and the homogeneous magnetization, respectively.

In the case of order-disorder phase transitions of adsorbates on metal surfaces, order parameters are defined according to the symmetry broken during the transitions. If the symmetry change affects the long-range order at the phase surface, LEED spot intensities may also be used to represent an order parameter.

In practice, numerical simulations of order transitions of either type will appear partly smeared due to finite size effects, i.e. from the simulations being carried out on finite lattice sizes.

The criterion to determine the critical temperature of the transition, i.e.  $T_C$ , is the inflection point in the  $\Psi(T)$  curve. It marks the transition from an ordered regime to a disordered regime. Thus,  $\Psi(T)$  data from Metropolis Monte Carlo simulations are conveniently fitted to a sigmoidal curve

$$\Psi(T) = \frac{(A_1 - A_2)}{(1 + e^{(T-T_C)/A_3})} + A_2, \quad (5.57)$$

where  $A_1$ ,  $A_2$ ,  $A_3$ , and  $T_C$  are fitting parameters.

Analogous to the energy and the heat capacity, the phase transition can also be determined from the fluctuations in the order parameter  $\psi$

$$\chi(T) = \frac{\langle \psi^2 \rangle - \langle \psi \rangle^2}{Nk_B T}. \quad (5.58)$$

The susceptibility  $\chi(T)$  peaks at the order-disorder transition studied,  $N$  is the total number of atoms.

The order parameter  $\psi(T)$  and its susceptibility  $\chi(T)$  can only measure phase transitions where the  $c(2 \times 2)$  symmetry is broken.

### 5.5.1 Limitations

Even though simple and powerful, the Metropolis algorithm becomes inefficient at phase transitions because of sampling problems. This is a known problem of Metropolis algorithm [48]. Here, we discuss these problems in the context of phase transitions in chemisorbed layers, i.e. lattice-gas models.

In a first order phase transition, the canonical distribution at the phase transition exhibits a double peak structure due to the two-phase coexistence typical at first-order phase transitions [58]. Conventional Metropolis Monte Carlo simulation is not efficient, since it takes an extremely long time to tunnel from one peak to the other in energy space. As a consequence, the algorithm easily gets trapped inside metastable states and exhibits hysteresis, i.e. the behavior of the system in the transition region depends on its thermal history. Due to this uneven energy landscape, very long simulation times are needed to properly sample the energy space of the system near a first order phase transition.

In second order transitions the Metropolis algorithm suffers from "critical slowing down". This problem arises from the fact that the long-range critical correlations of the adsorbates correspond to the occurrence of large clusters of correlated adsorbates. It takes a very long time until such a cluster disintegrates and finally disappears by many subsequent trials as dictated by the metropolis algorithm. As a consequence, the correlation time  $\tau$  of

the Metropolis algorithm is very large and very long simulation times are needed to obtain accurate estimates near the phase transition.

Additionally, the standard Metropolis algorithm suffers from inefficient sampling at low temperatures because the acceptance probabilities becomes quite small and virtually nothing happens for a long time.

There are a number of Monte Carlo algorithms which seek to overcome these difficulties. The continuous time or N-fold way to Monte Carlo algorithm [48,53] has an acceptance probability equal to 1 at every step. Other algorithms, like the Swendsen and Wang algorithm, or the Wolff algorithm [48,53], reduce the critical slowing down by conducting moves on whole correlated clusters. However, none of these algorithms seems suitable for every type of problem. All of the algorithms mentioned before are based on generating a canonical distribution of the type in Eq. (5.49). A Monte Carlo algorithm which avoids all of these problems of acceptance in energy space can be constructed by shifting the acceptance rule to entropy space.

## 5.6 Wang-Landau/Monte Carlo approach

In this approach, one first recognizes that the partition function can either be written as a sum over all states  $i$  or over all energies  $E$ , i.e.

$$Z = \sum_i e^{-E_i/k_B T} \equiv \sum_E \Omega(E) e^{-E/k_B T}, \quad (5.59)$$

where  $\Omega(E)$  is the configurational density of states (CDOS), i.e. the number of all possible states (or configurations) for a fixed energy level  $E$  of the system. Since  $\Omega(E)$  is independent of temperature  $T$ , it can be used to find all properties of the system at all temperatures. In fact, once  $\Omega(E)$  is known, the partition function  $Z$  follows automatically and from it all of the thermodynamic properties of the system.

Instead of generating a canonical distribution, Eq. (5.49), at a given temperature  $T$ , the Wang-Landau algorithm aims at estimating  $\Omega(E)$  directly via a random walk that produces a flat histogram in energy space [58-62]. The algorithm has been discussed in Section 2.4.4 Here, we discuss the way thermodynamic properties are calculated from the Wang-Landau Monte Carlo simulations.

From the density of states, the internal energy  $U$  can be calculated by taking the canonical average of the microscopic energy  $E$

$$U \equiv \langle E \rangle = \frac{\sum_E E \Omega(E) e^{-E/k_B T}}{\sum_E \Omega(E) e^{-E/k_B T}}. \quad (5.60)$$

The heat capacity can be determined from the fluctuations of the internal energy

$$C_V = \frac{\langle E^2 \rangle - \langle E \rangle^2}{k_B T^2}, \quad (5.61)$$

where  $\langle E^2 \rangle$  is given by

$$\langle E^2 \rangle = \frac{\sum_E E^2 \Omega(E) e^{-E/k_B T}}{\sum_E \Omega(E) e^{-E/k_B T}}. \quad (5.62)$$

The free energy can be calculated directly from the partition function

$$F = -k_B T \ln Z = -k_B T \ln \left( \sum_E \Omega(E) e^{-E_i/k_B T} \right), \quad (5.63)$$

and the entropy can then be easily computed from

$$S = \frac{U - F}{T}. \quad (5.64)$$

The nature of the phase transition (first order or continuous) can be conveniently determined by plotting the canonical distribution at the transition temperature  $T_C$

$$P(E, T_C) = \Omega(E) e^{-E_i/k_B T_C}. \quad (5.65)$$

A canonical distribution which exhibits a single peak indicates a continuous phase transition, where there is no phase coexistence. If the canonical distribution is double-peaked, it indicates a first-order phase transition. Every peak corresponds to a stable phase and the transition is characterized by phase coexistence. The latent heat for a temperature-driven first order phase transition can be estimated from the energy difference between the double peaks.

The acceptance rule of the Wang-Landau algorithm is proportional to the reciprocal of the CDOS. As a consequence, the algorithm performs a random walk in energy space and is not limited by the slow sampling of first-order transitions, metastable states or critical slowing down.

The Wang-Landau algorithm has not yet been as extensively employed and assessed as the Metropolis Monte Carlo algorithm. Some understanding of the convergence and limitations of the method have already been provided [65]. However, more work is needed to better determine under which circumstances the method offers substantial advantage over other approaches, and how the method can be further improved.

## 5.7 Monte Carlo simulations on a simple model

The use of discrete Fourier transforms leads to the calculation of the order parameter  $\Psi$ , while statistical mechanics and thermodynamics lead to the heat capacity parameter  $C_V$ . The physical meaning of these parameters can be demonstrated and interpreted using the Metropolis/Monte Carlo simulation on the simple model defined above. Several identical Monte Carlo simulations need to be performed for the same set at different temperatures to be able to discuss phase transitions.

The Monte carlo simulation set up is the following:

Calculation parameter	Value
Particle	$p$
Surface	$s$
Lattice parameter	$a$
Coverage $\Theta$	0.5 ML
Supercell	$10 \times 10$
part.-part. interaction energy	+0.1eV
Monte carlo steps	$10^8$
Start configuration	Random

Table 5.2: Monte Carlo/Metropolis set up for simple adsorbate/substrate ( $p/s$ ) model

### 5.7.1 Order parameter

The parameter needs to be estimated at the end of the simulation by calculating the degree of ordering of the final state. The initial configuration does not count in the calculation of the parameter. For perfect ordering (in this simple model case  $c(2 \times 2)$ ), we get  $\Psi = 1$ . Full disorder leads to  $\Psi = 0$ . The unstable state, called the critical phase, can be determined from the  $\Psi = f(T)$  curve. It is located exactly at the transition between the full ordered state and the full disordered state. Fig. (5.4) shows the order-disorder transition from the evolution of the order parameter  $\Psi$  in the temperature range from 500K to 2500K. At low temperature we observe that the Monte Carlo simulation finds the perfect ordering  $c(2 \times 2)$  corresponding to a coverage  $\Theta = 0.5\text{ML}$ . This is the logical ordering as the interaction between the particles is repulsive for the first nearest neighbour at a distance  $a$  (lattice parameter). The increase of temperature shows a stability in the ordering till 1100K. Then, the phase starts to disorder smoothly around 1200K, to decrease monotonically from this temperature to 1400K, where the order parameter  $\Psi = 0.05$ . The fully disordered state starts at 1500K where  $\Psi = 0.2$  and remains stable up to 2500K.  $\Psi$  decreases very slowly in this region

Note that the full disorder with  $\Psi = 0$  is very difficult to obtain on any structure. In practice a system is fully disordered when  $\Psi \approx 0.1$ . For more details about the critical phase a combination of the order parameter and the heat capacity parameter is a convenient measure. The next curve shows the evolution of the heat capacity in terms of temperature.

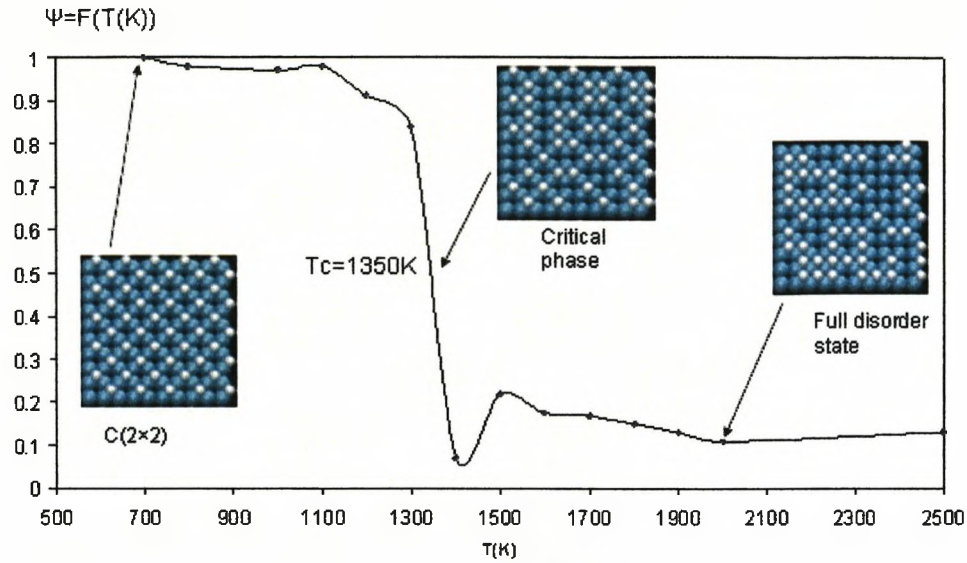


Figure 5.4: Curve  $\Psi = f(T)$

### 5.7.2 Heat capacity

During the Monte Carlo simulation one needs to collect the value of the total energy of the system to obtain the heat capacity at the end of the calculation. The total energy value of the system needs to be collected in two forms:

- $\langle E^2 \rangle$ : average of the squared total energies
- $\langle E \rangle^2$ : square of the averaged total energies

The heat capacity also depends on the temperature  $T$  of the system and the Boltzmann constant  $k_B$ . The value is given by:

$$C_V = \frac{\langle E^2 \rangle - \langle E \rangle^2}{k_B T}. \quad (5.66)$$

This parameter admits a maximum and two minima. The fully ordered state leads to a minimum in terms of the heat capacity. Another stable state is fully disorder and also leads to a minimum of the heat capacity. The maximum is reached at the critical phase of the system during heating. Fig. (5.5) shows the order-disorder transition in terms of the heat capacity  $C_V$  in the temperature range from 500K to 2500K. At low temperature, so for a  $\Psi = 1$ , we observe a minimum of  $C_V = f(T)$ . This corresponds to a small difference between  $\langle E^2 \rangle$  and  $\langle E \rangle^2$ .  $C_V$  increases monotonically to a maximum value of  $0.06 \text{ meV/K}$  at 1350K. From this point the heat capacity decreases with temperature. The peak in the curve corresponds to the critical phase. The critical phase is the most unstable state for a adsorbate/substate system. The normal workspace of a Monte Carlo simulation is therefore between 0K and the critical temperature at about 1300K.



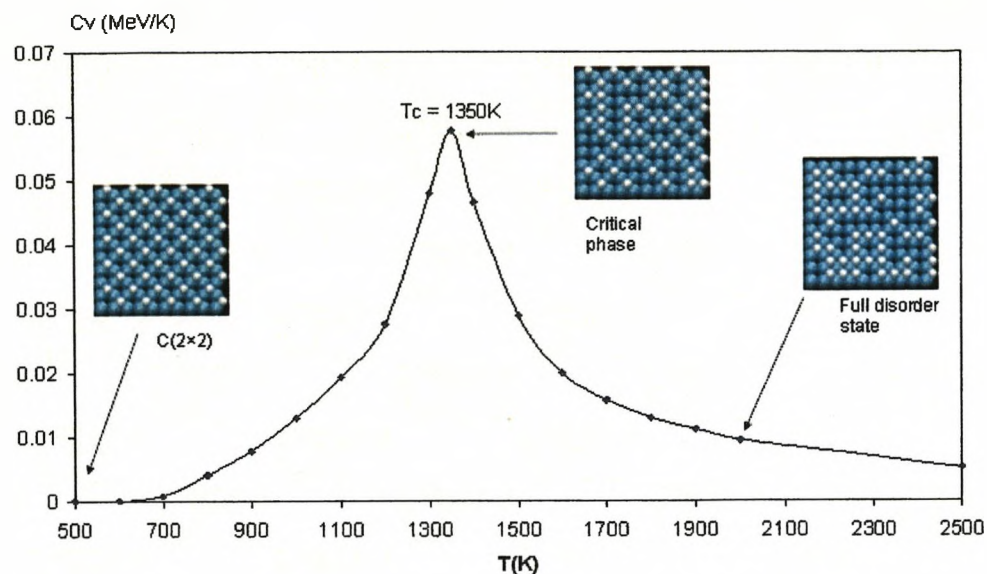


Figure 5.5: Curve  $C_V = f(T)$

## 5.8 Summary

This section pointed out the different methods to study any kind of adsorbate/substrate system and to adapt these methods to systems of very large molecules like bitartrate on copper(110). The parameters characterize the behavior of the molecules at surfaces. They can be used to predict stability and instability. The heat capacity parameter is implemented in the Metropolis/Monte Carlo code for the study of the tartaric acid on copper (110). The order parameter calculated using the unit cell of the ordering of the bitartrate on Copper at 400K is also implemented in the code. The combination between these two parameters gives specific determination of the order-disorder phase transition. Then the Lattice-Gas Hamiltonian is used to construct the different configurations of molecules onto the surface.

## Chapter 6

# Chiral Ordering Process in the Adsorption of Tartaric Acid Molecules on Cu(110)

Although chiral surfaces offer intriguing possibilities in a range of technological fields such as nonlinear optical materials, heterogeneous enantioselective catalysis and sensor devices, it is only recently that the manifestation of chirality in two dimensions has been captured with the advent of sophisticated surface science techniques[143-165]. A particularly successful way of endowing a nonchiral metal surface with chirality is via the adsorption of complex organic molecules. The presence of the organic functionality provides chiral selectivity for already reactive metal catalysts. There is a manifold of chiral expressions that can be realized via this approach from the creation of local chiral motifs to the supramolecular assembly of chiral organizations; they have been reviewed elsewhere[143,144]. Interestingly, it is found that chirality is not simply limited to systems in which chiral molecules are adsorbed at achiral surfaces[144-154] but can also be displayed in systems where no initial chirality is present, i.e., from the adsorption of achiral molecules at achiral surfaces[155-162]. Much of the work published on aspects of two-dimensional chirality deals with physisorbed or weakly adsorbed systems[155,161,162], and especially the subtle influence of stereochemical alterations on both the local and the organizational characteristics. For systems, where a strong molecule-metal interaction exists, a very rich adsorption phase space can often be found, where the nature of the adsorbate can change significantly with coverage and temperature. Thus, a deeper understanding of the factors that affect two-dimensional chirality requires a range of spectroscopic techniques that not only probe the nature of extended supramolecular assemblies but are also able to relate this information to the detailed nature of the local adsorption unit. A case in point is the behavior of the chiral molecule, (R,R)-tartaric acid (see Fig. 6.1), on the achiral Cu(110) surface[143-146,151], where chiral expression encompasses both, the creation of a variety of local chiral motifs and a range of supramolecular chiral assemblies, with the nature of the former intimately controlling the nature of the latter.

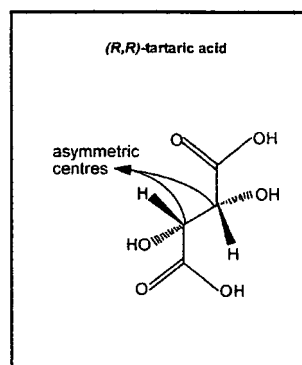


Figure 6.1: Diagram showing the (R,R)-tartaric acid molecule and the two asymmetric carbons

## 6.1 Experimental research

The systems bitartrate/Cu(110) and bisuccinate/Cu(110) have been extensively researched experimentally at the Surface Science Research Centre in the group of R. Raval. The experimental conditions and results shown below have been previously published [143-147] and this section displays the most important parts of this work. The tartaric acid molecule[180] has been deposited in Ultra High Vacuum (UHV) conditions and the imaging results have been carried out by Scanning Tunneling Microscopy (STM).

### 6.1.1 STM imaging conditions

The STM experiments have been carried in an Omicron Vacuumphysik variable temperature VT-STM chamber with facilities for STM, LEED, AES, and sample cleaning. All STM experiments were carried out with the sample at room temperature. The images were acquired in constant current mode.

In each chamber, the Cu(110) crystal was cleaned by cycles of Ar<sup>+</sup> ion sputtering, flashing, and annealing to 800K. The surface ordering and cleanliness were monitored by LEED and AES. (R,R) tartaric acid (99%) obtained from Sigma Aldrich used without further purification. The adsorbate sample was contained in a small resistively heated glass tube, separated from the main vacuum chamber by a gate valve and differentially pumped by a turbo molecular pump. Before sublimation, the sample was outgassed at 330-340K. The sample was then heated to 370K and exposed to the copper crystal. During sublimation the main chamber pressure was typically  $2 \times 10^{-9}$  mbar. The copper crystals were provided with a purity of 99.99% (4N), and alignment accuracies of 0.5 degree and 0.1 degree for the RAIRS and the STM experiments, respectively.

### 6.1.2 Adsorption of Tartaric acid on Copper(110)

The chiral influence of (R,R)-tartaric acid on Cu(110) can be discerned at two levels: firstly at the local level, where adsorption events conserve the chiral centers and thus give rise to point chirality and, secondly, at the organizational level where self-assembled struc-

tures form which are chiral in arrangement and thus destroy the mirror symmetry of the underlying surface[143-146,151]. Various phases are observed for (R,R)-tartaric acid on Cu(110)[146]. Here, we concentrate only on the low coverage phases, namely the  $c(4 \times 2)$  phase created at room temperature (300K) and the  $(1 \times 2, -9 \times 0)$  phase created at a higher temperature (400K). RAIRS data have shown that the former phase consists of the monotartrate unit that bonds to the surface via its single carboxylate functionality, while the latter phase consists of the doubly deprotonated bitartrate species bonded with both carboxylate groups to the metal surface with the  $C_2 - C_3$  bond parallel to the surface. Previous DFT[166] calculations confirm the general adsorption configuration for the bitartrate and, additionally, show that the adsorption site is across the long bridge site on the Cu(110) surface with each of the four carboxylate oxygens placed on top of a metal atom. Although the bitartrate unit is thermodynamically preferred at low coverage, the monotartrate unit forms upon initial adsorption at room temperature due to kinetic factors, and only upon heating to 400K is the bitartrate phase created. An activation barrier of roughly  $73 \text{ kJ mol}^{-1}$  is associated with this transformation[151]. In the 300-400K temperature range the tartaric acid is capable of existing in at least three different forms. The adsorption of tartaric acid at 300K never leads

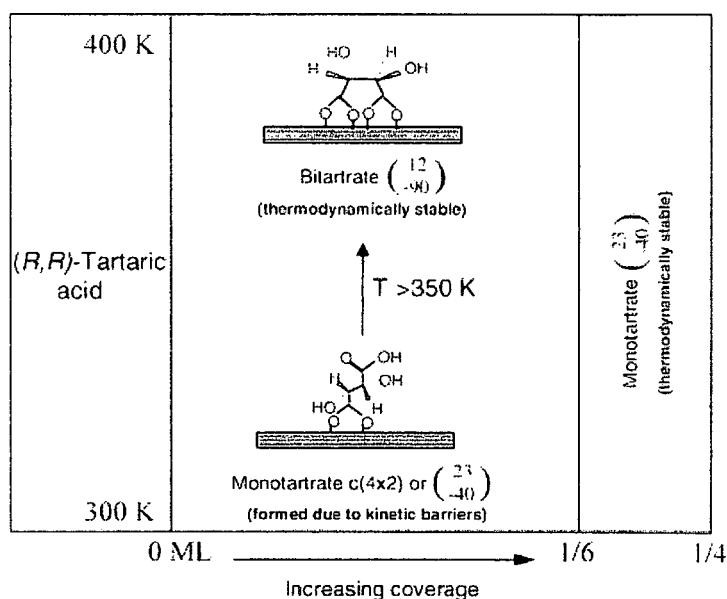


Figure 6.2: Schematic adsorption phase diagram showing the molecular nature and two-dimensional order adopted by tartaric acid on a Cu(110) surface as a function of coverage, temperature, and time[180].

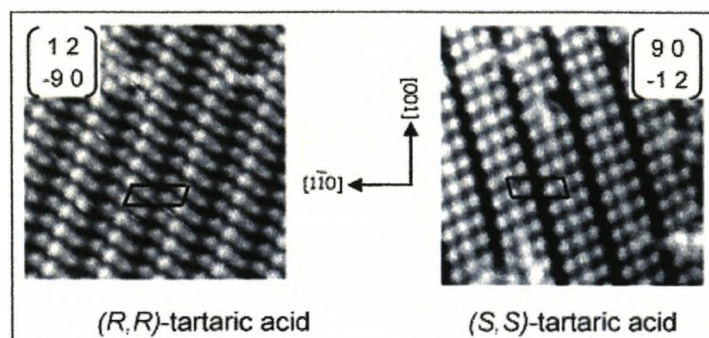
to the formation of the bitartrate species, and instead, islands of monotartrate molecules are always formed upon adsorption at 300K[146,151]. Conversion to the thermodynamically preferred bitartrate species then only occurs when temperature is raised to 400K. The experimentalists attribute this general behavior to an increased propensity for intermolecular interactions in the tartaric acid system due to additional COOH/OH hydrogen bonding between the acid groups and hydroxyl groups of adjacent monotartrate molecules[146]. This encourages the formation of high density islands, which locally reach the threshold cov-

erage that favors the monotartrate species. Under the flux conditions used in experiments, the rate of island growth exceeds the rate of the second deprotonation to form the bitartrate species, and so the monotartrate species is formed first. Fig. (6.2) illustrates this with a schematic adsorption phase diagram comparing the behavior of both succinic and tartaric acids in the temperature range 300 and 400K. The different LEED structures found for each characteristic bonding of the molecules are also indicated.

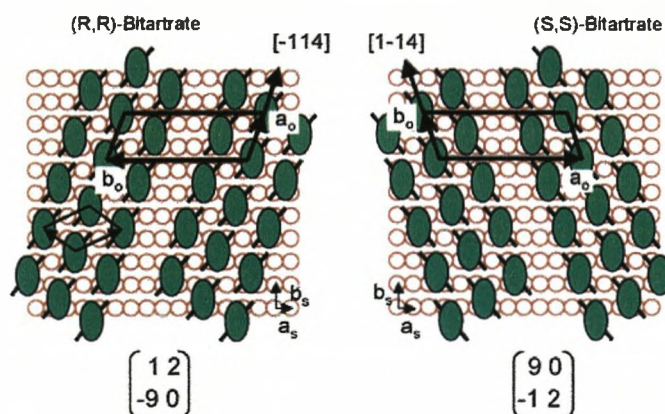
The  $c(4 \times 2)$  arrangement corresponds to a local coverage of 0.25ML and is identical to that occupied by the monotartrate phase[146]. It would, therefore, seem that the loss of the chiral centers does not materially affect either the density or the organizational packing of this phase. It also does not influence the chirality of the organization which remains as the achiral  $c(4 \times 2)$  for the chiral monotartrate[146]. Therefore, it would seem that the primary influence on packing and positional organization is determined by the general nature of the adsorption motif and its molecule-metal interactions; in this case, the monocarboxylate-copper interaction. The alteration at the chiral center causes a lesser, second order effect, namely in the detail of the supramolecular H-bonding. The imaged  $(1\ 2, -9\ 0)$  (R,R)-bitartrate and  $(9\ 0, -1\ 2)$  (S,S)-bitartrate phases have large repeat unit cells of  $23.04\text{\AA} \times 7.68\text{\AA}$  with  $\alpha = \pm 19.47^\circ$  degree, a coverage of 1/6ML and also display chains of "trimer" molecules that lie along nonsymmetry directions, thus endowing the system with a similar organizational chirality. So, again, it appears that the general nature of the bicarboxylate adsorption motif with its two COO-Cu bonding interactions is the primary factor determining the overall nature, ordering, density, and chirality of the superstructure adopted, regardless of whether the adsorbed molecule is chiral or achiral. In previous research and reports of these systems, it was assumed that the intermolecular hydrogen bonding between neighboring bitartrate molecules governed the nature of the superstructure, forcing growth along nonsymmetry directions. Subsequent DFT calculations showed that the neighboring molecules in the bitartrate structure are too far apart for intermolecular hydrogen bonding interactions to occur and only intramolecular H-bonds were present. These calculations suggested that supramolecular assembly was instead governed via through-space lateral interactions and/or through-metal lateral interactions. It was shown that H-bonding interactions of any kind are not the driving force for the chiral assembly. Equally, the through-space lateral interactions and/or through-metal interactions must be dominated by the metal-molecule interactions so that both systems produce a similar trimer chain structure. So, overall, the presence of the OH groups at the chiral centers does not affect the general type of supramolecular assembly. Instead, their influence is exerted more subtly within the finer detail of the self-assembly.

By looking at the unit cell within each chain it can be seen that the (R,R)-tartrate chain possesses a  $(3\ 1, -2\ 1)$  structure growing in the  $[-1\ 1\ 4]$  direction (Fig. (6.3b)) and the (S,S)-tartrate chain grows along the  $[1\ -1\ 4]$  direction. Here, it is possible that the intramolecular H-bonds between the OH groups at the chiral center and the bonding carboxylate groups affect the detail of the metal-molecule interaction by influencing the precise distortion of the adsorbate backbone and the bonding carboxylate groups.

Finally, one considers the relative stabilities of the bitartrate phases. Temperature programmed desorption (TPD) data from the bitartrate adlayer show explosive desorptions at around 440K (see Fig. (6.4)). Inspection of the thermal evolution products shows that no desorption of the molecular ion is observed, indicating that the data are not monitoring des-



(a) STM images of tartaric acid molecules on Cu(110)



(b) Adsorption models for (R,R) and (S,S) tartaric acids on Cu(110)

Figure 6.3: (a) Depiction of the  $(1\ 2, -9\ 0)$  and  $(9\ 0, -1\ 2)$  bitartrate phases formed after the adsorption of (R,R)-tartaric acid and (S,S)-tartaric acid, respectively, on Cu(110). STM images ( $108\text{\AA} \times 108\text{\AA}$ ) [ $V=-1.7\text{V}; I=1.18\text{nA}$ ] showing the (R,R)-tartaric acid  $(1\ 2, -9\ 0)$  phase and ( $108\text{\AA} \times 108\text{\AA}$ ) [ $V=-2.73\text{V}; I=1.02\text{nA}$ ] showing the (S,S)-tartaric acid  $(9\ 0, -1\ 2)$  phase (b) Adsorption model of the bitartrate phases on Cu(110). Structural models of the bitartrate phases of the two tartaric acid enantiomers on Cu(110): (S,S)-bitartrate  $(9\ 0, -1\ 2)$  and (R,R)-bitartrate  $(1\ 2, -9\ 0)$ . The  $(3\ 1, -2\ 1)$  unit cell is also shown for the (R,R)-bitartrate phase showing the packing within the chain[180]

orption of the whole adsorbate but rather the products of surface decomposition of adsorbed molecules. In other words, reaction limited desorption processes are observed, suggesting that the molecule-metal interaction is so strong that intramolecular bonds break prior to metal-molecule bonds, with the decomposition products,  $H_2$ ,  $CO_2$ , and  $CO$  released in a sharp peak. From the TPD information, this suggests that the presence of OH groups leads to a significant destabilization of the intramolecular bitartrate bonds. Although the TPD data in this case give no information of the relative strengths of the molecule-metal interactions, it does point to very different temperature stabilities that arise in surface phases from small changes to the molecular structure.

For the (R,R)-bitartrate system the major factors governing the creation of the chiral superstructure must be induced by the bicarboxylate-Cu interactions, to create a similar super-

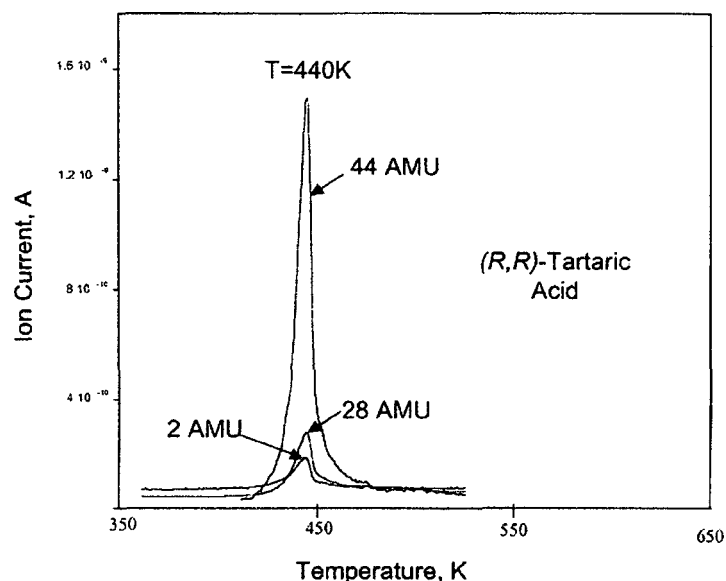


Figure 6.4: Thermal stability of the bicarboxylate phases is demonstrated by TPD data for the (R,R)-bitartrate (1 2,-9 0) phase created on Cu(110) at 400K[180]

structure. However, (R,R)-bitartrate yields a single domain of one-handedness only suggesting that the presence of the OH groups at the chiral centers crucially restricts the distortion/reconstruction to one-handedness only. One notes that DFT calculations on (R,R)-bitartrate on Ni(110)[147] show an energy difference of 6 kJ/mol between the two mirror image distorted/reconstructed adsorption motifs, sufficient to ensure that over 90% of the nucleation points at 300K would be of the lower energy form. The role of the OH groups as "chiral directors" of the supramolecular assembly is illustrated when adsorption of the (S,S)-bitartrate unit is examined, Fix. (6.3b). Here, the rigid adsorption structure of the bitartrate unit forces the OH groups to lie in a uniquely defined direction that is reflected in space compared to the (R,R)-bitartrate unit. As a result, the energy preference of the local adsorption unit is switched to the opposite distortion/reconstruction, and thus, chiral lateral interactions are switched in direction and the induction and propagation of the chiral assembly occurs in the mirror image construct, leading to a mirror chiral surface. Therefore, from this work, one may conclude that overall global or local chirality is determined principally at the nucleation stage. Finally for the (R,R)-bitartrate system, the OH groups force the molecular distortion/reconstruction to adopt a favored chirality, which then generates one favored chiral domain only, bestowing the system with global chirality at the macroscopic scale. For the (S,S)-enantiomer, the OH group alignment is reflectionally flipped, and the mirror distortion/reconstruction is created, generating the mirror chiral organization. The OH groups are, therefore, important as chiral propagators or directors and enable asymmetry to be promoted to chirality.

## 6.2 Theoretical Research

The collective behavior of atoms or molecules chemisorbed on a single-crystal substrate is characterized by their tendency to form distinct phases which possess well defined two-dimensional (2D) periodicity and order. This phenomenon is caused by the operation of interactions between the adsorbed particles. The stability of a surface phase depends on the temperature  $T$  and the coverage  $\Theta$  of the chemisorbed species. Phase transitions may occur depending on variations in  $(\Theta, T)$ -space for a specified system, which are conveniently described by means of the adsorbate phase diagram of the system.

The phase diagram of atoms and molecules adsorbed on surfaces is a central topic in surface science and enters directly into the discussion of many important processes at surfaces such as heterogeneous catalysis. Among others, this includes:

- At temperatures below critical, when ordered phases are formed in the adsorbed overlayer, the kinetics of different surface phenomena obviously cannot be described by simple equations that do not take into account the ordering.
- Information of phase diagrams enables evaluation of the scale of lateral interactions between adsorbed particles, which may strongly influence the kinetics of different processes even at temperature above the critical one.
- The problem of describing phase transitions provides examples and tests of theoretical models of 2D critical phenomena.

Much research has been carried out on phase transitions at surfaces (see e.g. [49],[167-171]). Experimentally, order-disorder phase transitions of chemisorbed species at surfaces can be quantitatively characterized by means of low-energy electron diffraction (LEED) measurements. Theoretically, two dimensional phase transitions are usually discussed in terms of the Ising model (Section 2.4.3). Up to now, the lateral interaction energies of the Ising model, have been usually determined empirically, e.g. by fitting to experimental LEED phase diagrams (see e.g. [49]). As explained in Section 2.4.4, the microscopically correct procedure is to derive the lateral interactions from first principles calculations. In this way, predictive calculations of surface phase diagrams for arbitrary systems are in principle possible. In order to properly understand the power and limitation of this approach, a description of the principles and approximations behind the theoretical description of phase transitions in chemisorbed layers is necessary.

The following exposition is complementary to the theoretical approach described in Chapter 2. The emphasis here is put on the application of the theory described in Chapter 2 to the phase transitions in chemisorbed layers.

### 6.2.1 Phase transitions in two dimensions

In the physical sciences, a phase is a set of states of a macroscopic physical system that have relatively uniform chemical composition and physical properties (i.e. density, crystal structure, index of refraction, and so forth). Those states correspond to local minima in the free energy space. The most familiar examples of phases are solids, liquids, and gases.



Less familiar phases include plasmas, Bose-Einstein condensates and fermionic condensates, strange matter, liquid crystals, superfluids and supersolids, and the paramagnetic and ferromagnetic phases of magnetic materials. In two dimensions, chemisorbed atoms or molecules constituting a phase possess well defined two-dimensional (2D) periodicity and order.

Although phases are conceptually simple, they are hard to define precisely. A good definition of a phase of a system is a region in the parameter space of the system's thermodynamic variables in which the free energy is analytical. Equivalently, two states of a system are in the same phase if they can be transformed into each other without abrupt changes in any of their thermodynamic properties.

All the thermodynamic properties of a phase (the entropy, heat capacity, magnetization, compressibility, and so forth) may be expressed in terms of the free energy and its derivatives. For example, the entropy is simply the first derivative of the free energy with respect to temperature. As long as the free energy remains analytic, all the thermodynamic properties will be well-behaved.

When a system goes from one phase to another, there will generally be a stage where the free energy is non-analytic. This is known as a phase transition. Familiar examples of phase transitions are melting (solid to liquid), freezing (liquid to solid), boiling (liquid to gas), and condensation (gas to liquid). Due to this non-analyticity, the free energies on either side of the transition are two different functions, so one or more thermodynamic properties will behave very differently after the transition. The property most commonly examined in this context is the heat capacity. During a transition, the heat capacity may become infinite, jump abruptly to a different value, or exhibit a "kink" or discontinuity in its derivative.

Phase transitions occur because all systems in thermodynamic equilibrium seek to minimize their free energy  $F$ :

$$F = U - TS, \quad (6.1)$$

In general terms, a phase transition is a change of order. Order is determined by the competition between energy  $U$  and entropy  $S$ , the former wanting to produce order, the latter wanting to destroy it. Thus the free energy  $F$  is the thermodynamic quantity which controls the state of order.

One phase will replace another at a given temperature  $T$  because different states (e.g., liquid/vapor, magnetic/non magnetic, cubic/tetragonal) partition their free energy between the internal energy  $U(T)$  and the entropy  $S(T)$  in different ways. It is useful to characterize competing phases and phase transitions in terms of a so-called order parameter. By construction, the order parameter has a non-zero value in one phase (usually the high symmetry state) and vanishes in the disordered (low symmetry state) phase. For the familiar cases of a liquid-vapor phase transition and a ferromagnet, appropriate order parameters are the density difference between the liquid and the vapor and the homogeneous magnetization, respectively.

In the case of chemisorbed atoms on surfaces, the order parameter can be formulated in terms of lateral periodicity so that the LEED diffraction spots of the surface may be used as order parameter. The phase transition can also be characterized by an abrupt sudden change in one or more of the thermodynamic properties (e.g. the heat capacity  $C_V$ ). Both

approaches, i.e. order parameter and thermodynamic properties, should lead to the same results, if the order parameter is chosen properly.

A common type of phase transition taking place in chemisorbed overlayers of atoms is an order-disorder phase transition. Here, a phase transition takes place between an ordered state, with well defined two dimensional periodicity and symmetry, and a disordered state. An example of such a transition is schematically depicted in Fig. (6.5). At low

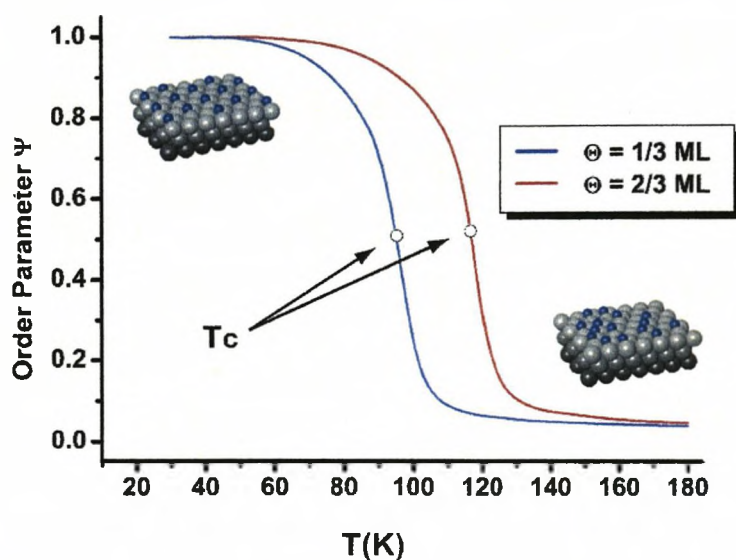


Figure 6.5: Schematic representation of LEED diffraction intensity measurements (order parameter  $\Psi(T)$ ) as a function of temperature for constant coverage  $\Theta$ . The inflection point of the  $\Psi(T)$  curve marks the critical temperature  $T_C$  of the phase transition. A higher coverage slightly changes the critical temperature of the system

temperatures, the adsorbed atoms (small dark spheres in Fig. 6.5) possess well defined two-dimensional periodicity and order. As the temperature increases, the disorder replaces the order and an order-disorder phase transition occurs. The degree of order of the atoms can e.g. be measured by means of LEED diffraction intensity measurements. Fig. 6.5 shows a typical result of LEED measurements, where the LEED diffraction intensity (order parameter  $\Psi$ , see chapter 2) is plotted against the temperature  $T$  for constant coverage  $\Theta$ . The inflection point of the  $\Psi$  versus  $T$  curve marks the critical temperature  $T_C$  at which the phase transition takes place. By carrying out similar measurements for different coverage  $\Theta$ , the order-disorder phase diagram of the system can be constructed from the  $(\Theta, T_C)$  data.

The behavior of the order parameter near the transition temperature  $T_C$  distinguishes two rather different transformation scenarios. A discontinuous change in the order parameter occurs at a first-order transition. In this case, two independent free energy curves simply cross one another. The system abruptly changes from one distinct equilibrium phase to a second distinct equilibrium phase. First order transitions exhibit the familiar phenomena of phase coexistence, nucleation and growth.

By contrast, two competing phases become indistinguishable at  $T_C$  for a continuous phase

transition (there is no phase coexistence, e.g. liquid-gas transition at the critical temperature). Here, the order parameter rises smoothly from zero as the temperature is lowered, although there are large fluctuations in its value around the average. One typically finds that the order parameter at a continuous transition varies as  $(T - T_C)^\beta$  for  $T$  very near to  $T_C$ . Moreover, the numerical value of the critical exponent  $\beta$  (and a few other related exponents [48]) only depends on a few physical properties, e.g. the symmetry of the system, the dimensionality of the order parameter (scalar, vector, etc.) and the dimensionality of space. This property is called universality and it implies that near the critical point  $T_C$  the properties of phases are largely independent of the underlying microscopic physics, so that the same types of phase arise in a wide variety of systems.

## 6.2.2 Molecular theory of 2D phase transitions

There are two basic approaches that can be followed in constructing a molecular theory of phase transitions. The simpler of these uses directly the thermodynamic condition defining that equilibrium state under a given set of constraints, for example, that the free energy must be a minimum for fixed temperature.

Suppose one considers two phases of the system I and II. It is, in principle, possible to calculate the free energy of phases I and II assuming that they are isolated from one another and also that they are stable over the whole temperature range of interest. A schematic plot is displayed in Fig. (6.6). As shown in Fig. (6.6), the phase I has a lower free energy for  $T < T_C$  whereas the phase II has lower free energy for  $T > T_C$ . The temperature  $T_C$  can then be identified as the critical temperature of the phase transition. The method described

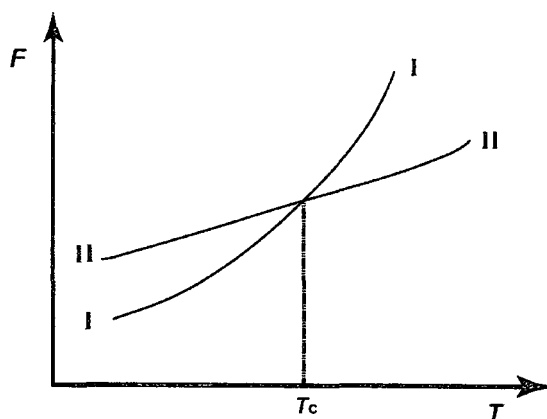


Figure 6.6: Schematic representation of the location of a transition point by comparing the free energies for each of the phases I and II. The critical temperature of the phase transition is denoted by  $T_C$

above is the standard thermodynamic approach[19]. It has been extended to the study of surface phase diagrams [172-174] by evaluating the appropriate thermodynamic functions by means of ab-initio calculations. This is a powerful connection, not only improving the link between thermodynamics and atomic-level computations, but also increasing the predictive range of ab-initio techniques. However, this approach has limitations. Most

prominently, the results are restricted to the number of considered configurations, i.e. only the stability of exactly those structures plugged in can be compared. The method is not able to predict stable structures outside the ones a priori considered.

The second approach is based on the postulation of statistical mechanical models (e.g. the lattice gas model, see Section 2.5.1) that retains only the skeleton of the real properties of the system. It is then hoped that, through this abstraction process, the most important physical interactions governing the phase behavior of the system are retained in the model; and, as a consequence, the effect of the configurational entropy on phase stability can be accurately evaluated. Such an approach has the potential of truly predictive power, in the sense that it is able, in principle, to predict new stable configurations different from the ones considered in the parametrization of the model.

When the parameters of the statistical mechanical model are derived from first-principles calculations, we are talking about first-principles statistical mechanics. In the context of this thesis, this approach is understood as the use of modern electronic structure methods to provide information used to parameterize interactions of statistical mechanical models.

### **First-principles statistical mechanics modelling of surface transitions**

The formal statistical mechanics procedure for calculating  $F$  in Eq. 6.2 is well defined. Quantum-mechanical calculations can be performed to compute the energy  $E(s)$  of different microscopic states  $s$  (configurations) of a system, which then must be summed up in the form of a partition function  $Z$

$$Z = \sum_s e^{-E(s)/k_B T}, \quad (6.2)$$

from which the free energy is derived as  $F = U - TS = -k_B T \ln(Z)$ , where  $k_B$  is Boltzmann's constant. The partition function  $Z$  corresponds to the canonical ensemble, which is appropriate for the usual experimental conditions of surface phase transition measurements (LEED experiments) at constant coverage  $\Theta$ .

The sum in Eq. 6.2 runs over all possible microscopic states  $s$  of the system. This is an astronomically large number which precludes the direct application of quantum mechanical calculations to obtain thermodynamic quantities from Eq. 6.2. Thus, physical insight into the problem has to be used in order to simplify the partition function  $Z$ .

Atoms are identical particles indistinguishable from each other. As such, their collective behavior is described by Bose-Einstein or statistics, i.e. the counting in Eq. 6.2 has to be done taking into account that the particles are indistinguishable. However, the potential energy of atoms adsorbed on metal surfaces usually has very localized minima corresponding to the adsorption site of the atoms. The chance of any two particles exchanging places by a tunneling motion is small. Thus, the effects arising from Bose-Einstein statistics are negligible; they only make themselves felt if the particles can exchange places. The same argument applies to the atoms in the metal substrate: the chance of the particles exchanging places is extremely small and so quantum statistics play no role. As a result, the atoms in the system can be treated as classical distinguishable particles. Additionally, a lattice corresponding to the minima in the potential energy surface can be used as coordinate system for the atoms. With these simplifications, the partition function  $Z$  for the substrate +

adsorbate system can be conveniently factored as follows[175]

$$Z = \sum_L \sum_{\sigma \in L} \sum_{v \in \sigma} \sum_{e \in v} e^{-E(L,\sigma,v,e)/k_B T}, \quad (6.3)$$

where

- $L$  is the so-called parent lattice. it is a set of sites where atoms can sit. In principle, the sum would be taken over any Bravais lattice augmented by any motif. Reconstructions of the substrate could be considered by this term. The only requirement is that the potential energy exhibits well defined minima.
- $\sigma$  is a configuration of the parent lattice. It specifies which type of atom rests on each site.
- $v$  denotes the displacement of each atom away from its local equilibrium position.
- $e$  is a particular electronic state when the nuclei are constrained to be in a state described by  $\sigma$  and  $v$ .
- $E(L, \sigma, v, e)$  is the energy of the system in a state characterized by  $L, \sigma, v$  and  $e$ .

Each summation in Eq. 6.3 defines an increasingly coarser level of hierarchy in the set of microscopic states. For instance, the sum over  $v$  includes all displacements such that the atoms remain close to the undistorted configuration  $\sigma$  on lattice  $L$ . While in principle exact, Eq. 6.3 represents a formidable task to be dealt with by first principles calculations.

### 6.2.3 Molecular vibrations

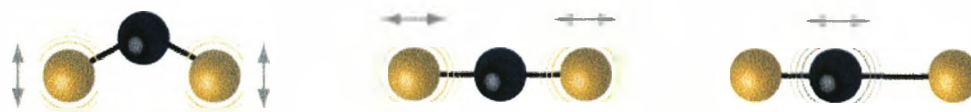


Figure 6.7: Vibrational modes of  $CS_2$ : Bending mode (left), symmetric stretching mode (middle), and antisymmetric stretching mode (right).

The discussion is based on Fig. 6.8, which shows a typical potential energy curve of a diatomic molecule. In regions close to  $R_e$  (at the minimum of the curve) the potential energy can be approximated by a parabola, so one can write

$$V = \frac{1}{2} k x^2 \quad x = R - R_e, \quad (6.4)$$

where  $k$  is the force constant of the bond. The steeper the walls of the potential (the stiffer the bond), the greater the force constant.

To see the connection between the shape of the molecular potential energy curve and the

value  $k$ , note that one can expand the potential energy around its minimum by using a Taylor expansion:

$$V(x) = V(0) + \left(\frac{dV}{dx}\right)_0 x + \frac{1}{2} \left(\frac{d^2V}{dx^2}\right)_0 x^2 + \dots \quad (6.5)$$

The term  $V(0)$  can be set arbitrarily to zero. The first derivative of  $V$  is 0 at the minimum. Therefore, the first surviving term is proportional to the square of the displacement. For small displacements one can ignore all the higher terms, and so write

$$V(x) \approx \frac{1}{2} \left(\frac{d^2V}{dx^2}\right)_0 x^2. \quad (6.6)$$

Therefore, the first approximation to a molecular potential energy curve is parabolic a potential, and one can identify the force constant as

$$k = \left(\frac{d^2V}{dx^2}\right)_0. \quad (6.7)$$

If the potential energy curve is sharply curved close to its minimum, then  $k$  will be large. Conversely, if the potential energy curve is wide and shallow, then  $k$  will be small.

The Schrödinger equation for the relative motion of two atoms of masses  $m_1$  and  $m_2$  with a parabolic potential energy is

$$-\frac{\hbar}{2m_{eff}} \frac{d^2\psi}{dx^2} + \frac{1}{2} kx^2\psi = E\psi, \quad (6.8)$$

where  $m_{eff}$  is the effective mass:

$$m_{eff} = \frac{m_1 m_2}{m_1 + m_2}. \quad (6.9)$$

From the Schrödinger equation for a particle of mass  $m_{eff}$  undergoing harmonic motion, one can write down the permitted vibrational energy levels:

$$E_v = \left(v + \frac{1}{2}\right)\hbar\omega \quad \omega = \left(\frac{k}{m_{eff}}\right), \quad (6.10)$$

and  $v = 0, 1, 2, \dots$ . The vibrational terms of a molecule, the energies of its vibrational states expressed in wavenumbers, are denoted  $G(v)$ , with  $E_v = hcG(v)$ , so

$$G(v) = \left(v + \frac{1}{2}\right)\tilde{\nu} \quad \tilde{\nu} = \frac{1}{2\pi c} \left(\frac{k}{m_{eff}}\right)^{1/2}. \quad (6.11)$$

It is important to note that the vibrational terms depend on the effective mass of the molecule, not directly on its total mass. This dependence is physically reasonable for, if atom 1 were as heavy as brick wall, then one would find  $m_{eff} \approx m_2$ , the mass of the lighter atom. The vibration would then be that of a light atom relative to that of a stationary wall (this is approximately the case in HI, for example, where the I atom barely moves and  $m_{eff} \approx m_H$ ). For a homonuclear diatomic molecule  $m_1 = m_2$ , and the effective mass is half the total mass:  $m_{eff} = \frac{1}{2}m$ .

## Anharmonicity

A parabola cannot be correct at all extensions because it does not allow a bond to dissociate. At high vibrational excitations the swing of the atoms (more precisely, the spread of the vibrational wavefunction) allows the molecule to explore regions of the potential energy curve where the parabolic approximation is poor and additional terms in the Taylor expansion of  $V$  Eq. 6.4 must be retained. The motion then becomes anharmonic, in the sense that the restoring force is no longer proportional to the displacement. Because the actual curve is less confining than a parabola, one can anticipate that the energy levels become less widely spaced at high excitations. One approach to the calculation of energy

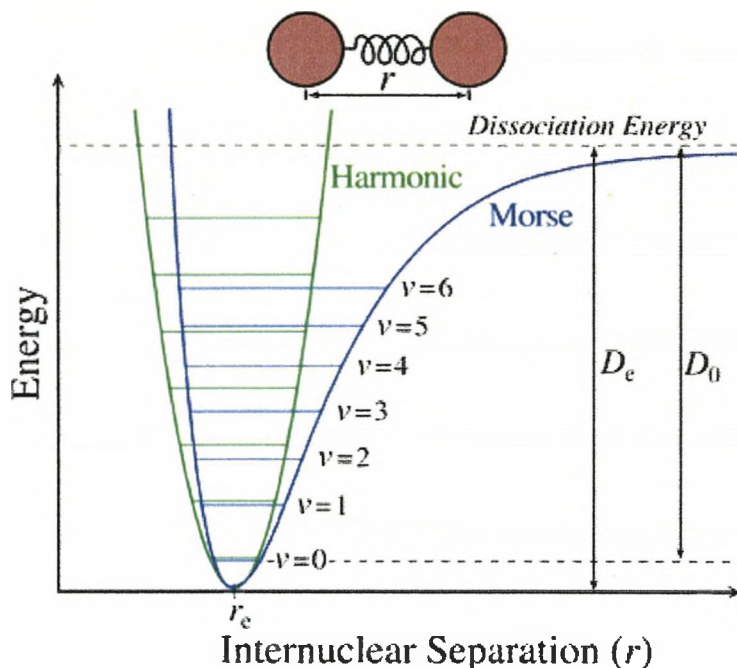


Figure 6.8: The Morse potential (blue) and harmonic oscillator potential (green). Unlike the energy levels of the harmonic oscillator potential, which are evenly spaced by  $\hbar\omega$ , the Morse potential level spacing decreases as the energy approaches the dissociation energy. The dissociation energy  $D_e$  is larger than the true energy required for dissociation  $D_0$  due to the zero point energy of the lowest ( $v = 0$ ) vibrational level.

levels in the presence of anharmonicity is to use a function that resembles the true potential energy more closely. The Morse potential energy is

$$V = hcD_e \left(1 - e^{-a(R-R_e)}\right)^2 \quad a = \left(\frac{m_{eff}\omega^2}{2hcD_e}\right)^{1/2}, \quad (6.12)$$

where  $D_e$  is the depth of the potential minimum (Fig. 6.8). Near the well minimum the variation  $V$  with displacement resembles a parabola (as can be checked by expanding the exponential as far as the first term) but, unlike a parabola, Eq. 6.12 allows for dissociation

at large displacements. The Schrodinger equation can be solved for the Morse potential and the permitted energy levels are

$$G(\nu) = \left(\nu + \frac{1}{2}\right)\tilde{\nu} - \left(\nu + \frac{1}{2}\right)^2 x_e \tilde{\nu} \quad x_e = \frac{a^2 \hbar}{2\mu\omega} = \frac{\tilde{\nu}}{4D_e}. \quad (6.13)$$

The parameter  $x_e$  is called the anharmonicity constant. The number of vibrational levels of a Morse oscillator is finite, and  $\nu = 0, 1, 2, \dots, \nu_{max}$ , (as shown in Fig. 6.8). The second term in the expression for  $G$  subtracts from the first with increasing effect as  $\nu$  increases, and hence gives rise to the convergence of the levels at high quantum numbers.

Although the Morse oscillator is quite useful theoretically, in practice the more general expression

$$G(\nu) = \left(\nu + \frac{1}{2}\right)\tilde{\nu} - \left(\nu + \frac{1}{2}\right)^2 x_e \tilde{\nu} + \left(\nu + \frac{1}{2}\right)^3 y_e \tilde{\nu} + \dots \quad (6.14)$$

where  $x_e, y_e, \dots$  are empirical constants characteristic of the molecule, is used to fit the experimental data and to find the dissociation energy of the molecule. When anharmonicities are present, the wavenumbers of transitions with  $\Delta\nu = +1$  are

$$\Delta G_{\nu+\frac{1}{2}} = \tilde{\nu} - 2(\nu + 1)x_e \tilde{\nu} + \dots \quad (6.15)$$

The latter equation shows that when  $x_e \neq 0$  the transitions move to lower wavenumbers as  $\nu$  increases.

Anharmonicity also accounts for the appearance of additional weak absorption lines corresponding to the transitions  $2 \leftarrow 0, 3 \leftarrow 0$ , etc., even though these first, second, ... overtones are forbidden by the selection rule  $\Delta\nu = \pm 1$ . The first overtone, for example, gives rise to an absorption at

$$G(\nu + 2) - G(\nu) = 2\tilde{\nu} - 2(2\nu + 3)x_e \tilde{\nu} + \dots \quad (6.16)$$

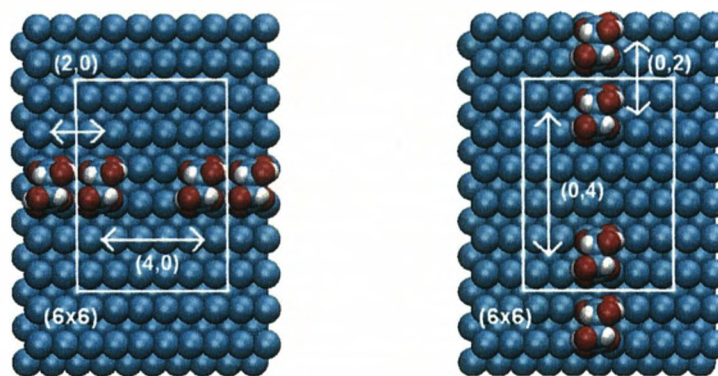
The reason for the appearance of overtones is that the selection rule is derived from the properties of harmonic oscillator wavefunctions, which are only approximately valid for an anharmonicity oscillator, all values of  $\Delta\nu$  are allowed, but transitions with  $\Delta\nu > 1$  are allowed only weakly if the anharmonicity is slight.



## 6.3 Application to the Bi-tartrate/Cu(110) system

### 6.3.1 Periodic Boundary conditions and limits of the system

The  $(6 \times 6)$  unit cell used to derive the lateral interaction is illustrated in Fig. 6.9. This cell was chosen because it is the largest cell which can be simulated in a reasonable amount of time. The k-mesh used for all calculations, for the defined  $(6 \times 6 \times 4)$  cell, was  $(3 \times 2 \times 1)$ . These two  $(6 \times 6)$  unit cells give evidence of the difficulty of the task, when it comes to



(a) Horizontal limit of  $(6 \times 6)$  cell (b) vertical limit of  $(6 \times 6)$  cell

Figure 6.9: These two figures show the limitations caused by the large size of the bitartrate radicals and the small size of the  $(6 \times 6)$  unit cell used to perform DFT calculations to obtain the configurations for the Lattice Gas Hamiltonian. The vectorial positions  $(4,0)$  and  $(0,4)$  are defined as negligible with respect to their complementary distances  $(2,0)$  and  $(0,2)$  respectively on the X and Y axes of the  $(6 \times 6)$  unit cell.

define the positions with respect to the periodic boundary conditions. In vectorial terms one can define the positions between a hollow site and its nearest neighbor hollow site position as  $(1,0)$  on the X axis and  $(0,1)$  on the Y axis. The molecular positions from  $(1,0)$  to  $(3,0)$  or from  $(0,1)$  to  $(0,3)$  respectively on the X and Y axes can be calculated assumed to interactions by linear equations. Two molecular positions at a distance  $(4,0)$  or  $(0,4)$  remain undetermined. This is caused by the periodic boundary conditions on the  $(6 \times 6)$  cell each of them amounts to the complementary distance with respect to the  $(6 \times 6)$  cell being smaller than the distance within the cell (see Fig. 6.9).

### 6.3.2 Lattice Gas Hamiltonian (LGH)

To evaluate the binding energies of the bitartrate radicals during the Metropolis/Monte Carlo simulations, we used a Lattice Gas Hamiltonian (LGH). Including nearest neighbor pair and triple interactions, together with the on-site interaction, the LGH is given by:

$$E^{latt} = \sum_i \sigma_i E_0 + \frac{1}{2} \sum_{i,j} V^{pair}(d_{ij}) \sigma_i \sigma_j + \frac{1}{3} \sum_{i,j,k} V^{trio}(d_{ij} d_{jk} d_{kl}) \sigma_i \sigma_k \sigma_l. \quad (6.17)$$

Here,  $i$  represents the on-site position of a given particle,  $j$  and  $k$  run over the corresponding neighboring sites. Thus, the Lattice Gas Hamiltonian contains three different parts,

including the on-site interaction for the bitartrate radicals on hollow sites, the second part for the nearest neighbour pair interactions, and the last part for the nearest neighbour triple interactions. In this section 27 configurations of bitartrate ions on Cu(110), which have been used for the fitting of the Lattice Gas Hamiltonian parameters, are presented with the corresponding LGH expansion and DFT binding energies.

The PW91 exchange correlation functional has been used and the computational set up is equivalent to the one discussed in the first Chapter. The numbering of the listed structures follows the one listed in the Appendix B. The 13 parameters of the LGH formula have been obtained by solving the resulting set of 27 linear equations using a least square fit. Due to the small size of the unit cell used to calculate the ground state energies of all the 27 configurations, the periodic boundary conditions play an active role for determining the Lattice Gas Hamiltonian. In the case of a  $6 \times 6$  cell the degree of freedom is very low due to the large size of the molecules. If we add the periodic boundary conditions to the Lattice Gas Hamiltonian for a specific configuration the result can be (See Fig. 6.10): The

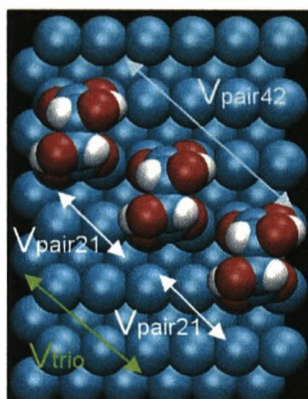


Figure 6.10: Schematic illustration of the interactions involved in a triple molecular configuration. In an infinite unit cell, considering that the on-site particle is located at the (0,0) position, one obtains:  $E^{latt} = E_0 + 2V_{(2,-1)}^{pair} + V_{(4,-2)}^{pair} + V_{(2,-1;4,-2)}^{trio}$

different configurations are represented by schematic illustrations where large red spheres represent the oxygen atoms, white spheres hydrogen atoms of the Bitartrate radicals. The Blue spheres represent the copper atoms of the (110) surface. Additionally in all figures the  $(6 \times 6)$  unit cell is shown. In this case the triple molecular interaction energy can be calculated considering an infinite unit cell and a small and finite  $(6 \times 6)$  unit cell. For the finite cell there are additional interactions to take in account in order to determine the triple interaction energy of this configuration:

$$E^{latt} = E_0 + 2V_{(2,-1)}^{pair} + V_{(4,-2)}^{pair} + V_{(-2,-2)}^{pair} + V_{(2,-1;4,-2)}^{trio} + 2V_{(2,-1;-2,-2)}^{trio}.$$

In the case chosen above, the trio interaction could not be determined by linear equations because of the unsolvable interactions due to the periodic boundary conditions, so this specific configuration was not a part of the Lattice Gas Hamiltonian used for the study of bitartrate on Copper(110).

### 6.3.3 LGH and Chirality for the R,R-Bitartrate/Cu110 system

The complete Lattice Gas Hamiltonian set has been also determined taking into account the chirality of the R,R-bitartrate ions. In fact in terms of distances one obtains different configurations due to chirality. Two bitartrate ions located at (2,1) and (2,-1) positions with respect to a third one located at the (0,0) position are not equivalent in term of configuration due to chirality. This has to be taken in account in the LGH to represent two different pair interactions. However, due to the small size of the unit cell ( $6 \times 6$ ), two mirror configurations can then be equivalent because of the periodic boundary conditions, especially the configurations located at (3,y) and (x,3) with x and y varying from 0 to 3 in terms of vectorial positions of the hollow sites as initially defined above. This is due to the equal distance between the two molecules within the ( $6 \times 6$ ) cell and their complementary positions due to periodic boundary positions. This particularity lowers the number of DFT calculations in order to obtain the full set of Lattice Gas Hamiltonian. Fig. (6.11) represents the full Lattice Gas Hamiltonian set performed by DFT calculations. With respect to the periodic boundary conditions some pair configurations are equivalent as discussed above. All trio interactions are different with respect to their mirror image configurations. Some pair and triple interactions are achiral, like the pair interactions situated onto the black line and at the bottom of the image. The horizontal and vertical lines are also geometrically achiral. The complete set of LGH has 27 set different configurations. Due low progress in DFT calculations (it takes 3 weeks for each configuration with k-points ( $3 \times 2 \times 1$ )) and the low degree of freedom on the ( $6 \times 6$ ), cell this work has taken effectively two years. The following subsection presents the lateral interaction values and the method to determine each of those has been explained and described in the Appendix A.

### 6.3.4 Lateral interactions

The process of deriving lateral interaction parameters from first principles calculations remains to date a delicate task. There are some general guidelines to obtain the lateral interaction parameters, but their actual application strongly depends on the system at hand. Even though the following discussion uses the expression "interaction parameters between bitartrate radicals", it must be clear that such parameters refer to the interaction of bitartrate ions through the Cu(110) substrate. Which configuration(s) should one use to derive the lateral interaction parameters? This is one of the crucial questions when applying the cluster expansion methodology (CE). There are different criteria aiding in selecting configurations for the expansion. The main criterium to select structures for the CE is the ground state search, i.e. selection of configurations based on the energetic ground state of the system as a function of the coverage. The application of such criteria for bitartrate/Cu(110) rapidly runs into trouble because configurations produced by the ground state search are frequently based on unit cells beyond the actual calculation possibilities of DFT of present.

There are 25 possible molecular positions on the  $6 \times 6$  unit cell of Copper (110). These positions can be represented by letters from A to Y and are going to describe in the following part the configurations used to construct the Lattice Gas Hamiltonian. The results of the calculations using this unit cell depicted in Fig. 6.12 are presented in table 6.1. All calculations in Table 6.1 correspond to bitartrate adsorbed only on the hollow sites of the

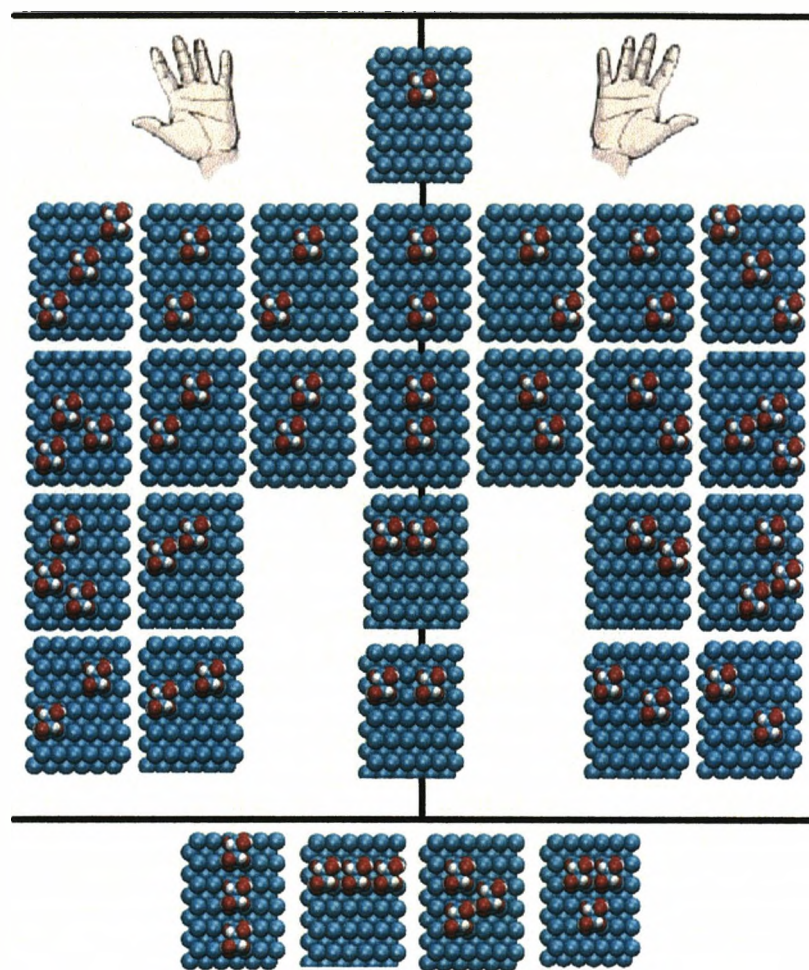


Figure 6.11: Complete Lattice Gas Hamiltonian of the bitartrate/Cu(110) system. By taking into account the chirality of the R,R-bitartrate radicals the LGH is divided in three parts: at the bottom of the image and situated onto the black line, achiral configurations; left hand, the chiral configurations, complete set; and right hand, its complete mirror set of chiral configurations. Some configurations in the chiral part (left hand) and its mirror part (right hand) are equivalent due to the periodic boundary conditions and the small size of the  $(6 \times 6)$  cell

Cu(110) cell. These sites of the  $(6 \times 6)$  cell have been identified with the letters explained above. Table 6.1 lists the position of the molecules on the unit cell (denoted by letters), the coverage  $\Theta$  and the adsorption energy. The table 6.1 gives the complete Lattice Gas Hamiltonian set of configurations and interactions. One can observe the on-site adsorbate/substrate interaction which is  $E_{ads} = -6.418 eV$  and corresponds to a chemisorption phenomenon described by the experimental research. The pair interactions do not exceed 35 meV in average, while the triple interactions average below 25 meV. One notes that the molecular interactions increase constantly with respect to the number of molecules on the copper surface. To determine the value of the interactions corresponding to the con-

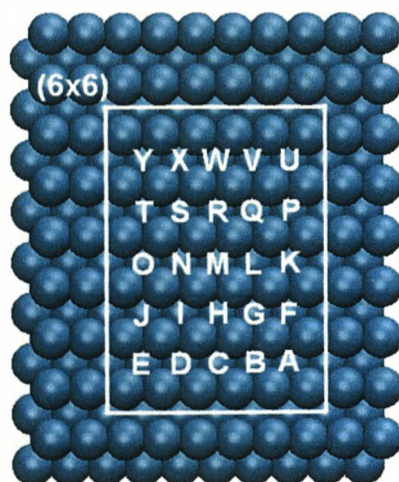


Figure 6.12: Schematic illustration of the Cu(110) surface showing the unit cell used to carry out DFT calculations for the bitartrate/Cu110 system. The white letters on the site are used to label each configuration in Table 6.1

figurations calculated by DFT, some linear equations are needed. This part of the work is described in the Appendix B.

Positions	$\Theta$ (ML)	Molecular interactions	$E_{ads}(meV)$
R	1/9	0	-6418.3
RA	2/9	2int(2,-3)	+24.6
RB	2/9	2int(1,-3)	+30.5
RC	2/9	2int(0,3)	+35.2
RD	2/9	2int(1,3)	+31.0
RE	2/9	2int(2,3)	+25.3
RF	2/9	int(2,-2)	+34.0
RG	2/9	int(1,-2)	+19.7
RH	2/9	int(0,2)	+11.2
RI	2/9	int(1,2)	+17.2
RJ	2/9	int(2,2)	+34.1
RK	2/9	int(2,-1)	+62.0
RO	2/9	int(2,1)	+77.1
RT	2/9	int(2,0)	+67.3
TQ	2/9	2int(3,0)	+14.4
TL	2/9	2int(3,-1)	+21.6
TG	2/9	2int(3,-2)	+28.8
TRP	1/3	2int(2,0) + 3 int(2,0;4,0)	-5.5
WMC	1/3	2int(0,2) + 3 int(0,2;0,4)	-1.0
ISL	1/3	2int(0,2) + 2int(2,1) + 2int(2,-1) + 3 int(2,1;0,2)	+6.0
HSQ	1/3	2int(2,0) + 2int(1,2) + 2int(1,-2) + 3 int(1,2;-1,2)	+7.6
EMU	1/3	2int(2,2) + 3int(2,2;4,4)	-25.7
AMY	1/3	2int(2,-2) + 3int(2,-2;4,-4)	-29.2
EGN	1/3	2int(1,2) + 2int(2,-1) + 4int(3,1) + 3int(1,2;3,1)	-68.1
AIL	1/3	2int(1,-2) + 2int(2,1) + 4int(3,-1) + 3int(2,1;3,-1)	-56.6
JCS	1/3	2int(2,-1) + 2int(1,2) + 4int(1,3) + 3int(1,2;2,-1)	-60.3
CFQ	1/3	2int(2,1) + 2int(1,-2) + 4int(1,3) + 3int(1,-2;2,1)	-35.7

Table 6.1: Adsorption and formation energies, i.e.  $E_{ads}$  (per site), for different configurations of Tartaric acid molecules on Cu(110) obtained from DFT calculations. The surface unit cell used in the calculations is depicted in Fig. 6.9. The k-mesh of Monkhorst-Pack special k-points for every surface unit cell is  $(3 \times 2 \times 1)$ . The letters denote the positions of the Bitartrates radicals in the unit cell according to the nomenclature described in Fig. 6.12. The number of interactions takes in account the periodic boundary conditions of the  $(6 \times 6)$  unit cell of the copper(110) surface

## 6.4 Metropolis/Monte Carlo Simulations (First part)

This section presents the First Metropolis/Monte Carlo tests carried out using the values of the DFT calculations of different configurations of bitartrates on copper forming the Lattice Gas Hamiltonian. The average total energy values of the different interactions has to decrease with respect to the number of molecules on the surface. For the pair interaction one finds an average of  $\langle E_{pair} \rangle = 33.5 meV$ . For the triple interactions between the bitartrate

molecules, the absolute average energy values decreases to  $\langle E_{trio} \rangle = 24.5meV$ . Taking in account these results are used the on-site, the pair, and the trio interactions to perform the Metropolis/Monte Carlo simulations.

The construction of the Lattice Gas Hamiltonian is added to the Metropolis/Monte Carlo program and the result is studied at a temperature  $T$  and coverage  $\Theta$ . The logical temperature used for the first simulations equals the temperature of formation of the complete chemisorption of the tartaric acid molecules on copper (110). The experimentalists find a temperature of  $T = 400K$  for which the bitartrate has four Cu-O bonds with the surface.

### 6.4.1 Simulations with complete Lattice Gas hamiltonian

The simulations performed on the R,R-bitartrate/Cu(110) system start by studying the coverage within a constant unit cell and temperature. The temperature of chemisorption of the bitartrate radicals on copper reported by the experimentalists,  $T = 400K$ , is used as reference. By choosing a large unit cell, successive Metropolis/Monte carlo simulations with different coverages will give information on the pattern, the unit cell and the growth direction. So far no statistical mechanics and order parameters are used. The set up of the Monte Carlo simulations can be summed up as follows: The particle used to perform

Calculation parameter	Value
Particle	R,R-Bitartrate
Surface	Cu(110)
Lattice parameter	$a_m = 2.5743\text{\AA}$ $a_n = 3.6400\text{\AA}$
Temperature $T$	400K
Coverage $\Theta$	from 0.20ML to 0.80ML
Supercell	(27 × 27)
Molecular interaction energies	27 Configurations (see previous section)
Monte carlo steps	$10^8$
Start configuration	Random

Table 6.2: Monte Carlo/Metropolis set up for R,R-bitartrate/Cu(110) system

the simulations is the R,R-bitartrate, the surface is Copper(110). The Lattice parameters  $a_m = 2.5743\text{\AA}$  and  $a_n = 3.6400\text{\AA}$  are state-of-the-art constants for the copper (110) surface. The temperature is  $T = 400K$  as discussed above. Each Monte Carlo simulation is started with a random configuration: for a specific coverage the program distributes particles on the copper surface until the coverage is reached. The size of the supercell is (27 × 27). The number of Monte Carlo steps is one hundred billion. The only varying parameter is the coverage  $\Theta$  which is chosen to be increasing from 0.20ML to 0.80ML at successive calculations, the results are in Fig. 6.13:

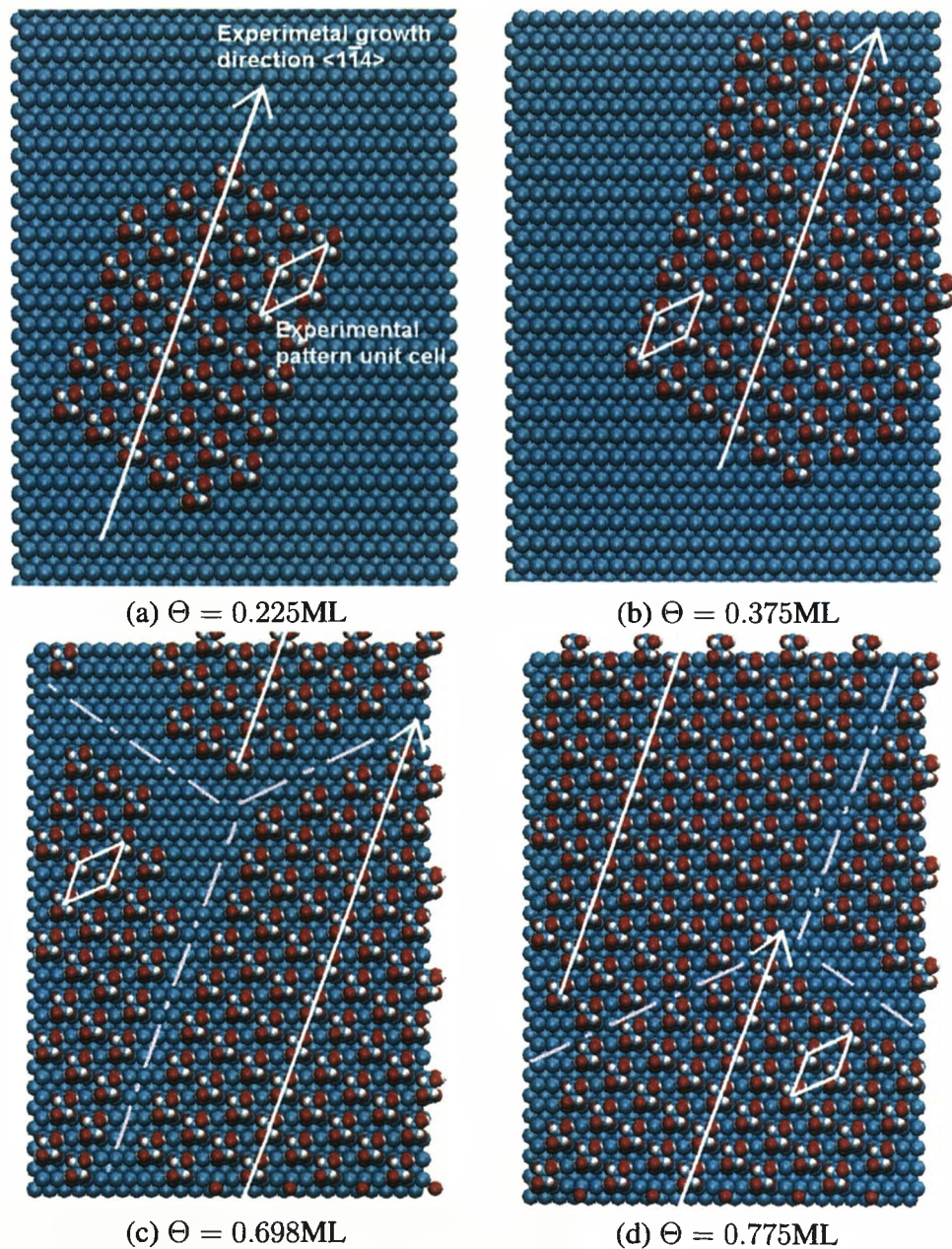


Figure 6.13: Figures showing the result of a Metropolis/Monte carlo simulation performed on the R,R-bitartrate/Cu(110) system in equivalent conditions with an increase of the coverage to study its evolution. (a) MC simulation at  $\Theta = 0.225\text{ML}$ . (b) MC simulation at  $\Theta = 0.375\text{ML}$ . (c) MC simulation at  $\Theta = 0.700\text{ML}$ . (d) MC simulation at  $\Theta = 0.775\text{ML}$ .



These four figures (a),(b),(c) and (d) show the evolution of an organization of R,R-bitartrate molecules on copper (110). At very low coverage  $\Theta = 0.225\text{ML}$  one observes that the interaction between the molecules is globally attractive. A group of molecules sticking together shows a specific and homogeneous ordering. This arrangement grows along a specific direction,  $\langle 1\bar{1}4 \rangle$ . This growth direction is in agreement with the previous experimental research on the subject. At a higher coverage  $\Theta = 0.375\text{ML}$ , we observe a similar pattern unit cell. This domain grows in the same direction as above but its width is not controlled and seems to rise with higher coverage. At very high coverage for  $\Theta = 0.700\text{ML}$  and  $\Theta = 0.775\text{ML}$  one observes clearly the growth direction with an ordering going beyond the cell limits and stopped by the limits of the system. However the width of the ordering still increases continuously with the coverage.

## 6.5 Metropolis/Monte Carlo Simulations (Second Part)

This section presents the final results of Metropolis/Monte Carlo simulations considering that a force breaks the global ordering of the phase demonstrated in the last section into trimers growing along the same direction  $\langle 1\bar{1}4 \rangle$ . The molecular pattern unit cell remains the same, but the empty space between the trimers changes the global unit cell of the system. An order parameter will be calculated taking into account the experimental global unit cell (with the empty space) and the heat capacity parameter can be determined in the simulations by measuring the total energy of the system. Thanks to these two parameters one can discuss the phase transition and the accuracy of the simulations above or below the critical temperature. The vibration of the OH bonds is found to be the origin of the repulsive interaction.

### 6.5.1 Order parameter

Considering the experimental ordering of bitartrate radicals and the growth direction, it is possible to study the phase transitions thanks to the order parameter and statistical mechanics parameters such as  $C_V$  (the heat capacity). The ordering pattern of the R,R-bitartrate on Cu(110) can be represented by a  $(2 \times 2)$  matrix  $(9 \ 0, 1 \ 2)$ . The growth direction of the system is  $\langle 1\bar{1}4 \rangle$ . The difficulty is to find a unit cell which matches the ordering of the phase, and which can be calculated by a discrete Fourier transform. This new unit cell takes into account the smallest number of molecules involved in the ordering and the empty space separating the molecules as they grow by trimers along the specific direction.

#### Discrete Fourier Transform

Surface phase transitions are usually discussed in terms of an order parameter  $\Psi$ [68,202,203]. It can be a scalar, a vector, or a tensor of higher rank. The order parameter is defined to be zero above  $T_c$ , if there is no long-range order, and it is usually normalized to unity for a fully ordered state.

To look at lateral periodicity on a surface, we can choose as an order parameter the low-energy-electron-diffraction (LEED) intensity of a suitable diffraction spot. Thus, as in LEED intensity measurements, the critical temperature of the order-disorder transition can be estimated from the inflection point of the curve  $\Psi$  versus  $T$  for constant  $\Theta$ .

The order parameter  $\Psi$  is supposed to measure the periodicity of a surface structure with a defined symmetry. As such, it can conveniently be evaluated by Fourier transform techniques. The information in real space is transformed into frequency space and patterns in real space can then be effectively detected. The configurations of particles in a lattice can be represented as matrices. Thus, a specific ordering behaviour can be measured by applying the discrete Fourier transform to the matrix representation and extracting the Fourier coefficients that correspond to the frequency of the ordered configuration. The discrete

Fourier transform of a vector  $\mathbf{x}$  is given by [84]

$$\begin{bmatrix} w_n^{1-1} & w_n^{1-2} & \dots & w_n^{1-n} \\ w_n^{2-1} & w_n^{2-2} & \dots & w_n^{2-n} \\ \vdots & \vdots & \ddots & \vdots \\ w_n^{n-1} & w_n^{n-2} & \dots & w_n^{n-n} \end{bmatrix} \begin{bmatrix} x_1 \\ x_2 \\ \vdots \\ x_n \end{bmatrix} = \begin{bmatrix} c_1 \\ c_2 \\ \vdots \\ c_n \end{bmatrix} \quad (6.18)$$

where  $w_n^{r-s} = e^{\frac{-2i\pi(r-1)(s-1)}{n}}$ , and  $\mathbf{c}$  is the vector of Fourier coefficients; Eq. 6.18 can be also expressed in matrix notation as

$$\mathbf{F}\mathbf{x} = \mathbf{c}, \quad (6.19)$$

where  $\mathbf{F}$  is called the Fourier matrix. Note that  $\mathbf{F}$  is a symmetrical matrix.

Since the ordering on a surface takes place in 2 dimensions, the discrete Fourier transform has to be applied in 2 dimension. Two dimensional Fourier transforms simply involve a number of one dimensional Fourier transforms. More precisely, a 2 dimensional transform of a matrix is achieved by first transforming each row, replacing each column with its transform. The 2 dimensional Fourier transform of a  $(n \times n)$  matrix  $A$  is given by

$$\mathbf{F}(\mathbf{F}\mathbf{A}^T)^T = \mathbf{c}, \quad (6.20)$$

where the transpose, T symbol, refers to the transpose without conjugate.

#### The specific Bitartrate/Cu110 ordering

The ordering corresponding to the chemisorption of Bitartrate on Cu(110) is illustrated in Fig. (6.4) only. One type of structure is possible for the R,R-bitartrate, its unit cell can be described by the following matrix notation, which defines the unit cell unambiguously:

$$M_{R,R} = \begin{pmatrix} 9 & 0 \\ 1 & 2 \end{pmatrix}. \quad (6.21)$$

This matrix notation will be (9 0,1 2) in the text.

The molecules form extended molecular rows along the  $\langle 1\bar{1}4 \rangle$  direction. These parallel rows are assembled in groups of three, each group separated from the next by an empty space (trough). These troughs can provide a chiral adsorption site on the otherwise achiral Cu(110) surface. The self-assemblies were originally attributed to the close proximity of the  $\alpha$ -hydroxy groups on the neighboring bitartrates, leading to intermolecular hydrogen bonding.

Usually, spin variables (+1 if the site is occupied, -1 if the site is empty) are used when calculating order parameters. However, the calculation with point variables (+1 if the site is occupied, 0 if the site is empty) is readily carried out. One only needs to convert every element of the point configuration (usually given as a matrix of +1 and 0) to a spin configuration through the relationship

$$S_i = 2n_i - 1, \quad (6.22)$$

and apply the order parameter formula developed for spin variables. The direct calculation with point variables is also possible. However, additional normalization factors should be

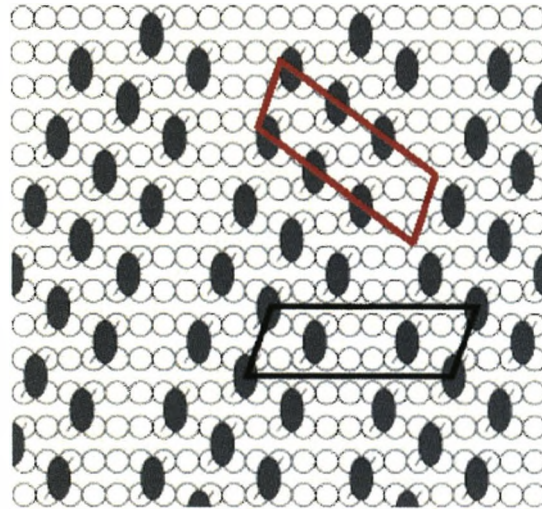


Figure 6.14: Ordered phase of Bitartrate on Cu(110). The black line sketches the (9 0,1 2) unit cell, this unit cell contains 3 molecules. The red line sketches the simplified unit cell used to mathematically calculate the order parameter taking in account the empty space. This simplified cell contains also 3 molecules

found in order to ensure that  $\Psi = 1$  for a fully ordered state.

The configuration can be described by decomposing the original simplified lattice into 4 sublattices made up of sites connected by next nearest neighbors bonds. Each sublattice now has a lattice constant related to the original lattice with respect to the geometry of the bitartrate ion. The total magnetization of every sublattice is given by

$$M_\alpha = \sum_{i \in \alpha} s_i \quad \alpha = A, B, C, D.$$

The order parameter can be written in terms of the magnetization  $M_\alpha$ . In order to do so, one has to express the (9 0,1 2) ordering in terms of  $M_\alpha$ . This is accomplished by writing the simplified unit cell (red line in Fig. 6.14) in matrix notation. Note that one can transform the simplified unit cell configuration into a linear lattice by rotation. The corresponding

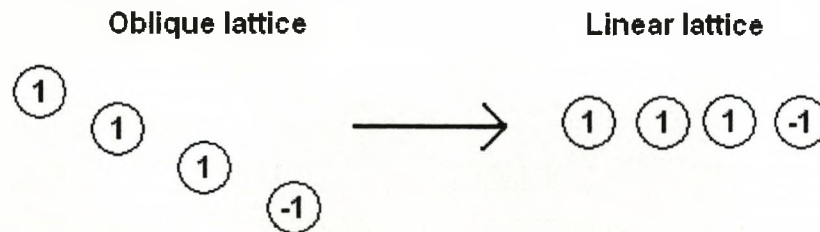


Figure 6.15: the (9 0,1 2) unit cell simplified in an oblique lattice and its linear equivalent representation

configurations for the (9 0,1 2) simplified unit cell are obtained by exchanging 1 and -1.

Thus one can set up a general matrix for this configuration in terms of the magnetizations  $M_\alpha$  according to the sublattices:

$$M = \frac{1}{4} \begin{bmatrix} M_A & M_B & M_C & M_D \end{bmatrix}. \quad (6.23)$$

The particular case of the adsorption of bitartrate on Cu(110) is that none of the unit cells one can choose in any of the directions along the rectangular surface is reversible in terms of spin. One can thus transform the previous matrix into a new matrix which contains the same information for the same dimensions. If we simplify the parameters of the matrix as  $M_A = M_C = M_D = 1$  and  $M_B \neq M_A$  one obtains the following result:

$$M = \frac{1}{4} \begin{bmatrix} M_A & M_A & M_A & M_B \end{bmatrix}. \quad (6.24)$$

The next step is to Fourier transform the  $(4 \times 1)$  matrix  $M$ . For that purpose one needs the  $(4 \times 4)$  Fourier matrix. From the definition in Eq. (6.18) we obtain:

$$F_4 = \begin{bmatrix} 1 & 1 & 1 & 1 \\ 1 & -i & -1 & i \\ 1 & -1 & 1 & -1 \\ 1 & i & -1 & -i \end{bmatrix}. \quad (6.25)$$

By applying Eq. (6.24) to Eq. (6.25) we get to a final result of the discrete Fourier transform

$$c = \begin{bmatrix} 3M_A + M_B & 0 & 0 & 0 \end{bmatrix}. \quad (6.26)$$

From this Fourier transform it is possible to derive the order parameter for the  $(9\ 0,1\ 2)$  configuration. The matrix component  $3M_A + M_B$  for the specific case where  $M_A = M_C = M_D = 1$  and  $M_B \neq M_A$  which represents the frequency of the  $(9\ 0,1\ 2)$  configuration. It is degenerate and its algebraic expression can be used as an order parameter

$$\Psi' = 3M_A + M_B. \quad (6.27)$$

The expression in Eq. (6.27) can be conveniently normalized to 1 by finding its maximum value. Since  $\Psi'$  measures the frequency of the  $(9\ 0,1\ 2)$  configuration, its value must be maximum when the surface exhibits such a configuration. If this is the case, then assuming that  $M_B = -M_A$  one can simplify  $\Psi'$  to

$$\|\Psi'\| = 2M_A, \quad (6.28)$$

$\|\Psi'\|$  is the factor by which Eq. (6.27) should be divided in order to normalize  $\Psi'$  to 1.  $\|\Psi'\|$  can be conveniently expressed in terms of the number of particles  $n$ , as the number of lattice sites is difficult to obtain due to the geometry of the oblique unit cell contained in a square or rectangular supercell for the Monte Carlo simulations. For the assumed  $(9\ 0,1\ 2)$  configurations  $M_A = n$  as for this specific case all the particles are contained in the  $M_A$  sublattices which equals 1 and then for this case  $M_B = -1$ , Thus:

$$\Psi = \frac{1}{2n}(3M_A + M_B). \quad (6.29)$$

The computational implementation of the order parameter given by Eq. (6.29) is straightforward. We only need to count each particle of the surface used in the simulation and calculate its order parameter by verifying that its environment matches the discrete Fourier transform. For disordered states  $\Psi = 0$  and for ordered states with  $(9\ 0,1\ 2)$  symmetry  $\Psi = 1$ . By cooling down the system near the critical temperature  $T_C$ , the order parameters  $\Psi$  rapidly increase from values near zero (disorder) to one (order). The inflection point of the curve corresponds to the order-disorder transition temperature for a given  $\Theta$  (coverage). The order parameter's accuracy can be verified, for that purpose, thermodynamic methods (e.g. heat capacity measurements) are necessary.

## 6.5.2 Vibration of the OH bonds of the R,R-bitartrate

The upper OH bond of the R,R-bitartrate has been studied in order to discover its effect on the ordering on copper(110) from 300K to 500K. We have selected the configurations for which the OH bonds of two different bitartrate are at the closest distance, in the clusters formed as a result of the Metropolis/Monte Carlo simulations performed above, to determine if they affect the cluster growth along the  $\langle 1\bar{1}4 \rangle$  direction.

Fig. 6.16 shows a hydrogen atom linked to a oxygen on the upper part of a Bitartrate ion. This hydrogen can, due to vibration, move by translation or rotation or both around its oxygen and produce free energy. Our aim in this section is to calculate within a wide range of temperatures the vibrational energy caused by the OH bond and the effect on a cluster of Bitartrate radicals if this vibrational energy is added to several molecules in a line. This vibrational energy of the OH bond of each bitartrate radical can be written as  $E_{\nu-OH}$ . One bitartrate ion has two OH bond on its upper carbon atoms, but only one of those is interacting with the next bitartrate ion at the shortest distance between the OH bonds of the two bitartrate considered. The vibrational energy between two molecules counts as one interaction; if three molecules are involved we get two vibrational interactions and so forth. The calculations of vibrational energies lead to a curve shown in Fig. 6.17. This curve represents the vibrational free energy  $F$ , well known from the following equation:

$$F = ZPE - TDS. \quad (6.30)$$

From this equation, the  $DS$  part represents the vibrational entropy taken for the vibrational partition function.  $ZPE$  is the zero point energy of the harmonic oscillator. This is also the reason why the vibrational energy does not equal zero at  $T = 0K$  because the  $ZPE$  value still remains. Fig. 6.17 shows two curves: the red curve represents the addition of two vibrational energy components of two isolated molecules, and the green curve represent the vibrational energy of two molecules interacting with each other within the configuration described in Fig. 6.18.

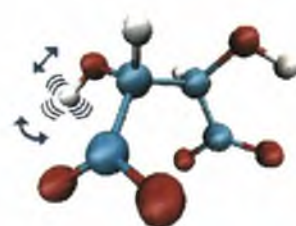


Figure 6.16: Bitartrate ion with the vibrational effect localized at the hydrogen atom of one of its two OH bonds. Two vibrational effects are involved between the oxygen and the hydrogen of an OH bond: the translation and the rotation.

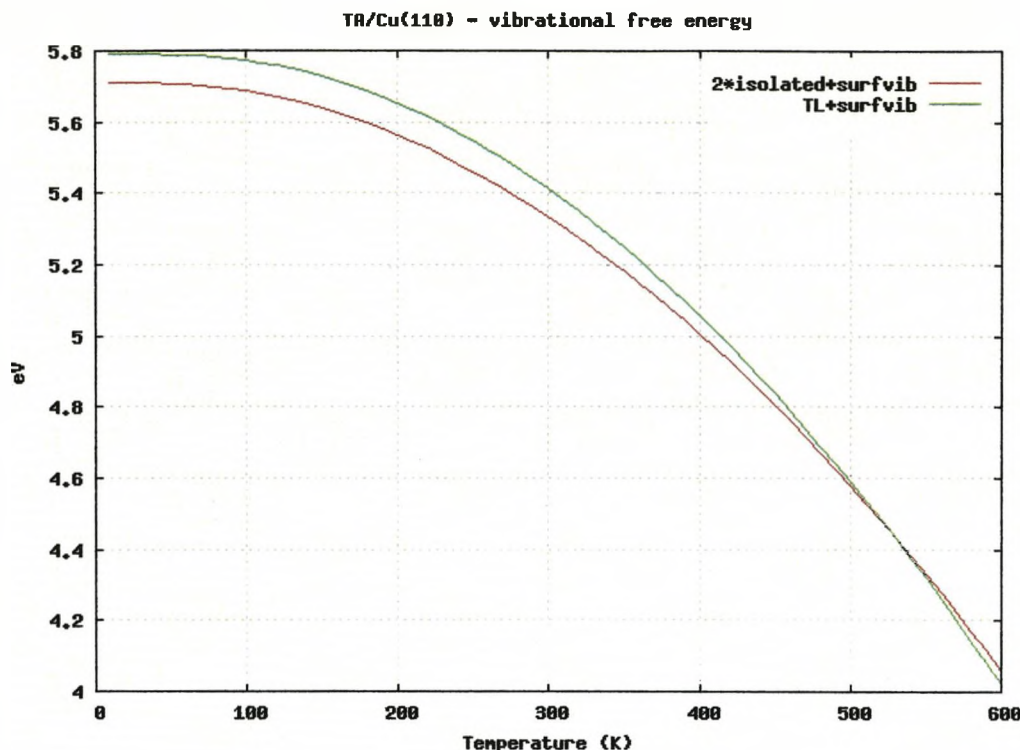


Figure 6.17: Result of the vibrational energy calculated for two Bitartrate ions on Copper (110). The red curve represents the addition of two vibrational energy components of two isolated molecules. The green curve represents the vibrational energy of two molecules interacting with each other within the configuration described in Fig. 6.18.

It is important to note that two interacting molecules (green curve on Fig. 6.17) have ZPE components larger than two isolated molecules (red curve on Fig. 6.17) because upon interactions three translations and three rotations (of one OH bond of a bitartrate) turn into low energy vibrational modes (with their corresponding ZPE). As the temperature increases, the excited levels of these extra modes for the two interacting molecules get populated more and more and this causes  $DS$  to increase more rapidly for interacting bitartrate than for two isolated bitartrate radicals. This is one of the causes of the crossing of the two interacting particles curve (in green on Fig. 6.17) with the curve for non interacting (in red on Fig. 6.17) at higher temperature. The other cause is the small shifts in energy for the modes of two interacting Bitartrate radicals upon interaction, which affect the curvature of  $T * DS$  for two interacting bitartrates.

If we add the vibrational interaction to the Lattice Gas Hamiltonian, we have to select each parameter of the LGH, for two or three particles interactions, where the specific configuration described in Fig. 6.18 is involved. Then the addition of the vibrational component will be added to a specific new parameter containing three or four molecules successively configured as the two molecules described in

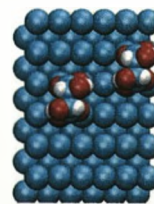


Figure 6.18: Configuration, within the ordering, creating the vibrational interaction energy of the OH groups of two Bitartrate ions

Fig. 6.18. The second set of Metropolis/Monte Carlo simulations will show how and where the cluster breaks, and if the growth direction  $\langle 1\bar{1}4 \rangle$  and the thermodynamic properties are conserved. Then the comparison between the statistical mechanics, represented by the specific heat, and the order parameter will give the evidence of the accuracy of the new vibrational parameters.

### 6.5.3 Implementing the OH bond vibration in the LGH

Two components of the Lattice Gas Hamiltonian are affected by the addition of the vibrational energy of the OH groups of tartaric acid. A new and independent parameter is added to the complete LGH set. This parameter contains the vibrational interaction energy of four bitartrates together in a line. The vibrational energy of the OH bond  $E_{\nu-OH}$  at a given temperature  $T$  influences the ordering pattern of the Bitartrate/Cu(110) system simulated by Metropolis/Monte Carlo methods. Fig. 6.19 displays the pair, trio and quattro interactions that are affected by the vibrational interaction energy. The pair and the trio

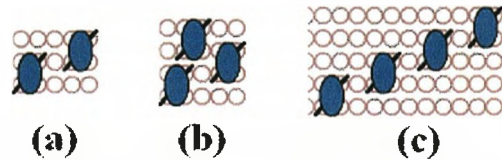


Figure 6.19: The pair, trio and quattro interactions containing the OH bond vibrational energy. (a) and (b) configurations are part of the Lattice Gas Hamiltonian and influence the molecular ordering, (c) is the independent vibrational parameter influencing the macroscopic ordering.

configuration in Fig. 6.19 are already part of the Lattice Gas Hamiltonian. They both contain one vibrational interaction of the OH bond  $E_{\nu-OH}$ . This vibrational component increases the value of the pair interaction energy, and then decreases the value of the trio interaction energy. They are calculated respectively by  $int_{(pair)} = int_{(pair-DFT)} + E_{\nu-OH}$  and  $int_{(trio)} = int_{(trio-DFT)} - 3/4E_{\nu-OH}$ . The quattro interaction energy is calculated by  $int_{(quattro)} = 0 + 3E_{\nu-OH}$  as it contains the three times the vibrational interaction energy of the OH bond.



### 6.5.4 Bitartrate/Cu(110) thermodynamic properties

The thermodynamic properties of bitartrate/Cu(110) at  $\Theta = 0.5\text{ML}$  and  $\Theta = 0.3\text{ML}$  calculated from Metropolis/Monte Carlo simulations are shown in Fig. 6.20. We choose different systems to perform these Monte Carlo simulations. The simulation at  $\Theta = 0.5\text{ML}$  was performed in a  $40 \times 26$  cell with an accuracy of 50 million Monte Carlo steps. The simulation at  $\Theta = 0.3\text{ML}$  was performed in a  $60 \times 40$  cell with 20 million Monte Carlo steps.

The specific heat  $C_V(T)$  and the order parameter  $\Psi(T)$  show an abrupt change at the critical temperature of the phase transition,  $T_C$ . Furthermore, all estimates of the critical temperature at  $\Theta = 0.5\text{ML}$  lead approximately to the same value, i.e.  $T_C = 2600\text{K}$  for both the order parameter and the specific heat. At  $\Theta = 0.3\text{ML}$  the estimates shows the same accuracy and lead to a critical temperature of  $T_C = 1850\text{K}$  for the order parameter and the heat capacity. These results cannot be confirmed by the experiments as the critical temperature  $T_C$  is beyond the physical stability of the bitartrate and the tartaric acid molecule (around  $500\text{K}$ ).

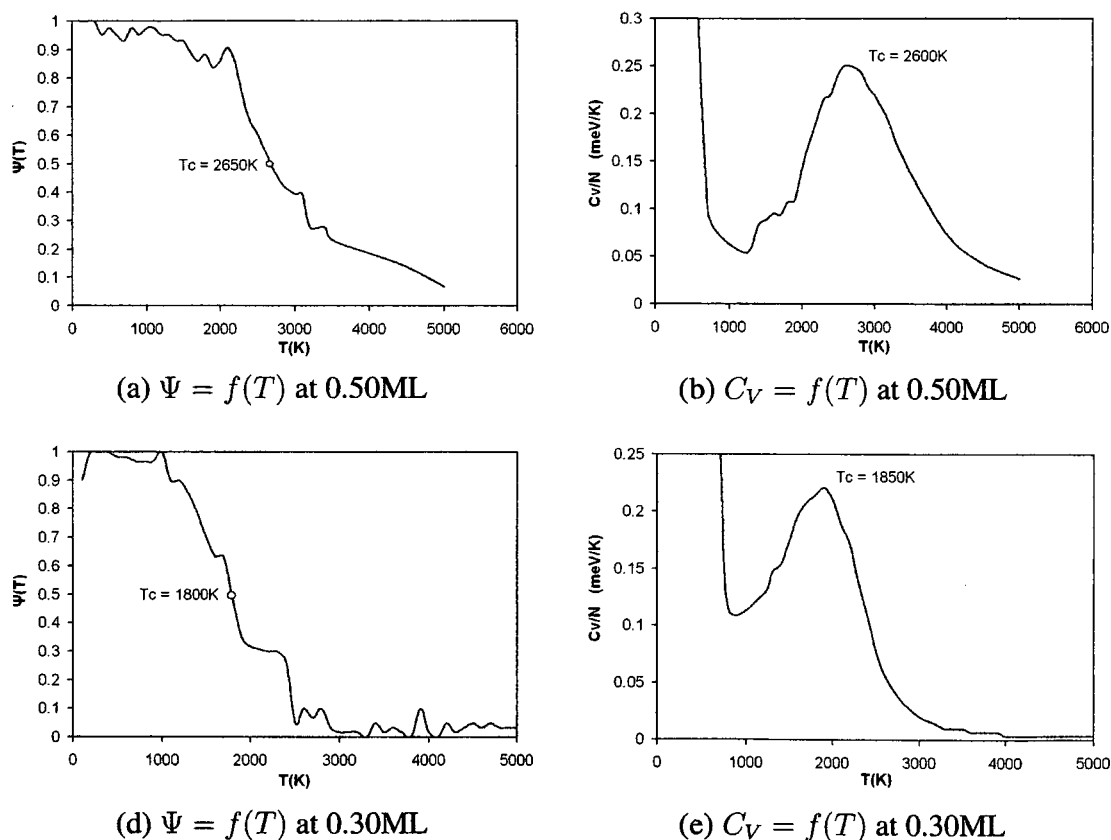


Figure 6.20: Thermodynamic properties of the Bitartrate/Cu(110) system for  $\Theta = 0.5\text{ML}$  and  $\Theta = 0.3\text{ML}$  calculated from Metropolis/Monte Carlo simulations.  $N$  represents the number of molecules. (a-b) Order parameter and heat capacity for  $\Theta = 0.5\text{ML}$ . (c-d) Order parameter and heat capacity for  $\Theta = 0.3\text{ML}$ .

We performed the Metropolis Monte Carlo simulations with a better accuracy by increasing the size of the cell and the number of Monte Carlo steps in order to determine a more precise critical temperature  $T_C$  and sharpened phase transition. We trace the evolution of the order parameter  $\Psi$  with respect to the temperature  $T$  at two different coverage values  $\Theta = 0.3\text{ML}$  and  $\Theta = 0.5\text{ML}$ . Both simulations were performed under the same condition using a  $90 \times 90$  cell and an accuracy of 100 million Monte Carlo steps. We observe that the critical temperature increases with the coverage. This result is in agreement with the schematic representation of LEED diffraction intensity measurements in Fig. (6.5) (order parameter  $\Psi(T)$ ) as a function of temperature for constant coverage  $\Theta$ . The inflection point of the  $\Psi(T)$  curve marked the critical temperature  $T_C$  of the phase transition at different temperature with respect to different coverage values as the curves in Fig. 6.21 shows.

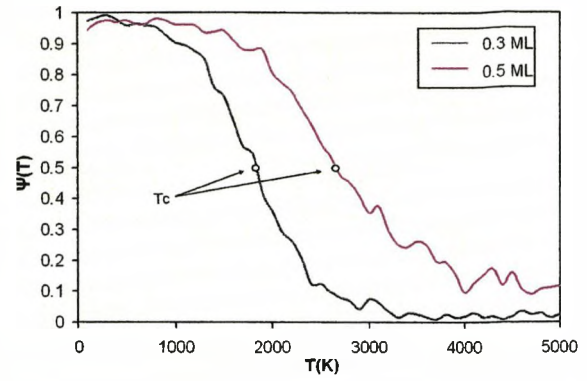


Figure 6.21: Estimate of Phase transition and critical temperature  $T_C$  at  $\Theta = 0.5\text{ML}$  and  $\Theta = 0.3\text{ML}$  for bitartrate/Cu(110) system in agreement with the schematic representation of LEED diffraction intensity measurements as a function of temperature  $T$  for constant coverage  $\Theta$ .

Snapshots of the order-disorder phase transition configurations of bitartrate/Cu(110) at  $\Theta = 1/2\text{ML}$  are shown in Fig. 6.22. At 400K, trimers are growing in lines along the  $\langle 1\bar{1}4 \rangle$  direction separated by large gaps. These lines stop because of the periodic boundary conditions and discontinuity due to the asymmetrical geometry of the ordering. At the critical temperature  $T_c = 2600\text{K}$ , the size of the ordering pattern is shortened mixed to a complete disorganized feature of bitartrate radicals, so that arbitrarily organized and disorganized clusters are formed. The above described critical slowing down of the Metropolis

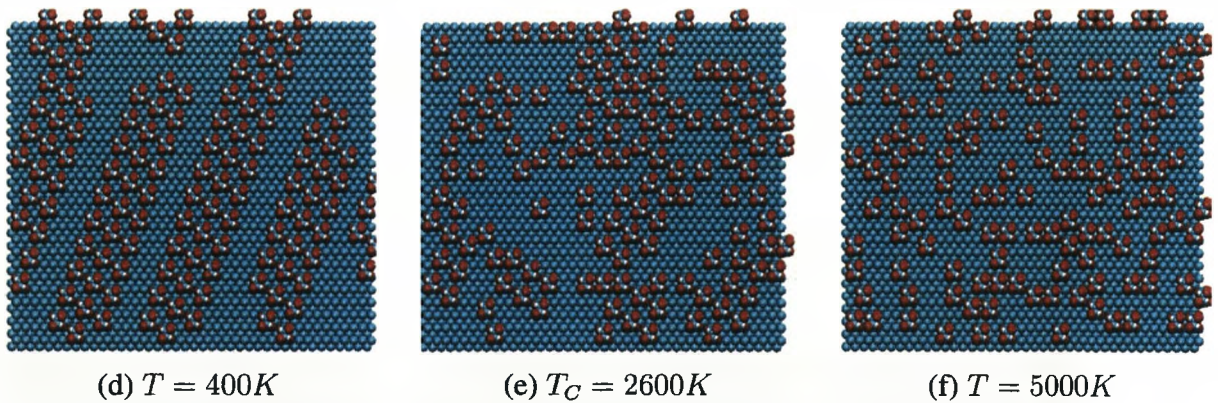


Figure 6.22: Snapshots, in a  $40 \times 26$  cell, of the order-disorder phase transition configurations of Bitartrate/Cu(110) at  $\Theta = 1/2\text{ML}$ . The critical temperature of the transitions is  $T_c = 2600\text{K}$ .

algorithm has to do with small clusters which are formed at  $T_c$ . It is quite difficult for the algorithm to move one of these large organized domains, because it has to be done molecule by molecule. Each move has a high probability of being rejected because the lateral interactions stabilize all atoms that are part of the cluster. Other approaches called cluster algorithms like Wolff and Swendsen-Wang algorithms try to avoid this problem by sampling entire cluster of particles[48].

At 5000K the full disordered state is reached, the organized clusters are no longer found. Therefore the order parameter  $\Psi$  rarely equals 0 due to small randomly organized trimers that can still be found.

### 6.5.5 Diagrams of phase and ordering limits

We performed Metropolis/Monte carlo simulations at constant temperature  $T$  and vibration of the OH bond  $E_{v-OH} = 50\text{meV}$ , at the temperature of formation of Bitartrate trimers reported by the experimentalists, on the bitartrate/Cu(110) system, i.e.  $T = 400\text{K}$ . Starting from the minimum coverage to the maximum  $\Theta = 0.76\text{ML}$  we observe the evolution of the phase by the order parameter  $\Psi(T)$  with respect to the coverage  $\Theta$ . These simulations are performed to find an agreement of the coverage limits of the bitartrate ordering pattern on copper (110) at 400K. The system used to perform this kind of calculation is a  $40 \times 26$  cell and an accuracy of 50 million Monte Carlo steps. The curve in Fig. 6.23 displays the  $\Psi = f(\Theta)$  curve at 400K and the some snapshots taken at different coverages see (Fig. 6.24): Fig. 6.23 shows the evolution of the order parameter with respect to the coverage in

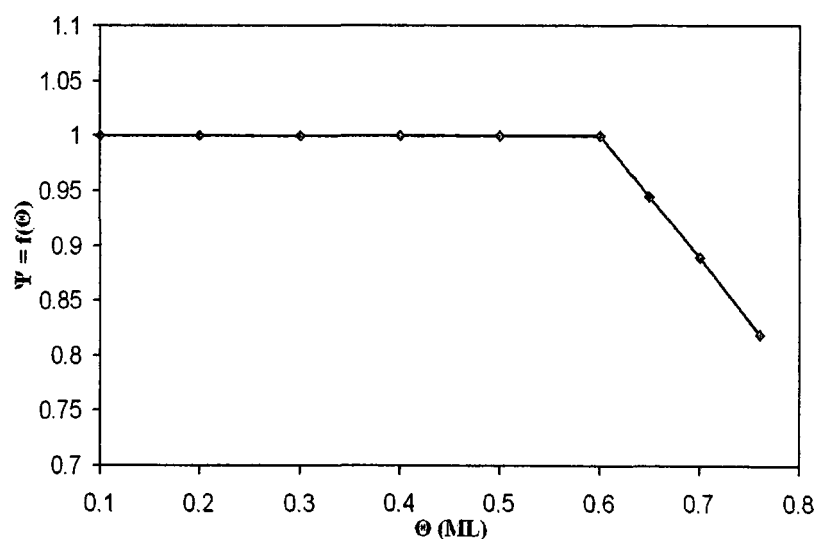


Figure 6.23:  $\Psi = f(\Theta)$  at 400K and constant vibrational energy of the OH bond  $E_{v-OH} = 50\text{meV}$  for the Bitartrate/Cu(110) system from the Metropolis/Monte Carlo simulations in a  $40 \times 26$  cell and 50 million Monte Carlo steps.

the curve  $\Psi = f(\Theta)$ . The order parameter remains constant at  $\Psi = 1$  until  $\Theta = 0.60\text{ML}$  and falls dramatically above this coverage to a value of  $\Psi = 0.82\text{ML}$  at  $\Theta = 0.76\text{ML}$ . This

indicates that with respect to the order parameter, a certain limit of the coverage can be tolerated in order to still consider the ordering described by the experiments. At  $\Theta = 0.76\text{ML}$ , the maximum coverage obtained by the random distribution of the particles on the copper surface, we obtain an order parameter  $\Psi = 0.82\text{ML}$  that we could define as the limit of the ordering of the phase (trimers growing along the  $\langle 1\bar{1}4 \rangle$  direction) described by the STM images. The snapshots shown in Fig. 6.24 gives a visual representation of how the parti-

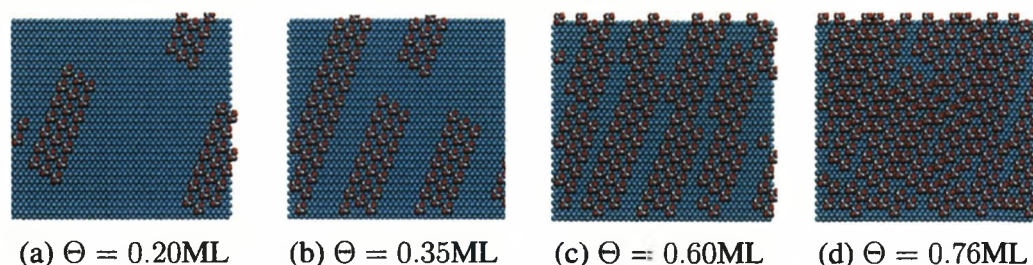


Figure 6.24: Thermodynamic properties of the Bitartrate/Cu(110) system for  $\Theta = 0.5\text{ML}$  and  $\Theta = 0.3\text{ML}$  calculated from Metropolis/Monte Carlo simulations.  $N_0$  represents the number of molecules. (a-b) Order parameter and heat capacity for  $\Theta = 0.5\text{ML}$ . (c-d) Order parameter and heat capacity for  $\Theta = 0.3\text{ML}$ .

cles orders with a constant increase of the coverage  $\Theta$ . At low coverage  $\Theta = 0.20\text{ML}$ , we observe a small cluster of bitartrate radicals organized in trimers growing in the  $\langle 1\bar{1}4 \rangle$  direction in a system globally attractive. As the coverage increases, the ordering remains globally the same, on the image representing a coverage of  $\Theta = 0.35\text{ML}$ . At  $\Theta = 0.60\text{ML}$  we observe the trimers giving longer ordering along the same direction but separated by a gap formed by the trimers growing along the  $\langle 1\bar{1}4 \rangle$  direction.

The ordering phase is completely saturated at  $\Theta = 0.76\text{ML}$  but the order parameter still shows a high value of  $\Psi = 0.82\text{ML}$  characteristic of a globally ordered phase. The gap formed by the vibration of the OH bond is destroyed by the saturation of bitartrate radicals on the copper surface. From the curve  $\Psi = f(\Theta)$  and the snapshots showing the ordering on the bitartrate/Cu(110) surface we can conclude that the coverage describing most accurately the ordering of bitartrate ions on the copper(110) surface is  $\Theta = 0.60\text{ML}$ . Above this limit the system no longer describes the ordering of the phase reported by the experimentalists as the saturation of bitartrate ions destroys the gap between the trimers growing along the  $\langle 1\bar{1}4 \rangle$  direction.

### Low temperature Phase diagram ( $T, \Theta$ )

The OH bond vibration of a bitartrate radical, chemisorbed on the Copper surface, is evolving with respect to the temperature, We can thus trace a ( $T, \Theta$ ) phase diagram. This phase diagram shows at different temperature and coverages the evolution of the two phases reported in last section, and also a possible disordered state. The disordered state can occurs at very high temperature as the order-disorder transition showed in the section (6.2.1), or it can occur at high coverage. The following ( $T, \Theta$ ) diagram shows the evolution of the phases of the bitartrate/Cu(110) system taking in account the OH bonds vibrations: This ( $T, \Theta$ ) diagram shows that the increased temperature leads to a transition from one phase

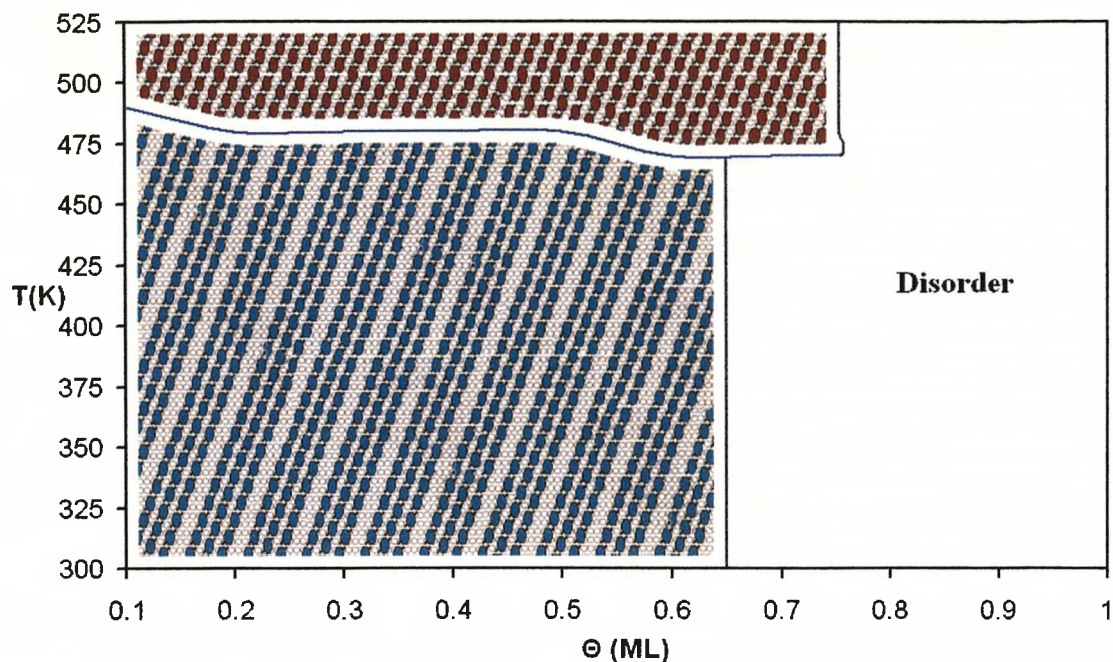


Figure 6.25: Low temperature phase diagram ( $T, \Theta$ ): This curve shows three different domains. At low temperature and low coverage the ordering grows in trimers along the  $\langle 1\bar{1}4 \rangle$  direction. If we increase the temperature to 475K the pattern changes to a cluster of bitartrate radicals growing along the same direction  $\langle 1\bar{1}4 \rangle$ , and more compact than the previous one. Both of these phases lead to disorder if the coverage goes beyond  $\Theta = 0.75\text{ML}$ .

(trimers) to another (cluster) at low and medium coverage. At 475K the vibration of the OH bonds reaches the limit of the biphasic transition energy, reported in the previous section of  $E_{\nu-OH} = 18\text{meV}$ . Below this energy we obtain trimers, above this point clusters. Both of these domains vanish at very high coverage and lead to a completely disordered state. This agrees with the evolution of the  $\Psi = f(\Theta)$  displayed in section (6.5.6), which showed an order parameter  $\Psi$  constantly decreasing as the coverage  $\Theta$  increases above 0.65ML.

### 6.5.6 Summary

The thermodynamic properties of a system in thermodynamic equilibrium completely characterize its macroscopic state. Phase transitions in a system are identified by abrupt changes in the thermodynamic properties of the system.

Thermodynamics establishes relationships among the macroscopic properties of the system which are based on the laws of thermodynamics. The link of the macroscopic properties to the microscopic states of the system is provided by statistical mechanics.

The probability function of any statistical ensemble can be derived from the variational statement of the second law of thermodynamics, and the Gibbs entropy formula.

The connection between the statistical description and thermodynamics is made through a

thermodynamic potential, according to the constraints imposed on the ensemble. For the canonical ensemble, the connection with thermodynamics is made through the free energy  $F$ .

Phase transitions in chemisorbed layers are conveniently simulated in the canonical ensemble, because this ensemble mimics the typical experimental conditions used when measuring such transitions (constant number of particles). However, the simulations can also be carried out in the grand canonical ensemble (constant chemical potential).

The phase transitions can be classified as

- First-order phase transitions: Characterized by phase separation, metastable states and hysteresis.
- Continuous phase transitions: Characterized by critical fluctuations and divergence of the spatial correlations in the system.

The Metropolis algorithm is most widely used in Monte Carlo simulations. The algorithm suffers, however, from limitations near phase transitions due to the uneven energy landscape (first-order phase transitions) or critical slowing down (continuous phase transitions). The Wang-Landau Monte Carlo algorithm avoids these problems, because it is based on a random walk in energy space.

The thermodynamic properties of the bitartrate/Cu(110) system (calculated from Metropolis/Monte Carlo simulations) at  $\Theta = 1/3\text{ML}$  shows a continuous phase transition at  $T_C = 1850\text{K}$  which is above the temperature at which the tartaric acid molecule and the bitartrate radical decompose. This high critical temperature is due to the high energy of the Lattice Gas Hamiltonian interactions. For this both sets of interaction (with and without the OH bond vibration) the Metropolis/Monte Carlo algorithm performed very well at the phase transition. By carrying out similar simulations at different temperature  $T$  and vibration energies of OH bond  $E_{\nu-OH}$ , we can construct the Bitartrate/Cu(110) phase diagram  $E_{\nu-OH} = f(T)$ . It displays at  $\Theta = 0.50\text{ML}$  the limit between two phases, clusters and trimers, growing along the same direction  $\langle 1\bar{1}4 \rangle$ . This diagram is incomplete, it has to be extended in a third dimension taking into account the coverage.

Then the curve  $\Psi = f(\Theta)$  at  $400\text{K}$  indicates full coverage of the ordered phases of the Bitartrate/Cu(110) system. It turns out that the coverage of the ordered phase observed by the experimentalists is  $\Theta = 0.60\text{ML}$ . One thus finds in this particular system that vibrations play a crucial role in the ordering process.

# Chapter 7

## Conclusion

The main aim of this thesis was to study first-principles statistical mechanics for the calculations of adsorbate phase-diagrams. The main system under study, i.e. the bitartrate/Cu(110) system, proved to be a difficult one because of the very small energies determining the ground state configurations compared to the on-site energy (6418 meV) due to chemisorption. Thus, first an exposition about the conclusion related to the studied methodology will be presented and finally, the conclusions regarding the systems under study will be discussed.

We also computed the chlorododecane/Si(111) systems which produced stable and switching corralled silicon adatom according to experimental research. The different conformations of chlorododecane, that theoretically created the same effects, have been determined using Density Functional Theory and electron transport (STM) simulations.

### 7.1 The Chlorododecane/Si(111) systems

#### 7.1.1 Stable corral

The stable corral's electronic property appear to originate from induced dipoles in the Si(111)-(7 × 7) surface, known to be metallic in nature. We have shown that the addition of dipole moments induced by single molecules on both sides of the corralled silicon adatom does not equal the dipole moment produced by the corral. This corral has therefore induced an extra dipole coming from the charge-transfer into the corralled adatom. The computed surplus charge on the corralled silicon adatom accounts for its experimentally observed darkening in the STM images.

Variation in chain length and chain substituents could provide a means to the self-assembly of nano-corrals and filled corrals (nano-dots) of varied but defined size and electronic properties

#### 7.1.2 Switching corral

We reported a single-atom electronic switch in silicon due to molecularly induced field effects. Small changes in configuration of self-assembled pair of dipolar adsorbate molecules

that surround a silicon atom are shown to have a large electronic effect characterized by a high and a low conductance. The finding that small changes in conformation of molecules can have substantial external electronic effects should be of interests in contexts ranging from nanoscale electronics to molecular biology.

## **7.2 The Bitartrate/Cu(110) system**

The multiscale nature of our methodology led to a microscopic and macroscopic study of the bitartrate/Cu(110) system. Thus we present first the conclusions of the microscopic study and afterwards, we discuss the conclusions of the macroscopic study.

### **7.2.1 First-principles calculations and ground state line**

Due to the high energy accuracy demanded by the proper description of highly correlated systems like bitartrate/Cu(110), it was necessary to use one unit cell in the first principles calculations:  $(6 \times 6)$  with a  $(3 \times 2 \times 1)$  k-point mesh.

We have investigated many of the approaches which have been proposed in the literature in order to determine the interaction parameters of the Lattice Gas Hamiltonian.

The simplest of the approaches (within the first-principles statistical mechanics methodology) is to use a square system of equations in order to derive the parameters. That is, to set up a linear system of equations where the number of unknown variables (interaction parameters) is the same as the number of first principles energies. Thus, the parameters are obtained by simply inversion of the system of equations. The interactions selected for the expansion are typically short-range pairs and trios.

The natural extension of the square system approach is to use more equations (first-principles energies) than unknowns (interaction parameters).

### **7.2.2 Macroscopic study**

The Metropolis/Monte Carlo simulations for bitartrate/Cu(110) with the addition of the OH-bond vibration component performed very well at the phase transitions under study. The analysis of the Bitartrate/Cu(110) thermodynamic properties at the phase transitions led to the conclusion that there are continuous or second-order phase transitions. The order parameter calculated by the discrete Fourier transform method gives an accurate location of the phase transition. The accuracy of this parameter and the heat capacity parameter to locate the critical temperature increases with the size of the cell and the number of Monte Carlo steps.

The critical temperature of each system always depends on the coverage. The high critical temperatures of the Bitartrate/Cu(110) system are a consequence of the high lateral interactions operating in this system.

The addition of the OH-bond vibrational component to the Lattice Gas Hamiltonian strengthens the ordering and still leads to thermodynamic stability as we could see with the heat capacity. Therefore at very high coverage the gap between the growing trimers cannot be



controlled. The Monte Carlo simulations determine a specific full coverage of the ordering from 0.60 to 0.65ML.

### **7.3 Final words**

This thesis studied the first-principles statistical mechanics approach as used in the calculation of the Bitartrate/Cu(110) phase diagram. Experimental results (from the literature) are used for comparison only and not for fitting purposes. That means, all of our results are based on theory. Such an approach is very powerful, because many processes and ideas can, in principle, be studied theoretically without actually carrying out (many expensive) experiments. Thus, the design and engineering of material and technological processes should benefit enormously from first-principles methodologies.

Yet, as the systems under study become more and more relevant for technological applications, the computational complexity increases dramatically and the need for experiments cannot be substituted. However, the improvement in hardware and, above all, methods and algorithms, should gradually push the frontier of practical applicability of first-principles methodologies. We have studied here a small area of a subject that constitutes nowadays a vast field of research.

Thus, our technological progress will benefit dramatically from the increasing application of quantum and statistical mechanics. This demands a lot of understanding and ingenuity in order to apply and engineer the consequences of those theories. At stake is the advancement of our knowledge in order to create sustainable technological processes and ways of living, given the limited natural resources of our planet.

## Appendix A

# Metropolis/Monte carlo program on a simple model in Fortran 90

### A.1 Diagram of Metropolis/Monte carlo step by step (canonical ensemble)

- Canonical ensemble:  $N, V, T$  constant

- Metropolis method: To generate a new configuration with probabilities

0. Generate the initial configuration (random or  $c(2 \times 2)$ )

Beginning of the MC cycle

1. Calculate  $E_{old}$

2. Randomly select a particle

3. Random displacement (or rotation)

4. Calculate  $E_{new}$

5. Accept the move with probability (Metropolis method)

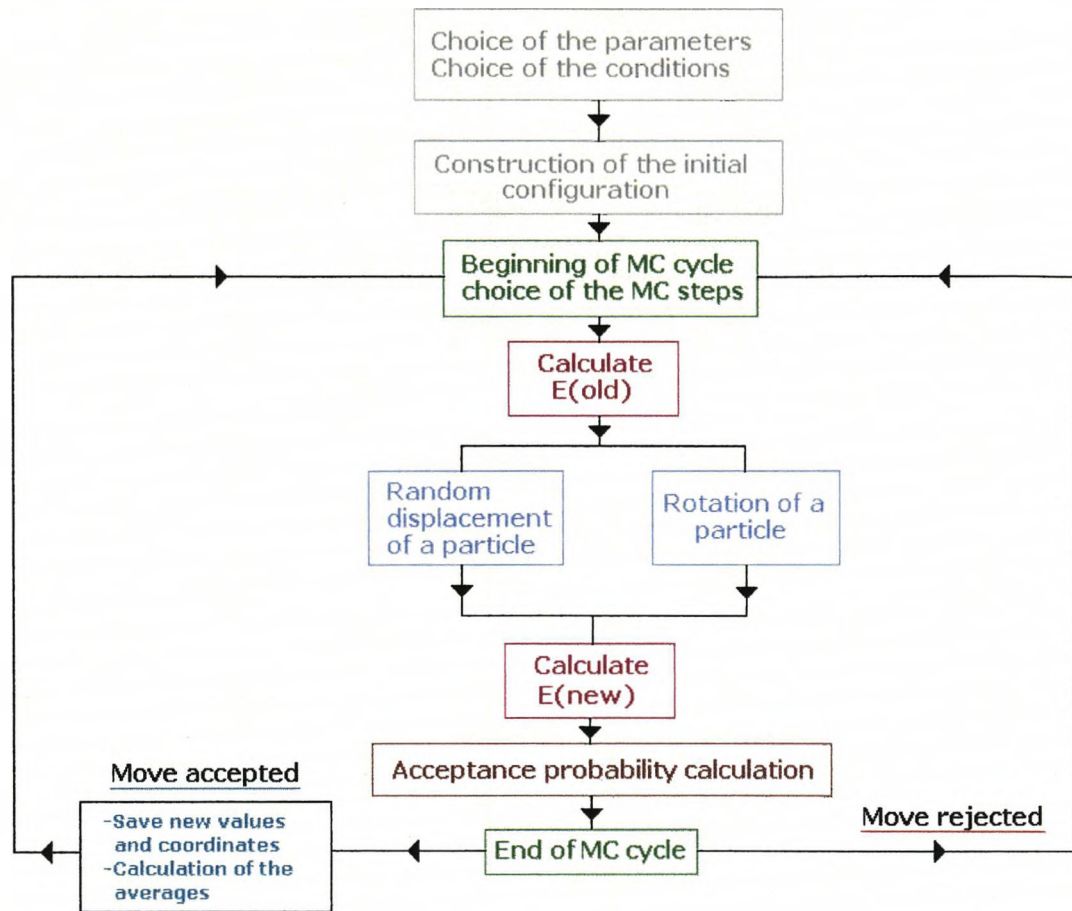
$E_n < E_o$  accept (the move)

$E_n > E_o$  accept with probability  $\exp[-(E_n - E_o) / kT]$

(Periodic boundary conditions)

End of MC cycle

## A.2 Diagram of Metropolis/ Monte carlo in the canonical ensemble



### A.3 Main features of Metropolis/Monte carlo program

Choice of the parameters

Initial configuration

do

en1=EN

typ=1  
call rand\_pos(mat,typ,xrp,yrp)  
x1=xrp, y1=yrp

typ=0  
call rand\_pos(mat,typ,xrp,yrp)  
x2=xrp, y2=yrp

mat(x1,y1)=0  
mat(x2,y2)=1  
call tot\_EN(mat,EN,ei0,ei1)  
en2=EN  
mat(x1,y1)=1  
mat(x2,y2)=0

metropolis conditions  
acceptance: save new values+ add MC step  
Rejection: add MC step

If (count.eq.mcs+1) then  
exit  
end if  
end do

## A.4 Parameters of the simulations

```
real, parameter: k=8,617339E-5
real *8: enT,enT2

print *, "temperature:"
read(*,*) T

print *, "MC steps:"
read(*,*) mcs

print *, "starting configuration, R or C:"
read(*,*) st
start=0
select case (st)
case ("c", "C")
start=1
end select
```

## A.5 Initial configurations

```
if (start.eq.1) then
do v=1,10
do u=1,5                                %% Start c(2x2) %%
if (mod(v,2) .eq.0) then
mat (u*2,v)=0
else
mat (u*2-1,v)=0
end if, end if, end do

else
do
xr= int (rand()*10)+1                    %% Start random %%
yr= int (rand()*10)+1
if (mat(xr,yr).eq.1) then
mat(xr,yr)= 0
nb=nb+1
end if
tt= int (10*10*(1-cov))
if (tt.eq.nb) then
exit
end if, end do, end if
```

## A.6 Metropolis probabilities to accept or reject a move

```
if (en2 .lt. en1) then
  mat(x2,y2)=1
  mat(x1,y1)=0           %% Acceptance %%
  enT=enT+en2
  enT2=enT2+en2*en2
  EN=en2

  count=count+1

else
  if (exp(-(en2-en1)/(k*T)) .gt. rand()) then
    mat(x2,y2)=1
    mat(x1,y1)=0
    enT=enT+en2           %% probability %%
    enT2=enT2+en2*en2
    EN=en2

    count=count+1

  else
    enT=enT+en1           %% Rejection %%
    enT2=enT2+en1*en1
    EN=en1

    count=count+1

  end if, end if
```

## A.7 Subroutine for the nearest neighbors detection

### Subroutine Number of nearest neighbours

```
NNE=0

id=xn+1
if (id.gt.10) then
id=id-10
end if

ig=xn-1
if (ig.lt.1) then
ig=ig+10
end if

%% periodic boundary
%% conditions %%

jh=yn-1
if (jh.gt.10) then
jh=jh-10
end if

jb=yn+1
if (jb.lt.1) then
jb=jb+10
end if

NNE=id + ig + jb + jh
```



## A.8 Subroutine for the total energy of the system

### Subroutine Total energy of the system

```
EN=0
do ii=1,10           %% periodic boundary
do jj=1,10           conditions %%
if mat(ii,jj).eq.1) then
xn=ii
yn=jj
call near_numb (mat,xn,yn,NNE)
EN=NNE*ei1+ei0
```

## A.9 Subroutine for random selection of a particle

### Subroutine Random selection

```
do
xe= int(rand()*10)+1
ye= int(rand()*10)+1

if (mat (xe,ye) .eq. typ) then
xrp=xe
yrp=ye
exit
end if, end do
```

## A.10 Subroutines of the heat capacity $C_V$ and the order parameter $\Psi$

### Subroutine Order parameter

```
matf=mat*2-1  
  
do r = 1,10  
do q = 1,5  
  
if (mod(r,2).eq.0) then  
ma=ma+matf(2*q-1,r)  
mb=mb+matf(2*q ,r)  
  
else  
ma=ma+matf(2*q, r)  
mb=mb+matf(2*q-1,r)  
  
end if, end do, end do  
  
Psi = sqrt ((ma-mb)*(ma-mb)/100)
```

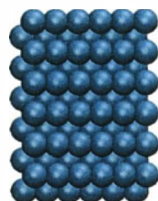
### Subroutine Heat capacity parameter

```
cv = ((enT2/mcs)-(enT*enT) / (mcs*mcs))) / (k*T*T)
```

## Appendix B

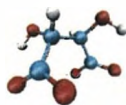
# Tartaric acid on Copper(110) / Lattice Gas Hamiltonian

### B.1 Clean surface



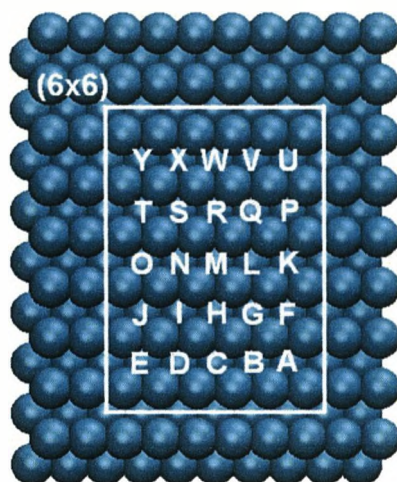
$$E_{surf} = -475.051eV$$

### B.2 Bitartrate ion

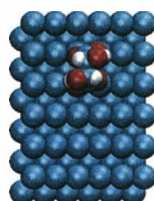


$$E_{tar} = -87.458eV$$

### B.3 Positions on Copper surfaces

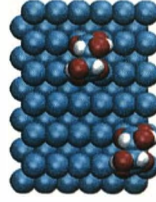


### B.4 Adsorption energy of one molecule at the R position



$$\begin{aligned}E_{ads} &= E_{tot} - (E_{surf} + E_{mol}) \\E_{ads(R)} &= E_{tot(R)} - (E_{Cu(110)} + E_{tar}) \\E_{ads(R)} &= -568.927 - (-475.051 - 87.458) \\E_{ads(R)} &= -6.418eV\end{aligned}$$

## B.5 Adsorption energy of two molecules at R and A

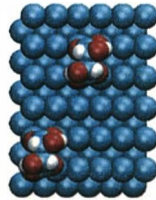


$$\begin{aligned}
 E_{ads} &= E_{tot} - (E_{surf} + 2E_{mol}) \\
 E_{ads(RA)} &= E_{tot(R)} - (E_{Cu(110)} + 2E_{tar}) \\
 E_{ads(RA)} &= -662.705 - (-475.051 - 2(87.458)) \\
 E_{ads(RA)} &= -6.369eV/particle
 \end{aligned}$$

$$\begin{aligned}
 E_{ads(RA-R)} &= +0.0491eV \\
 PBC : E_{ads(RA-R)} &= 2int(2, -3) + 2int(-4, -3)
 \end{aligned}$$

$$int(2, -3) = +24.6meV$$

## B.6 Adsorption energy of two molecules at R and E

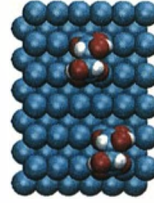


$$\begin{aligned}
 E_{ads} &= E_{tot} - (E_{surf} + 2E_{mol}) \\
 E_{ads(RE)} &= E_{tot(R)} - (E_{Cu(110)} + 2E_{tar}) \\
 E_{ads(RE)} &= -662.702 - (-475.051 - 2(87.458)) \\
 E_{ads(RE)} &= -6.368eV/particle
 \end{aligned}$$

$$\begin{aligned}
 E_{ads(RE-R)} &= +0.0505eV \\
 PBC : E_{ads(RE-R)} &= 2int(2, 3) + 2int(-4, 3)
 \end{aligned}$$

$$int(2, -3) = +25.3meV$$

## B.7 Adsorption energy of two molecules at R and B

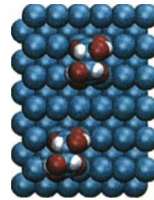


$$\begin{aligned}
 E_{ads} &= E_{tot} - (E_{surf} + 2E_{mol}) \\
 E_{ads(RB)} &= E_{tot(R)} - (E_{Cu(110)} + 2E_{tar}) \\
 E_{ads(RB)} &= -662.681 - (-475.051 - 2(87.458)) \\
 E_{ads(RB)} &= -6.357eV/particle
 \end{aligned}$$

$$\begin{aligned}
 E_{ads(RB-R)} &= +0.0610eV \\
 PBC : E_{ads(RB-R)} &= 2int(1, -3) + 2int(-5, -3)
 \end{aligned}$$

$$int(2, -3) = +30.5meV$$

## B.8 Adsorption energy of two molecules at R and D

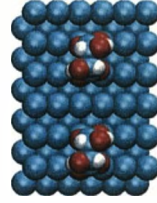


$$\begin{aligned}
 E_{ads} &= E_{tot} - (E_{surf} + 2E_{mol}) \\
 E_{ads(RD)} &= E_{tot(R)} - (E_{Cu(110)} + 2E_{tar}) \\
 E_{ads(RD)} &= -662.679 - (-475.051 - 2(87.458)) \\
 E_{ads(RD)} &= -6.356eV/particle
 \end{aligned}$$

$$\begin{aligned}
 E_{ads(RD-R)} &= +0.0619eV \\
 PBC : E_{ads(RD-R)} &= 2int(1, 3) + 2int(-5, 3)
 \end{aligned}$$

$$int(2, -3) = +30.9meV$$

## B.9 Adsorption energy of two molecules at R and C

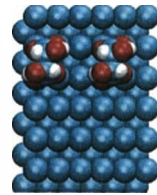


$$\begin{aligned}
 E_{ads} &= E_{tot} - (E_{surf} + 2E_{mol}) \\
 E_{ads(RC)} &= E_{tot(R)} - (E_{Cu(110)} + 2E_{tar}) \\
 E_{ads(RC)} &= -662.662 - (-475.051 - 2(87.458)) \\
 E_{ads(RC)} &= -6.348eV/particle
 \end{aligned}$$

$$\begin{aligned}
 E_{ads(RC-R)} &= +0.0703eV \\
 PBC : E_{ads(RC-R)} &= 2int(0, 3)
 \end{aligned}$$

$$int(0, 3) = +35.1meV$$

## B.10 Adsorption energy of two molecules at T and Q



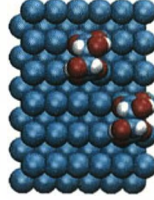
$$\begin{aligned}
 E_{ads} &= E_{tot} - (E_{surf} + 2E_{mol}) \\
 E_{ads(TQ)} &= E_{tot(R)} - (E_{Cu(110)} + 2E_{tar}) \\
 E_{ads(TQ)} &= -662.745 - (-475.051 - 2(87.458)) \\
 E_{ads(TQ)} &= -6.389eV/particle
 \end{aligned}$$

$$\begin{aligned}
 E_{ads(TQ-R)} &= +0.0288eV \\
 PBC : E_{ads(TQ-R)} &= 2int(3, 0)
 \end{aligned}$$

$$int(3, 0) = +14.4meV$$



## B.11 Adsorption energy of two molecules at R and F



$$E_{ads} = E_{tot} - (E_{surf} + 2E_{mol})$$

$$E_{ads(RF)} = E_{tot(R)} - (E_{Cu(110)} + 2E_{tar})$$

$$E_{ads(RF)} = -662.735 - (-475.051 - 2(87.458))$$

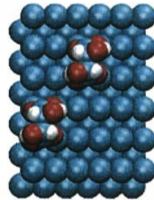
$$E_{ads(RF)} = -6.384eV/particle$$

$$E_{ads(RF-R)} = +0.0339meV$$

$$PBC : E_{ads(RF-R)} = int(2, -2) + int(-4, -2) + int(2, 4) + int(-4, 4)$$

$$int(2, -2) = +34.0meV$$

## B.12 Adsorption energy of two molecules at R and J



$$E_{ads} = E_{tot} - (E_{surf} + 2E_{mol})$$

$$E_{ads(RJ)} = E_{tot(R)} - (E_{Cu(110)} + 2E_{tar})$$

$$E_{ads(RJ)} = -662.679 - (-475.051 - 2(87.458))$$

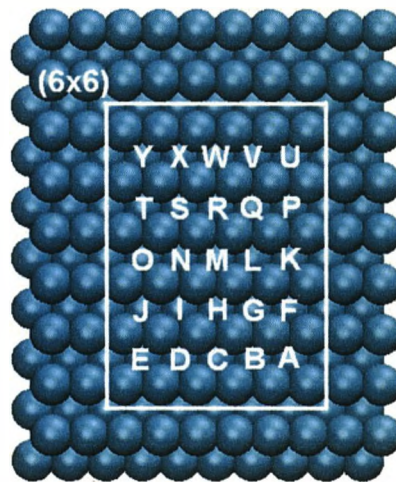
$$E_{ads(RJ)} = -6.384eV/particle$$

$$E_{ads(RJ-R)} = +0.0341eV$$

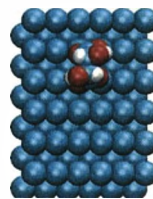
$$PBC : E_{ads(RJ-R)} = int(2, 2) + int(-4, 2) + int(2, -4) + int(-4, -4)$$

$$int(2, 2) = +34.1meV$$

### B.3 Positions on Copper surfaces

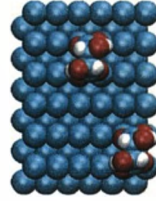


### B.4 Adsorption energy of one molecule at the R position



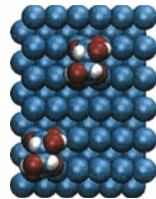
$$\begin{aligned} E_{ads} &= E_{tot} - (E_{surf} + E_{mol}) \\ E_{ads(R)} &= E_{tot(R)} - (E_{Cu(110)} + E_{tar}) \\ E_{ads(R)} &= -568.927 - (-475.051 - 87.458) \\ E_{ads(R)} &= -6.418eV \end{aligned}$$

## B.5 Adsorption energy of two molecules at R and A



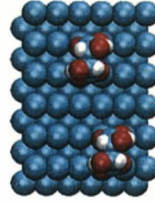
$$\begin{aligned}
 E_{ads} &= E_{tot} - (E_{surf} + 2E_{mol}) \\
 E_{ads(RA)} &= E_{tot(R)} - (E_{Cu(110)} + 2E_{tar}) \\
 E_{ads(RA)} &= -662.705 - (-475.051 - 2(87.458)) \\
 E_{ads(RA)} &= -6.369eV/particle \\
 \\ 
 E_{ads(RA-R)} &= +0.0491eV \\
 PBC : E_{ads(RA-R)} &= 2int(2, -3) + 2int(-4, -3) \\
 \\ 
 int(2, -3) &= +24.6meV
 \end{aligned}$$

## B.6 Adsorption energy of two molecules at R and E



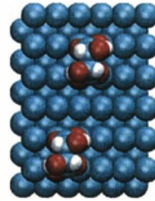
$$\begin{aligned}
 E_{ads} &= E_{tot} - (E_{surf} + 2E_{mol}) \\
 E_{ads(RE)} &= E_{tot(R)} - (E_{Cu(110)} + 2E_{tar}) \\
 E_{ads(RE)} &= -662.702 - (-475.051 - 2(87.458)) \\
 E_{ads(RE)} &= -6.368eV/particle \\
 \\ 
 E_{ads(RE-R)} &= +0.0505eV \\
 PBC : E_{ads(RE-R)} &= 2int(2, 3) + 2int(-4, 3) \\
 \\ 
 int(2, -3) &= +25.3meV
 \end{aligned}$$

## B.7 Adsorption energy of two molecules at R and B



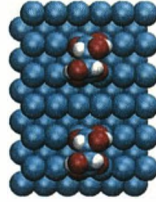
$$\begin{aligned}
 E_{ads} &= E_{tot} - (E_{surf} + 2E_{mol}) \\
 E_{ads(RB)} &= E_{tot(R)} - (E_{Cu(110)} + 2E_{tar}) \\
 E_{ads(RB)} &= -662.681 - (-475.051 - 2(87.458)) \\
 E_{ads(RB)} &= -6.357\text{eV/particle} \\
 \\ 
 E_{ads(RB-R)} &= +0.0610\text{eV} \\
 PBC : E_{ads(RB-R)} &= 2int(1, -3) + 2int(-5, -3) \\
 \\ 
 int(2, -3) &= +30.5\text{meV}
 \end{aligned}$$

## B.8 Adsorption energy of two molecules at R and D



$$\begin{aligned}
 E_{ads} &= E_{tot} - (E_{surf} + 2E_{mol}) \\
 E_{ads(RD)} &= E_{tot(R)} - (E_{Cu(110)} + 2E_{tar}) \\
 E_{ads(RD)} &= -662.679 - (-475.051 - 2(87.458)) \\
 E_{ads(RD)} &= -6.356\text{eV/particle} \\
 \\ 
 E_{ads(RD-R)} &= +0.0619\text{eV} \\
 PBC : E_{ads(RD-R)} &= 2int(1, 3) + 2int(-5, 3) \\
 \\ 
 int(2, -3) &= +30.9\text{meV}
 \end{aligned}$$

## B.9 Adsorption energy of two molecules at R and C

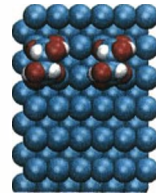


$$\begin{aligned}
 E_{ads} &= E_{tot} - (E_{surf} + 2E_{mol}) \\
 E_{ads(RC)} &= E_{tot(R)} - (E_{Cu(110)} + 2E_{tar}) \\
 E_{ads(RC)} &= -662.662 - (-475.051 - 2(87.458)) \\
 E_{ads(RC)} &= -6.348eV/particle
 \end{aligned}$$

$$\begin{aligned}
 E_{ads(RC-R)} &= +0.0703eV \\
 PBC : E_{ads(RC-R)} &= 2int(0, 3)
 \end{aligned}$$

$$int(0, 3) = +35.1meV$$

## B.10 Adsorption energy of two molecules at T and Q

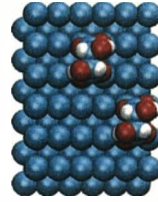


$$\begin{aligned}
 E_{ads} &= E_{tot} - (E_{surf} + 2E_{mol}) \\
 E_{ads(TQ)} &= E_{tot(R)} - (E_{Cu(110)} + 2E_{tar}) \\
 E_{ads(TQ)} &= -662.745 - (-475.051 - 2(87.458)) \\
 E_{ads(TQ)} &= -6.389eV/particle
 \end{aligned}$$

$$\begin{aligned}
 E_{ads(TQ-R)} &= +0.0288eV \\
 PBC : E_{ads(TQ-R)} &= 2int(3, 0)
 \end{aligned}$$

$$int(3, 0) = +14.4meV$$

## B.11 Adsorption energy of two molecules at R and F

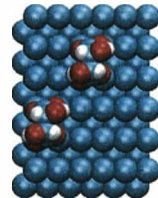


$$\begin{aligned}
 E_{ads} &= E_{tot} - (E_{surf} + 2E_{mol}) \\
 E_{ads(RF)} &= E_{tot(R)} - (E_{Cu(110)} + 2E_{tar}) \\
 E_{ads(RF)} &= -662.735 - (-475.051 - 2(87.458)) \\
 E_{ads(RF)} &= -6.384eV/particle
 \end{aligned}$$

$$\begin{aligned}
 E_{ads(RF-R)} &= +0.0339meV \\
 PBC : E_{ads(RF-R)} &= int(2, -2) + int(-4, -2) + int(2, 4) + int(-4, 4)
 \end{aligned}$$

$$int(2, -2) = +34.0meV$$

## B.12 Adsorption energy of two molecules at R and J

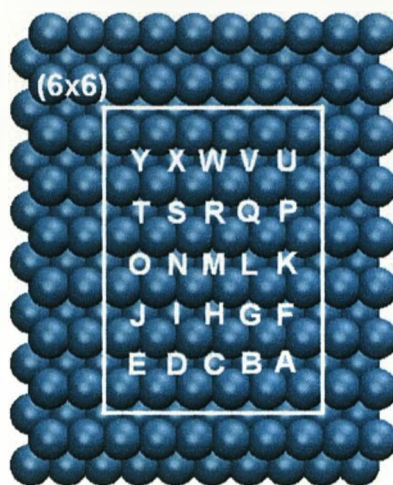


$$\begin{aligned}
 E_{ads} &= E_{tot} - (E_{surf} + 2E_{mol}) \\
 E_{ads(RJ)} &= E_{tot(R)} - (E_{Cu(110)} + 2E_{tar}) \\
 E_{ads(RJ)} &= -662.679 - (-475.051 - 2(87.458)) \\
 E_{ads(RJ)} &= -6.384eV/particle
 \end{aligned}$$

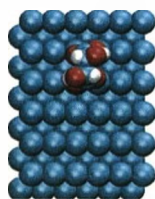
$$\begin{aligned}
 E_{ads(RJ-R)} &= +0.0341eV \\
 PBC : E_{ads(RJ-R)} &= int(2, 2) + int(-4, 2) + int(2, -4) + int(-4, -4)
 \end{aligned}$$

$$int(2, 2) = +34.1meV$$

### B.3 Positions on Copper surfaces

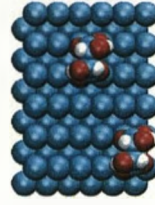


### B.4 Adsorption energy of one molecule at the R position



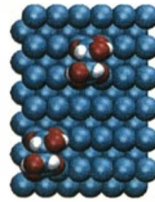
$$\begin{aligned} E_{ads} &= E_{tot} - (E_{surf} + E_{mol}) \\ E_{ads(R)} &= E_{tot(R)} - (E_{Cu(110)} + E_{tar}) \\ E_{ads(R)} &= -568.927 - (-475.051 - 87.458) \\ E_{ads(R)} &= -6.418eV \end{aligned}$$

## B.5 Adsorption energy of two molecules at R and A



$$\begin{aligned}
 E_{ads} &= E_{tot} - (E_{surf} + 2E_{mol}) \\
 E_{ads(RA)} &= E_{tot(R)} - (E_{Cu(110)} + 2E_{tar}) \\
 E_{ads(RA)} &= -662.705 - (-475.051 - 2(87.458)) \\
 E_{ads(RA)} &= -6.369eV/particle \\
 \\ 
 E_{ads(RA-R)} &= +0.0491eV \\
 PBC : E_{ads(RA-R)} &= 2int(2, -3) + 2int(-4, -3) \\
 \\ 
 int(2, -3) &= +24.6meV
 \end{aligned}$$

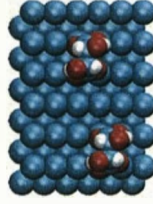
## B.6 Adsorption energy of two molecules at R and E



$$\begin{aligned}
 E_{ads} &= E_{tot} - (E_{surf} + 2E_{mol}) \\
 E_{ads(RE)} &= E_{tot(R)} - (E_{Cu(110)} + 2E_{tar}) \\
 E_{ads(RE)} &= -662.702 - (-475.051 - 2(87.458)) \\
 E_{ads(RE)} &= -6.368eV/particle \\
 \\ 
 E_{ads(RE-R)} &= +0.0505eV \\
 PBC : E_{ads(RE-R)} &= 2int(2, 3) + 2int(-4, 3) \\
 \\ 
 int(2, -3) &= +25.3meV
 \end{aligned}$$



## B.7 Adsorption energy of two molecules at R and B

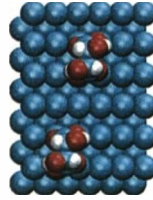


$$\begin{aligned}
 E_{ads} &= E_{tot} - (E_{surf} + 2E_{mol}) \\
 E_{ads(RB)} &= E_{tot(R)} - (E_{Cu(110)} + 2E_{tar}) \\
 E_{ads(RB)} &= -662.681 - (-475.051 - 2(87.458)) \\
 E_{ads(RB)} &= -6.357eV/particle
 \end{aligned}$$

$$\begin{aligned}
 E_{ads(RB-R)} &= +0.0610eV \\
 PBC : E_{ads(RB-R)} &= 2int(1, -3) + 2int(-5, -3)
 \end{aligned}$$

$$int(2, -3) = +30.5meV$$

## B.8 Adsorption energy of two molecules at R and D

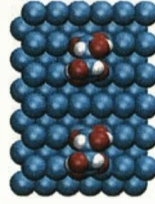


$$\begin{aligned}
 E_{ads} &= E_{tot} - (E_{surf} + 2E_{mol}) \\
 E_{ads(RD)} &= E_{tot(R)} - (E_{Cu(110)} + 2E_{tar}) \\
 E_{ads(RD)} &= -662.679 - (-475.051 - 2(87.458)) \\
 E_{ads(RD)} &= -6.356eV/particle
 \end{aligned}$$

$$\begin{aligned}
 E_{ads(RD-R)} &= +0.0619eV \\
 PBC : E_{ads(RD-R)} &= 2int(1, 3) + 2int(-5, 3)
 \end{aligned}$$

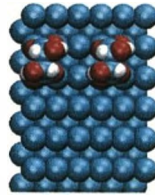
$$int(2, -3) = +30.9meV$$

## B.9 Adsorption energy of two molecules at R and C



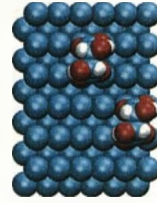
$$\begin{aligned}
 E_{ads} &= E_{tot} - (E_{surf} + 2E_{mol}) \\
 E_{ads(RC)} &= E_{tot(R)} - (E_{Cu(110)} + 2E_{tar}) \\
 E_{ads(RC)} &= -662.662 - (-475.051 - 2(87.458)) \\
 E_{ads(RC)} &= -6.348eV/particle \\
 \\ 
 E_{ads(RC-R)} &= +0.0703eV \\
 PBC : E_{ads(RC-R)} &= 2int(0, 3) \\
 \\ 
 int(0, 3) &= +35.1meV
 \end{aligned}$$

## B.10 Adsorption energy of two molecules at T and Q



$$\begin{aligned}
 E_{ads} &= E_{tot} - (E_{surf} + 2E_{mol}) \\
 E_{ads(TQ)} &= E_{tot(R)} - (E_{Cu(110)} + 2E_{tar}) \\
 E_{ads(TQ)} &= -662.745 - (-475.051 - 2(87.458)) \\
 E_{ads(TQ)} &= -6.389eV/particle \\
 \\ 
 E_{ads(TQ-R)} &= +0.0288eV \\
 PBC : E_{ads(TQ-R)} &= 2int(3, 0) \\
 \\ 
 int(3, 0) &= +14.4meV
 \end{aligned}$$

## B.11 Adsorption energy of two molecules at R and F

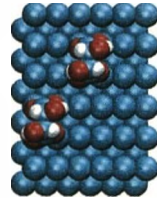


$$\begin{aligned}
 E_{ads} &= E_{tot} - (E_{surf} + 2E_{mol}) \\
 E_{ads(RF)} &= E_{tot(R)} - (E_{Cu(110)} + 2E_{tar}) \\
 E_{ads(RF)} &= -662.735 - (-475.051 - 2(87.458)) \\
 E_{ads(RF)} &= -6.384eV/particle
 \end{aligned}$$

$$\begin{aligned}
 E_{ads(RF-R)} &= +0.0339meV \\
 PBC : E_{ads(RF-R)} &= int(2, -2) + int(-4, -2) + int(2, 4) + int(-4, 4)
 \end{aligned}$$

$$int(2, -2) = +34.0meV$$

## B.12 Adsorption energy of two molecules at R and J

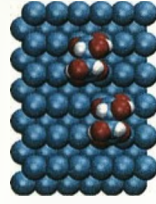


$$\begin{aligned}
 E_{ads} &= E_{tot} - (E_{surf} + 2E_{mol}) \\
 E_{ads(RJ)} &= E_{tot(R)} - (E_{Cu(110)} + 2E_{tar}) \\
 E_{ads(RJ)} &= -662.679 - (-475.051 - 2(87.458)) \\
 E_{ads(RJ)} &= -6.384eV/particle
 \end{aligned}$$

$$\begin{aligned}
 E_{ads(RJ-R)} &= +0.0341eV \\
 PBC : E_{ads(RJ-R)} &= int(2, 2) + int(-4, 2) + int(2, -4) + int(-4, -4)
 \end{aligned}$$

$$int(2, 2) = +34.1meV$$

### B.13 Adsorption energy of two molecules at R and G

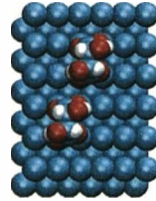


$$\begin{aligned}
 E_{ads} &= E_{tot} - (E_{surf} + 2E_{mol}) \\
 E_{ads(RG)} &= E_{tot(R)} - (E_{Cu(110)} + 2E_{tar}) \\
 E_{ads(RG)} &= -662.763 - (-475.051 - 2(87.458)) \\
 E_{ads(RG)} &= -6.398eV/particle
 \end{aligned}$$

$$\begin{aligned}
 E_{ads(RG-R)} &= +0.0197eV \\
 PBC : E_{ads(RG-R)} &= int(1, -2) + int(-5, -2) + int(1, 4) + int(-5, 4)
 \end{aligned}$$

$$int(2, -1) = +19.7meV$$

### B.14 Adsorption energy of two molecules at R and I

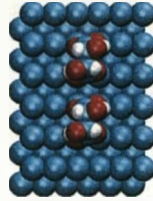


$$\begin{aligned}
 E_{ads} &= E_{tot} - (E_{surf} + 2E_{mol}) \\
 E_{ads(RI)} &= E_{tot(R)} - (E_{Cu(110)} + 2E_{tar}) \\
 E_{ads(RI)} &= -662.769 - (-475.051 - 2(87.458)) \\
 E_{ads(RI)} &= -6.401eV/particle
 \end{aligned}$$

$$\begin{aligned}
 E_{ads(RI-R)} &= +0.0172eV \\
 PBC : E_{ads(RI-R)} &= int(1, 2) + int(-5, 2) + int(1, -4) + int(-5, -4)
 \end{aligned}$$

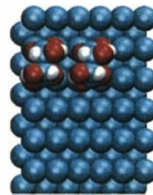
$$int(2, 1) = +17.2meV$$

## B.15 Adsorption energy of two molecules at R and H



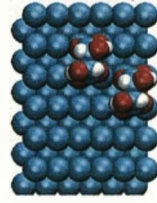
$$\begin{aligned}
 E_{ads} &= E_{tot} - (E_{surf} + 2E_{mol}) \\
 E_{ads(RH)} &= E_{tot(R)} - (E_{Cu(110)} + 2E_{tar}) \\
 E_{ads(RH)} &= -662.781 - (-475.051 - 2(87.458)) \\
 E_{ads(RH)} &= -6.407eV/particle \\
 \\ 
 E_{ads(RH-R)} &= +0.0112eV \\
 PBC : E_{ads(RH-R)} &= int(0, 2) + int(0, 4) \\
 \\ 
 int(0, 2) &= +11.2meV
 \end{aligned}$$

## B.16 Adsorption energy of two molecules at R and T



$$\begin{aligned}
 E_{ads} &= E_{tot} - (E_{surf} + 2E_{mol}) \\
 E_{ads(RT)} &= E_{tot(R)} - (E_{Cu(110)} + 2E_{tar}) \\
 E_{ads(RT)} &= -662.668 - (-475.051 - 2(87.458)) \\
 E_{ads(RT)} &= -6.351eV/particle \\
 \\ 
 E_{ads(RT-R)} &= +0.0673eV \\
 PBC : E_{ads(RT-R)} &= int(2, 0) + int(4, 0) \\
 \\ 
 int(0, 2) &= +67.3meV
 \end{aligned}$$

## B.17 Adsorption energy of two molecules at R and K

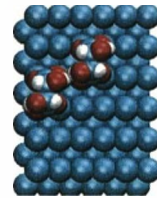


$$\begin{aligned}
 E_{ads} &= E_{tot} - (E_{surf} + 2E_{mol}) \\
 E_{ads(RK)} &= E_{tot(R)} - (E_{Cu(110)} + 2E_{tar}) \\
 E_{ads(RK)} &= -662.679 - (-475.051 - 2(87.458)) \\
 E_{ads(RK)} &= -6.356eV/particle
 \end{aligned}$$

$$\begin{aligned}
 E_{ads(RK-R)} &= +0.0620eV \\
 PBC : E_{ads(RK-R)} &= int(2, -1) + int(-4, -1) + int(2, 5) + int(-4, 5)
 \end{aligned}$$

$$int(2, -1) = +62.0meV$$

## B.18 Adsorption energy of two molecules at R and O

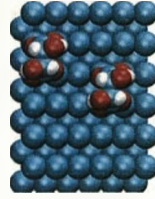


$$\begin{aligned}
 E_{ads} &= E_{tot} - (E_{surf} + 2E_{mol}) \\
 E_{ads(RO)} &= E_{tot(R)} - (E_{Cu(110)} + 2E_{tar}) \\
 E_{ads(RO)} &= -662.649 - (-475.051 - 2(87.458)) \\
 E_{ads(RO)} &= -6.401eV/particle
 \end{aligned}$$

$$\begin{aligned}
 E_{ads(RO-R)} &= +0.077eV \\
 PBC : E_{ads(RO-R)} &= int(2, 1) + int(-4, 1) + int(2, -5) + int(-4, -5)
 \end{aligned}$$

$$int(2, 1) = +77.1meV$$

## B.19 Adsorption energy of two molecules at T and L

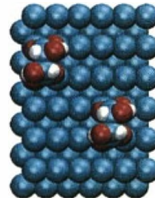


$$\begin{aligned}
 E_{ads} &= E_{tot} - (E_{surf} + 2E_{mol}) \\
 E_{ads(TL)} &= E_{tot(R)} - (E_{Cu(110)} + 2E_{tar}) \\
 E_{ads(TL)} &= -662.717 - (-475.051 - 2(87.458)) \\
 E_{ads(TL)} &= -6.375\text{eV/particle}
 \end{aligned}$$

$$\begin{aligned}
 E_{ads(TL-R)} &= +0.0432\text{eV} \\
 PBC : E_{ads(TL-R)} &= 2int(3, -1) + 2int(3, 5)
 \end{aligned}$$

$$int(3, -1) = +21.6\text{meV}$$

## B.20 Adsorption energy of two molecules at T and G

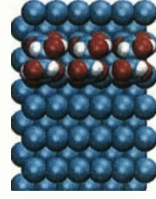


$$\begin{aligned}
 E_{ads} &= E_{tot} - (E_{surf} + 2E_{mol}) \\
 E_{ads(TG)} &= E_{tot(R)} - (E_{Cu(110)} + 2E_{tar}) \\
 E_{ads(TG)} &= -662.688 - (-475.051 - 2(87.458)) \\
 E_{ads(TG)} &= -6.361\text{eV/particle}
 \end{aligned}$$

$$\begin{aligned}
 E_{ads(TG-R)} &= +0.0576\text{eV} \\
 PBC : E_{ads(TG-R)} &= 2int(3, -2) + 2int(3, 4)
 \end{aligned}$$

$$int(3, -2) = +28.8\text{meV}$$

## B.21 Adsorption energy of three molecules at T, R and P

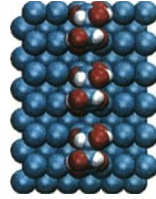


$$\begin{aligned}
 E_{ads} &= E_{tot} - (E_{surf} + 3E_{mol}) \\
 E_{ads(TRP)} &= E_{tot(R)} - (E_{Cu(110)} + 3E_{tar}) \\
 E_{ads(TRP)} &= -756.325 - (-475.051 - 3(87.458)) \\
 E_{ads(TRP)} &= -6.300eV/particle
 \end{aligned}$$

$$\begin{aligned}
 E_{ads(TRP-R)} &= +0.01182eV \\
 PBC : E_{ads(TRP-R)} &= 2int(2, 0) + 2int(4, 0) + 3int(2, 0; 4, 0)
 \end{aligned}$$

$$int(2, 0; 4, 0) = -5.5meV$$

## B.22 Adsorption energy of three molecules at W, M and C



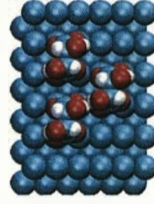
$$\begin{aligned}
 E_{ads} &= E_{tot} - (E_{surf} + 3E_{mol}) \\
 E_{ads(WMC)} &= E_{tot(R)} - (E_{Cu(110)} + 3E_{tar}) \\
 E_{ads(WMC)} &= -756.620 - (-475.051 - 3(87.458)) \\
 E_{ads(WMC)} &= -6.398eV/particle
 \end{aligned}$$

$$\begin{aligned}
 E_{ads(WMC-R)} &= +0.01974eV \\
 PBC : E_{ads(WMC-R)} &= 2int(0, 2) + 2int(0, 4) + 3int(0, 2; 0, 4)
 \end{aligned}$$

$$int(0, 2; 0, 4) = -0.9meV$$



## B.23 Adsorption energy of three molecules at I, S and L

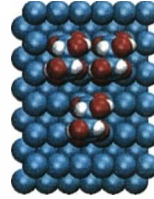


$$\begin{aligned}
 E_{ads} &= E_{tot} - (E_{surf} + 3E_{mol}) \\
 E_{ads(ISL)} &= E_{tot(R)} - (E_{Cu(110)} + 3E_{tar}) \\
 E_{ads(ISL)} &= -756.361 - (-475.051 - 3(87.458)) \\
 E_{ads(ISL)} &= -6.312eV/particle
 \end{aligned}$$

$$\begin{aligned}
 E_{ads(ISL-R)} &= +0.106eV \\
 PBC : 3E_{ads(ISL-R)} &= 2int(0, 2) + 2int(2, 1) + 2int(2, -1) + 3int(2, 1; 0, 2)
 \end{aligned}$$

$$int(2, 1; 0, 2) = +6.0meV$$

## B.24 Adsorption energy of three molecules at H, S and Q

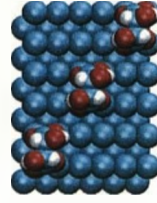


$$\begin{aligned}
 E_{ads} &= E_{tot} - (E_{surf} + 3E_{mol}) \\
 E_{ads(HSQ)} &= E_{tot(R)} - (E_{Cu(110)} + 3E_{tar}) \\
 E_{ads(HSQ)} &= -756.448 - (-475.051 - 3(87.458)) \\
 E_{ads(HSQ)} &= -6.341eV/particle
 \end{aligned}$$

$$\begin{aligned}
 E_{ads(HSQ-R)} &= +0.077eV \\
 PBC : 3E_{ads(HSQ-R)} &= 2int(2, 0) + 2int(1, 2) + 2int(1, -2) + 3int(1, 2; -1, 2)
 \end{aligned}$$

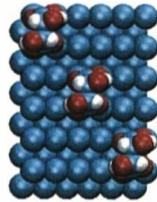
$$int(1, 2; -1, 2) = +7.6meV$$

## B.25 Adsorption energy of three molecules at E, M and U



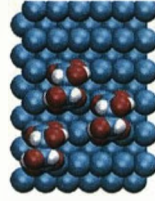
$$\begin{aligned}
 E_{ads} &= E_{tot} - (E_{surf} + 3E_{mol}) \\
 E_{ads(EMU)} &= E_{tot(R)} - (E_{Cu(110)} + 3E_{tar}) \\
 E_{ads(EMU)} &= -756.498 - (-475.051 - 3(87.458)) \\
 E_{ads(EMU)} &= -6.358eV/particle \\
 \\ 
 E_{ads(EMU-R)} &= +0.0604eV \\
 PBC : E_{ads(EMU-R)} &= 2int(2, 2) + 3int(-2, -2; 2, 2) \\
 \\ 
 int(-2, -2; 2, 2) &= -2.6meV
 \end{aligned}$$

## B.26 Adsorption energy of three molecules at A, M and Y



$$\begin{aligned}
 E_{ads} &= E_{tot} - (E_{surf} + 3E_{mol}) \\
 E_{ads(AMY)} &= E_{tot(R)} - (E_{Cu(110)} + 3E_{tar}) \\
 E_{ads(AMY)} &= -756.741 - (-475.051 - 3(87.458)) \\
 E_{ads(AMY)} &= -6.438eV/particle \\
 \\ 
 E_{ads(AMY-R)} &= -0.0169eV \\
 PBC : E_{ads(AMY-R)} &= 2int(2, -2) + 3int(-2, 2; 2, -2) \\
 \\ 
 int(-2, 2; 2, -2) &= -29.2meV
 \end{aligned}$$

## B.27 Adsorption energy of three molecules at E, G and N

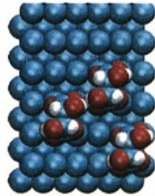


$$\begin{aligned}
 E_{ads} &= E_{tot} - (E_{surf} + 3E_{mol}) \\
 E_{ads(EGN)} &= E_{tot(R)} - (E_{Cu(110)} + 3E_{tar}) \\
 E_{ads(EGN)} &= -756.638 - (-475.051 - 3(87.458)) \\
 E_{ads(EGN)} &= -6.405eV/particle
 \end{aligned}$$

$$\begin{aligned}
 E_{ads(EGN-R)} &= +0.0136eV \\
 PBC : 3E_{ads(EGN-R)} &= 2int(1, 2) + 2int(2, -1) + 4int(3, 1) + 3int(1, 2; 3, 1)
 \end{aligned}$$

$$int(1, 2; 3, 1) = -68.1meV$$

## B.28 Adsorption energy of three molecules at A, I and L

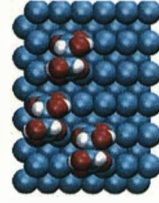


$$\begin{aligned}
 E_{ads} &= E_{tot} - (E_{surf} + 3E_{mol}) \\
 E_{ads(AIL)} &= E_{tot(R)} - (E_{Cu(110)} + 3E_{tar}) \\
 E_{ads(AIL)} &= -756.549 - (-475.051 - 3(87.458)) \\
 E_{ads(AIL)} &= -6.375eV/particle
 \end{aligned}$$

$$\begin{aligned}
 E_{ads(AIL-R)} &= +0.0433eV \\
 PBC : 3E_{ads(AIL-R)} &= 2int(1, -2) + 2int(2, 1) + 4int(3, -1) + 3int(2, 1; 3, -1)
 \end{aligned}$$

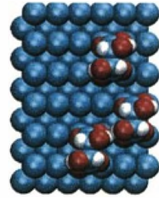
$$int(2, 1; 3, -1) = -56.6meV$$

## B.29 Adsorption energy of three molecules at J, C and S



$$\begin{aligned}
 E_{ads} &= E_{tot} - (E_{surf} + 3E_{mol}) \\
 E_{ads(JCS)} &= E_{tot(R)} - (E_{Cu(110)} + 3E_{tar}) \\
 E_{ads(JCS)} &= -756.679 - (-475.051 - 3(87.458)) \\
 E_{ads(JCS)} &= -6.385eV/particle \\
 \\ 
 E_{ads(JCS-R)} &= +0.0334eV \\
 PBC : 3E_{ads(JCS-R)} &= 2int(2, -1) + 2int(1, 2) + 4int(1, 3) + 3int(1, 2; 2, -1) \\
 \\ 
 int(1, 2; 2, -1) &= -60.3meV
 \end{aligned}$$

## B.30 Adsorption energy of three molecules at C, F and Q



$$\begin{aligned}
 E_{ads} &= E_{tot} - (E_{surf} + 3E_{mol}) \\
 E_{ads(CFQ)} &= E_{tot(R)} - (E_{Cu(110)} + 3E_{tar}) \\
 E_{ads(CFQ)} &= -756.475 - (-475.051 - 3(87.458)) \\
 E_{ads(CFQ)} &= -6.350eV/particle \\
 \\ 
 E_{ads(CFQ-R)} &= +0.0681eV \\
 PBC : 3E_{ads(CFQ-R)} &= 2int(2, 1) + 2int(1, -2) + 4int(1, 3) + 3int(1, -2; 2, 1) \\
 \\ 
 int(1, -2; 2, 1) &= -35.7meV
 \end{aligned}$$

# Bibliography

- [1] D.P. Landau, in Handbook of Materials Modeling, Part B, *edited by S. Yip, Springer, Berlin* (2005).
- [2] J.S. McEwen, S.H. Payne and C. Stampfl, *Chem. Phys. Lett.* **361**, 317 (2002)
- [3] H. Tang, A. Van der Ven and B.L. trout, , *Phys. Rev. B* **70**, 45420 (2004)
- [4] M. Borg, C. Stampfl, A. Mikkelsen, J. Gustafson, E. Lundgren, M. Scheffler, and J.N. Andersen, *Chem. Phys. Chem* **6**, 1 (2005)
- [5] A. Zunger, in Statics and Dynamics of Alloy Phase Transformations, edited by P.E.A Turchy and A. Gonis, New york (1994)
- [6] C. Stampfl, H.J. Kreuzer, S.H. Payne, H. Pfnur, and M. Scheffler, *Phys. Rev Lett.* **83**, 2993 (1999)
- [7] K.A. Fichthorn and M. Scheffler, *Phys, Rev. Lett.* **84**, 5371 (2000)
- [8] K. Reuter, D. Frenkel, and M. Scheffler, *Phys. Rev. Lett.* **93**, 116105 (2004)
- [9] F. Zhou, G. Grigoryan, S.R. Lustig, A.E. Keating, G. Ceder, D. Morgan, *Phys. Rev. Lett.* **95**, 148103-1 (2005)
- [10] K. Schwarz, P.Blaha, and G.K.H Madsen, *Comput. Phys. Commun.* **147**, 71 (2002)
- [11] K. Reuter, C. Stampfl, and M. Scheffler, in Handbook of Materials Modeling, Part A, *edited by S. Yip, Springer, Berlin*, (2005)
- [12] R.M. Nieminen, *J. Phys.: Condens. Matter* **14**, 2859 (2002).
- [13] E. Kaxiras, Y. Bar-Yam, J.D. Joannopoulos, and K.C. Pandey, *Phys. Rev. B* **35**, 9625 (1987)
- [14] M. Scheffler, in Physics of Solid Surfaces, , *edited by J. Koukal, Elsevier Amsterdam*, (1987)
- [15] K. Reuter and M. Scheffler *Phys. Rev. B* **65**, 035406 (2002)
- [16] K. Reuter and M. Scheffler *Phys. Rev. B* **68**, 045407 (2003)
- [17] G. Ceder, *Curr. Opin. Sol. Stat. Mat. Sci.*, **3**, 533 (1998)

- [18] D. Alfe, G.A. de Wijs, G. Kresse, and M.J. Gillan, *Inter. J. Quant. Chem.*, **77** 871 (1999)
- [19] R.S. Berry, S.A. Rice and J. Ross, *Physical Chemistry*, Oxford, New York (2000)
- [20] C.B. Duke, E.W. Plummer (Editors), *Frontiers in Surface and Interface Science*, *Elsevier*, Amsterdam (2002)
- [21] C. Kittel, *Introduction to Solid State Physics*, *Wiley*, New York (1996)
- [22] R.I. Masel, *Principles of Adsorption and Reactions on Solid Surfaces* *Wiley*, New York (1996)
- [23] A. Groß, *Theoretical Surface Science: A Microscopic Perspective*, *Springer*, Berlin (2003)
- [24] J. Behler, B. Delley, S. Lorenz, K. Reuter, and M. Scheffler, *Phys. Rev. Lett.*, **94**, 036104 (2005)
- [25] K. Oura, V.G. Lifshits, A.A. Saranin, A.V. Zotov and M. Katayama, *Surface Science: An introduction*, *Springer*, Berlin (2003)
- [26] G. Ertl, *Langmuir*, **3**, 4 (1987)
- [27] I. Langmuir, *J. Am. Chem. Soc.*, **40**, 1361 (1918)
- [28] M. Born and J.R. Oppenheimer, *Ann. Phys.*, **84** 457 (1927)
- [29] W. Kohn, *Rev. Mod. Phys.*, **71**, 1253 (1999)
- [30] R.G. Parr and W. Yang, *Density-Functional Theory of Atoms and Molecules*, *Oxford University Press*, Oxford (1989)
- [31] P. Hohenberg and W. Kohn, *Phys. Rev. B* **136**, 846 (1964)
- [32] W. Kohn and L.J. Sham, *Phys. Rev. A* **140**, 1133 (1965)
- [33] P.A Dirac, *M. Proc. Cambridge Philos. Soc.*, **26**, 376 (1930)
- [34] D.M. Ceperley and B.J. Alder, *Phys. Rev. Lett.* **45**, 566 (1980)
- [35] J. Kohanoff and N.I. Gidopoulos, in *Handbook of Molecular Physics and Quantum Chemistry*, Vol. 2, edited by S. Wilson, *Wiley*, New York (2003)
- [36] F. Bloch, *Z. Phys.*, **52**, 555 (1928)
- [37] G. te Velde and E.J. Baerends, *Chem. Phys.* **177**, 399 (1993)
- [38] T.L. Beck, *Rev. Mod. Phys.* **72**, 1041 (2000)
- [39] J.E. Pask and P.A. Sterne, in *Handbook of Materials Modeling*, Part A, edited by S. Yip, *Springer*, Berlin (2005)

- [40] D.J. Singh, *Planewaves, Pseudopotentials and the LAPW Method*, Kluwer Academic, Boston (1994)
- [41] H.L Skriver, *The LMTO Method*, Springer, Berlin (1984)
- [42] D. Vanderbilt, *Phys. Rev. B*, **41**, 7862 (1990)
- [43] P.E. Blochl, *Phys. Rev. B*, **50**, 17953 (1994)
- [44] R.M. Martin, *Electronic Structure: Basic Theory and Practical Methods*, Cambridge University Press, Cambridge (2004)
- [45] H.J. Monkhorst and J.D. Pack, *Phys. Rev. B* **13**, 5188 (1976)
- [46] S. Froyen, *Phys. Rev. B*, **29**, 3168 (1989)
- [47] J. Moreno and J.M. Soler, *Phys. Rev. B*, **45**, 13891 (1992)
- [48] M.E.J. Newman and G.T. Barkema, *Monte Carlo Methods in Statistical Physics*, Oxford University Press, New York (1999)
- [49] K. Binder and D.P. Landau, in *Molecule Surface Interactions*, Vol. LXXVI edited by K.P. Lawley, Wiley, Chichester (1989)
- [50] D. Chandler, *Introduction to Modern Statistical Mechanics*, Oxford University Press, New York (1987)
- [51] E. Ising, *J. Phys.* **31**, 253 (1925)
- [52] L. Onsager, *Phys. Rev.* **65**, 117 (1944)
- [53] D.P. Landau and K. Binder, *A Guide to Monte Carlo Simulations in Statistical Physics*, Cambridge University Press, Cambridge, England (2000)
- [54] W.M.C. Foulkes, L. Mitas, R.J. Needs, and G. Rajagopal, *Rev. Mod. Phys.* **73**, 33 (2001)
- [55] M. Metropolis, A.W. Rosenbluth, M.N. Rosenbluth, A.H. Teller and E. Teller, *J. Chem. Phys.* **21**, 1087 (1953)
- [56] S. Kirkpatrick, C.D. Gelatt and M.P. Vecchi, *Science* **20**, 671 (1983)
- [57] Y. Okamoto, in *the Monte Carlo Method in the Physical Sciences*, edited by J.E. Gubernatis, AIP, New York (2003)
- [58] F. Wang and D.P. Landau, *Phys. Rev. Lett.* **86**, 2050 (2001)
- [59] F. Wang and D.P. Landau, *Phys. Rev. E* **64**, 056101 (2001)
- [60] D.P. Landau and F. Wang, *Comput. Phys. Commun.* **147**, 674 (2002)
- [61] D.P. Landau and F. Wang, *Braz. J. Phys.* **34**, 354 (2004)

- [62] D.P. Landau, S.H. Tsai, and M. Exler, *Am. J. Phys.* **72**, 1294 (2004)
- [63] J. Lee, *Phys. Rev. Lett.* **71**, 211 (1993)
- [64] C. Zhou and R.N. Bhatt, *Phys. Rev. E* (2006)
- [65] P. Dayal, S. Trebst, S. Wessel, D. Wurtz, M. Troyer, S. Sabhapandit, and S.N. Coppersmith, *Phys. Rev. Lett.* **92**, 097201 (2004)
- [66] H.K. Lee, Y. Okave, D.P. Landau, *Comp. Phys. Comm.* (2006)
- [67] K.W. Kolasinski, *Surface Science: Foundations of Catalysis and Nanoscience*, Wiley, New York (2002)
- [68] P. Piercy, K. De'Bell and H. Pfnur, *Phys. rev. B* **45**, 1869 (1992)
- [69] M. Sandhoff, H. Pfnur and H.U. Everts, *Surface Science* **280**, 185 (1993)
- [70] L.D. Roelofs, T.L. Einstein, N.C. Bartelt, and J.D. Shore, *Surface Science* **176**, 295 (1986)
- [71] H. Ezzehar, L. Stauffer, H. Dreysse and M. Habar, *Surface Science* **331-333**, 144 (1995)
- [72] D.J. Liu, T.L. Einstein, P.A. Sterne and L.T. Wille, *Phys. Rev. B* **52**, 9784 (1995)
- [73] C. Stampfl, H.J. Kreuzer, S.H. Payne and M. Scheffler, *Appl. Phys. A* **69**, 471 (1999)
- [74] C. Stampfl, *Catal. Today* **105**, 17 (2005)
- [75] J.M. Sanchez, F. Ducastelle, and D. Gratias, *Physica A* **128**, 334 (1984)
- [76] J.W. Conolly and A.R. Williams, *Phys. rev. B* **27**, 5169 (1983)
- [77] G.D. Garbulsky and G. Ceder, *Phys. Rev. B* **51**, 67 (1995)
- [78] A. Zunger, L.G. Wang, G.L.W. Hart and M. Sanati, *Modell. Simul. Mater. Sci. Eng.* **10**, 685 (2002)
- [79] A. van de Walle and G. Ceder, *J. Phase Equilib.* **23**, 348 (2002)
- [80] M.H.F. Sluiter and Y. Kawazoe, *Phys. Rev. B* **68**, 85410 (2003)
- [81] S. Muller, *J. Phys.: Condens Matter* **15**, R1429 (2003)
- [82] G. Strang, *Introduction to Applied Mathematics*, Wellesley-Cambridge Press, MA, (1986)
- [83] D.P. Landau, *Phys. rev. B* **27**, 5604 (1983)
- [84] J. Glosli and M. Plischke, *Can. J. Phys.* **61**, 1515 (1983)



- [85] H.B. Callen, *Thermodynamics and an Introduction to Thermostatistics*, Wiley, New York, (1985)
- [86] R. Bowley and M. Sanchez, *Introductory Statistical Mechanics*, Oxford University Press, New York (1999)
- [87] C.G. Chakrabarti and K. De, *Internat. J. Math. and Math. Sci.* **23**, 243 (2000)
- [88] P. Ehrenfest, *Proc. Roy. Akad. Sci. (Amsterdam)* **36**, 153 (1933)
- [89] M. Sandhoff, H. Pfner, and H.U. Everts, *Europhys. Lett.* **25**, 105 (1993)
- [90] Donhauser, Z.J.; Mantooth, B.A.; Kelly, K.F.; Bumm, L.A.; Monnell, J.D.; Stapleton, J.J.; Price, D.W.; Rawlett, A.M.; Allara, D.L.; Tour, J.M. Weiss, P.S. *Science* **292**, 2303 (2003)
- [91] Ramachandran, G.K.; Hopson, T.J.; Rawlett, A.M.; Nagahara, L.A.; Primak, A.; Lindsay, S.M. *Science* **300**, 1413 (2003)
- [92] Moore, A.M.; Dameron, A.A.; Mantooth, B.A.; Smith, R.K.; Fuchs, D.J.; Cizek, J.W.; Maya, F. Yao, Y.X.; Tour, J.M.; Weiss, P.S. *J. Am. Chem. Soc.* **128**, 1959 (2006)
- [93] Blum, A.S.; Kushmerick, J.G.; Long, D.P.; Patterson, C.H.; Yang, J.C.; Henderson, J.C.; Yao, Y.X.; Tour, J.M.; Shashidhar, R.; Ratna, B.R. *Nat. Mater.* **4**, 167 (2005)
- [94] Chen, J.; Reed, M.A.; Rawlett, A.M.; Tour, J.M. *Science* **286**, 1550 (1999)
- [95] Reed, M.A.; Zhou, C.; Muller, C.J.; Burgin, T.P.; Tour, J.M. *Science* **278**, 252 (1997)
- [96] Dameron, A.A.; Cizek, J.W.; Tour, J.M.; Weiss, P.S. *J. Phys. Chem. B* **108**, 16761 (2004)
- [97] Piva, P.G.; DiLabio, G.A.; Pitters, J.L.; Zikovsky, J.; Rezeq, M.; Dogel, S.; Hofer, W.A.; Wolkow, R.A. *Nature* **435**, 658 (2005)
- [98] Dobrin, S.; Harikumar, K.R.; Jones, R.V.; Li, N.; McNab, I.R.; Polanyi, J.C.; Sloan, P.A.; Waqar, Z.; Yang, J.; Ayissi, S.; Hofer, W.A. *Surf. Sci.* **600**, L43 (2006)
- [99] Moreno-Herrero, F.; de Jager, M.; Dekker, N.H.; Kanaar, R.; Wyman, C.; Dekker, C. *Nature* **437**, 440 (2005)
- [100] Guise, O.L.; Ahner, J.W.; Jung, M.C.; Goughnour, P.C.; Yates, J.T. *Nano Lett.* **2**, 191 (2002)
- [101] Kresse, G.; Hafner, J; *Phys. Rev. B* **47**, 558 (1993)
- [102] Kresse, G.; Furthmuller, J; *Phys. Rev. B* **54**, 11169 (1996)
- [103] Hofer, W.A.; Redinger, J. *Surf. Sci.* **447**, 51 (2000)
- [104] Palotas, K.; Hofer, W.A. *J. Phys.: Condens matter* **17**, 2705 (2005)

- [105] Stroschio, J.A.; Celotta, R. *J. Science* **306**, 242 (2004)
- [106] Bartels, L.; Meyer, G.; Rieder, K.-H. *Appl. Phys. Lett.* **71**, 213 (1997)
- [107] Jiang, G.P.; Polanyi, J.C.; Rogers, D. *Surf. Sci.* **544**, 147 (2003)
- [108] Sloan, P.A.; Palmer, R.E. *Nature* **434**, 367 (2005)
- [109] Lastapis, M.; Martin, M.; Riedel, D.; Hellner, L.; Comtet, G.; Dujardin, G. *Science* **308**, 1000 (2005)
- [110] Zumbusch, A.; Fleury, L.; Brown, R.; Bernard, J.; Orrit, M. *Phys. Rev. Lett.* **70**, 3584 (1993)
- [111] Dickson, R.M.; Cubitt, A.B.; Tsien, R.Y.; Moerner, W.E. *Nature* **388**, 355 (1997)
- [112] Stipe, B.C.; Rezaei, M.A.; Ho, W.; Gao, S. Persson, M.; Lundqvist, B.I. *Phys. Rev. Lett.* **78**, 4410 (1997)
- [113] Sloan, P.A.; Hedouin, M.F.G.; Palmer, R.E.; Persson, M. *Phys. Rev. Lett.* **80**, 3085 (1998)
- [114] Dujardin, G.; Mayne, A.; Robert, O.; Rose, F.; Joachim, C.; Tang, H. *Phys. Rev. Lett.* **80**, 3085 (1998)
- [115] Shih, C.K.; Feenstra, R.M.; Martensson, P.J. *Vac. Sci. Technol. A* **8**, 3379 (1990)
- [116] Mayne, A.J.; Lastapis, M.; baffou, G.; Soukiassian, L.; Comtet, G.; Hellner, L.; Dujardin, G. *Phys. rev. B* **69**, 045409 (2004)
- [117] Lauhon, L.J.; Ho, W. *J. Chem. Phys.* **111**, 5633 (1999)
- [118] Trenhaile, B.R.; Antonov, V.N.; Xu, G.J.; Nakayama, K.S.; Weaver, J.H. *Surf. Sci.* **583**, L135 (2005)
- [119] Dobrin S., Harikumar K.R. and Polanyi J.C. *J. Phys. chem. B* **110**, 8010 (2006)
- [120] Dobrin S., Harikumar K.R., Jones R.V., McNab I.R., Polanyi J.C., Waqar Z. and Yang J. (S Y) Molecular dynamics of haloalkane corral-formation and surface halogenation at Si(111)-7×7 *J. Chem. Phys.* **125**, 133407 (2006)
- [121] M.F. Crommie, C.P. Lutz, D.M. Eigler *Science* **262**, 218 (1993)
- [122] H.C. Manoharan, C.P. Lutz, D.M. Eigler *Nature* **403**, 512 (2000)
- [123] S.-W. Hla, K.F. Braun, K.-H. Rieder *Phys. Rev. B* **67**, 201402(R) (2003)
- [124] A. Aviram, M.A. Ratner *Chem. Phys. Lett.* **29**, 277 (1974)
- [125] C. Joachim, J.K. Gimzewski, A. Aviram *Nature* **408**, 541 (2000)
- [126] R.A. Wolkow *Ann. Rev. Phys. Chem.* **50**, 413 (1999)

- [127] M.A. Rezaei, B.C. Stipe, W. Ho *J. Chem. Phys.* **110**, 4891 (1999)
- [128] P.H. Lu, J.C. Polanyi, D. Rogers *J. Chem. Phys.* **111**, 9905 (1999)
- [129] S. Alavi, R. Rousseau, S.N. Patitsas, G.P. Lopinski, R.A. Wolkow, T. Seideman *Phys.Rev. Lett.* **85**, 5372 (2000)
- [130] S.L. Silva, F.M. Leibsle *Surf. Sci.* **441**, L904 (1999)
- [131] L. Giancarlo, D. Cyr, K. Muyskens, G.W. Flynn *Langmuir* **14**, 1465 (1998)
- [132] D.E. Brown, D.J. Moffatt, R.A. Wolkow *Science* **279**, 542 (1998)
- [133] S. Dobrin, S. Lu, F.Y. Naumkin, J.C. Polanyi, J.(S.Y.) Yang *Surf. Sci.* **573**, L363 (2004)
- [134] M. Dubois, C. Delerue, G. Allan *Phys. Rev. B* **71**, 165435 (2005)
- [135] J.J. Boland, J.S. Villarrubia *Phys. Rev. B* **41**, 9865 (1990)
- [136] S. Dobrin, K.R. Harikumar, C.F. Matta, J.C. polanyi *Surf. Sci.* **580**, 39 (2005)
- [137] R.J. Hamers, R.M. Tromp, J.E. Demuth *Phys. rev. lett.* **56**, 1972 (1986)
- [138] J.E. Northrup *Phys. Rev. lett.* **57**, 154 (1986)
- [139] G. Binnig, H. Rohrer, Ch. Gerber, E. Weibel *Phys. Rev. lett.* **50**, 120 (1983)
- [140] T. Sakurai, Y. Hasegawa, T. Hashizume, A. Kamyia, I. Ide, I. Sumita, H.W. Pickering, S. Hyodo *J. Vac. Sci. Tech. A* **8**, 259 (1990)
- [141] J.P. Perdew, J.A. Chevary, S.H. Vosko, K.A. Jackson, M.R. Pederson, D.J. Singh, C. Jiolhais *Phys. Rev. B* **46**, 11169 (1996)
- [142] W.A. Hofer, A.S. Foster, A.L. Shluger *Rev. mod. Phys.* **75**, 1287 (2003)
- [143] Barlow, S.M.; Raval, R. *Surf. Sci. Rep.* **50**, 201 (2003)
- [144] Raval, R. *Curr. Opin. Solid. State Mater. Sci.* **7**, 67 (2003)
- [145] Ortega Lorenzo, M.; Baddeley, C.J.; Muryn, C.; Raval, R. *Nature* **404**, 376 (2000)
- [146] Ortega Lorenzo, M.; Haq, S.; Bertrams, T.; Murray, P.; Raval, R.; Baddeley, C.J. *J. Phys. Chem. B* **103(48)**, 10661 (1999)
- [147] Humblot, V.; Haq, S.; Muryn, C.; Hofer, W.; Raval, R. *J. Am. Chem. Soc.* **124**, 503 (2002)
- [148] Jones, T.E.; Baddeley, C.J. *Surf. Sci.* **513**, 453 (2002)
- [149] Jones, T.E.; Baddeley, C.J. *Surf. Sci.* **519**, 237 (2002)

- [150] Ernst, K.H.; Kuster, Y.; Fasel, R.; Muller, M.; Ellerbeck, U. *Chirality* **13**, 675 (2001)
- [151] Ortega Lorenzo, M.; Humblot, V.; Murray, P.; Baddeley, C.J.; Haq, S.; Raval, R. *J. Catal.* **205**, 123 (2002)
- [152] Raval, R. *CATTECH* **5**, 12 (2001)
- [153] Zhao, X. *J. Am. Chem. Soc.* **122**, 12584 (2000)
- [154] Kuhnle, A.; Linderoth, T.R.; Hammer, B.; Besenbacher, F. *Nature* **415**, 891 (2002)
- [155] De Feyter, S.; Gesquiere, A.; Wurst, K.; Amabilino, D.B.; Veciana, J.; De Schryver, F.C. *Angew. Chem., Int. Ed.* **40**, 3217 (2001)
- [156] Barth, J.V.; Wechesser, J.; Trimarchi, G.; Vladimirova, M.; De Vita, A.; Cai, C.; Brune, H.; Gunter, P.; Kern, K. *J. Am. Chem. Soc.* **124**, 7991 (2002)
- [157] Lopinski, G.P.; Moffat, D.J.; Wayner, D.D.; Wolkow, R.A. *Nature* **392**, 909 (1998)
- [158] Barlow, S.M.; Kitching, K.J.; Haq, S.; Richardson, N.V. *Surf. Sci.* **401**, 322 (1998)
- [159] Weckesser, J.; Barth, J.V.; Cai, C.; Muller, B.; Kern, K. *Surf. Sci.* **431**, 168 (1999)
- [160] Schunack, M.; Petersen, L.; Kuhlne, A.; Laegsgaard, E.; Stensgaard, I.; Johansen, I.; Besenbacher, F. *Phys. Rev. Lett.* **86**, 456 (2001)
- [161] Viswanathan, R.; Zasadzinski, J.A.; Schwartz, D.K. *Nature* **368**, 440 (1994)
- [162] Bohringer, M.; Mortenstern, K.; Schneider, W.-D.; Berndt, R. *Angew. Chem. Int. Ed.* **38**, 821 (1999)
- [163] McFadden, C.F.; Cremer, P.S.; Gellman, A.J. *Langmuir* **12**, 2483 (1996)
- [164] Attard, G.A. *J. Phys. Chem. B* **105**, 3158 (2001)
- [165] Scholl, D.S.; Asthagiri, A.; Power, T.D. *J. Phys. Chem. B* **105**, 4771 (2001)
- [166] Barbosa, L.A.M.M.; Sautet, P. *J. Am. Chem. Soc.* **123**, 6639 (2001)
- [167] W.H. Weinberg *Ann. Rev. Phys. Chem.* **34**, 217 (1983)
- [168] L.D. Roelofs and P.J. Estrup *Surf. Sci.* **125**, 51 (1983)
- [169] E. Bauer in *Structure and Dynamics of Surfaces II*, edited by R. Vanselow and R. Howe, Springer, Berlin (1987)
- [170] B.N.J. Persson *Surf. Sci. Rep.* **15**, 1 (1992)
- [171] L.D. Roelofs in *Handbook of Surface Science Vol. 1*, edited by W.N. Unertl, Elsevier, Amsterdam (1996)
- [172] J. Greeley and M. Mavrikakis *Surf. Sci.* **540**, 215 (2003)

- [173] K. Reuter and M. Scheffler *Phys. Rev. Lett.* **90**, 046103 (2003)
- [174] W. Zhang, J.R. Smith and X.G. Wang *Phys. Rev. B* **70**, 024103 (2004)
- [175] A. van de Walle and G. Ceder *Rev. Mod. Phys.* **74**, 11 (2002)
- [176] Masel, R.I.; Ed. Principles of Adsorption and Reaction on Solid Surfaces; Wiley Series in Chemical Engineering; Wiley: New York (1996)
- [177] Raval, R. *J. Phys.: Condens. Matter* **14**, 4119 (2002)
- [178] V. Blum and A. Zunger *Phys. Rev. B* **70**, 155108 (2004)
- [179] S. Dobrin, K.R. Harikumar, T.B. Lim, I.R. McNab, J.C. Polanyi, P.A. Sloan, Z. Waqar, J.(S.Y.) Yang, S. Ayissi, W.A. Hofer *Nanotechnology* **18**, 044012 (2007)
- [180] V. Humblot, M.O. Lorenzo, C.J. Baddeley, S. Haq, R. Raval *J. Am. Chem. Soc.* **126**, 6460 (2004)
- [181] R.O. Jones and O. Gunnarsson *Rev. Mod. Phys.* **61**, 689 (1989)
- [182] M. Levy *Proc. Natl. Acad. Sci. USA* **76**, 6062 (1979)
- [183] J.E. Harriman, *Phys. Rev. A* **24**, 680 (1981)
- [184] Hamann et al., *Phys. Rev. Lett.* **43**, 1494 (1979)
- [185] G. Kresse, D. Joubert, *Phys. Rev. B* **59**, 1758 (1999)
- [186] J. Harris and R.O Jones, *J. Phys. F* **4**, 1170 (1974)
- [187] Parr and Yang, Density-Functional Theory of atoms and molecules, *Oxford University Press* (1989)
- [188] Perdew, and Zunger, *Phys. Rev. B* **23**, 5048 (1981)
- [189] Langreth and Mehl, *Phys. Rev. B* **28**, 1809 (1983)
- [190] Becke, *Phys. Rev. A* **38**, 3098 (1988)
- [191] P. Perdew and Y. Wang, *Phys. Rev. B* **33**, 8800 (1986)
- [192] Lee et al., *Phys. Rev. Lett.* **60**, 163 (1988)
- [193] Perdew et al., *Phys. Rev. B* **46**, 6671 (1992)
- [194] Perdew et al., *Phys. Rev. Lett.* **77**, 3865 (1996)
- [195] Zhang and Yang, *Phys. Rev. Lett.* **80**, 890 (1998)
- [196] E.H. Lieb and S. Oxford, *Int. J. Quantum Chem.* **19**, 427 (1981)
- [197] Hammer et al., *Phys. Rev. B* **59**, 7413 (1999)

- [198] Teter et al., *Phys. Rev. B* **40**, 12255 (1989)
- [199] Davidson *Phys. Rev. Lett.* **50**, 1339 (1983)
- [200] D.M. Wood and A. Zunger *J. Phys. A* **18**, 1343 (1985)
- [201] P. Pulay *Chem. Phys. Lett.* **73**, 393 (1980)
- [202] Methfessel and Paxton, *Phys. Rev. B* **40**, 3616 (1989)